# Effects of Flange Holes on Flexural Behavior of Steel Beams

# EFFECTS OF FLANGE HOLES ON FLEXURAL BEHAVIOR OF STEEL BEAMS

**By**
**P. (Lathan) Arasaratnam**
**M.A.Sc**

A Thesis
Submitted to the School of Graduate School
In Partial Fulfillment of the Requirements
For the Degree of
Doctor of Philosophy

McMaster University

Doctor of Philosophy (2008)
(Civil Engineering)

McMaster University
Hamilton, Ontario

TITLE: Effects of Flange Holes on Flexural Behavior of Steel Beams

AUTHOR: P. (Lathan) Arasaratnam
M.A.Sc
McMaster University, Ontario, Canada

SUPERVISORS: Dr. K.S. Sivakumaran and Dr. M.Tait

NUMBER OF PAGES: xxv, 350

To My Dad
Who left me, midway through my PhD.

"The Best Preparation for Tomorrow is to do today's work very well."
This was my father's motto, and this is one of many lessons that he taught me.

You were, are and will always be my beacon of Strength, Character, and Hard work just to name a few.
I humbly dedicate this thesis to My Dad

# ABSTRACT

When fastener holes are made in structural beams, the Canadian Steel Design Code CAN/CSA-S16.01 -Clause 14.1 (CSA, 2003) states that no deduction in flexural strength is needed for holes up to 15% of the gross flange area. This clause was established many years ago, however, over the years the mechanical characteristics of structural steel have changed. This research study focused on the effects of flange holes on the flexural behavior of steel I-beams made of ASTM A992 steel. This study was conducted primarily based on an experimental investigation involving 25 beam specimens. Holes of various diameters, ranging form 0% to 48% of the gross flange area were laid by drilling holes (a) in the midspan of the tension flange and (b) in the midspan of both the tension and compression flanges. Additionally, beams having holes with fasteners (snug tight) were performed. Based on the test results, this study recommended a design approach, which is analogous to an axial tension member provision as per the current CAN/CSA-S16.01 (CSA, 2003) standard. Accordingly, the effects of holes on the flexural strength can be ignored if the gross-section plastic moment is greater than a modified net-section fracture moment hence, beam members shall be designed to carry the gross-section plastic moment. Otherwise, the beam members shall be designed to carry the modified net-section fracture moment. The comparison of the recommended procedure with the 15% exemption rule as per current steel standard S16.01 (CSA, 2003) demonstrated that the current code provision is unnecessarily conservative for steel grades such as A992 steel. On the other hand, the current provision may be more unconservative for high

strength steels such as HSLA 80 steel, ASTM A913 Grade 60 and HPS-485W having a minimum yield-to-ultimate strength ratio value of more than 0.85.

The analytical portion of the research study involved the application of nonlinear finite element method to verify and comprehend the experimental results. The analytical study was conducted using ADINA FE program. The test beams were modeled using 4-node shell element that includes both geometric and material nonlinearities. The material model utilized in the FE analysis was developed based on the experimental-numerical simulation of standard tensile coupons.

ACKNOWLEDGEMENTS

Firstly, I wish to express my deep gratitude to my advisors Prof. Sivakumaran and Prof. Tait for their interest, encouragement and insight throughout this research. Their constructive criticism had a major impact on developing my way of thinking and research.

To my supervisory committee members, Prof. Dieter Stolle and Prof. Mukesh Jain. Thank you for your constant enthusiasm in my work and the knowledge you have shared with me from your respective areas of expertise.

I would like to thank Mr. Sandesh Acharya for his valuable discussion and assistance over more than three years. A word of thanks is due to the summer students Mr. Niel Van England and Mr. Paul Herema for their help during the experimental work at Applied Dynamic Laboratory. Also, I would like to thank the lab technicians Mr. David Parret, Mr. Maurice Forget, Mr. Peter Koudys and Mr. Kent Wheeler for their assistance in the laboratory. Thanks to Mrs. Carol Robinson, Mrs. Rebecca Woodworth and Mrs. Tatiana Dobrovolska, of the Civil Engineering Department, for their assistance and support with many administrative duties during my graduate studies.

The financial supports of the Dept. of Civil Engineering, McMaster University and the CISC-Steel Structures Education Foundation are gratefully acknowledged. The donation of test beams by the Dymin Steel Suppliers is gratefully acknowledged.

Last, but by no means least, I would like to say that no words can express my gratitude to my mum, Mrs. Ranjinidevi Arasaratnam for everything she does for me. Special thanks are due to my elder brother Mr. Bremillan Arasaratnam and my younger brother Mr. Ienkaran Arasaratnam and my sister Mrs. Karthika Premendra. Without their continuous support, love, prayer and encouragement throughout my life I would have never been the one I am now.

# NOTATIONS AND ABBREVIATIONS

## Abbreviations

AISC-American Institute of Steel Construction

AS4100-Australian Standard for the Design of Steel Structures

BS5950-British Standard for the Design of Steel Structures

CISC-Canadian Institute of Steel Construction

CSA-Canadian Standard Association

LRFD-Load and Resistance Factor Design

OWSJ-Open Web Steel Joist

## Notations

| | |
|---|---|
| $A$ | - Cross-sectional area |
| $A_{fe}$ | - Effective flange area |
| $A_{fn}$ | - Net flange area |
| $A_{fg}$ | - Gross flange area |
| $A_{fh}$ | - Flange hole area |
| $A_g$ | - Gross cross-section area |
| $A_n$ | - Net cross-section area |
| $A_{wg}$ | - Gross web area |
| $b$ | - Flange width |

$d$ - Beam depth

$E$ - Elastic modulus

$E_{sh}$ - Strain hardening modulus

$e_f$ - Elongation at fracture

$F_u$ - Tensile strength

$F_{un}$ - Ultimate strength of perforated sample

$F_{u,t}$ - True stress value corresponding to onset of necking

$F_y$ - Yield strength

$h$ - Web height

$I_{fh}$ - Second moment of area of flange holes about neutral axis of net-section

$I_{fhe}$ - Effective second moment of area of flange holes

$I_g$ - Second moment of area of gross cross-section

$I_n$ - Second moment of area of net cross-section

$K_e$ - Effective net area coefficient

$L$ - Clear span length (support to support distance)

$L_{cr}$ - Critical unbraced length

$L_m$ - Midspan length

$L_s$ - Shear span length

$M$ - Moment

$M_d$ - Design moment calculated based on code provisions

$M_{dp}$ - Design moment calculated based on proposed method

$M_{fn}$ - Calculated net-section fracture moment ($Z_n F_u$)

$M_{fnm}$ - Modified net-section fracture moment ($0.85\, Z_n F_u$)

$M_m$ - Maximum measured moment

$M_p$ - Calculated gross-section plastic moment based on measured material properties and measured cross-sectional dimensions (mean value)

$M_{pi}$ - Calculated gross-section plastic moment based on measured material properties and measured cross-sectional dimensions of each individual beam

$M_{pl}$ - Proportional moment obtained experimentally

$M_{p-nom}$ - Nominal plastic moment

$M_y$ - Calculated yield moment based on measured material properties and measured cross-sectional dimensions (mean value)

$M_{yi}$ - Calculated yield moment based on measured material properties and measured cross-sectional dimensions of each individual beam

$m$ - Ratio between the strain at strain hardening and yield strain

$n$ - Material constant

$P$ - Load

$P_m$ - Maximum measured load

$P_p$ - Calculated gross-section plastic load (mean value)

$P_{pi}$ - Calculated gross-section plastic load for each individual beam

| | |
|---|---|
| $P_{pl}$ | - Proportional load obtained experimentally |
| $P_{p-nom}$ | - Nominal plastic load |
| $P_u$ | - Ultimate measured load |
| $P_y$ | - Calculated yield load (mean value) |
| $P_{yi}$ | - Calculated yield load for each individual beam |
| $R_m$ | - Rotation capacity corresponding to maximum moment |
| $R_y$ | - Total available rotation capacity |
| $r_y$ | - Radius of gyration about minor axis of bending |
| $S_x, S_g$ | - Elastic section modulus of gross cross-section |
| $S_n$ | - Elastic section modulus of net-section |
| $t$ | - Flange thickness |
| $w$ | -Web thickness/ weighting factor |
| $Z_x, Z_g$ | - Plastic section modulus of gross cross-section |
| $Z_n$ | - Plastic section modulus of net cross-section |
| $\bar{y}$ | - Shift in neutral axis of net section w.r.t the neutral axis of gross section |
| $\rho_h$ | - Ratio between hole area and gross flange area |
| $\varepsilon_e$ | - Engineering strain |
| $\varepsilon_f$ | - Strain at facture |
| $\varepsilon_{f,t}$ | - True strain at fracture |

$\varepsilon_t$ - True strain

$\varepsilon_u$ - Strain at ultimate stress (engineering)

$\varepsilon_{u,t}$ - True strain value corresponding to onset of necking

$\varepsilon_y$ - Yield strain (engineering)

$\Delta_f$ - Midspan deflection at fracture

$\Delta_m$ - Midspan deflection corresponding to maximum load

$\Delta_y$ - Midspan deflection corresponding to yield load

$\Delta_p$ - Midspan deflection corresponding to plastic load under ideal elastic perfectly plastic behavior (mean value)

$\Delta_{pi}$ - Elastic midspan deflection corresponding to plastic load under ideal elastic-perfectly plastic behavior associated with individual beam member

$\Delta_p^+$ - Midspan deflection corresponding to plastic moment on the ascending branch

$\Delta_p^-$ - Midspan deflection corresponding to plastic moment on the descending branch

$\Delta_{p-nom}$ - Midspan deflection corresponding to nominal plastic load under ideal elastic Perfectly plastic behavior

$\theta_{ep}$ - End rotation corresponding to plastic moment under ideal elastic perfectly plastic behavior (mean value)

$\theta_{epi}$ - End rotation corresponding to plastic moment under ideal elastic perfectly plastic behavior associated with individual beam member

$\theta_{ep-nom}$ - Nominal end rotation corresponding to nominal plastic moment under ideal elastic perfectly plastic behavior

$\theta_f$ - Rotation corresponding to fracture moment

$\theta_m$ - Rotation corresponding to maximum moment

$\theta_p$ - Rotation corresponding to plastic moment under ideal elastic-perfectly plastic behavior (mean value)

$\theta_{pi}$ - Rotation corresponding to plastic moment under ideal elastic-perfectly plastic behavior associated with individual beam member

$\theta_p^+$ - Rotation corresponding to plastic moment on the ascending branch

$\theta_p^-$ - Rotation corresponding to plastic moment on the descending branch

$\theta_{p-nom}$ - Nominal rotation corresponding to nominal plastic moment under ideal elastic perfectly plastic behavior

$\theta_y$ - Rotation corresponding to yield moment

# TABLE OF CONTENTS

# LIST OF TABLES

## LIST OF FIGURES

# CHAPTER: 1

# INTRODUCTION

## 1.1 Introduction

It is often necessary to have holes in the flanges and webs of steel beams for a wide variety of reasons such as installation of fasteners for connections, passages for tie rods, pipes, conduits, ducts, etc. In this document, unless otherwise specified, holes denote open holes and fastener holes. As a general rule, holes in the flanges should be avoided in high moment regions and holes in the webs should be avoided in high shear regions. In practice, however, it is not always possible to avoid the placement of holes in flanges in high moment regions. An example of such a situation is bolted flange plate connections in steel building frames. It should be noted that holes for passing pipes, conduits, ducts, etc. through the webs tend to be large holes and should be completely avoided in the flanges of flexural members. The analysis of the impact of such large holes on the flexural behavior of steel members is beyond the scope of this study.

The primary focus of this study is to investigate the effects of flange holes on the flexural behavior of steel I-beams made of ASTM A992 steel. In this document, a distinction is made between open holes and fastener holes. An open hole is defined as a hole with no fasteners. A fastener hole is defined as a hole with a sung-tight fastener of standard size and the fastener transmits loads by means of bearing. Figure 1.1 shows the difference between [A] an open hole and [B] a fastener hole under tension and compression. Note that the figure relates a single plate, which simulates the tension and compression flanges of a flexural member. In this thesis, unless otherwise specified, general reference of holes means open holes and fastener holes.

The presence of either open holes or fastener holes in a tension member reduces its load carrying capacity. Various research studies (Kulak et al., 1995) have provided relevant data to establish net area formulas and design provisions that account for the effects of holes in direct tension members. Thus, tension members are always designed on the basis of net section area. However, unlike a tension member, a compression member having fastener holes is generally designed on the assumption that its gross cross section is effective in resisting the applied load. For the case of fastener holes in a compression member, it is assumed that the bolt can adequately transmit the compression load across the hole. Since the bolts effectively replace the material removed by the holes, fastener holes in a compression member have no weakening effect (Williams and Harris, 1957). On the contrary, open holes will weaken a compression member.

The behavior of the tension flange with holes in a flexural member is significantly different than that of an axial tension member with holes. An axial tension member fractures once the net section reaches its tensile strength ($A_n F_u$). Thus, the design load of axial tension members with holes shall be established based on net section area as per the current code provisions. However, the deformation of the tension flange in a flexural member may be limited by the restraint provided by the web. Therefore, the strain across the net flange section cannot increase rapidly without a corresponding localization of strain in the web (Dexter et al., 2002). This inherent behavior due to flange-web interaction of a flexural member might have encouraged the code writers to ignore a certain percentage of holes with respect to the gross flange area without penalizing its full plastic moment capacity (provided that the beam is adequately braced).

## 1.2 Practical Applications - Flexural Members Having Flange Holes

This section briefly describes a few practical applications of flexural members having holes in their flanges. These applications include: bolted flange plate connections in moment resisting frames; column-tree moment-resisting frames; beam bearing on bottom flange girder connection; the assemblage of Gerber-girder system with open-web steel joists (OWSJ); Crane runways of an overhead crane; and splice connections.

***Bolted Flange Plate connection in Moment Resisting Frames***: Structural steel frames, including building frames, may be constructed either by welding the structural members together or by bolting the members together, or by both welding and bolting. In fact, ever since welded connections exhibited brittle fractures during the 1994 Northridge earthquake, bolted flange plate connections are considered to be an attractive alternative

(Schneider and Teeraparabwong 2002). Figure 1.2 shows a bolted flange plate moment connection. It is often necessary to have holes in the flanges of the steel flexural members (beams, joints, girders, etc.), for this type of connection. In this connection, the flange plates were shop welded to the column while the field assembly of the beam-to-column joint was fully bolted. In such a connection, the critical moment may occur at the end of the beam. Therefore, the effect of flange and/or web holes must be properly considered.

***Column-tree Moment Resisting Frames***: In a column-tree moment-resisting frame system, short segments of a girder, usually 300 mm-900 mm, are welded to the columns in the shop and the middle segment of the girder is erected in the field and bolted to the end of the short girder stub as shown in Figure 1.3. Therefore, the system is a shop-welded, field-bolted steel structure. The shop-welded, field-bolted column-tree system is ideal for construction during cold weather as well as for projects where field welding is too costly or cannot be easily done. During the 1995 Great Hanshin earthquake, the modern engineered steel column-tree systems in the affected areas performed well (Astaneh-ASL 1997). For this type of connection, the critical moment may occur in the bolted connection region. Thus, the design of the middle segment of the girder must take into account flange and/or web fastener holes.

***Connections with Beam Bearing on Bottom Flange Girder***: A new type of beam-to-girder connection has recently been proposed in building construction in the United States. This connection consists of the beam bearing directly on the bottom flange of the girder, as illustrated in Figure 1.4. This type of connection is useful with deep deck (more than 75 mm) composite slabs in order to offset the increase in the floor depth caused by additional slab depth as well as with commonly used deck depths (less than or equal to 75 mm) in which floor-to-floor height needs to be minimized. This connection is economical and easy to construct (Lee 2001). A lateral stabilizing angle and erection bolts through the bottom flange are required to complete this construction. In this case, the critical moments in the main girder may occur in the hole region thus, the effects of holes in the tension flange needs to be considered.

***Gerber-Girder System with OWSJs***: Open-web steel joists (OWSJ) and Gerber-girder system are popular combination of roofing system in single storey buildings and in low-rise buildings. Figure 1.5 shows a typical layout of a Gerber girder system with OWSJ. A relatively new requirement in the Occupational Safety and Health Administration regulations for open web steel joist erection in the USA (OSHA 2004) stipulates that connection of individual steel joists to steel structures in bays spanning 12 m (≈ 40 feet) or more shall be fabricated to allow for field bolting of joists during erection. There is a possibility that this trend may be introduced in Canada through Provincial Health and Safety Boards (CISC 2007). This Regulation warrants fabrication of round or slotted holes in open-web steel joist bearing seats and the flanges of supporting girders. Note that these bolts are temporary erection bolts and that the final connection must be made by welding or by other means. Though the joist manufactures recommend that bolts be left in the holes, the bolts are not intended to transfer any load from one member to another), this is an example for holes with fasteners.

***Crane Runway***: Several different types of cranes, such as overhead traveling, under slung, gantry, and monorail, are commonly in use. The overhead traveling crane is the most common in heavy industrial type buildings as they are able to carry the heaviest loads (Ricker 1982). As seen in Figure 1.6, the crane beam bottom flanges are bolted to the crane column and the top flanges are bolted to the rail. In order to fasten the crane beam by bolting, holes must be made in the flanges. Therefore, the design of a crane beam, which is to withstand the primary loads due to vertical loading including impact through flexure and shear must consider the influence of holes in the flanges of the beam.

***Splices***: Splice connections are often required in beams/girders when the lengths of members are limited by fabrication, transportation, or the handling facility. A commonly used field splice is one that is made with cover plates which are connected to the main members by bolting (Kulak and Green, 1990). In practical applications, field splices are preferably located at points of dead load contraflexure or reasonably close to it. This is usually done based on the assumption that a splice is a weak point and failure can occur at this point. However, various studies have demonstrated that bolted splices do not create weak points (Douty and McGuire, 1965, Fisher and Struik, 1974). This research was further reinforced by the statement by Kulak et al., (1987) that "the properly proportioned flange splice can carry the full moment capacity of the cross section".

Figure 1.7 shows a bolted splice connection. In bolted splice connections, the ultimate flexural strength of the member may be reduced by the holes. Therefore, the fastener holes must be taken into account in designing the member strength.

***Cover-Plated Beam/Girder:*** Cover plated beams/girders are used in new bridge construction and bridge renovation or restoration projects. Additional plates are added to the flanges to increase the moment capacity of existing beams/girders. In general, the cover plates are fastened to primary beam sections either by welding or by bolting. Figure 1.8 shows a typical cross section view of a cover plated I-section. It can be seen from Figure 1.8, that holes are needed in the flanges of beam sections to fasten the cover plates to the primary beam.

## 1.3 Problem Statement

The influence of holes in the flanges and/or webs on the flexural behavior of steel beams has been a topic of debate for many years. Early North American design codes permitted a designer to place holes in the flange up to 15% of the gross flange area. If holes remove more than 15%, the section properties shall be calculated on the basis of area removed that are in excess of 15%. Typically, only the yield moment would be used at the hole locations (AISC 1963). The 15% exemption provision was developed based on Lilly and Carpenter's (1939) study on riveted plate girders made of ASTM A7 steel having a yield-to-tensile strength ratio of 0.5. This provision was also supported by the findings of other researchers that followed (Douty and McGuire, 1965).

The current trend in steel construction industry is to use higher strength steels such as ASTM A992, A913 Gr.50, A913 Gr.65, HPS 50W and HPS 70W, which have better structural performance over traditionally used steel grades such as ASTM A7 and A36 steels. High strength steels generally exhibit a higher yield-to-ultimate strength ratio than conventional structural steels. The yield-to-ultimate strength ratio is the primary factor in determining the percentage of holes to the gross flange area that can be ignored in the design of flexural members with flange holes (Dexter et al., 2002 and Yuan, 2004). In addition, the 15% exemption rule as per the early North American standards does not take into account the strain hardening potential of a material in terms of the yield-to-ultimate strength ratio.

The question that arises when the flanges and/or webs of a flexural member have holes in the critical moment regions is: what effects do these holes have on the strength of the net section? Various international standards provide different procedures to account for holes in the flanges and/or webs of flexural members. Clause 14.1 of the CAN/CSA-S16.01 (CSA 2003) standard still uses the 15% exemption rule, even for high strength steels; in proportioning the flexural members having fastener holes in the flanges. The CSA (2003) code provision treats the case of fastener holes differently, in which net-section calculation shall be applied for holes other than fastener holes (i.e., no exemption is permitted for open holes in the flanges of a beam/girder).

A comparison of several international code provisions demonstrates that the 15% exemption rule as per the current CAN/CSA-S16.01 (CSA 2003) standard is more restrictive for widely used structural steel grades such as 350W steel. Conversely, the 15% exemption rule may be unconservative for high strength/high performance steels having yield-to-ultimate strength ratios of more than 0.8.

This study investigates the impact of flange open holes and fastener holes on the flexural behavior of steel beams. The beams investigated were W-shaped sections conforming to ASTM A992 steel grade. The following factors provided the impetus for this study;

- During the 1994 Northridge earthquake flange welded web-bolted type connections fractured in more than 200 moment-resisting steel frame buildings in the Los Angeles region (Teeraparbwong 2001). Since then a fully field bolted flange plate connection alternative has been proposed for use in steel moment resisting frames. In a fully bolted connection, holes need to be made in the flanges and/or webs of a beam member. If the holes occur in the critical moment region, the strength of the flexural member may be altered. Therefore, it is essential to have a design formula that can reliably predict the strength of such beams.
- Holes in the flanges and/or webs of a beam/girder member are required for other applications including Open-web steel joists with Gerber-girder system, crane run-

ways, splice connections, connections with the beam bearing on bottom flange girder, etc. A suitable design practice needs to be enforced for beam/girder having flange holes in the critical moment region in order to ensure they perform in a safe and reliable manner.

- A comparison of different international code provisions dealing with the issue on the proportion of flexural members having open holes and fastener holes in the flanges revealed that the current CAN/CSA-S16.01 (CSA 2003) standard (15% exemption rule) needs to be updated.
- Recently introduced high strength (high performance) steels such as ASTM A992, A913, HSLA 80 steel and HPS 485W, which are becoming popular in North America and elsewhere, exhibit higher yield-to-ultimate strength ratios, in some instances more than 0.85 (Dexter et al., 2002). The increase in yield-to-ultimate strength ratios of such steel grades may result in a lower amount of holes that can be ignored in the design of a flexural member without penalizing its gross cross-section moment capacity. Therefore, it is imperative that a design provision, addressing the proportion of flexural members having flange holes, considers the variation in yield-to-ultimate strength ratios of different steel grades.

## 1.4 Scope and Objective

The main objective of this study was to investigate the influence of flange holes on the flexural behavior of steel I-beams. To meet this objective, twenty five beam tests having holes of different percentage of net flange area-to-gross flange area ratios, were tested to establish the flexural behavior in terms of the strength and ductility. The mode of failure associated with each test was also established. The goal of this research was to develop a design process to accurately estimate the strength of a flexural member having holes in the flanges. Additionally, the following points were considered to be within the scope of this investigation:

- compare and assess the applicability of the 15% exemption rule in the current CAN/CSA-S16.01 (CSA 2003) standard along with the corresponding rules from various other international code provisions; AISC-LRFD (2005), AISC-LRFD (1999), BS5950 (BSI 2001) and AS4100 (SA 1998).
- develop FE model and verify the models with experiment results.
- develop an analytical model based on the experimental results on the issue of the proportion of flexural members having flange holes.
- provide a recommendation on the modification of the current CSA (2003) code provision.

## 1.5 Research Methodology

This study consisted of five main phases to achieve the scope and objectives.

- Phase-I: involved an experimental investigation of ASTM A992 steel flexural members. Beam specimens with holes (of various diameters) in the tension flange only, holes in both the tension and compression flanges, as well as holes with "snug-tight" fasteners of various diameters in both the tension and compression flanges were tested. All tests were performed as a simply supported beams subjected to two point load in the midspan.

- Phase-II: involved an experimental study of mechanical characteristics of ASTM A992 and 350W steel grades. The overall stress-stain relationship was established by performing standard tension coupon tests in accordance with the A370-02 specification (ASTM 2002). This phase also included the load-deformation behavior of tension members having a hole in the middle region (perforated samples). Holes of various diameters (i.e., different net area-to-gross area ratio values) were considered.
- Phase-III: dealt with the development of analytical material models that could capture the post ultimate strength behavior including fracture of a direct tension member. In the development of an analytical material model, an experimental-numerical analysis of standard tensile coupon was performed. The developed material constitutive relation was used to input the material characteristics in finite element (FE) models of the perforated tension samples. The load-deformation behavior of the test samples and that of the FE models were subsequently compared.
- Phase-IV: involved a numerical study using FE modeling of the test beams. The developed FE models were verified using the experimental results.
- Phase-V: proposed an analytical formula to predict the design moment at hole locations. The design moment calculation based on the proposed method was

compared with various code methods such as CSA (2003) code, AISC-LRFD (2005) code, AISC-LRFD (1999) code, BS5950 (BSI 2001) code and AS4100 (SA 1998) code. The relevant discussions and conclusions were made based on the applicability of the clause 14.1 of the current CAN/CSA-S16.01 (CSA 2003) standard.

## 1.6 Organization of the Thesis

The thesis comprises eight chapters which are organized as follows:

- **Chapter 2:**

covers the relevant studies and related issues on the effects of holes in the flanges and or/webs on flexural strength of steel beams. A brief introduction on the historical development of structural steel grades is also presented in this chapter.

- **Chapter 3:**

provides various international design provisions dealing with the proportion of flexural members having flange and/or web holes. This chapter also summarizes the application of different international code procedures by considering various scenarios such as: (1) holes in the tension flange only; (2) holes in both flanges; and (3) fastener holes in both flanges. In this chapter, theoretical calculation of the moment capacity based on the net-area concept is compared with the code methods.

- **Chapter 4:**

presents an experimental program including the test procedure associated with the flexural members having various (net flange area)-to-(gross flange area) ratio values. All of the instrumentation used in the test program, as well as the location and description of these equipments, are described in this chapter. The data reduction processes are also summarized.

- **Chapter 5:**

contains the test results associated with the twenty five flexural tests. Observations made during each beam test, associated failure modes are summarized in this chapter. A comparison of test results with the various code based estimations is provided. A design method has been proposed based on the experimental test results. The design moment calculations as per the proposed method and the code method have been compared.

- **Chapter 6:**

presents the mechanical characteristics of ASTM A992 steel and 350W steel grades, established using standard tensile coupon tests. Material constitutive relations were developed by simulating the experimental load-displacement behavior of standard tensile coupons. These material models were used in FE simulation of perforated samples having various net-area-to-gross area ratio values. The predicted load-displacement responses were compared with the test results of similar samples.

**Chapter 7:**

deals with a comparison study based on the FE method for the flexural experiments provided in Chapters 4 and 5. This chapter also presents details pertaining to the FE modeling technique used. The predicted global and local behaviors of flexural members were compared with the experimental results. The factors contributing to discrepancies of the experimental and numerical results were discussed.

- **Chapter 8:**

summarizes and concludes the important findings from this study. Additionally, this chapter recommends a design modification to Clause 14.1 of the current CAN/CSA-S16.01 (CSA 2003) standard, which is related to the proportion of flexural members with flange holes.

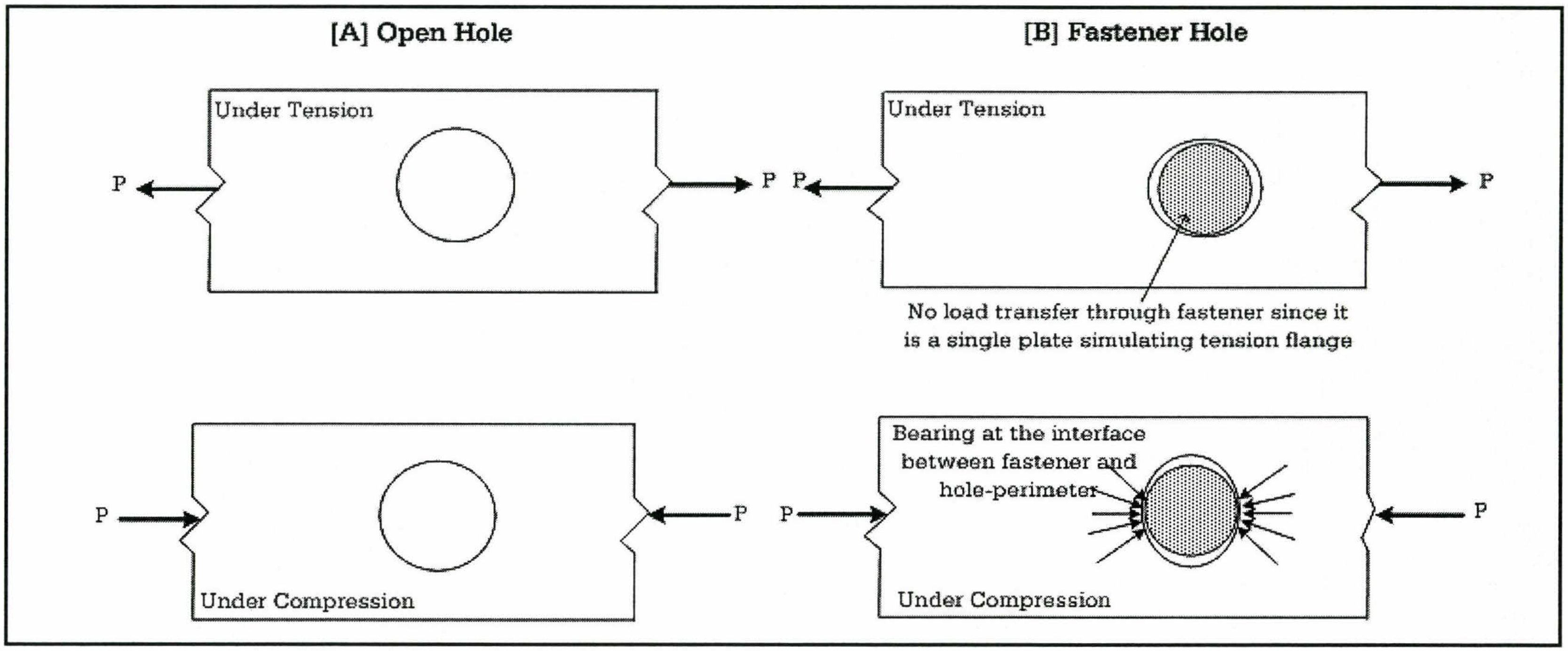


Figure 1.1: Differences between Open Hole and Fastener Hole under Tension and Compression Load

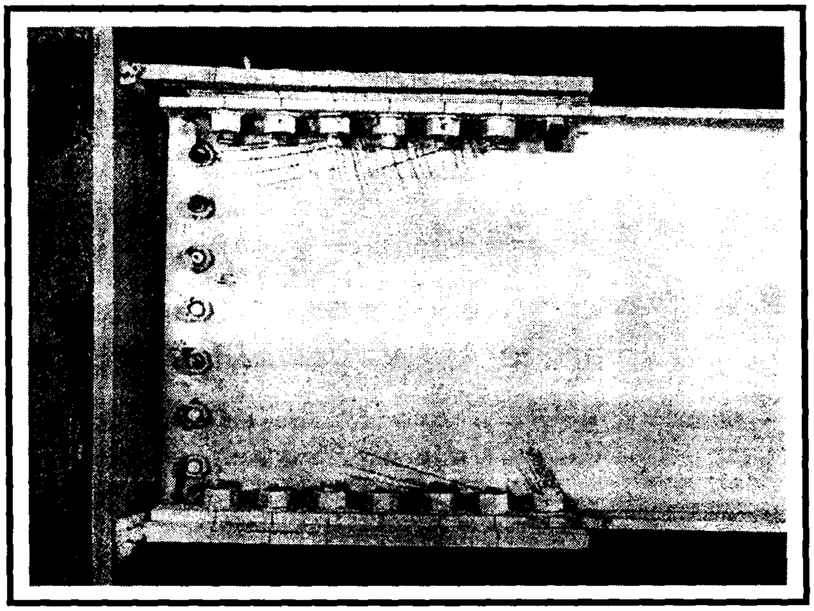

Figure 1.2: Typical Field Assembly of a Bolted Flange Plate Connection
(Chen and Patel, 1981)

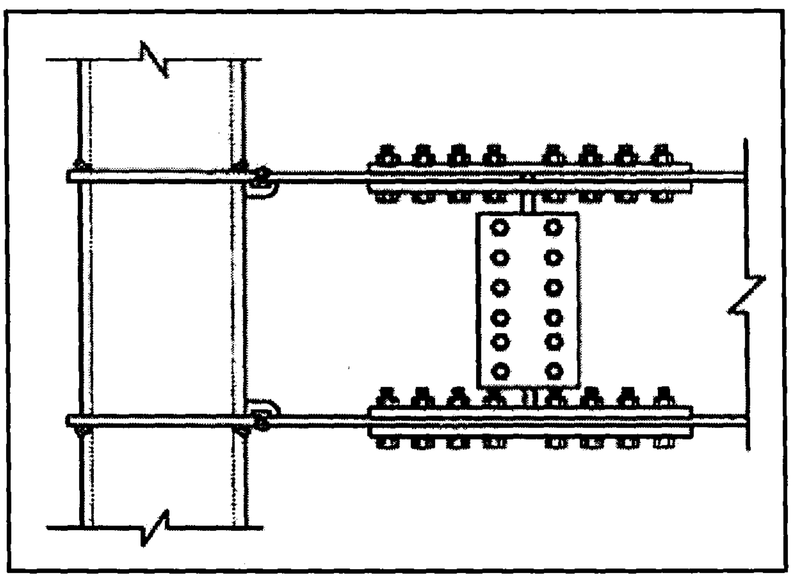

Figure 1.3: Typical Configuration of Column-Tree Moment-Resisting Frames
(Astaneh-Asl 1997)

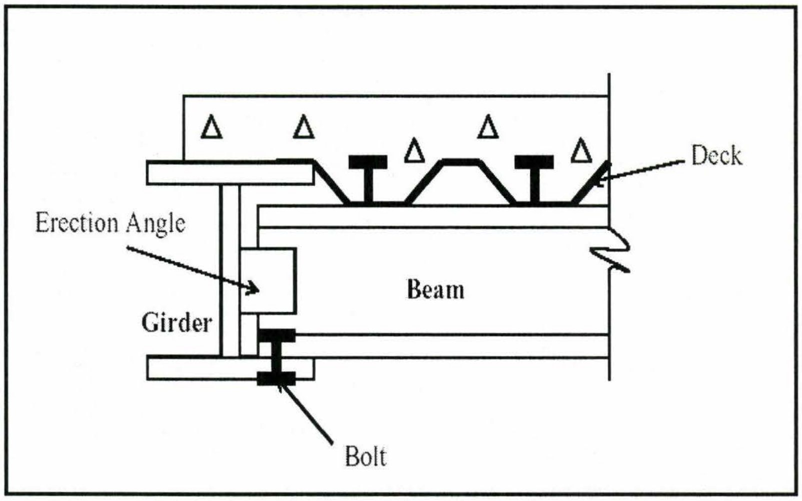


Figure 1.4: Typical Connection with Beam Bearing on Bottom Flange
(Lee 2001)

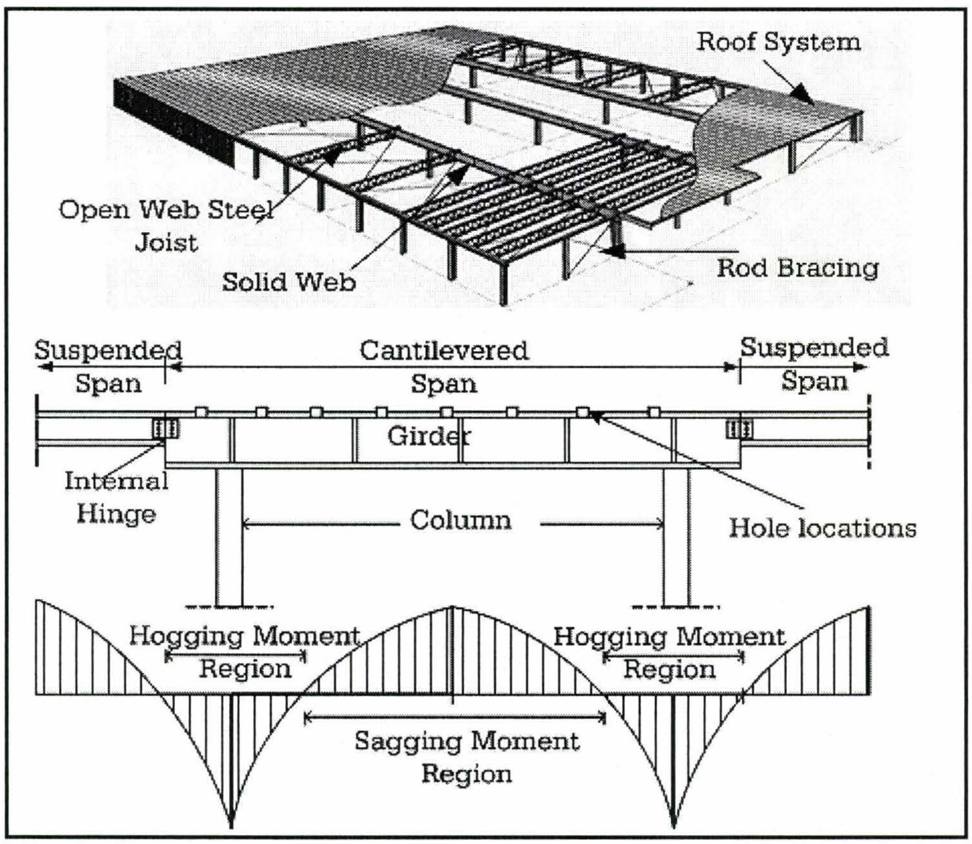


Figure 1.5: Typical Structural Layout of a Gerber Girder System

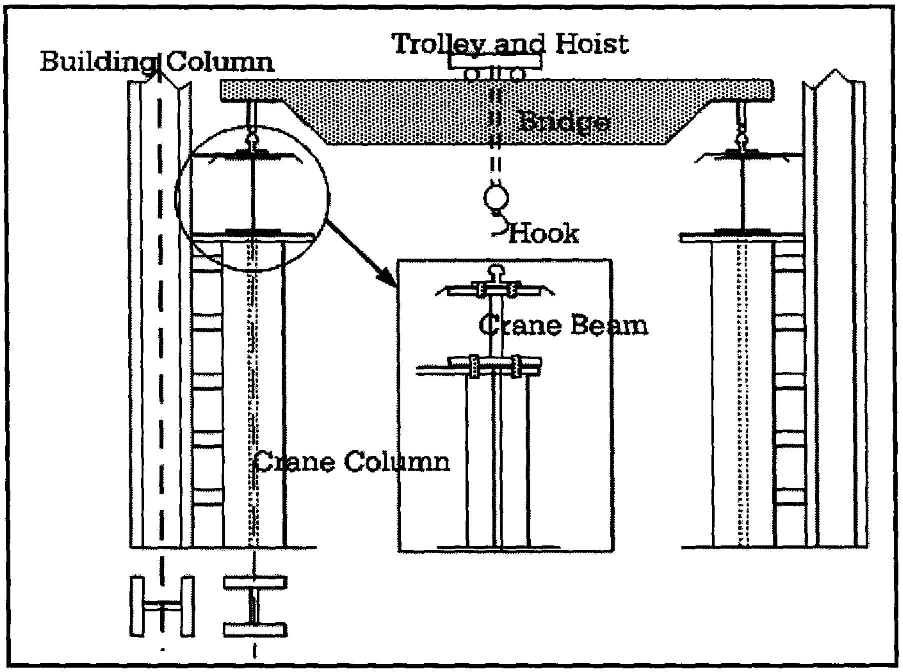


Figure 1.6: Structural Overview of an Overhead Crane

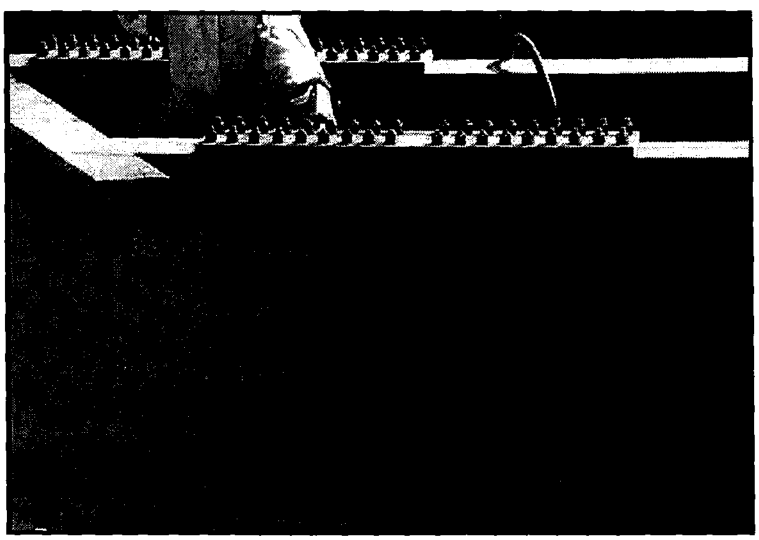

Figure 1.7: Moment Splice Connection

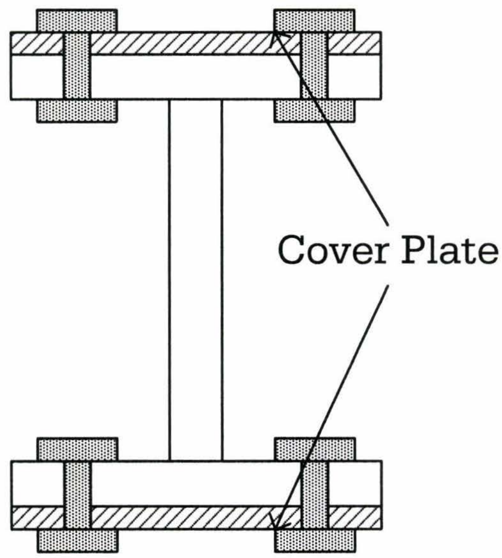


Figure 1.8: Typical Assemblage of Cover Plates

# CHAPTER: 2

# LITERATURE REVIEW

## 2.1 Introduction

This chapter reviews pertinent published materials on the flexural strength of structural steel beams with holes in the flanges and/or webs. As noted previously, in this document, unless otherwise specified, holes mean open holes and fastener holes. A historical development of structural steels used in the construction industry is briefly summarized. This chapter also presents the early North American code provisions dealing with the issue on the design of flexural members with holes in the flanges and/or webs. Additionally, this chapter discusses how these early code provisions have been modified based on research studies over the last few decades.

## 2.2 Historical Development of Structural Steel Grades

Early North American structural steel standards for buildings (CSA Standards, ASTM Standards) permitted mild-carbon steel with minimum specified yield strength values of 190 MPa-225 MPa and corresponding ultimate strength values of 380 MPa-450 MPa, resulting in a yield-to-ultimate strength ratio value of 0.5 (ASTM 1999). The growth of advanced technology over the last fifty years in the steelmaking industry has enabled steel producers to make steel grades with relatively higher properties. In the 1960's, ASTM A36 steel with slightly improved steel properties was introduced as a structural steel replacing the use of mild carbon steel. The steel conformed to this specification, ASTM A36, has a minimum specified yield strength of 250 MPa and ultimate strength varying from 400 MPa to 550 MPa. Thus, the associated yield-to-ultimate strength ratio values range between 0.45 and 0.62 (Fletcher 1979).

Currently, a minimum specified yield strength of 350 MPa is the norm in Canada. In the 1990's, Grade 350W became the only grade for W and HP shapes produced by Algoma (CISC 2007). The 350W grade steel has a minimum specified yield strength of 350 MPa and ultimate strength ranging between 450 MPa and 650 MPa, resulting in yield-to-ultimate strength ratio values between 0.54 and 0.78.

The ASTM A992 steel grade is currently used steel specification for building construction; it was developed as the result of an industry initiative during the 1990s. This steel has been produced since 1997 under the description "Enhanced A572 Grade 50" (Bjorhovde et al., 2001). The major advantage of the A992 steel is its better material definition. It has an upper limit on yield strength of 450 MPa and a lower limit on tensile strength of 450 MPa. The Canadian standard CSA G40.21 350W steel grade is equivalent to ASTM A572 Grade 50. Although the minimum yield and ultimate strengths of the 350W steel are closer to that of the ASTM A992 steel, the A992 steel has an additional requirement that the yield-to-ultimate strength ratio value may not exceed 0.85. In order to ensure adequate ductility, the A992 specification requires that minimum elongation over 200 mm gauge length be 18% and over 50 mm gauge length be 21% (Bjorhovde et al., 2001).

Relatively recent steel making technology such as the Quenching and Self Tempering Process (QST), which is an advancement of Thermo-Mechanical Controlled Process (TMCP), enables the production of steel with higher strength, improved weldability and higher fracture toughness. Steels produced using these types of advanced processes have improved mechanical characteristics as well as improved weldability and are referred to as high performance steels (HPS). The steel grades such as ASTM A913 Grade 50 and Grade 65, HPS 50W and HPS 70W are widely used high performance structural steels employed in the construction of high rise buildings and bridges. The use of the HPS steels saves up to 20% weight reduction over widely used Grade 50 steels (Günther 2005). The ASTM A913 Grade 50 steel has minimum yield and ultimate strengths of 345 MPa and 450 MPa, respectively, resulting in a yield-to-tensile strength ratio value of 0.77. On the other hand, ASTM A913 Grade 65 has minimum yield and ultimate strengths of 450 MPa and 550 MPa, respectively, resulting in a yield-to-ultimate strength ratio value of 0.82. The HPS 70W steel has a minimum yield strength of 485 MPa and ultimate strength varying between 585 MPa and 760 MPa. Thus, the associated yield-to-ultimate strength ratio values vary between 0.64 and 0.83. Therefore, over the last fifty years, the yield-to-ultimate strength ratio of structural steel grades has increased from 0.5 to 0.85 and in some instances even more than 0.85 (Dexter et al., 2002).

## 2.3 Flexural Members with Flange Holes: Previous Studies

Lilly and Carpenter (1939) studied the impact of rivet holes on the flexural stresses of plate girders. The test data collected from this study was used to establish the effective moment of inertia of a plate girder having rivet holes in the flanges and web. The effects of such holes on the cross-section strength of plate girders under working load condition were reported. Since all the tests reported in this study were conducted under working load condition, the plate girders were not loaded to failure.

However, Lilly and Carpenter (1939) achieved their objectives by testing simply supported, constant length plate girders with various cross-sectional areas. Combinations of a web plate and four angles with four cover plates were used to fabricate three different cross-sections as shown in Figure 2.1. The plate girders were tested in four different series. The first series of tests included different cross-sections, but no holes were placed in the girders in the constant moment region. The second series used the same girders of the first series, but with 17.5 mm (11/16 inch) holes in both flanges in the constant moment region placed at a pitch of 127 mm (5 inch). The third series of tests included machine bolts in the holes of the beams used in the second series. The fourth series included rivets instead of machine bolts used in the third series. It should be noted that the same girders were reused in each series of tests as they were not tested to failure.

A second series of tests were performed using the same cross-sectional dimensions however, the pitch of the holes was changed from 127 mm (5 inch) to 64 mm (2.5 inch). Midspan deflections and both the compression and tension flange stresses were recorded during each test. The following conclusions were derived based on the test results;

- The measured flange stresses were well correlated with the calculated stresses established on the basis of moment of inertia of the gross cross-section.
- The value of the effective moment of inertia was influenced by the rivet pitch and rivet diameter.
- Strain measurements indicated that the neutral axis remained at the center of gravity of the gross cross section instead of the center gravity of the net cross section in all cases considered.
- Midspan deflection calculated based on the gross moment of inertia had a good correlation with the measured test results.

It should be noted that the plate girders used in this study utilized mild-carbon steel having a yield-to-tensile strength ratio of approximately 0.5. The holes in this test series removed only a maximum 23% of the gross tension flange area. Following this landmark study, the AISC (1963) specification allowed the use of gross moment of inertia except when the area of holes exceeded 15% (as a conservative) of the gross flange area, in which case the area in excess of 15% must be deducted from the flange area to establish an effective flange area (Zahorsky, 1994). Some of the reasons given by AISC (1963) for using the 15% exemption rule were; [1] Plate girders including crane runways scarcely failed in the tension flange, but they usually failed in the compression flange and web, thus, the capacity of the section was to be determined based on the compression flange and web of the plate girder and [2] the flange area removed for rivet holes was normally less than 15% of the gross flange area and the friction within the tight rivet heads alleviates stress concentrations around hole region. However, the maximum exemption of 15% was established considering the fact that friction may not be counted when there are many rivet holes across one cross-section.

Kicinsky (1963) experimentally investigated the influence of flange holes on the flexural stresses of wide-flange beams. The effect of both open holes and holes in which rivets have been placed was investigated. A rolled beam, having flange width, flange thickness, web depth and web thickness of 175 mm, 10 mm, 380 mm and 7.5 mm, respectively, conforming to ASTM A7 steel was tested under working load condition. The experiment was limited to an investigation of three transverse sections of the beam; (1) a section containing rivets in both flanges, (2) a section which was entirely free of holes and (3) a section which initially contained holes in the tension flange and ultimately contained holes in both flanges. Figure 2.2 illustrates a photograph image of the test set-up. Since the beam loading was symmetrical, each of the sections was subjected to the same bending moment, which produced stresses well within the elastic limit of the beam. The following conclusions were derived from the experimental test results;

- although the maximum amount of holes of 23% of the gross flange area removed, no serious weakening of the beam occurs.
- neither the holes containing rivets nor the open holes in the flanges produced any noticeable movement of the neutral axis.
- the maximum flexural stresses predicted by AISC (1963) – based on the 15% exemption rule, agreed within 1.2% and 1.8%, respectively, of the experimental tensile and compressive stresses for the condition when holes occurred in only one flange; 2.1% and 7.4% for the condition when holes occurred in both flanges.
- the American Railway Engineering Association (AREA 1956) method, which used the gross section for the estimation of compressive stresses, predicted maximum compressive stresses agreeing within 0.5% of the experimental results. However, the tensile stresses as per the AREA (1956) method varied by a maximum of 15% as compared to the experimental results.
- the flexural stresses determined by the theoretical method closely agreed with the AREA (1956) method.
- the rivets in the compression flange were partially effective in transferring the flexural stresses.

Douty and McGuire (1965) studied the ultimate resisting moment of beams with fastener holes in both flanges. The main purpose of this study was to see if and under what conditions it is possible to develop the gross plastic moment of a beam having holes in both flanges. The test included beams with no holes (solid beam), beams with open holes in the flanges and spliced beams having a different number of standard fasteners. The W410X54 beam sections conformed to ASTM A7 steel possessing minimum specified yield and ultimate strengths of 230 MPa, 450 MPa, respectively (yield-to-ultimate strength ratio of 0.5). The fasteners used in this study conformed to ASTM A325 material. As shown in Figure 2.3, the test beams were simply supported at both ends and loaded with two manually operated hydraulic jacks. Each beam was laterally braced at the reaction, loading and midspan locations.

The test results indicated that all beam specimens reached a maximum moment which was equal to or slightly higher than the theoretical plastic moment, although the spliced beams had a maximum net flange area-to-gross flange area ratio of 77% (i.e., fastener holes removed 23% of the gross flange area). Moreover, it can be concluded from this study that, although the holes removed more than 15% of the gross flange area, the beam specimens capacity exceeded the theoretical gross-section plastic moment. Therefore, it was evident that the 15% exemption rule was more restrictive for steel grades such as ASTM A7 steel having a yield-to-ultimate strength ratio of 0.5.

In 1971, Chen and Patel tested 12 full-scale beams in which four of the test specimens were bolted flange plate (BFP) connections. The beam specimens conformed to ASTM A572 Grade 55 steel material with the minimum specified yield and ultimate strengths of 380 MPa and 485 MPa, respectively, resulting in a yield-to-ultimate strength ratio value of 0.78. The fasteners conformed to ASTM A325 and A490 steels. In this literature, only the fully bolted beams were considered since the effects of holes on the flexural capacity of steel beams of particular interest. The test specimens designated as C6 and C7 in the original research (Chen and Patel, 1971), were considered to be small size joints that consisted of a W360X110 (W14X74) beam and a W250X89 (W10X60) column section. The other two test specimens designated as C8 and C9, represented a medium size joint in which each specimen had a W610X91 (W24X61) beam connected to a W14X136 (not available in metric scale) column. Specimen C6 and C7 were designed such that the top and bottom flange plates could develop the full plastic bending capacity of the girder. Eight 25 mm diameter A490 fasteners were used in these connections. The difference between specimen C6 and C7 was the shear resistance. Specimen C6 was a seated beam connection while specimen C7 was a shear tab design. Specimens C8 and C9 were designed to investigate the difference between a slip-critical design (C8) versus a connection designed for bearing strength of flange plate bolts (C9). All four bolted flange plate connections in this study were tested to failure by using a monotonically applied static load. The load was applied to the column while the other ends of the girders were pinned. The experimental results indicated that the beam sections under consideration reached their full plastic moment capacity, although the fastener hole removed 21% of the gross flange area. Therefore, it can be concluded that although the 15% exemption rule was violated in these tests, the flexural members attained their gross-section plastic moment capacity. Hence, the 15% exemption rule was relatively restrictive even for ASTM A572 Grade 55 steel having a yield-to-ultimate strength ratio of 0.78.

In 1994, Zahorsky conducted eight full-scale flexural tests to investigate the effect of holes in the flanges of steel beams on the moment capacity. All the beam specimens used in this study conformed to Grade 50 steel with an average yield and ultimate strengths of 345 MPa, 473 MPa, respectively, resulting in a yield-to-ultimate strength ratio of 0.73. The test program included two series of test beams. The first series included a standard wide flange cross-section with a cover plate added on the compression flange. The second series included similar beam sections those considered in the first series, but without a cover plate. The beam specimens were simply supported at the ends and two point loads were applied in the midspan. Beam specimens originally designated in this research work as B1 through B5 had the following dimensions; length of 6096 mm, flange width of 127 mm, flange thickness of 6.4 mm, web depth of 305 mm and web thickness of 3.2 mm. Beam B6 had the same nominal cross-section as beams B1 through B5, however, the length of the beam specimen was 7722 mm. The compression flanges of beam specimens B1 through B6 included a cover plate having nominal dimensions of 152 mm wide and 7.9 mm thick. Beam specimens B7 and B8 were tested with no cover plate.

Figure 2.4 illustrates the layout of the test set-up and the geometrical dimension of specimen B6. Specimens B1 and B2 were tested as solid beams thus, acting as control beams. In specimens B3, B4 and B5, a set of two 17.5 mm (11/16 inch) diameter holes were placed in both flanges. As seen in Figure 2.4, specimen B6 had three sets of holes having the diameters of 14.3 mm (9/16 inch), 17.5 mm (11/16 inch) and 20.6 mm (13/16 inch) in both flanges. Specimen B7 had the same length and cross-section as beams B1 and B2 (control beam). Specimen B8 had a length of 6960 mm with two sets of 14.3 mm (9/16 inch) and 17.5 mm (11/16 inch) diameter holes in both flanges. Specimens B1 through B5 were laterally supported at 2134 mm from the ends of the beam, whereas B6 and B8 were laterally supported at 3023 mm and at 2565 mm from the ends of each beam, respectively. Test results indicated that beam specimens B1 through B6 exhibited failure due to local buckling of the compression flange outside of the cover plated zone. Beam B7, with no cover plate, failed as a result of local flange buckling of the compression flange within the constant moment region. However, the failure of beam B8 was triggered as a result of lateral torsional buckling.

It was noted that the prediction of design moment as per the AISC-LRFD (1986) code provision, which employs the 15% exemption rule, had good correlation with the test results (maximum variation 8%) than the AISC-LRFD (1994) code method (maximum variation 12%). Moreover, from the test results, Zahorsky (1994) recommended that the holes of normal size up to 30% of the gross flange area can be allowed for steel grades such as Grade 50. If the holes exceed 30% of the gross flange area, the effects of holes may be treated similar to the AISC-LRFD (1994) code method, which will be given in the following section. Thus, the effect of holes can be ignored if

$$A_{fn} \geq 0.7 A_{fg} \tag{2.1}$$

Otherwise, the effective flange area, $A_{fe} = 5/6(F_u / F_y)A_{fn}$, shall be used to establish the net section properties.

In 2002, Schneider and Teeraparbwong investigated the inelastic behavior of eight full-scale bolted flange plate connections. The specimens were designed to cause either inelastic behavior in the flange plates or in the girder beyond the flange plate connection. Accordingly, the specimens used in this study were designed to fail at different locations. As the focus of the current investigation is on the effects of flange holes on the flexural behavior of steel beams, here only specimens B2, B3 and B5 were considered. These three specimens were designed to exhibit a failure through either net section of the flanges or gross section of the beam member by local instability. Specimen B2 failed due to ductile tearing through the flanges of the girder. It was noted in the paper (Schneider and Teeraparbwong, 2002) that the failure initiated at the net section of the row of bolts farthest from the face of the column flange. It should be noted that, although the fastener holes resulted in removal of 28% of the gross flange area of the girder, the specimen was able to reach a moment slightly higher than the gross-section plastic moment capacity. However, specimen B3 was designed to fail outside of the flange plate connection. Specimen B3 failed as a result of girder hinging, that is, the full gross area was effective. Specimen B5 was designed similar to B3. However, the only difference was that specimen B5 had a clamp plate, having a thickness of 25 mm, added to the last two row of the fasteners in the connection farthest from the face of the column flange. The addition of the clamp plate triggered the failure of specimen B5 due to local instability.

Dexter et al., (2002) performed experimental investigations and analytical studies on axial tension members having various net area-to-gross area ratios and a flexural member made of HPS70W steel with a minimum specified yield strength of 480 MPa. The main objectives of this study were to:

- examine the strength and ductility performance of tension members and the tension flange of a flexural member made of HPS70W steel (or equivalent to ASTM A709 Grade 70 steel)
- verify the applicability of the AISC-LRFD (1999) code provisions dealing with the design of tension members and the design of flexural members having holes in the flanges made of HPS70W steel.

The first phase of the study by Dexter et al (2002) included the testing and analysis of wide-plate specimens simulating the behavior of an axial tension member. The wide-plate specimens had the cross-section dimensions of 203 mm wide and 19 mm thick. In performing the wide-plate tests, various net area-to-gross area ratios were considered. The wide-plate test results were used to establish the factors that control the ductility of the tension members made of HPS70W steel in terms of the nominal net section fracture strength-to-nominal gross section yield strength, $A_{fn}F_u / A_{fg}F_y$, ratio. Moreover, the tensile ductility of the wide-plates made of HPS 70W steel was compared with that of the similar specimens made of HPS 50W steel (equivalent to the ASTM A709 Grade 50 steel) exhibiting greater strain hardening potential and HPS100W steel possessing lower strain hardening potential.

The second phase of Dexter's study (2002) involved in the flexural testing of a girder with solid flanges. The girder featured a tension flange that was identical in cross-sectional dimensions to the wide-plate specimens. The notion of performing this flexural test was to compare the behavior of the tension flange with the behavior of the wide-plate specimens (tension member) and hence, to characterize the ductility demand associated with the tension flange in a flexural member. Conclusions drawn from this study included;

- the flexural members made of Grade 50 steel had adequate ductility provided that the net area-to-gross area of the tension flange ratio was grater than or equal to the yield-to-ultimate strength ratio, (i.e., $A_{fn} / A_{fg} \geq [F_y / F_u]$).
- the flexural members made of HPS70W or higher strength steel such as ASTM A514 steel exhibited adequate ductility provided that $A_{fn} / A_{fg} \geq 1.1[F_y / F_u]$.

The current AISC-LRFD (2005) code provision was revised and updated on the basis of Dexter's (2002) conclusions and recommendations.

Yuan (2004) investigated the effects of different methods used to make holes (drilling, punching, flame cutting, etc) on the strength and ductility of steel plates and T-shaped specimens subjected to axial tension. The dimensions of steel plates were 1219 mm long, 76 mm wide and 12.7 mm thick. The holes diameters were 14.3 mm, 20.6 mm and 27 mm, resulting in net area-to-gross area ratio values ranging between 64.6% and 81%. The steel plates conformed to ASTM A36 and ASTM A588 steel grades. The ASTM A36 steel had the measured yield and ultimate strengths of 326 MPa and 530 MPa, respectively, resulting in a yield-to-tensile strength ratio value of 0.62, whereas the ASTM A588 steel had the measured yield and ultimate strengths of 525 MPa and 591 MPa, respectively, resulting in a yield-to-tensile strength ratio value of 0.89.

The T-shaped specimens were obtained from W460X60 (W18X40) sections made of ASTM A992 steel grade having two different heat IDs (type-A and type-B). Type A of A992 steel had measured yield and ultimate strengths of 383 MPa and 469 MPa, respectively, resulting in a yield-to-tensile strength ratio of 0.82. Type-B of A992 steel had measured yield and ultimate strengths of 328 MPa and 447 MPa, respectively, resulting in a yield-to-ultimate strength ratio value of 0.73. As shown in Figure 2.5[A], the T-shaped specimens were bolted back-to-back to gusset plates which were clamped into the wedges of the test machine. The T-shaped specimen had a pair of 27 mm diameter holes at the mid-height resulting in a net flange area-to-gross flange area ratio of 63% while the net area-to-gross cross-section area ratio was 68%.

The test results indicated that the average strength ratio for all test specimens was 110% when compared to the ultimate strength of standard tensile coupons $[(P_u / A_n)/F_u]$ with a standard deviation of 6.7%. The comparison of test results on the basis of different steel material indicated that the tension specimens made of ASTM A36 steel exhibited higher ductility. The T-shaped specimen made of ASTM A992 type-B material with a yield-to-tensile strength ratio of 0.73 exhibited higher ductility than the ASTM A992 type-A steel specimen with a yield-to-tensile strength ratio of 0.82. This study also concluded that beam sections with the above steel grades may have sufficient ductility to develop the full plastic moment prior to tension flange fracture. This conclusion may be valid as long as the removal of hole area is less than 37% of the gross flange area. However, it is not appropriate to predict the ductility performance of a flexural member having holes in the tension flanges from the ductility performance of a direct tension member since the behavior of both members are considerably different due to the flange-web interaction.

## 2.4 Flexural Members with Flange Holes: Code Provisions

The earliest code provision on the flexural strength of steel beams with holes is due to American Railway Engineering Association (AREA 1910). According to this code provision, "*plate girders shall be proportioned either by the moment of inertia of their net section; or by assuming that the flanges are concentrated at their centers of gravity*". This provision represented a general practice until it was superseded by the 1920 specification, issued by the same organization. The 1920 specification stated: "*plate girders shall be proportioned either by the moment of inertia of their net section including compression side; or by assuming that the flanges are concentrated at their centers of gravity*". The difference between the 1910 and the 1920 code provisions was that the latter definition seemed to consider net sections associated with both the tension and the compression flange. This clause was revised in the subsequent editions of AREA (1956) method. Accordingly "*plate girders, I-beams and other members subjected to bending that produces tension on one face, shall be proportioned by the moment of inertia method. The neutral axis shall be taken along the center line of gravity of gross section. The tensile stress shall be computed from the moment of inertia of the entire net section and the compressive stress from the moment of inertia of the entire gross section*" (AREA 1956).

According to the first edition of the American Institute of Steel Construction (AISC) published in 1923, the flexural design of plate girders having rivet holes in the flanges and/or webs must be based on net sections (Galambos 1977). The next edition of the AISC (1936) however, permitted a designer to proportion a flexural member having holes in the flanges and/or webs based on the gross cross-section of the member. The revised version of the AISC specifications in 1961 however, allowed the use of the gross moment of inertia except when the area of the holes exceeded 15% of the flange area, in which case the area in excess of 15% must be deducted from the flange area to establish an effective flange area. The effective flange area is then used to calculate the effective moment of inertia. This provision was based in part on a research study performed on riveted plate girders by Lilly and Carpenter (1939). These were the historical code provisions for the flexural design of plate girders with holes in the early AISC specifications.

The first edition of the American Institute of Steel Construction-Load Resistance Factor Design was introduced in 1986 (AISC-LRFD 1986). According to this code provision, the 15% exemption rule had been used to take into account the effects of holes in the flanges of flexural members. In 1989, the ninth edition of the Allowable Stress Design version of the specification (AISC-ASD 1989) however, introduced revisions with regard to the design of flexural members having flange holes. Accordingly, the beams would still be proportioned by the moment of inertia of the gross section, but the holes in the flanges were treated in a completely different manner than any of the previous AISC specifications. The AISC-ASD (1989) specification introduced a mathematical formula based on the ratio of the fracture strength of the net flange area and the yield strength of the gross flange area to calculate an effective flange area. Accordingly, the AISC-ASD (1989) specification required no deduction for holes from the gross section of either flange provided that

$$0.5A_{fn}F_u \geq 0.6A_{fg}F_y \tag{2.2}$$

where $A_{fg}$ is the gross flange area and $A_{fn}$ is the net flange area (calculated on the basis of the specification for uniaxial tension members, Sections B1 and B2), and $F_y$ and $F_u$ are the yield and ultimate strengths of the flange material, respectively. However, if

$$0.5A_{fn}F_u < 0.6A_{fg}F_y \tag{2.3}$$

the effective tension flange area ($A_{fe}$) is then calculated as

$$A_{fe} = \frac{5}{6}\frac{F_u}{F_y}A_{fn} \tag{2.4}$$

According to Equation 2.1, AISC-ASD (1989) allows the use of larger holes in the flanges without penalty for the conventional steels such as ASTM A7 and A36 steels having the yield-to-ultimate strength ratio of approximately 0.5 (equivalent to 40% exemption) than the previous specification using the 15% exemption rule. However, when using steel grades such as 350W steel, ASTM A992 and other higher grades of steel having a yield-to-ultimate strength ratio of more than 0.71, this equation allows smaller holes than the 15% exemption rule. It is pertinent to note that no experimental test results were noted to support the mathematical formula as given in Equations 2.2 and 2.4, which was first introduced by the AISC-ASD (1989) specifications.

It should be noted that Equation 2.1 was established based on the ratio of the fracture strength of the net area to the yield strength of the gross area for an axial tension member (section B1 of the AISC specifications). According to the AISC-ASD (1989) standard, when dealing with an axial tension member, two major failure criteria need to be checked. The first is that the allowable stress for the yielding of gross cross-section shall not exceed $0.6F_y$ while the second requires that the allowable stress for the fracture of net cross-section be less than $0.5F_u$. If the behavior of the tension flange of a flexural member is identical to the behavior of an axial tension member when holes exist, a similar form of the criteria can be applied for the proportion of the flexural member with flange holes. However, it is pertinent to note that the relatively recent experimental studies have demonstrated that the behavior of an axial tension member is significantly different than the behavior of the tension flange having holes (Dexter et al., 2002 and Yuan, 2004).

In 1994, the second edition of the AISC-LRFD code provision adopted a procedure similar to the AISC-ASD (1989) standard. Again, two failure criteria need to be checked for an axial tension member having holes. The first failure criteria requires that the stresses on the gross cross-section be less than $0.9F_y$ while the second criteria requires that an average stress on the net section be less than $0.75F_u$. According to the AISC-LRFD (1994) code provision, a flexural member having flange holes was treated in a similar way as an axial tension member having holes. Thus, no deduction shall be made for bolt or rivet holes in either flange provided that

$$0.75A_{fn}F_u \geq 0.9A_{fg}F_y \tag{2.5}$$

where, $A_{fg}$ is the gross flange area and $A_{fn}$ is the net flange area, calculated on the basis of the specification for uniaxial tension members (Sections B1 and B2). However, if

$$0.75A_{fn}F_u < 0.9A_{fg}F_y \tag{2.6}$$

The member flexural properties shall be based on an effective tension flange area, $A_{fe} = 5/6(F_u/F_y)A_{fn}$.

Although the AISC-LRFD (1994) code provision employed different resistance factors; 0.9 for the gross section yield strength and 0.75 for the net section fracture strength, from the AISC-ASD (1989) code provision, which applied the safety factors (0.6 for the gross section yield strength and 0.5 for net section fracture strength) both code provisions yielded the same effective flange area (see Equations 2.3 and 2.6). The concern with the AISC-LRFD (1994) or AISC-ASD (1989) is complicated by the fact that these provisions had no published theoretical or experimental test data to support them other than the extrapolation from the provisions of the AISC specifications for direct axial tension members (Zahorsky 1994). Therefore, the AISC-LRFD (2005), which is currently in use, code provision was revised based on latest research studies (Dexter et al., 2002 and Yuan 2004). A detail explanation pertaining to this code provision along with other international code provisions will be provided in Chapter 3.

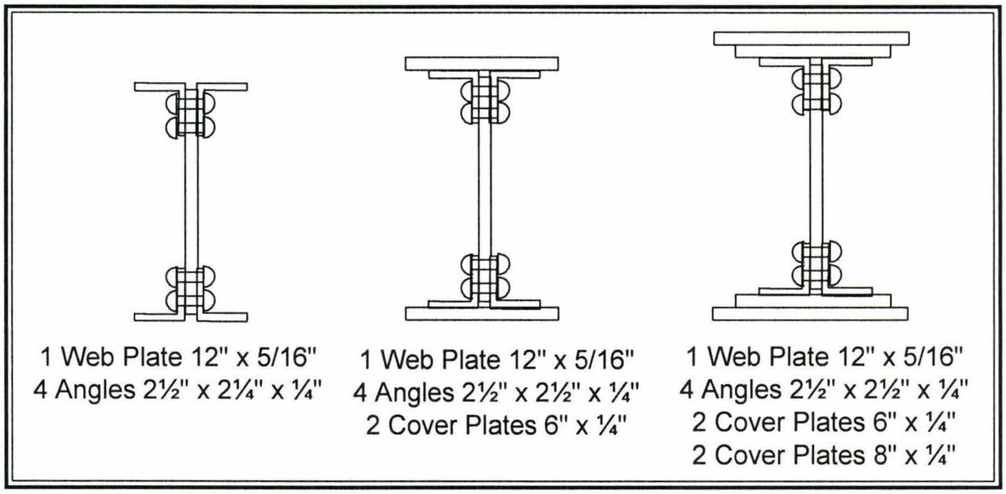


Figure 2.1: Typical Cross Sections of Test Specimens
(Lilly and Carpenter, 1939)

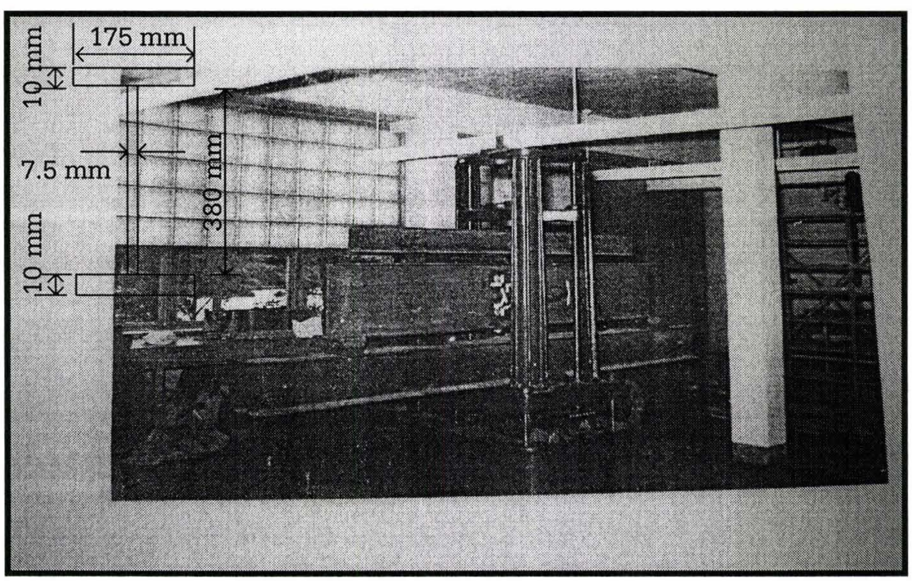


Figure 2.2: Photograph Image of Test Set-up (Kicinsky 1963)

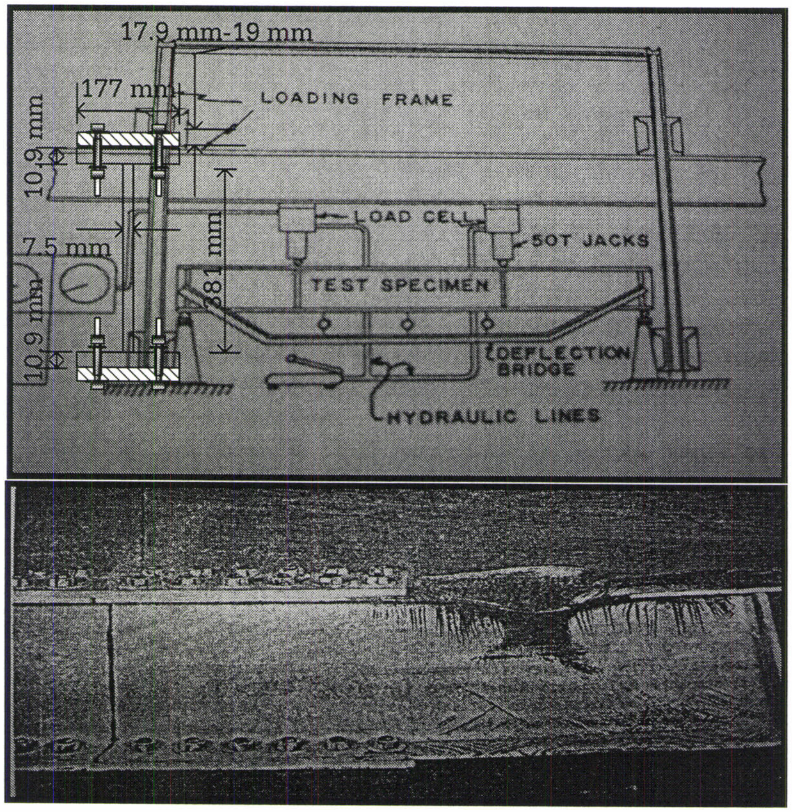


Figure 2.3: Photograph Image of Test Set-up (Douty and McGuire, 1965)

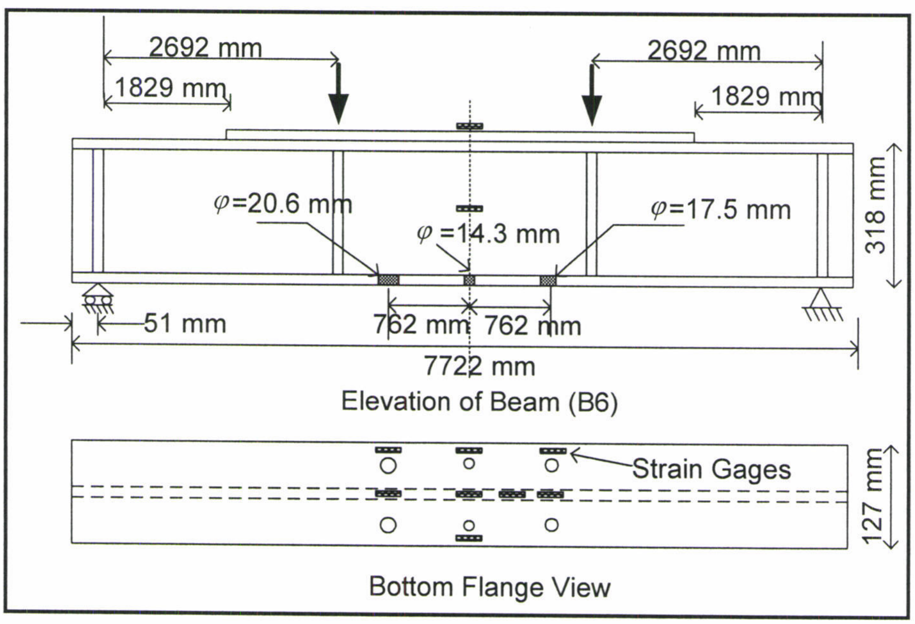


Figure 2.4: Typical Layout of Test Set-up (Zahorsky 1994)

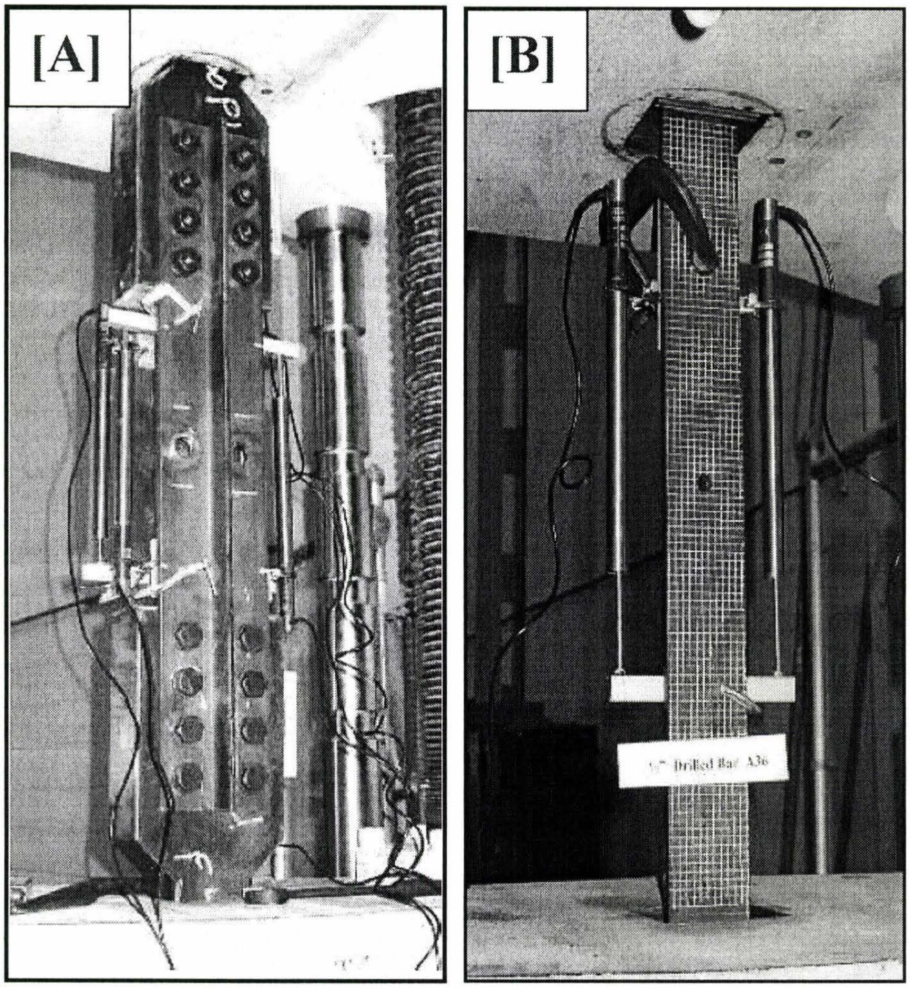


Figure 2.5: Photograph Image of Test Set-up (Yuan 2004)

# CHAPTER: 3

## REVIEW OF CODE PROVISIONS

### 3.1 Introduction

This chapter reviews five different international code provisions addressing the design of flexural members having holes in the flanges and /or webs. In this thesis report, unless otherwise specified, holes define open holes and fastener holes. The following five international standards are considered herein;

- Canadian Standard-CAN/CSA-S16.01 (CSA 2003)
- American Standard-AISC-LRFD (AISC 1999)
- American Standard-AISC-LRFD (AISC 2005)
- British Standard-BS5950-2000 (BSI 2001)
- Australian Standard-AS4100-1998 (SA 1998)

This chapter discusses how these standards differ from each other in attempting to account for the effects of flange holes on flexural strengths of steel beams. Also, the similarities between the standards in treating the effects of flange and/or web holes will be discussed. For the comparison, each standard will be applied to different practical scenarios. In general, beams with flange holes may fall into one of four different practical scenarios. Depending on the field applications, each scenario can be categorized as follows;

(a) Open holes in the tension flange only: this scenario represents field applications such as, (1) a supporting beam subjected to negative bending moment (hogging moment) in a roofing combination of open web steel joists with Gerber-girder system; (2) a connection with beam bearing on the bottom flange girder; (3) hanger type connections, etc. (see Chapter 1 for more details regarding these applications).

(b) Open holes in the compression flange only: this type of practical scenario may arise in a supporting beam subjected to positive bending moment (sagging moment) in a roofing combination of open web steel joists with Gerber-girder system (see Figure 1.5 in Chapter 1).

(c) Open holes in both flanges: although this situation rarely arises, it may characterize a governing scenario in terms of strength and ductility of a flexural member.

(d) Fastener holes in both flanges: this includes various practical applications such as different types of bolted connections in moment resisting frames, supporting beams in over-head cranes, beam-splice connections, bolted cover plate beams, etc. (see Chapter 1 for further details).

In addition to the code provisions considered, this chapter includes a theoretical approach that may be used by a designer based on net section calculations. Thus, sample calculations (based on theory) will be provided in this chapter to establish the flexural strength of beams having flange holes.

## 3.2 Flexural Members

As per the Canadian Steel Design standard-CAN/CSA-S16.01 (CSA 2003) a flexural member can be classified into four different classes; Class 1, Class 2, Class 3, and Class 4. Such classification is based on the maximum width-to-thickness ratios of the component elements subjected to compression. Figure 3.1 shows the typical moment-rotation relationships for different classes of beam sections. Class 1 sections permit attainment of the plastic moment, $M_p$, and subsequent redistribution of the bending moment, whereas Class 2 sections permit attainment of the plastic moment, $M_p$, but need not allow for subsequent moment redistribution (CSA 2003). Class 3 sections permit attainment of the yield moment, $M_y$. Class 4 sections generally have local buckling of elements in compression at low stresses and, thus, such sections fail at lower moment capacity prior to reaching yield moment capacity (see Figure 3.1). Most rolled and fabricated sections used as structural steel beams are Class 3 or better.

According to the AISC-LRFD (2005) standard, steel sections are classified as compact sections, noncompact sections, or slender element sections. Compact sections are capable of developing a fully plastic stress distribution and they possess a rotation capacity of approximately 3 before the onset of local buckling (Yura et al., 1978). Noncompact sections can develop partial yielding in compression elements before local buckling occurs, but will not resist inelastic local buckling at the strain levels required for a fully plastic stress distribution. Slender-element sections have one or more compression elements that will buckle elastically before the yield stress is achieved. Thus, Class 2 sections (as per the CSA (2003) standard) can be referred to as compact sections. Class 3 sections can be considered to be noncompact sections and Class 4 sections can be referred to as slender sections. Class 1 sections are called seismically compact sections in U.S.A codes.

### 3.2.1 Moment Resistance of Steel Beams

In addition to the compactness of the steel section, another important consideration for beam design is the lateral unsupported (unbraced) length of the member. However, when the compression flange of beams is adequately braced, the only stability limit state that prevents the attainment of maximum moment strength is the local buckling of the flanges and/or web plate elements. Local buckling can be prevented by limiting the slenderness of these component plates. The stress distribution on a typical wide-flange shape subjected to increasing bending moment is as shown in Figure 3.2. Under the action of an applied moment, the response of the beam can be divided into a number of stages as illustrated in Figure 3.2. Initially the flexural member will behave elastically with stress variation, which is assumed to be linear from zero at the neutral axis to a maximum at the extreme fiber of the flanges (Stage 1). As the moment is increased, the extreme fiber of the flanges will begin to yield (Stage 2). As the moment is increased further, yielding will progress inwardly and some portions of the cross-sections would have yielded while some portions adjacent to the neutral axis will remain in the elastic region (Stage 3). Beyond Stage 3, the most highly stressed regions will develop strains in excess of the yield strain, resulting in a local loss of stiffness. Moreover, the rotation of the beam member begins to increase rapidly. A further increase in the applied moment will cause this process to continue until the entire cross-section has yielded as shown in Stage 4. It should be noted that the stress distributions across the cross-section as illustrated in Stage 4 represents an ideal stress distribution due to the fact that the stresses closer to the neutral axis never reach the yield strength.

In theory, the moment at the onset of yielding is expressed as (Stage 2)

$$M_y = S_g F_y \tag{3.1}$$

where $S_g$ is the elastic section modulus about the axis of bending and $F_y$ is the minimum specified yield strength of the flange material. The subscript '$g$' denotes the gross-section. As the flexural member reaches the cross-section full plastic strength, the moment at this stage can be given as (Stage 4)

$$M_p = Z_g F_y \tag{3.2}$$

where $Z_g$ is the plastic section modulus of the gross-cross section.

### 3.2.2 Moment Resistance of Steel Beams with Flange Holes

When a beam is proportioned on the basis of flexural strength of the gross section the presence of holes in the flanges and/or webs may reduce the flexural strength. The theoretical moment resistance of such beams can be established based on net section properties. A theoretical prediction of flexural strength depends on the position of the neutral axis of the net section. For instance, when holes exist in either the tension or the compression flange of a flexural member, the net section properties such as the elastic net section modulus and the plastic net section modulus may be established by considering the changes in the position of the neutral axis. However, when equal size holes occur in both the tension and compression flanges of a symmetric section, the position of the neutral axis of the net section remains at the neutral axis associated with the gross cross-section. When holes contain fasteners a designer may consider the following two different approaches (denoted herein as Theory 1 and Theory 2);

Theory 1: as discussed, it is well understood that the effects of fastener holes in tension members is significant. Unlike member subjected to tension load, a compression members having fastener holes is designed on the assumption that its gross cross-sectional area will be effective in resisting the applied load. As the load is applied, the member will contract. Thus, it is assumed that the action of bolts in compression members is such that they replace the material removed for bolts. As such, Theory 1 considers a movement of the neutral axis from the gross cross-section to the net cross-section provided that a section is symmetric about the axis of bending.

Theory 2: in contrast to Theory 1, Theory 2 considers that fasteners in the compression flange are not effective and are analogous to the tension flange having fastener holes. That is, the neutral axis of the net-section remains at the neutral axis of the gross cross-section provided that a section is symmetric about the axis of bending.

However, in the past, the second approach has been traditionally practiced by design engineers as a conservative approach (Brockenbrough and Merritt, 1994).

It is pertinent to note that the calculation of flexural strength based on the cross-section using the theoretical approach does not account for strain hardening potential in terms of yield-to-ultimate strength ratios of steel grades. In other words, a moment reduction associated with a particular amount of flange holes is the same for a beam made of any different steel grades. However, various international code provisions under consideration, except the current CSA (2003) code, establish the impact of holes on the flexural strength of a beam by accounting for its strain hardening potential in terms of the yield-to-tensile strength ratio.

### 3.2.3 A Theoretical Approach: Sample Calculation

This section presents sample calculations pertaining to the prediction of flexural strength based on a theoretical approach. The sample calculations were made on four different beam sections; W610X101, W410X54, W530X72 and W200X42. As per the CAN/CSA-S16.01 (CSA 2003) standard, the beam sections W610X101 and W200X42 are classified as Class 1 while W410X54 and W530X72 are classified as Class 2 and Class 3, respectively. The nominal cross-sectional dimensions of the beam sections as given in CISC Handbook (2007) are presented in Table 3.1. The gross cross-section properties such as the second moment of area ($I_g$), plastic section modulus ($Z_g$) and elastic section modulus ($S_g$) are also summarized in Table 3.1.

The ratio between hole area and gross flange area is defined as:

$$\rho_h = \frac{A_{fh}}{A_{fg}} \tag{3.3}$$

where $A_{fh}$ is the flange hole area and $A_{fg}$ is the gross flange area.

Here, sample calculation procedure pertaining to the theoretical approach is provided for beam sections; W610X101 (Class 1) and W530X72 (Class 3). The calculations are shown corresponding to $\rho_h$=0.35 for the following two different cases;

Case-1 includes the beam sections having holes either in the tension or compression flange only.

Case-2 involves the beam sections with holes in both flanges.

**Case-1: holes in one flange (tension or compression flange)**

*a. Beam Section-W610X101 (Class 1-Steel Grade: $F_y = 350MPa$)*

Plastic moment capacity of the gross cross-section, $M_p = Z_g F_y$ = 2900x10$^3$ x 350

= 1015 kNm

Gross flange area, $A_{fg} = 228x14.9 = 3397\ mm^2$

Hole area, $A_{fh} = \rho_h\ A_{fg} = 0.35\ x\ 3397 = 1189\ mm^2$

Net flange area, $A_{fn} = A_{fg} - A_{fh} = 3397\text{-}1189 = 2208\ mm^2$

A shift in the position of the plastic neutral axis from gross cross-section to net cross-section,

$$\bar{y} = \frac{A_{fg} - A_{fn}}{2w} = \frac{3397 - 2208}{2x10.5} = 56.6\ mm$$

The plastic section modulus of the net section, $Z_n = Z_g - \rho_h A_{fg}\left(\frac{d-t}{2} + \bar{y}\right) + w\bar{y}^2$

$= 2517\ x10^3\ mm^3$

Thus, the flexural strength of net cross-section,

$$M_{pn} = Z_n F_y = 2517\ x10^3\ x\ 350 = 881\ kNm$$

The moment ratio (net/gross) corresponding to $\rho_h$ =0.35,

$$\frac{M_{pn}}{M_p} = \frac{881}{1015} = 0.87$$

*b. Beam Section-W530X72 (Class 3-Steel Grade: $F_y = 350MPa$)*

Yield moment capacity of the gross cross-section, $M_y = S_g F_y = 1520x10^3 x\ 350$

$= 532\ kNm$

Gross flange area, $A_{fg} = 207x10.9 = 2256\ mm^2$

Hole area, $A_{fh} = \rho_h\ A_{fg} = 0.35\ x\ 2256 = 790\ mm^2$

Net flange area, $A_{fn} = A_{fg} - A_{fh} = 2256\text{-}790 = 1466\ mm^2$

A shift in the position of elastic neutral axis from the gross cross-section to the net cross-section,

$$\bar{y} = \left[\frac{A_{fn}(t/2) + A_{fg}(d - t/2) + A_w(d/2)}{A_n}\right] - \left[\frac{d}{2}\right]$$

$(A_n = A_g - A_{fh})$, $\bar{y} = 24.3$ mm

The second moment of area of the flange hole about the shifted neutral axis,

$$I_{fh} = A_{fh}\left(\frac{t^2}{12} + \frac{(d-t)^2}{4} + \bar{y}^2 + (d-t)\bar{y}\right)$$

$$= 62.3\text{x}10^6 \text{ mm}^4$$

The second moment of area of the net section, $I_n = I_g - I_{fh} + A_g\bar{y}^2$

$$= 343\text{x}10^6 \text{ mm}^4$$

Thus, the effective elastic section modulus of net section, $S_n = \dfrac{I_n}{\left[\bar{y} + \dfrac{h}{2} + \dfrac{t}{2}\right]}$

$$=1221 \text{ x}10^3 \text{ mm}^3$$

where $h$ is the height of the web and $t$ is the flange thickness.

Thus, the flexural strength of net cross-section, $M_{yn} = S_n F_y$=1221x$10^3$ x 350

$$= 427 \text{ kNm}$$

The moment ratio (net/gross) corresponding to $\rho_h = 0.35$,

$$\frac{M_{yn}}{M_y} = \frac{427}{532} = 0.80$$

**Case-2: Holes in Both Flanges**

a. *Beam Section-W610X101 (Class 1)*

Net flange area, $A_{fn} = A_{fg} - A_{fh}$ = 3397-1189 = 2208 mm$^2$

Since the net-section is symmetry, $\bar{y} = 0$

The plastic section modulus of net section,

$$Z_n = Z_g - \rho_h A_{fg}(d-t) = 2201 \text{ x}10^3 \text{ mm}^3$$

Thus, the flexural strength of net cross-section, $M_{pn} = Z_n F_y$ = 2201x10$^3$x350

= 770 kNm

Thus, the moment reduction ratio corresponding to $\rho_h$ = 0.35,

$$\frac{M_{pn}}{M_p} = \frac{770}{1015} = 0.76$$

b. *Beam Section-W530X72 (Class 3)*

The second moment of area of the net-section, $I_n = I_g - 2I_{fh}$

= 296 x10$^6$ mm$^3$

The elastic section modulus of net cross-section, $S_n = \dfrac{I_n}{\left[\dfrac{h}{2}+\dfrac{t}{2}\right]}$

= 30 x10$^3$ mm$^3$

The flexural strength of net cross-section, $M_{yn} = S_n F_y$ = 1130 x10$^3$x350

= 395 kNm

Thus, the moment ratio (net/gross) corresponding to $\rho_h$ = 0.35,

$$\frac{M_{yn}}{M_y} = \frac{395}{532} = 0.74$$

Figure 3.3 shows the normalized moment capacity ($M_{pn} / M_p$ or $M_{yn} / M_y$) versus the hole area-to-gross flange area ratio ($\rho_h$-in percentage). The variation of the moment reduction with increasing hole area to gross flange area was established on the following beam sections; W610X101, W200X42, W410X54 and W530X72. When holes occurred in one flange, the theoretical moment resistance was higher for Class 1 and Class 2 section than Class 3 section (see Figure 3.3). However, when holes existed in both flanges, depending on the size of sections, relative moment reductions may be higher for Class 1 section than Class 3 section. For example, as seen in Figure 3.3, beam section W200X42, which is Class 1 section, had higher moment reduction than beam section W530X72, which is Class 3 for the case where holes occurred in both flanges. This may be attributed to the fact that when holes occur in both flanges the neutral axis of the net section will remain at the neutral axis of the gross section provided that equal amount of holes were removed from both flanges. Thus, depending upon the distance (lever arm) between the stress resultants (due to compression and tension), the theoretical moment resistance may be higher for Class 3 (W530X72) section than Class 1 (W200X42) section. Note that W530X72 section ($d = 524$ mm) is approximately 2.5 times deeper than W200X42 section ($d = 205$ mm). The theoretical moment capacities at 50% holes to the gross flange area were compared for four different beam sections considered. As indicated in Figure 3.3, for the case where holes occurred in one flange of beams

W610X101, W200X42 and W410X54, the moment capacities were of 80%, 79% and 71% of the full cross-section plastic moment capacity, respectively. Beam W530X72, which is Class 3 section, had 69% of its yield moment capacity of the gross cross-section. When 50% holes to the gross flange area of beam sections W610X101, W410X54 existed in both flanges, the moment capacities were 66% and 64% of their full cross-section plastic moment capacity, respectively. Beam section W530X72 having 50% holes to the gross flange area in both flanges had 63% of its gross cross-section yield moment. However, beam section W200X42 (test beam) having 50% holes of the gross flange area had 57% of its full cross-section plastic moment capacity. Therefore, it can be reasonably concluded that the impact of holes on compact sections having relatively small sectional properties, such as the test beam used in this investigation, is higher than the sections with larger sectional dimensions. Hence, beam sections, such as the test beam, may serve to represent a governing scenario dealing with the effects of flange holes on flexural capacity.

## 3.3 Code Provisions – An International Perspective

This section reviews five different international code provisions addressing the issue of flexural members having holes in the flanges. In this thesis document, unless otherwise indicated, holes mean open holes and fastener holes. Each of the code considered permits a certain amount of holes in the flanges of a flexural member such that the member can be proportioned on the basis of gross cross-section strength. The amount of holes permitted in codes is termed here as the "threshold value of holes". If the removal of flange material for holes exceeds the threshold value, different international code provisions also provide different design procedures to establish a design moment.

### 3.3.1 Canadian Steel Design Code - Limit States Design of Steel Structures: CAN/CSA-S16.01 (CSA 2003)

| **Clause 14.1: Proportions of beams and girders** |
|---|
| *"Beams and girders consisting of rolled shapes (with or without cover plates), hollow structural sections, or fabricated sections shall be proportioned on the basis of the properties of the gross section or the modified gross section. No deduction need be made for fastener holes in webs or flanges unless the reduction of flange area by such holes exceeds 15% of the gross flange area, in which case the excess shall be deducted. The effects of holes other than holes for fasteners shall be considered in accordance with Clause 14.3.3".* |

According to the clause 14.1 of the current CSA (2003) code provision, fastener holes up to 15% of the gross flange area can be ignored. If the fastener holes constitute more than 15% of the gross flange area, then the area removed in excess of 15% shall be deducted in establishing the effective section properties. The current CSA (2003) code provision differentiates the effects of fastener holes from the effects of open holes, in which case the net-section shall be considered regardless of the size of the holes. In other words, no exemption is permitted for holes other than fastener holes. Moreover, the CSA (2003) code provisions do not differentiate between the tension flange and the compression flange.

**Design procedure for flanges having more than 15% of fastener holes**

Fastener holes in both flanges:

If fastener holes area is more than 15% of the gross flange area, the net section properties shall be established as follows;

Step 1: calculate the fastener hole area = $A_{fh}$

Step 2: establish the fastener hole area-to-gross flange area ratio, $\rho_h = A_{fh} / A_{fg}$

Step 3: establish the plastic and elastic section modulus based on the assumption that equal size fastener holes are provided in both flanges.

Thus, the plastic section modulus of net section based on fastener holes area in excess of 15%, can be expressed as;

$$Z_n = Z_g - A_{fg}\left(\rho_h - \frac{15}{100}\right)(d-t) \tag{3.4}$$

where $Z_g$ is the plastic section modulus of the gross-section, $A_{fg}$ is the gross flange area, $d$ and $t$ are the web-depth and flange-thickness, respectively.

The corresponding elastic section modulus of net section can be expressed as;

$$S_n = S_g - A_{fg}\left(\rho_h - \frac{15}{100}\right)\left(\frac{(d-t)^2}{d}\right) \tag{3.5}$$

where $S_g$ is the elastic section modulus of the gross-section.

Note that Equation 3.5 is established based on the assumption that the second moment of area of fastener hole area itself is negligible in comparison with the second moment of area of the fastener hole area about the neutral axis of the net section of a beam section (Vinnakota 2006). This ignorance will result in an error in the order of ($t^2/6d$).

<u>Open holes in one flange (tension or compression flange)</u>:

The CSA (2003) code provision stipulates that the effects of holes other than fastener holes shall be treated in accordance with Clause 14.3.3. Accordingly, the section properties shall be established based on net section calculation. Thus, the plastic section modulus of net section can be expressed as;

$$Z_n = Z_g - \rho_h A_{fg}\left(\frac{d-t}{2} + \bar{y}\right) + w\bar{y}^2 \tag{3.6}$$

where $\bar{y}$ is the movement of neutral axis from the gross cross-section to net cross-section.

The elastic section modulus to the flange with holes can be expressed as;

$$S_n = \frac{(I_g + A_g \bar{y}^2) - I_{fh}}{\left(\frac{d}{2} + \bar{y}\right)} \tag{3.7}$$

where $I_g$ is the second moment of area of gross cross-section, $I_{fh}$ is the second moment of area of flange holes about the neutral axis of net section and $A_g$ is the gross cross-section area.

Open holes in both flanges:

According to the CSA (2003) code provision, the effective section properties shall be established based on net section calculation. Thus, for sections with open holes in both flanges, the plastic section modulus of net section can be expressed as;

$$Z_n = Z_g - \rho_h A_{fg}(d-t) \tag{3.8}$$

The elastic section modulus of net section can be expressed as;

$$S_n = S_g - \rho_h A_{fg}\left(\frac{(d-t)^2}{d}\right) \tag{3.9}$$

Note that Equations 3.8 and 3.9 are valid only if the cross-section is symmetric about the axis of bending and an equal amount of holes exist in both flanges.

### 3.3.2 American Steel Design Code - LRFD Specifications for Structural Steel Buildings (AISC-LRFD 2005)

**F13.1 Hole Reductions**

*"This section applies to rolled or built-up shapes, and cover-plated beams with holes, proportioned on the basis of flexural strength of the gross section. In addition to the limit states specified in other sections of this Chapter, the nominal flexural strength,* $M_n$, *shall be limited according to the limit state of tensile rupture of the tension flange".*

According to the current AISC-LRFD (2005) code provision, the effects of holes, regardless of the type of hole (whether open holes or fastener holes), shall be taken based on a comparison between the nominal fracture strength of net section and the nominal yield strength of gross section of the tension flange. The commentary of the AISC-LRFD (2005) standard reveals that if the holes are sufficient to affect the member strength, the critical stress is adjusted from $F_y$ to $F_u(A_{fn}/A_{fg})$ and this value is conservatively applied to the elastic section modulus of the gross cross-section ($S_g$). The AISC-LRFD (2005) code provision does not identify the effects of holes that may occur in webs, although the impact of holes in the webs may not be significant in determining the flexural strength. It is well understood that the flanges of a beam carry bending moment while the webs carry shear. As stated earlier, the current AISC-LRFD (2005) was revised based on the design recommendations suggested by Dexter et al., (2002) and Yuan (2004) who carried out tests on wide flange plates, T-shaped specimens having different percentages of hole openings. Therefore, by considering the origin of this code provision as well as by comparing the moment reductions (beyond a threshold value) with the other international standards, it can be reasonably concluded that the current AISC-LRFD (2005) applies to flexural members having open holes in both flanges.

**Design procedure for flanges with holes exceeding a threshold value**

Fastener holes in both flanges:

As per the AISC-LRFD (2005) code provision, the nominal flexural strength, $M_n$, shall be limited on the basis of the limit state of tensile rupture of the tension flange. Accordingly, the design moment at the hole location can be established as follows.

Step 1: the limit state of tensile rupture does not apply if $F_u A_{fn} \geq Y_t A_{fg} F_y$. $Y_t$=1.0 for $F_y / F_u \leq 0.8$ and 1.1, otherwise. In this case, the section can be designed to carry its full flexural strength capacity thus, $M_n = M_p$.

Step 2: if $F_u A_{fn} < Y_t A_{fg} F_y$, the nominal flexural strength, $M_n$, at the location of the holes in the tension flange shall not be taken greater than:

$$M_n = \left[ F_u \frac{A_{fn}}{Y_t A_{fg}} \right] S_g \tag{3.10}$$

where $F_y$ and $F_u$ are the yield and ultimate strengths of the flange material, respectively, $A_{fn}$ and $A_{fg}$ are the net area and gross area of the tension flange, respectively, $Y_t$ is the yield-to-ultimate strength ratio and $S_g$ is the elastic section modulus of the gross cross-section.

Holes in one flange (tension or compression flange):

According to the current AISC-LRFD (2005) code provision, the limit state of tension rupture shall be applied when holes exist in the tension flanges. Thus, the effects of holes in the tension flange shall be ignored if $F_u A_{fn} \geq Y_t A_{fn} F_y$, otherwise, the net section properties in terms of the plastic section modulus ($Z_n$) and the elastic section modulus ($S_n$) shall be established as per Equations 3.6 and 3.7, respectively. The current AISC-LRFD (2005) code does not provide any specific procedure for establishing the flexural strength of a beam when holes occur in the compression flange exclusively. Therefore, in such a situation, the only design option available for a designer is to establish the design moment based on net section. Accordingly, Equations 3.6 and 3.7 can be used to establish the effective section properties in terms of plastic section modulus ($Z_n$) and the elastic section modulus ($S_n$), respectively.

Holes in both flanges:

As discussed, the AISC-LRFD (2005) code provision treats the effects of the presence of fastener holes and open holes in a similar manner. Thus, when holes occur in both flanges of a flexural member, a similar design procedure as explained for the case where fastener holes occur in both flanges, can be adopted. Thus, use Equation 3.10 if $F_u A_{fn} < Y_t A_{fg} F_y$.

### 3.3.3 American Steel Design Code - LRFD Specifications for Structural Steel Buildings (AISC-LRFD 1999)

| |
|---|
| **B10. Proportions of beams and girders**<br>*"When rolled or welded shapes, plate girders and cover-plated beams are proportioned on the basis of flexural strength of the gross section: (a) If* $0.75F_uA_{fn} \geq 0.9F_yA_{fg}$*, no deduction shall be made for bolt or rivet holes in either flange and (b) If* $0.75F_uA_{fn} < 0.9F_yA_{fg}$*, the member flexural properties shall be based on effective tension flange area which is given by* $A_{fe} = (5/6)(F_y/F_u)A_{fn}$ *and the maximum flexural strength shall be based on the elastic section modulus".* |

The AISC-LRFD (1999) code provision predicts the flexural strength of the net section based on the ratio of the factored fracture strength ($0.75A_{fn}F_u$) of net section-to-the factored yield strength of the gross section ($0.9A_{fg}F_y$) of the flange. For a particular steel grade having a yield-to-ultimate strength ratio of less than 0.8, the current AISC-LRFD (2005) allows 20% more holes that can be exempted without reducing the flexural strength of a beam member over the AISC-LRFD (1999) code. Moreover, the AISC-LRFD (1999) considers the behavior of tension flanges similarly to that of direct tension members by applying the same limit state ($0.75F_uA_{fn} \geq 0.9F_yA_{fg}$) for both cases. However, various research studies have indicated that the behavior of the tension flange (in a flexural member) is not same as the behavior of a direct tension member (Dexter et al, 2002 and Yuan 2004). The current AISC-LRFD (2005) has been modified based on the findings of Dexter et al., (2002) and Yuan's (2004) study. Therefore, the AISC-LRFD (2005) treats the behavior of tension flanges completely different from direct tension members by specifying two different limit states.

**Design procedure for flanges with holes exceeding a threshold value**

Fastener holes in both flanges:

According to the AISC-LRFD (1999) code provision, when fastener holes occur in either flanges of a flexural member, the effects of such holes can be ignored as long as $0.75F_uA_{fn} \geq 0.9F_yA_{fg}$. Otherwise, the section properties shall be established on the basis of the effective tension flange area which is defined as follows;

$$A_{fe} = (5/6)(F_u / F_y)A_{fn} \tag{3.11}$$

Hence, the elastic section modulus of net section can be determined as (Vinnakota 2006)

$$S_n = S_g - \left(A_{fg} - A_{fe}\right)\left(\frac{(d-t)^2}{d}\right) \tag{3.12}$$

Holes in one flange (tension or compression flange):

As per the AISC-LRFD (1999) code provision, the limit state of net area fracture shall be applied to either flange. Thus, the effects of holes in the tension flange can be ignored if $0.75F_uA_{fn} \geq 0.9F_yA_{fg}$. Otherwise, the elastic section modulus of the net section shall be established based on Equation 3.7, regardless of the section compactness. That is, the elastic section modulus shall be used for compact and non-compact sections.

Holes in both flanges:

Clause B10 of the AISC-LRFD (1999) code provision differentiates the effects of open holes from the effects of fastener holes, in which the holes contain bolts or rivets. Therefore, when open holes exist in both flanges of a flexural member the section modulus of the net section must be established by using Equation 3.9. The only difference between Equation 3.9 and Equation 3.12, which is used for fastener holes, is that the latter equation considers the added benefit of the presence of fasteners inside the holes by employing an effective flange area. The effective flange area is greater than the net flange area for steel grades having a yield-to-ultimate strength ratio of less than 0.83 (see Equation 3.11).

Clause B10 of the AISC-LRFD (1999) dealing with the proportion of flexural members having fastener holes in the flanges has already been revised in the AISC-LRFD (2005). The purpose of reviewing this standard however, was to analyze and compare it with the corresponding design clause appears in the current AISC (AISC-LRFD 2005) standard. Also, it was to compare with the other corresponding international code provisions.

### 3.3.4 British Standard Steel Design Code – Structural Use of Steelwork in Building-BS5950-2000 (BSI 2001)

**Clause 4.2.2.5 - Proportions of beams/girders**

*"No allowance need be made for bolt holes in a compression flange (or leg). No allowance need be made for bolt holes in a tension flange (or leg) if, for the tension element,* $A_{t,net} \geq A_t / K_e$*, where* $A_t$ *is the area of the tension element,* $A_{t,net}$ *is the net area of the tension element after deducting bolt holes, and* $K_e$ *is the factor for effective net area given in 3.4.3. No allowance need be made for bolt holes in tension zone of the web unless there are also bolt holes in the tension flange at the same location. Furthermore, no allowance need be made for bolt holes in a web if the condition given above is satisfied when both* $A_t$ *and* $A_{t,net}$ *are based upon the complete tension zone, comprising the tension flange plus the tension zone of the web".*

The BS5950 (BSI 2001) code provision clearly recognizes the effects of fastener holes. Also, it provides a clear explanation on treating the compression flange and the tension flange differently when fastener holes are present. Unlike the AISC-LRFD (2005) code provision, the BS5950 (BSI 2001) code provision includes the treatment of fastener holes when they occur in the webs (within the tension zone) of a flexural member. Moreover, the BS5950 (BSI 2001) code provision considers an added benefit of having fasteners inside the holes by invoking an effective tension flange area, which is always greater than the net flange area for steel grades having a yield-to-ultimate strength ratio less than 0.83.

This is similar to the AISC-LRFD (1999) code provision. To be consistent with the previous equations, $A_{t,net}$, $A_t$ and $A_{eff}$ used in the BS5950 (BSI 2001) code provision have been replaced with $A_{fn}$, $A_{fg}$ and $A_{fe}$, respectively in the following discussion.

**Design procedure for flanges with holes exceeding a threshold value**

Fastener holes in both flanges:

According to the BS5950 (BSI 2001) code provision, when fastener holes occur in either the tension or the compression flange, the effects of fastener holes can be ignored in the tension flange if $A_{fn} \geq A_{fg} / K_e$. Otherwise, the section properties shall be established based on the effective tension flange area. The effective tension flange area in accordance with the BS5950 (BSI 2001) code provision is expressed as

$$A_{fe} = K_e A_{fn} \tag{3.13}$$

The effective net area coefficient, $K_e$, is defined as

$$K_e = F_u / 1.2F_y \tag{3.14}$$

where $F_u$ is the minimum specified ultimate strength and $F_y$ is the design yield strength. Additionally, the BS5950 (BSI 2001) standard specifies different values of $K_e$ for different steel grades; (1) for grade S275: $K_e$=1.2, (2) for grade S355: $K_e$=1.1, and (3) for grade S460: $K_e$=1.0. Note that Equation 3.14 can be used to determine $K_e$ for any type of steel grade. If the tension fracture limit state is violated, the net section properties in terms of the plastic section modulus and the elastic section modulus shall be established as follows

If $A_{fn} \leq A_{fg} / K_e$, $$Z_n = Z_g - \left(A_{fg} - A_{fe}\right)\left(\frac{d-t}{2} + \bar{y}\right) \tag{3.15}$$

If $A_{fn} \leq A_{fg} / K_e$, $$S_n = \frac{(I_g + A_g \bar{y}^2) - I_{fhe}}{\left(\frac{d}{2} + \bar{y}\right)} \tag{3.16}$$

where $I_{fhe}$ is the second moment of area of the effective flange when holes are filled with fasteners, $A_{fhe} = A_{fg} - A_{fe}$.

Holes in one flange (tension or compression flange):

As per the BS5950 (BSI 2001) code provision, the effects of holes other than fastener holes shall be accounted based on the net section calculations. Therefore, the effective section properties in terms of the plastic section modulus and the elastic section modulus can be established by employing Equations 3.6 and 3.7, respectively.

Holes in both flanges:

In this case, the section properties shall be established based on net section calculations. Therefore, the plastic section modulus and the elastic section modulus of the net section can be established by employing Equations 3.8 and 3.9, respectively.

### 3.3.5 Australian Steel Design Code - Steel Structures - AS4100 - 1998 (SA 1998)

| |
|---|
| **Clause 5.2.6: Proportions of beams/girders** |
| *Elastic and plastic section moduli-for sections without holes, or for sections with holes that reduce either of the flange areas by not more than* $100\{1-(F_y/0.85F_u)\}$ *%, the elastic and plastic section moduli may be calculated using the cross-section. For sections with holes that reduce either of the flange areas by more than* $100\{1-(F_y/0.85F_u)\}$ *%, the elastic and plastic section modules shall be calculated using either* $(A_n/A_g)$ *times the value for the gross section, in which* $A_n$ *is the sum of the net areas of the flanges and the gross area of the web, and* $A_g$ *the gross area of the section; or the net section.* |

The AS4100 (SA 1998) code provision treats the effects of open holes and fastener holes in an identical manner which is analogous to the AISC-LRFD (2005) code provision. The AS4100 (SA 1998) code provision recognizes the effects of holes in the web which is similar to the BS5950 (BSI 2001) code provision. The AS4100 (SA 1998) code provision accounts for the effects of holes in the whole web, whereas the BS5950 (BSI 2001) code considers the presence of holes in the web in the tension zone. Comparable to the AISC-LRFD (1999) code method, the AS4100 (SA 1998) code provision applies the limit state of net area fracture to either flange.

**Design procedure for flanges with holes exceeding a threshold value**

Fastener holes in both flanges:

As per the AS4100 (SA 1998) code provision, no deduction for fastener holes shall be made if the following condition is satisfied;

$$A_{fn} \geq \left( \frac{F_y}{0.85 F_u} \right) A_{fg} \tag{3.17}$$

If the condition is violated, $A_{fn} < \left( \frac{F_y}{0.85 F_u} \right) A_{fg}$, the net section properties in terms of the plastic section modulus and the elastic section modulus shall be established as

$$Z_n = \left[ \frac{2A_{fn} + A_{wg}}{A_g} \right] Z_g \tag{3.18}$$

$$S_n = \left[ \frac{2A_{fn} + A_{wg}}{A_g} \right] S_g \tag{3.19}$$

where $A_{fn}$ is the net section area of the tension or compression flange, $A_{wg}$ is the gross area of the web if the web has no holes and $A_g$ is the gross cross-section area. Equations 3.18 and 3.19 are based on the assumption that $A_{fn}$ is equal for the tension and the compression flange.

Holes in one flange (tension or compression flange):

When holes occur either in the tension or in the compression flange, the limit state of net section fracture shall be applied as provided above. Otherwise, the net section properties in terms of the plastic and elastic section modulus shall be established as follows

$$Z_n = \left[ \frac{A_{fg} + A_{fn} + A_{wg}}{A_g} \right] Z_g \tag{3.20}$$

$$S_n = \left[ \frac{A_{fg} + A_{fn} + A_{wg}}{A_g} \right] S_g \tag{3.21}$$

where $A_{fg}$ is the gross-area of the flange with no holes and $A_{fn}$ is the net area of the flange with holes.

Holes in both flanges:

Since the AS4100 (SA 1998) code provision treats the effects of fastener holes analogous to that of open holes, the design procedure associated with this case is the same as the design procedure associated with the case where fastener holes occur in both flanges.

## 3.4 "Threshold Values of Holes" for Different Steel Grades

The review of various international code provisions presented above indicates that fastener holes in the flanges of flexural members are of concern beyond a certain limit. Each of the standards considered establishes a threshold value pertaining to the amount of fastener holes that can be permitted without affecting the flexural strength of the gross cross-section. The current AISC-LRFD (2005) and the AS4100 (SA 1998) code provisions deal with fastener holes and open holes in the flanges in a similar manner, whereas the CSA (2003) and the BS5950 (BSI 2001) code provisions treat fastener holes differently than open holes in the flanges. Nevertheless, the design clauses in accordance with the AISC-LRFD (2005), AISC-LRFD (1999), BS5950 (BSI 2001) and AS4100 (SA 1998) standards establish a threshold value based on the yield-to-ultimate strength ratio of a steel grade. In regards to the threshold value, the CSA (2003) code permits a fixed 15% exemption for fastener holes irrespective of the material characteristics in terms of the yield-to-ultimate strength ratio.

Table 3.2 presents the flange hole exemption limits (threshold value) for different steel grades based on different standards. This table includes traditionally used steels such as mild carbon and A36 steel as well as the currently used steels; 350W, ASTM A572 Grade 60, ASTM A992, ASTM A913 Grade 50, A913 Grade 65 and HPS 70W. The ranges of yield strength, ultimate strength and resulting yield-to-ultimate strength ratio values for each steel grade considered are also provided in this table.

It can be observed from Table 3.2 that the CSA (2003) code provision is more restrictive for the mild carbon and ASTM A36 steels when compared with other code provisions. Conversely, the CSA (2003) code may be unconservative for steels such as ASTM A992, A913 Grade 50 and 65, HPS 70W, which are currently in use, in comparison with other code provisions. The old version of the AISC-LRFD (1999) code, the BS5950 (BSI 2001) code and the AS4100 (SA 1998) code provisions establish a similar threshold value for the same steel grades. However, the current AISC-LRFD (2005) code provision relaxes the threshold value so that larger flange holes may be provided without penalizing the gross cross-section moment capacity. Note that the current AISC-LRFD (2005) code has been revised based on the recent tests on tension members and flexural members made of HPS 70W steel (Dexter et al, 2002) as well as tension members and T-shaped specimens made of A992 steel (Yuan, 2004). These test results has yielded a conclusion that the flexural strength on net section can be better predicted by a comparison of quantities; $A_{fg}F_y$ and $A_{fn}F_u$. This is true for steel grades having $F_y / F_u \leq 0.8$. For $F_y / F_u > 0.8$, the $A_{fn}F_u$ is multiplied by a factor $Y_t$=1.1. This implies that smaller holes will be allowed in flanges made of steel grade having $F_y / F_u > 0.8$ over the similar flanges made of steel with $F_y / F_u \leq 0.8$. Nevertheless, the current AISC-LRFD (2005) allows relatively larger holes that can be made in the flanges without impacting the cross-section strength than other code provisions considered.

## 3.5 Moment Resistance of Beams with Flange Holes: Comparison of Code Provisions

In order that different code provisions may be compared, the variation of the normalized moment with increasing percentage of holes with respect to the gross flange area was established in accordance with various standards under consideration. The beam sections under consideration were; W610X101, W410X54 and W530X72, classified as Class 1, Class 2 and Class 3, respectively as per the CSA (2003) standard. The moment was normalized with respect to the plastic moment capacity for Class 1 and Class 2 sections and the yield moment capacity for Class 3 section. In order to depict how each code provision takes into account of the strain hardening potential of steel grades, two different steel grades 350W and A992 steels with yield-to-ultimate strength ratio values of 0.78 and 0.85, respectively, were assumed. Moreover, the practical scenarios such as (1) fastener holes in both flanges (2) open holes in one flange (tension flange or compression flange) and (3) open holes in both flanges were considered in this study.

### 3.5.1 Fastener Holes in Both Flanges

Figures 3.4[A] through 3.4[F] illustrate the normalized moment versus the percentage fastener hole area-to-gross flange area for beam sections W610X101 (Class 1), W410X54 (Class 2) and W530X72 (Class 3). The moment resistances were established on the basis of five different code provisions considered and theoretical calculations (see section 3.2.3). These figures correspond to 350W steel having yield-to-ultimate strength ratio of 0.78. The figures on the left side compare the CSA (2003) with the AISC-LRFD (2005 and 1999) codes while the figures on the right side compare the CSA (2003) with the BS5950 (BSI 2001) and the AS4100 (SA 1998) codes for three different classes of sections considered. For Class 1 and Class 2 sections, the AISC-LRFD (1999) predicted lower moment resistance than the other code methods beyond $\rho_h \geq 6.4\%$. This is due to the AISC-LRFD (1999) requirement that the flexural strength on the net section be established based on elastic section modulus, regardless of the section compactness (Vinnakota 2006). For the same steel, the AISC-LRFD (2005) allows fastener holes up to 22% of the gross flange area without penalizing the full plastic gross cross-section capacity. Beyond 22%, the variation of moment reduction with increasing $\rho_h$ as per the AISC-LRFD (2005) was relatively steeper than the variation of moment reductions based on the other design standards. This may be attributed to the fact that the AISC-LRFD (2005) adjusts the failure stress from $F_y$ to $F_u(A_{fn} / A_{fg})$ and applies this stress value conservatively to the elastic section modulus, regardless of the section compactness, beyond a threshold limit. This is comparable to the AISC-LRFD (1999) code provision. It is of interest to note that, for Class 1 and Class 2 sections, all code methods, except the AISC-LRFD (1999), allowed higher moment resistance than Theory 2. This is true up to $\rho_h$ = 30%. For Class 3 section however, Theory 2 established a moment resistance lower than the code methods (see Figures 3.4[E] and 3.4[F]). Moreover, for Class 1 and Class 2 sections, the variation of moment resistance as per the AS4100 (SA 1998) closely agreed with the variation of the average moment resistance determined based on Theory 1 and Theory 2. This is as a result of the effective section modulus as per the AS4100 (SA 1998) method being estimated by considering the proportion of the net flange areas plus gross web area to the gross cross-section area (see Equation 3.18). The variation of moment resistance determined on the basis of the CSA (2003) and the BS5950 (BSI 2001) were relatively close to each other up to $\rho_h$ = 30% for Class 1 and Class 2 sections. For $\rho_h$ >30%, the BS5950 (2001) allowed higher moment on the net section than the other code methods considered (see Figure 3.4[A] through 3.4[D]). However, for Class 3 section the AISC-LRFD (2005) permitted relatively higher moment resistance than the other codes. This was true up to $\rho_h \approx 32\%$. For $\rho_h > 32\%$, the CSA (2003) allowed higher moment resistance on net section (See Figures 3.4[E] and 3.4[F]).

Figures 3.5[A] through 3.5[F] show the normalized moment versus the percentage fastener hole area-to-gross flange area for three different classes of sections made of A992 steel having $F_y / F_u = 0.85$. For Class 1 and Class 2 sections, the CSA (2003) permitted higher moment than the other code methods. This was true for fastener holes up to 35% (see Figures 3.5[A] through 3.5[D]). Beyond 35%, the BS5950 (BSI 2001) allowed higher moment resistance over the other code methods and theoretical estimations. For Class 3 section, however, the CSA (2003) predicted higher moment for $\rho_h = 45\%$ (see Figures 3.5[E] and 3.5[F]). As seen in Figures 3.5[A] through 3.5[F], the BS5950 (BSI 2001) had good correlation with Theory 1.

### 3.5.2 Open Holes in Both Flanges

The clause 14.1 of the CSA (2003) standard stipulates that the effects of holes other than fastener holes shall be accounted on the basis of net section calculations. Thus, no exemption is allowed for such holes. Comparable to the CSA (2003) standard, clause 4.2.5.5 of the BS5950 (BSI 2001) standard takes into account the effects of fastener holes only. Therefore, the effects holes other than fastener holes shall be established by the theoretical net section calculations as per the BS5950 (BSI 2001) code provision. However, the AISC (AISC-LRFD 2005) standards including the old version (AISC-

LRFD 1999) treat the effects of open holes and fastener holes in an identical manner. Also, the AS4100 (SA 1998) considers the effect of fastener holes and that of open holes in the same manner.

Figures 3.6[A] through 3.6[F] present the variation of normalized moment versus the percentage of open holes to the gross flange area (in both flanges) for the 350W steel grade having $F_y / F_u$=0.78. As seen in Figures 3.6[A] and 3.6[C] relating Class 1 and Class 2 sections, respectively, Theory 2 established a lower moment than the AISC-LRFD (2005). This was true for $\rho_h \approx$30%. For $\rho_h$>30%, Theory 2 predicted higher moment than the AISC-LRFD (2005). In all ranges of the percentage of holes considered, the AS4100 (SA 1998) predicted higher moment than Theory 2 for Class 1, Class 2 and Class 3 sections (see Figures 3.6[B], 3.6[D] and 3.6[F]). As seen in the figures, the AISC-LRFD (1999) was excessively conservative over the other codes and Theory 2 for Class 1 and Class 2 section beyond $\rho_h$=6.7%.

Figures 3.7[A] through 3.7[F] illustrate the normalized moment versus the percentage of holes to gross flange area in both flanges of beam sections W610X101 (Class1), W410X54 (Class 2) and W530X72 (Class 3). These figures relate A992 steel grade having $F_y / F_u$=0.85. For Class 1 and Class 2 sections, the AISC-LRFD (2005) predicted higher moment over all other standards and Theory 2 for $\rho_h$=6.5%. However, for $\rho_h$>6.5%, Theory 2 predicted higher moment than the AISC-LRFD (2005). For Class 3 section, the AISC-LRFD (2005) allowed higher moment than Theory 2 for $\rho_h$=22% (see Figure 3.7[E]). For all three classes considered, the AS4100 (SA 1998) established higher moment than the AISC-LRFD (2005) and Theory 2. Since the CSA (2003) and the BS5950 (BSI 2001) treat the effects of open holes based on net-section calculations, they just follow Theory 2.

### 3.5.3 Open Holes in One Flange (Tension Flange or Compression Flange)

Figure 3.8[A] through 3.8[F] present the variation of normalized moment versus percentage of hole area to gross flange area for beams W610X101 (Class1), W410X54 (Class 2) and W530X72 (Class 3). These figures correspond to 350W steel grade having $F_y / F_u$=0.78. It can be noted (from these figures) that the AISC-LRFD (2005) required no moment reduction for $\rho_h$=22%. The previous version of the AISC code (AISC-LRFD 1999), however, required no moment reduction for $\rho_h$=6.7% for the same steel grade. For $\rho_h$>22%, the AS4100 (SA 1998) predicted higher moment than the other code methods and Theory 1.

Figures 3.9[A] through 3.9[F] show the variation of normalized moment versus percentage of holes to gross flange area (in one flange). These figures relate A992 steel grade having $F_y / F_u$=0.85. As seen in these figures, the AISC-LRFD (2005) required no moment reduction for $\rho_h$ =6.5%. For $\rho_h$ >6.5%, the AS4100 (SA 1998) predicted slightly higher moment over the other codes and Theory 1.

## 3.6 Summary

The following points summarize the discussions pertaining to the review of five different code provisions along with the net section calculations based on bending theory;

- Comparison of different standards indicated that the 15% exemption rule as per the current CSA (2003) standard was more restrictive for steel grades having yield-to-ultimate strength ratio values less than 0.8. However, it may be unconservative for steel grades having yield-to-ultimate strength ratio values greater than 0.8 (see Table 3.2).
- Comparison of the current and the previous provisions of the AISC (AISC-LRFD 2005 and 1999) standards indicated that the current version allowed 20% more holes to gross flange area than the previous version without deducting the gross section plastic moment capacity. This is true for steel grades having yield-to-ultimate strength ratio values less than 0.8. For steel grades having yield-to-ultimate strength ratio values of more than 0.8, the current version of the AISC-LRFD (2005) permitted 10% more holes to gross flange area than the previous version.
- Steel design standards; the AISC-LRFD (1999), the BS5950 (BSI 2001) and the AS4100 (SA 1998) seemed to provide a threshold value for a particular steel grade relatively in a similar manner

- Overall, the current AISC-LRFD (2005) code permitted a higher threshold value than the other standards considered.
- Overall, the AISC-LRFD (1999) was conservative over the other code methods and theoretical approach.

Table 3.1: Sectional Properties and Dimensions [CISC Handbook 2007]

| Designation | Properties | | | | Sectional Dimensions and Flange Area | | | | | |
|---|---|---|---|---|---|---|---|---|---|---|
| | $A_g$ | $I_g$ | $S_g$ | $Z_g$ | $b$ | $t$ | $A_{fg}$ | $d$ | $w$ | $h$ |
| | $mm^2$ | $10^6\ mm^4$ | $10^3\ mm^3$ | $10^3\ mm^3$ | mm | mm | $mm^2$ | mm | mm | mm |
| (1) | (2) | (3) | (4) | (5) | (6) | (7) | (8) | (9) | (10) | (12) |
| W610X101 [Class 1] | 13000 | 764 | 2530 | 2900 | 228 | 14.9 | 3397 | 603 | 10.5 | 573.2 |
| W410X54 [Class 2] | 6810 | 186 | 924 | 1050 | 177 | 10.9 | 1929 | 403 | 7.5 | 381.2 |
| W530X72 [Class 3] | 9120 | 400 | 1520 | 1750 | 207 | 10.9 | 2256 | 524 | 8.9 | 502.2 |
| W200X42 [Class 1] | 5310 | 40.9 | 399 | 445 | 166 | 11.8 | 1959 | 205 | 7.2 | 181.4 |

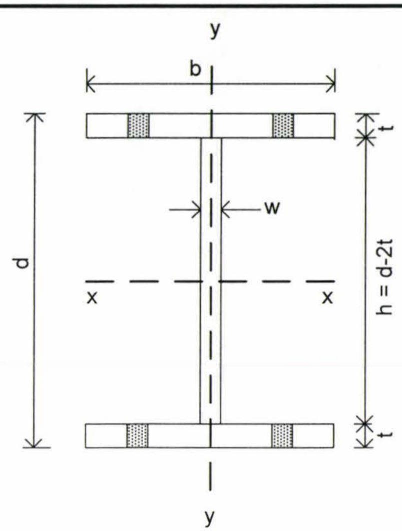

Table 3.2: Threshold Values for Different Steel Grades Based on Different Code Rule

| **Steel Grade** | **Mild-Steel** | **A36** | **350W** | **A572/ A572M (Gr:60)** | **A992/ A992M*** | **A913 (Gr:50)** | **A913 (Gr:65)** | **A709/ HPS-70W** |
|---|---|---|---|---|---|---|---|---|
| $F_y$ (MPa) | 190-225 | 250 | 350 | 420 | 345-450 | 345 | 450 | 485 |
| $F_u$ (MPa) | 380-450 | 400-550 | 450-650 | 515 | 450 | 450 | 550 | 585-760 |
| $F_y / F_u$ | 0.5 | 0.45-0.63 | 0.54-0.78 | 0.82 | 0.77-0.85 | 0.77 | 0.82 | 0.64-0.83 |
| **CAN/CSA-S16.01(CSA 2003)**: Limiting $A_{fn} / A_{fg}$ ratio [Threshold flange holes percentage] | 0.85 [15%] | 0.85 [15%] | 0.85 [15%] | 0.85 [15%] | 0.85 [15%] | 0.85 [15%] | 0.85 [15%] | 0.85 [15%] |
| **AISC-LRFD(2005)**: Limiting $A_{fn} / A_{fg}$ ratio [Threshold flange holes percentage] | 0.50 [50%] | 0.45-0.63 [37%-55%] | 0.54-0.78 [22%-46%] | 0.90 [10%] | 0.77-0.94 [6%-23%] | 0.77 [23%] | 0.90 [10%] | 0.64-0.91 [9%-36%] |
| **AISC-LRFD(1999)**: Limiting $A_{fn} / A_{fg}$ ratio [Threshold flange holes percentage] | 0.60 [40%] | 0.54-0.76 [24%-46%] | 0.65-0.94 [6%-35%] | 0.98 [2%] | 0.92-1.00 [0%-8%] | 0.92 [8%] | 0.98 [2%] | 0.77-1.00 [0%-23%] |
| **BS5950-2000 (BSI 2001)**: Limiting $A_{fn} / A_{fg}$ ratio [Threshold flange holes percentage] | 0.60 [40%] | 0.54-0.76 [24%-46%] | 0.65-0.94 [6%-35%] | 0.98 [2%] | 0.92-1.00 [0%-8%] | 0.92 [8%] | 0.98 [2%] | 0.77-1.00 [0%-23%] |
| **AS4100-1998 (SA 1998)**: Limiting $A_{fn} / A_{fg}$ ratio [Threshold flange holes percentage] | 0.59 [41%] | 0.53-0.74 [26%-47%] | 0.64-0.92 [8%-36%] | 0.96 [4%] | 0.91-1.00 [0%-9%] | 0.91 [9%] | 0.96 [4%] | 0.75-0.98 [2%-25%] |

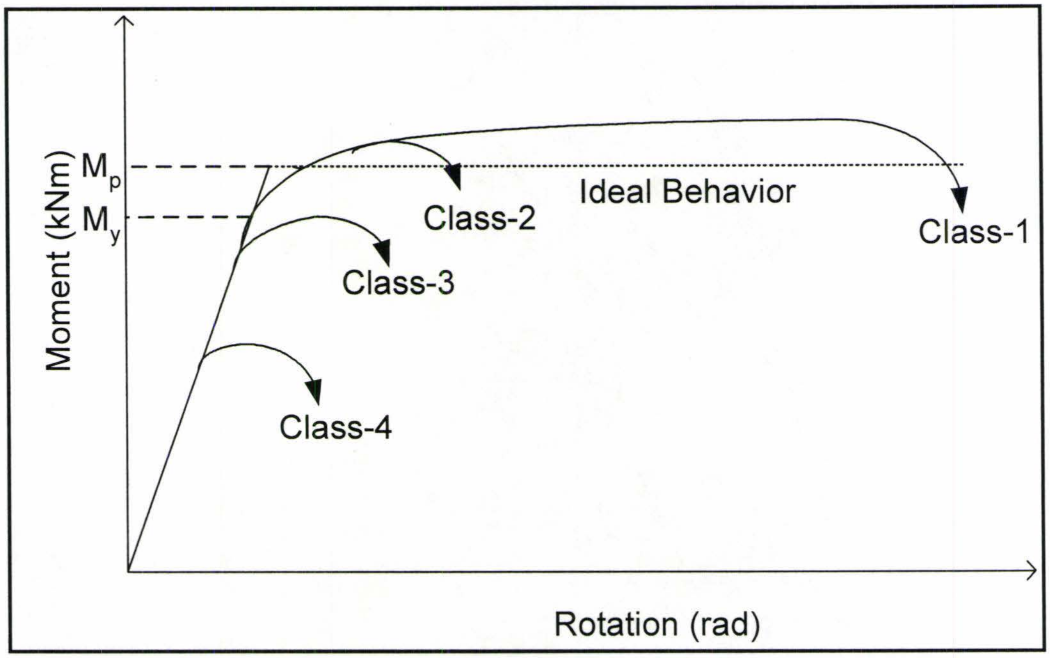


Figure 3.1: Moment-Rotation Relationships

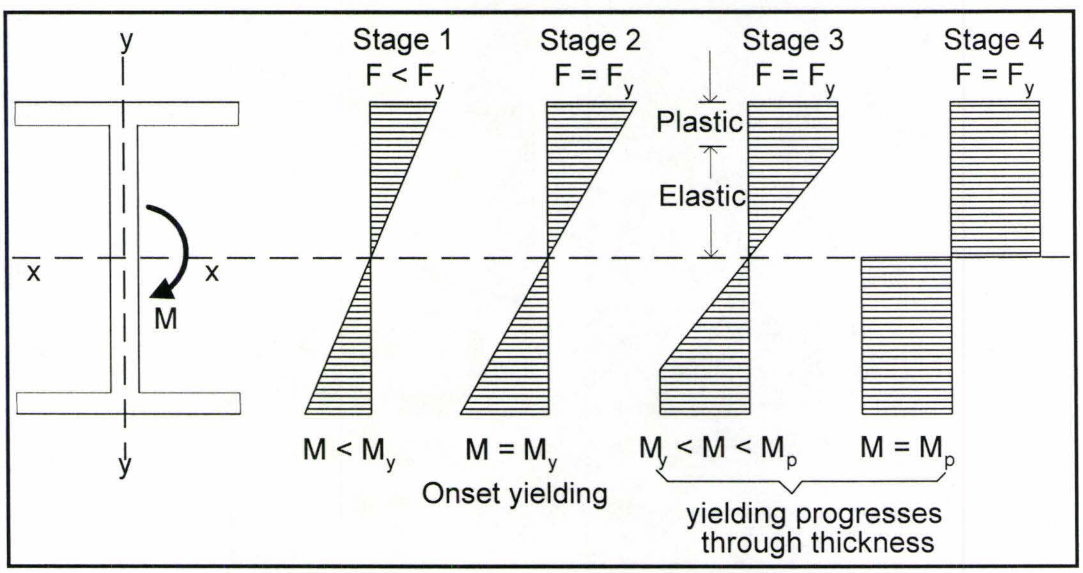


Figure 3.2: Stress Distribution at Different Stages of Loading

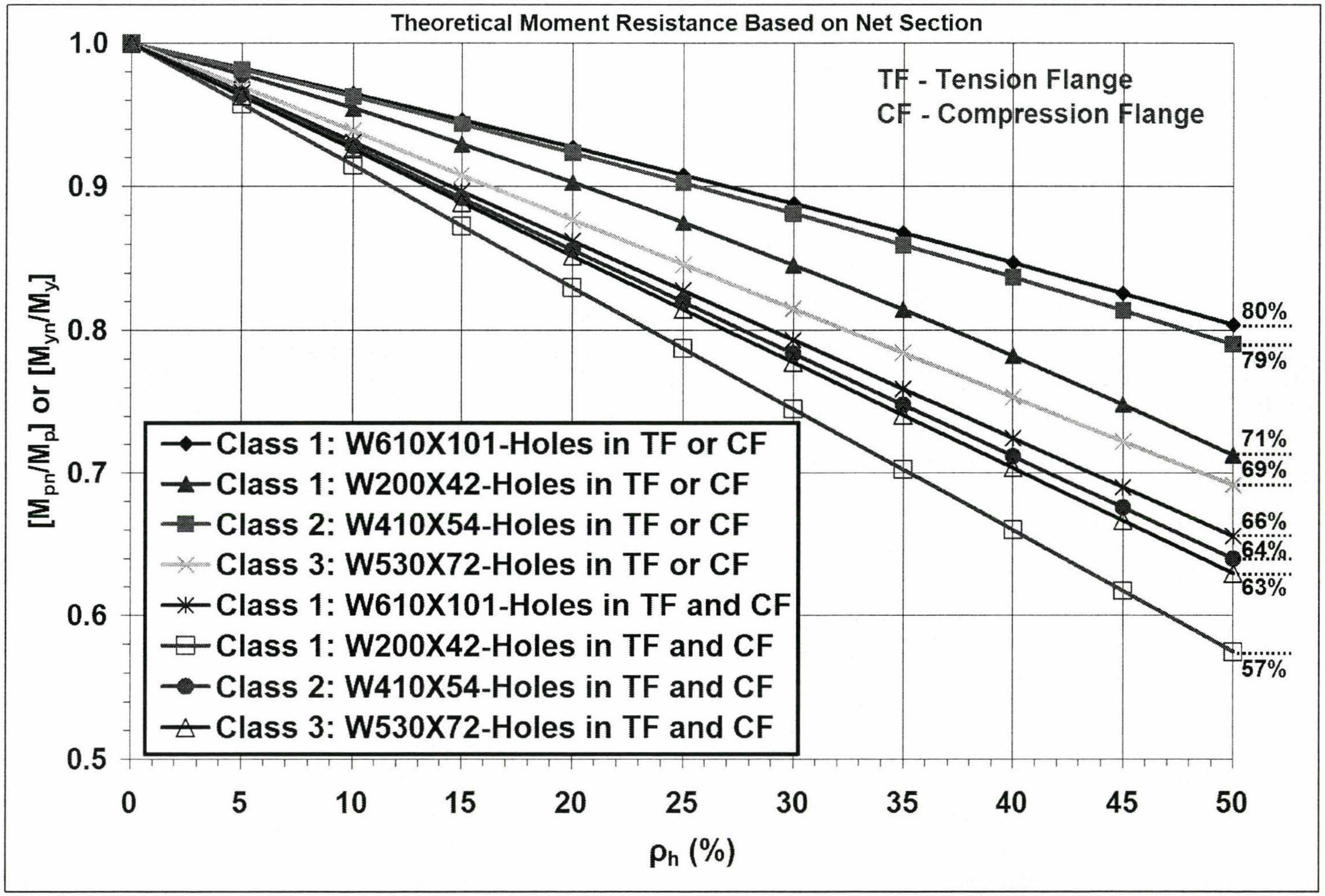


Figure 3.3: Theoretical Moment Resistance Based on Net Section

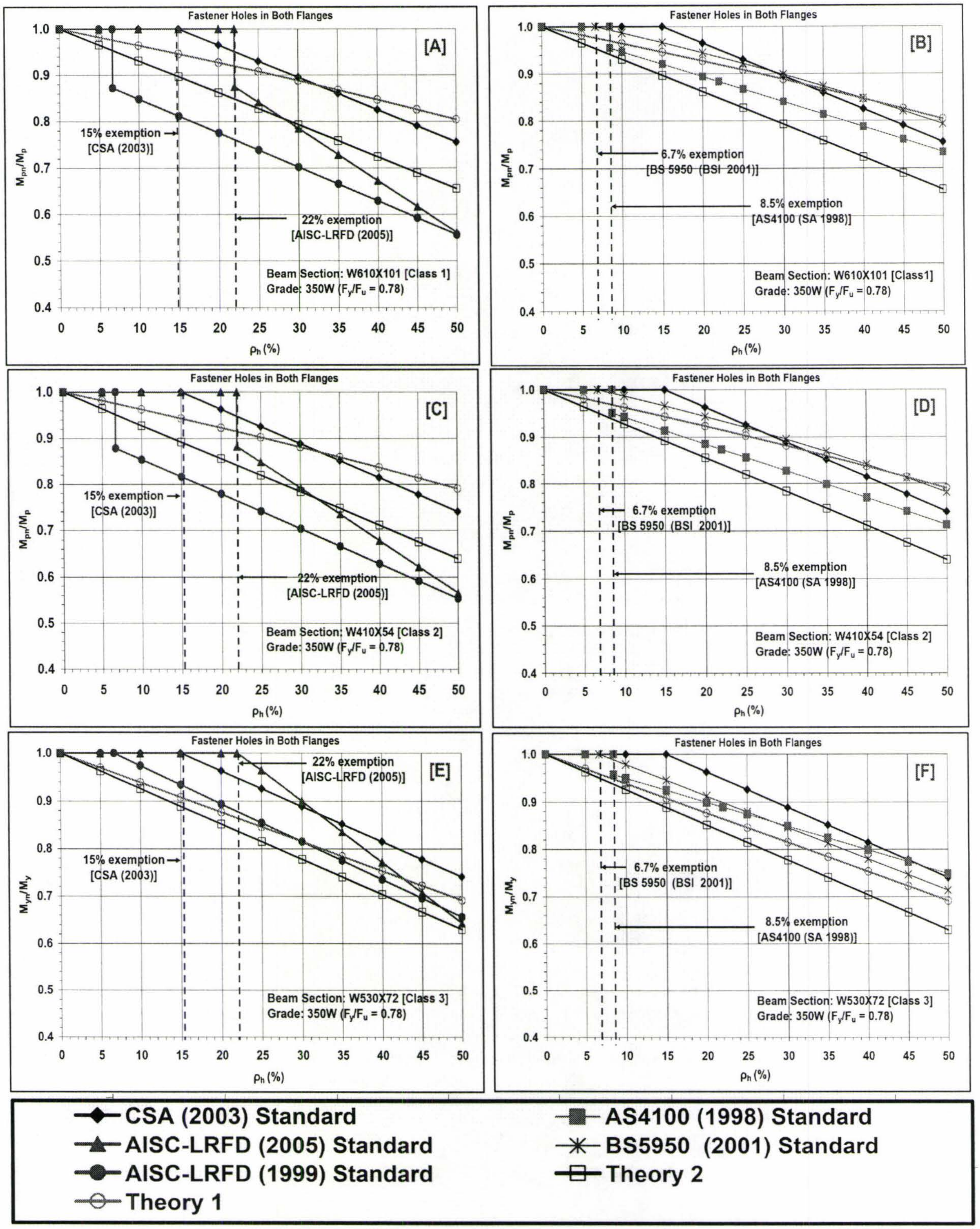


Figure 3.4: Comparison of Moment Reduction Established Based on Code Methods and Theory for 350W steel - Fastener Holes in Both Flanges

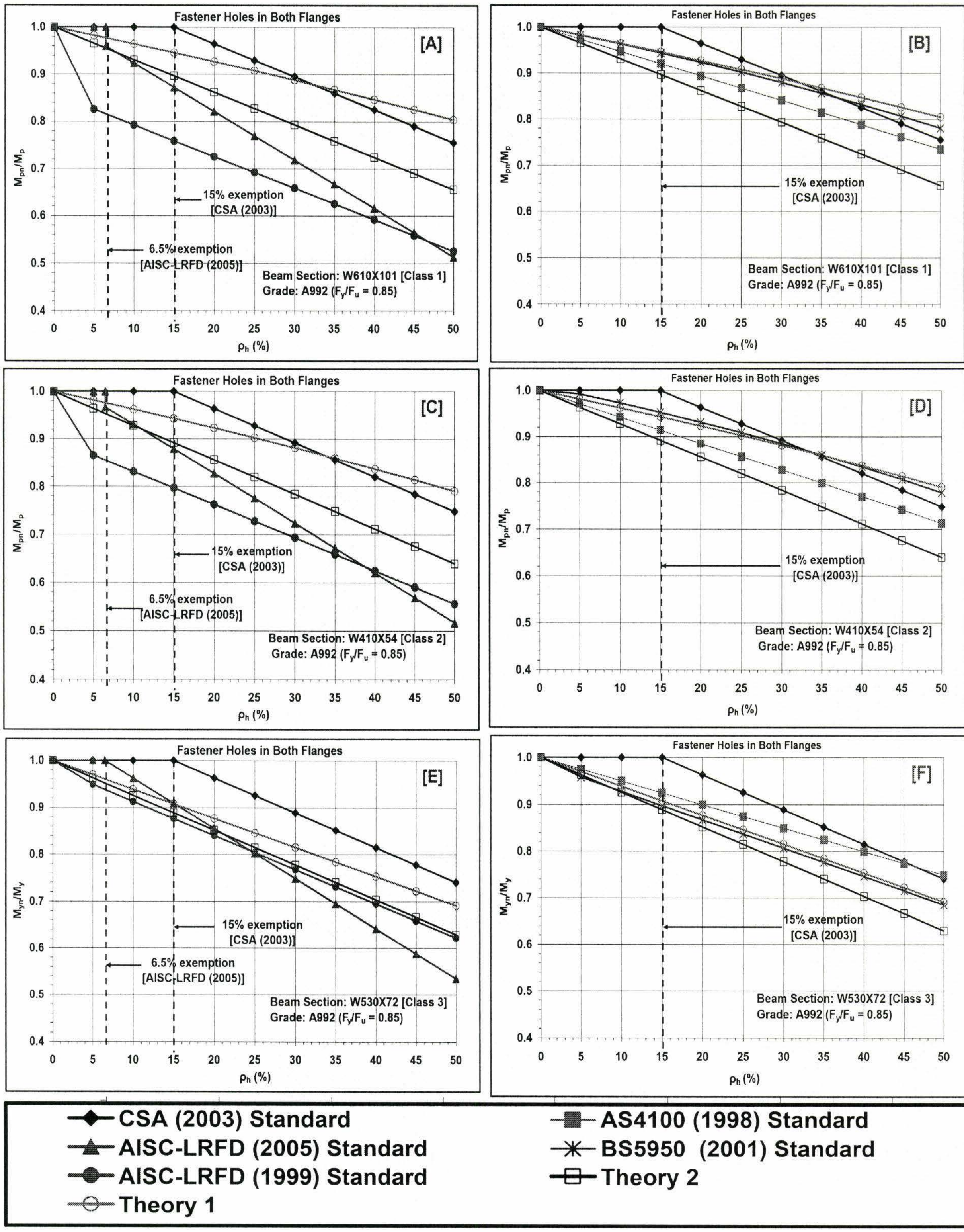


Figure 3.5: Comparison of Moment Reduction Established Based on Code Methods and Theory for A992 steel - Fastener Holes in Both Flanges

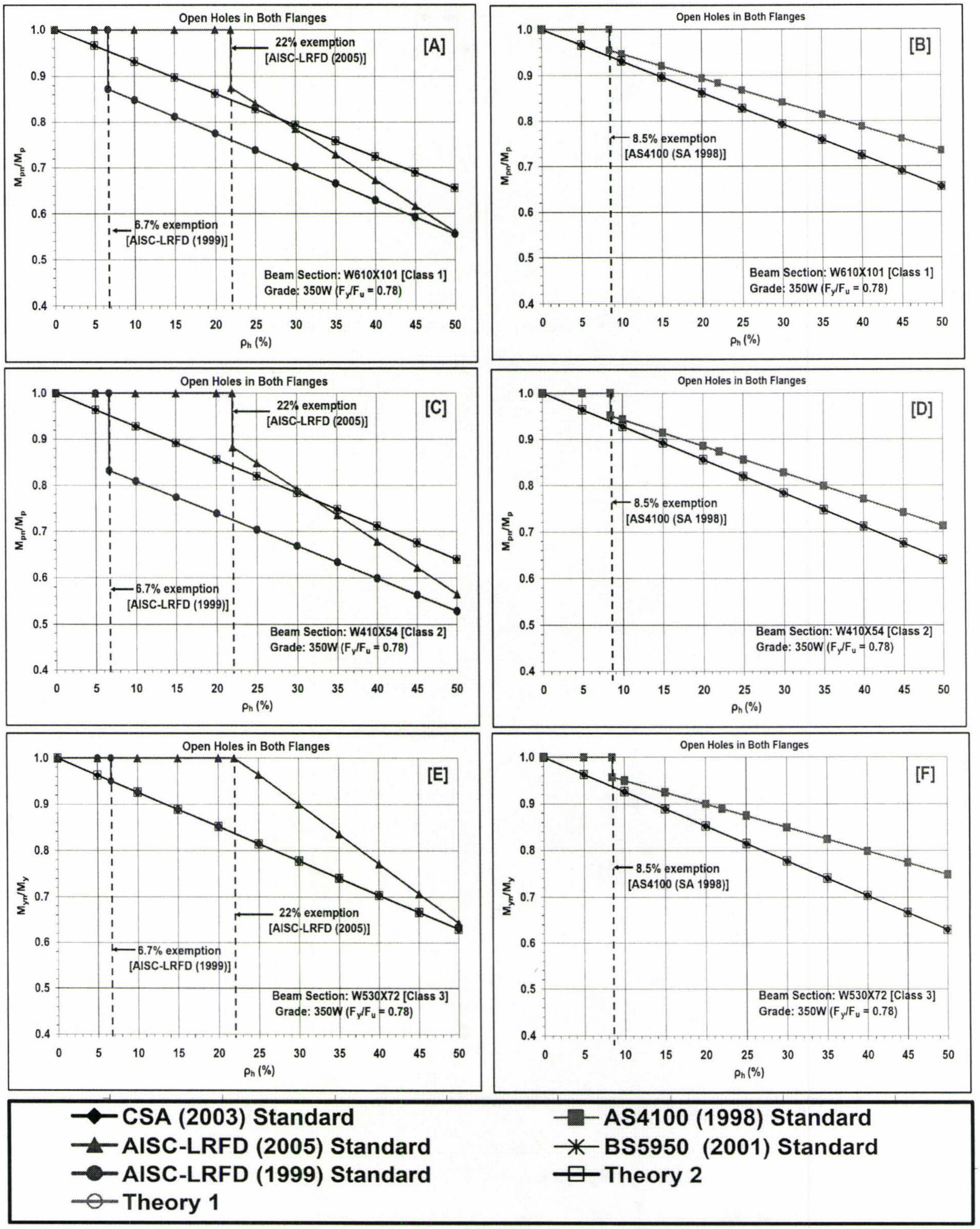


Figure 3.6: Comparison of Moment Reduction Established Based on Code Methods and Theory for 350W steel – Open Holes in Both Flanges

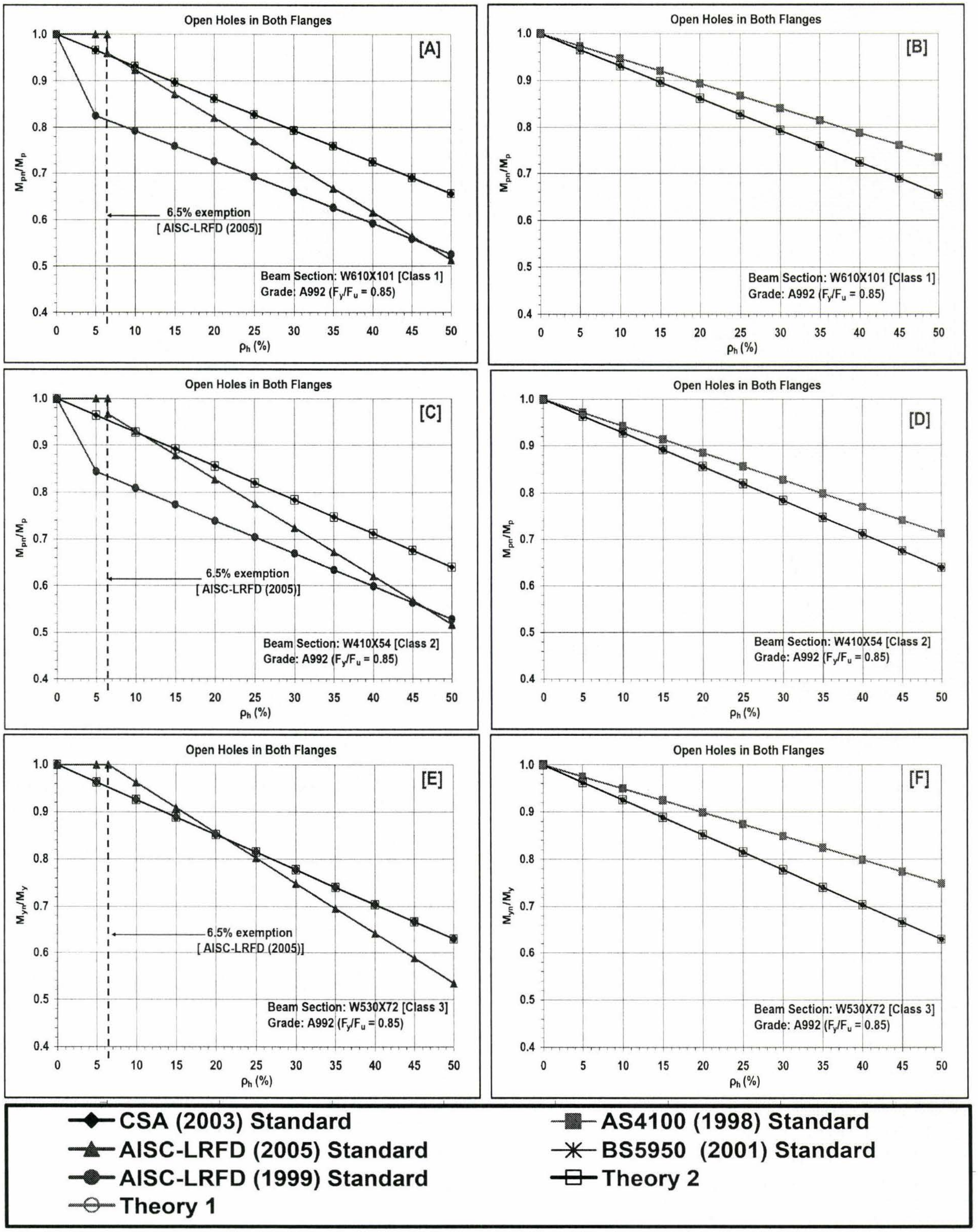


Figure 3.7: Comparison of Moment Reduction Established Based on Code Methods and Theory for A992 steel – Open Holes in Both Flanges

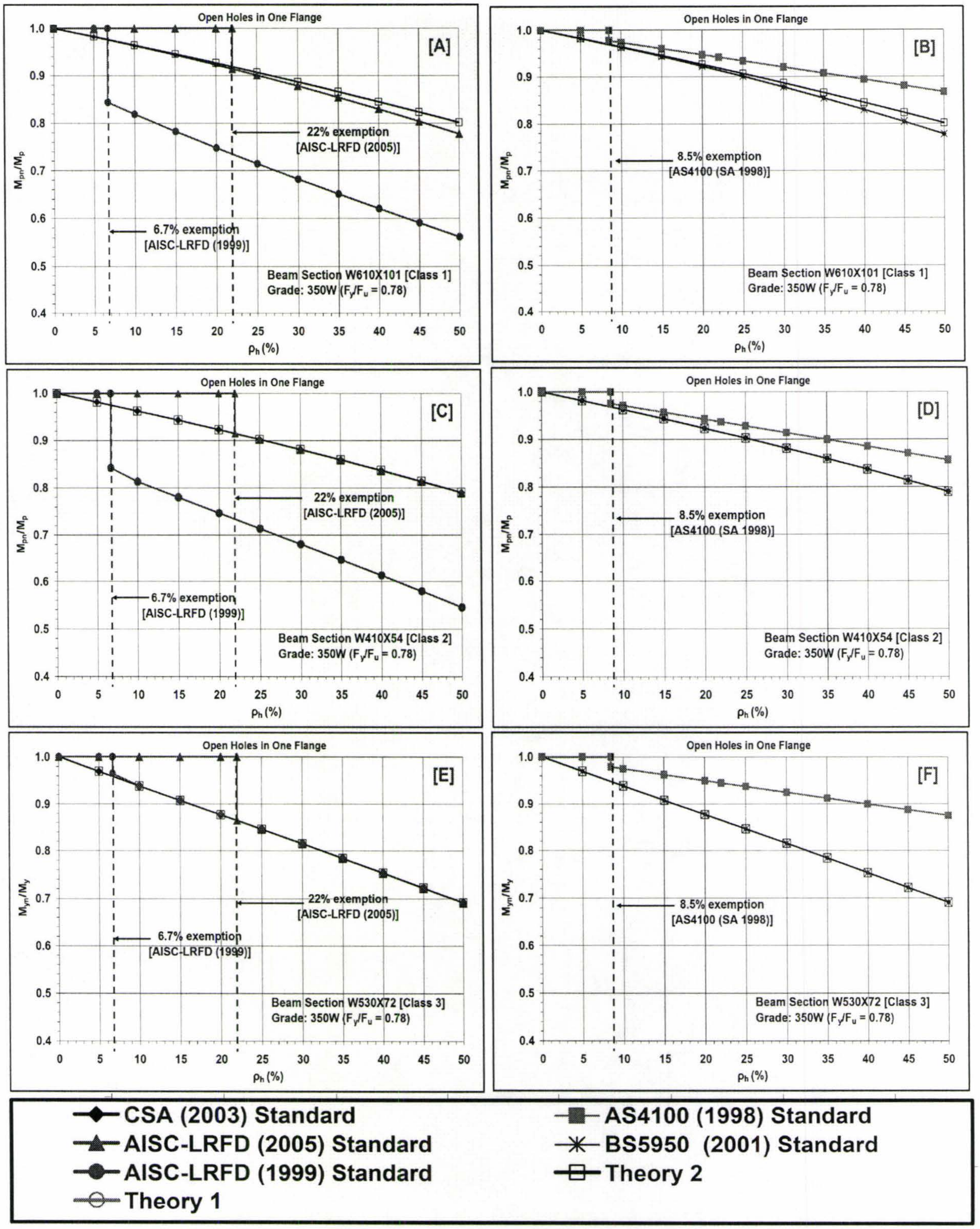


Figure 3.8: Comparison of Moment Reduction Established Based on Code Methods and Theory for 350W steel – Open Holes in One Flange

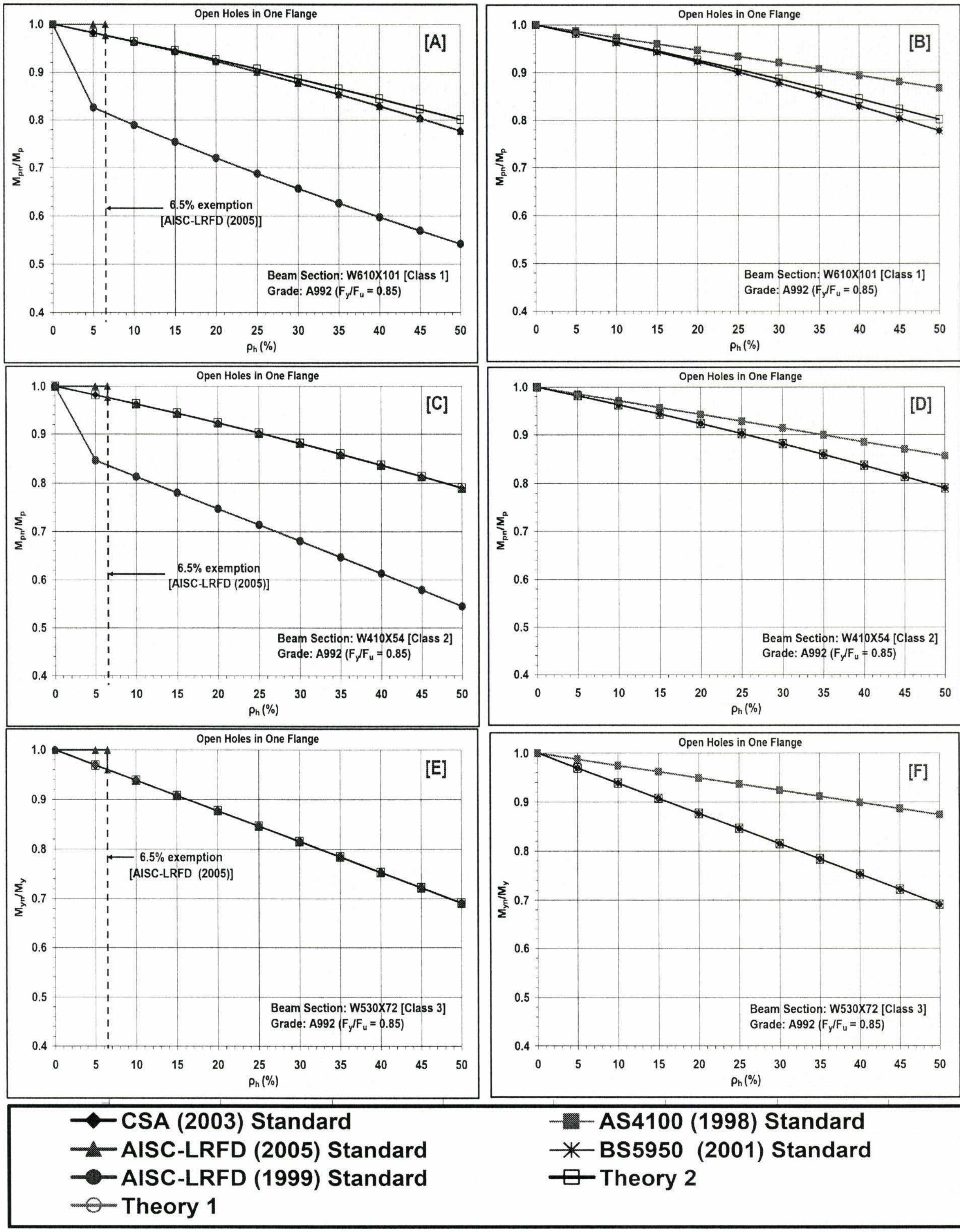


Figure 3.9: Comparison of Moment Reduction Established Based on Code Methods and Theory for A992 steel – Open Holes in One Flange

# CHAPTER: 4

# THE TEST PROGRAM

## 4.1 Introduction

The purpose of the test program presented here was to obtain experimental data, which was subsequently used to evaluate the impact of flange holes on the flexural behavior of steel beams. The specified steel grade of the beam specimens tested was ASTM A992 steel grade. This steel grade was of particular interest as it is widely used by industry and it is the grade most impacted by the new AISC specification (AISC, 2005). All beam tests were performed under four-point bending configuration creating a uniform moment region in the midspan. Holes in the flanges of beams were laid at the center midspan.

The geometrical and mechanical characteristics of beam specimens are presented in this chapter. A description of the test program, including the test matrix, overall test setup, support conditions, loading conditions, loading system, test procedure and test instrumentation, is also presented. Additionally, this chapter provides sample test results to illustrate and describe how the test results were processed and evaluated.

## 4.2 Description of Test Specimens

A total of twenty five W200X42 beam specimens were tested. These rolled steel beam specimens were obtained from the same production batch to minimize discrepancies associated with the material characteristics. Therefore, the test results obtained from the beam specimens can be directly compared and conclusions with regards to the impact of flange holes on flexural behavior made. The following factors were considered during the selection of the beam sections W200X42 used in this study;

- available capacity of the laboratory testing facility including the load cell and the stroke length of an actuator.
- typically used beam sizes in steel building frames.
- availability of beam sizes in the market.
- suitability of a beam size to serve the purpose of this investigation. For example, a deep beam may fail as a result of web yielding and/or web crippling in the critical shear regions and such failure modes were avoided in this study.

Since the investigation involved studying the effects of flange holes on the flexural behavior, all tests were conducted as simply supported at the ends of the beam specimens and subjected to two point loads in the midspan region. Thus, the midspan of each beam specimen experienced a uniform moment region. A pair of holes were made in the flanges (on either side of flange-web junction) at the center midspan. The responses of each test beam were established by measuring the load, deflections within the uniform moment region (at midspan, loading points, quarter points) and the end rotations. The mechanical characteristics of the steel grade of the beam material were established by conducting standard tensile coupon tests.

The beam tests performed in this investigation can be grouped into four different series. Series 1, 2, 3 and 4 involved 4, 13, 4 and 4 test specimens, respectively.

Series-1: This series involved the beam tests with solid flanges (no flange holes). A total of four beams identified herein as A100-1, A100-2, A100-3 and A100-4 were tested in this series. Regarding specimen identification labeling used in this study, A100 denotes the percentage of net flange area-to-gross flange area and the number following the hyphen indicates the test-number.

Series-2: This series included the beam tests with open holes in the tension flanges only. A total of seven different percentages of net flange area-to-gross flange area, $\rho_h$, ranging from approximately 90% to 50% were considered. The beams tested in this series were identified as A90-1, A85-1, A80-1, A75-1, A70-1, A60-1 and A50-1. Moreover, the beam specimens having $\rho_h$ (in percentage) of approximately 75%, 70% and 60% were repeated twice in order to:

(1) Establish a percentage of net flange area-to-gross flange area ($\rho_h$) beyond which the dominant failure mode would be net section fracture. It was observed that the beams having $\rho_h$ between 75% and 60% exhibited a mixed failure modes; (a) local buckling of the compression flange followed by net section fracture and (b) definite net section fracture through tension flange holes.

(2) Confirm the repeatability of test results.

(3) Minimize the repetition of beam tests under each category so that the remaining beam specimens would be used to explore the impact of holes on the flexural behavior in other cases such as open holes in both tension and compression flanges and fastener holes in both flanges. A total of thirteen beam tests were conducted in Series 2.

Series-3: This series of tests contained beams having open holes in both the tension and compression flanges. A total of four tests A85-B-1, A75-B-1, A70-B-1 and A60-B-1, where 'B' indicates both flanges, were performed in this series. The purpose of these tests was to investigate the impact of open holes in both flanges on the flexural behavior. Moreover, the test results in this series allowed comparisons to be made in order to evaluate the behavioral differences, in terms of strength and ductility, of a flexural member having open holes exclusively in the tension flange to a similar member having open holes in both flanges.

Series-4: This series involved beam tests with fastener holes in both tension and compression flanges. A total of four tests A85-F-1, A75-F-1, A70-F-1 and A60-F-1, wherein 'F' denotes fastener holes, were conducted in this series. High strength ASTM A490 bolts of standard sizes were inserted into the holes leaving a clearance of approximately 2 mm. The average measured fastener diameter used for beam tests A85-F-1, A75-F-1, A70-F-1 and A60-F-1 was of 10.4 mm, 19.9 mm, 23.9 mm and 29.6 mm, respectively. The purpose of these tests was to investigate the influence of fasteners, particularly in the compression flange.

### 4.2.1 Properties of Test Specimens

This section provides information pertaining to the geometric properties, mechanical characteristics and chemical properties of the beam specimens under consideration. The cross-sectional dimensions were measured along the length of each beam specimen. Each specimen was then, coated with whitewash (hydrated lime mixed with cold water) for better visual confirmation of the initiation of yielding during the test.

**Geometric Properties:** Figure 4.1 illustrates the locations along the length of the beam specimen at which the cross-sectional dimensions were measured. The sectional dimensions included; width of the tension and compression flanges ($b$), thickness of the tension and compression flanges ($t$), web depth ($d$), web thickness ($w$) and the beam length ($L$). As shown in Figure 4.1, the cross-sectional dimensions were measured at five different locations, including three locations within the midspan region and two locations in the shear span region. The measurements were taken at the center of the midspan (Section 3-3), 300 mm away from the center (Section 2-2 and 4-4) and 725 mm away from the center of the test beam (Sections 1-1 and 5-5).

Based on measurements at five sections, average dimensions were established. Table 4.1 presents the average measured dimensions of the tension flange, compression flange and web of each beam specimen. In addition, Table 4.1 includes the nominal dimensions for the W200X42 beam section used in this test program (CISC Handbook 2007). The average measured flange width was found to have a maximum variation of 1.7% when compared to the nominal flange width, whereas the average measured flange thickness varied as high as 5% from the nominal flange thickness. The average measured depth and thickness of webs varied by a maximum of 0.6% and 2.8%, respectively, as compared to the corresponding nominal dimensions. The average measured cross-sectional dimensions were found to be within the allowable values stipulated by the CISC Handbook (CISC 2007). Table 4.1 also contains the measured length for each beam specimen. Although the dimensions of the tension and compression flanges of a rolled section are expected to be the same, it was observed from the measurements that the dimensions (width and thickness) varied slightly.

Table 4.2 presents the sectional properties of each beam specimen calculated based on the average measured cross-sectional dimensions. The calculated sectional properties about the major axis included the second moment of area ($I_g$), the elastic section modulus ($S_g$) and the plastic section modulus ($Z_g$). In the calculation of sectional properties, the fillet area of the rolled section (W200X42) was also included. The contribution of fillet area was estimated by subtracting the sectional properties, calculated considering the section composed of three-rectangles of nominal dimensions, from the nominal sectional properties as stipulated in the CISC Handbook (CISC 2007). The contribution of fillet area on the sectional properties was included in the calculation of sectional properties based on the measured dimensions.

**Mechanical Characteristics:** As all twenty five beam specimens used in this investigation were obtained from the same production batch (same heat ID), a limited number of standard tensile coupon tests were performed. Six standard tension coupons; three flange and three web coupons, were cut along the length (rolling) direction of beam specimen A90-1. The coupons were obtained after the main test from the shear span region, which was subjected to low strain levels. The coupon tests were performed in accordance with the specification and recommendations provided by American Society for Testing and Material Standards A370-02 (ASTM 2002). More specific details of the test procedure including test speed, type of instruments used, measurements of dimensions, etc. adopted in this coupon test program are presented in Chapter 6.

Figures 4.2[A] and 4.2[B] illustrate the resulting stress-strain relationship of the tensile coupons obtained from the flanges and web of beam specimen A90-1. The engineering stress was calculated based on the applied load divided by the initial cross-sectional area, whereas the engineering strain was calculated based on the elongation measured by an extensometer divided by the initial gage length.

The web coupons obtained closer to the flange-web intersection exhibited higher yield and ultimate strengths and lower material ductility as compared to the coupon obtained at the middle part of the web. This can be attributed to the higher stresses that are exerted at the corner of rolled sections during the rolling process and faster cooling following rolling of the web due to their smaller thickness (Jaquess and Frank, 1999). As seen in

Figures 4.2[A] and 4.2[B], the coupons obtained from the flange and the middle-web exhibited a sharp yield point followed by a yield plateau, whereas the coupons obtained adjacent to the flange-web junction exhibited no yield plateau. The yield strength of the material was established by using 0.2% offset method, although the flange and the middle web coupons had a sharp yield point (Galambos 1998).

Table 4.3 summarizes the tensile test results of the flange and web coupons. The yield strength ($F_y$) of the flange coupons varied between 403 MPa and 413 MPa with an average of 409 MPa and the ultimate strength ($F_u$) ranged from 530 MPa to 534 MPa with an average of 531 MPa. The resulting average yield-to-ultimate strength ($F_y / F_u$) ratio for the flange coupons was estimated to be 0.77. The flange coupons had average yield and ultimate strains ($\varepsilon_y$ and $\varepsilon_u$) of approximately 0.22% and 15.5%, respectively, resulting in an average material ductility ratio of approximately 70. The strain at onset of strain hardening ($\varepsilon_{sh}$) varied from 1.23% to 1.36% with an average of 1.30%. The strain at fracture ($\varepsilon_f$) of the flange coupons varied between 22% and 24% resulting in an average of approximately 23%.

The web coupons obtained closer to the flange-web intersection exhibited average yield and ultimate strengths of 460 MPa and 560 MPa, respectively, resulting in an average $F_y / F_u$ ratio of 0.82. The average strains at the yield and the ultimate strength were 0.2% and 10.3%, respectively. The resulting material ductility ratio of these coupons was calculated to be 52. These coupons fractured at relatively lower strains with an average value of 15.6%.

The coupon obtained from the middle part of the web had yield and ultimate strengths of 409 MPa and 536 MPa, respectively. The resulting $F_y / F_u$ ratio was calculated to be 0.76, which was approximately 8% lower than the $F_y / F_u$ ratio of the web coupon that was obtained closer to the flange-web intersection. The yield and ultimate strains of the coupon obtained from the middle web were 0.22% and 14%, respectively. The resulting material ductility ratio was 64, which was 19% higher than that of the web coupons obtained closer to the flange-web junction. The onset of strain hardening value ($\varepsilon_{sh}$) and the fracture strain were measured to be 1.35% and 24.8%, respectively. The fracture strain for the middle web coupon was 37% higher than the fracture strain of the web coupons obtained adjacent to the flange-web junction.

Overall, the flange coupons and the middle web coupon exhibited similar stress-strain variations consisting of a sharp yield point followed by yield plateau. However, the web coupons obtained adjacent to the flange-web intersection had no sharp yield point and were found to have higher yield and ultimate strengths. The theoretical moment resistances in this study were established based on the yield strength of the flange coupons, although the yield strength of the web coupons (obtained closer to the flange-web intersection) varied considerably from the flange coupons. This was considered acceptable since the flange material governs the flexural behavior of rolled sections (Adams et al., 1964).

**Chemical Composition:** The beam specimens used in this investigation were associated with heat ID of 104846 as per the quality certificate supplied by the local steel supplier. Table 4.4 presents the chemical composition associated with the heat ID: 104846 extracted from the mill certificate provided by the steel supplier.

## 4.3 The Test Setup

### 4.3.1 An Overview

Figure 4.3 shows a schematic view of the test setup constructed for this study. The test beams were simply supported at both ends. The beams were loaded so that the midspan would experience a uniform bending moment. As seen in Figure 4.3, each beam had web stiffeners located at the support and loading locations to prevent web buckling.

The following subsections provide detailed descriptions of the support conditions, loading application, loading system, test specimen instrumentation and lateral bracing system used in this research program.

### 4.3.2 Support Condition

As shown in Figure 4.3, one end of the test beam was placed on a pin support, which consisted of a 75 mm diameter roller and a curved saddle plate. The function of the saddle plate was to prevent longitudinal movement while allowing large end rotation. The other end of the test beam was placed on a roller support which also consisted of a 75 mm diameter roller that could roll in and out in the longitudinal direction of the test beam while allowing large end rotation. Moreover, at the supporting ends, two bearing plates, each having the dimensions of 160 mm long, 160 mm wide and 15 mm thick, were placed between the test beam flanges and the rollers as illustrated in Figure 4.3. The purpose of using the bearing plates was to distribute the concentrated loads at the support locations in order to prevent failure of the beam due to web crippling and/or web yielding.

### 4.3.3 Loading Condition

As shown in Figure 4.3, the test beams were subjected to two point loads. The two point loads were applied to the test beam using a 1000 mm long transfer beam. The transfer beam consisted of hollow structural sections welded together back-to-back. The load was transferred through two rollers (50 mm diameter) spaced at the center-to-center distance of 750 mm on to the test beam (see Figure 4.3). At the loading locations, two bearing plates each having dimensions of 100 mm long, 160 mm wide and 15 mm thick were used between the rollers and the flange of the test beam (see Figure 4.3).

### 4.3.4 Lateral Bracing System

If a flexural member has a clear span (a distance between supports) exceeding the critical unbraced length, the member will fail by lateral torsional buckling (LTB) when subjected to in-plane bending. However, the LTB failure mode can be prevented by providing adequate lateral bracings. According to the current Canadian Steel Design code (CSA 2003), the longitudinal spacing between bracings is limited by the following equations for compact beam sections designed by plastic analysis:

$$L_{cr} = \frac{550 r_y}{\sqrt{F_y}}, \quad \text{for } \kappa < -0.5 \tag{4.1}$$

$$L_{cr} = \frac{980 r_y}{\sqrt{F_y}}, \quad \text{for } \kappa > -0.5 \tag{4.2}$$

where $L_{cr}$ is the critical unbraced length, $r_y$ is the radius of gyration about minor axis, $F_y$ is the yield strength of the flange material and $\kappa$ is the ratio of smaller factored moment to larger factored moment at opposite ends of unbraced length.

Since all beam specimens tested were from the same production batch and had similar cross-sectional dimensions, the radius of gyration ($r_y$) and the yield strength ($F_y$) of each beam specimen used were 41.3 mm (nominal value for W200x42 section) and 450 MPa (maximum expected value for A992 steel), respectively in establishing the spacing between the bracings. The first limit state, as provided by Equation 4.1, is applied for the case where uniform moment loading exits, whereas the second limit state, as provided by Equation 4.2, is applied for the case where moment gradient exists. Therefore, according to the current CAN/CSA-S16.01 (CSA 2003) standard, the critical spacing requirements between the braces which are to be placed in the uniform moment region and in the moment gradient region were of 1071 mm and 1910 mm, respectively. However, in the testing program, the beam specimens were laterally braced at the loading and the support locations. Since the midspan of each test beam which was subjected to a uniform moment loading was of 750 mm (<1071 mm) and the shear span which was subjected to a moment gradient loading was of 1075 mm (<1910 mm), respectively, the spacing requirements as per the CAN/CSA-S16.01 (CSA 2003) standard were satisfied.

Figure 4.4 shows the bracing system used in this investigation. The lateral bracing system was designed to have sufficiently high stiffness to prevent LTB while allowing the test beam to undergo a large vertical deflection. This bracing system consisted of a series of self standing bracing frames which were fabricated from the following components:

- Vertical member- W150X30 section with a height of approximately 1000 mm
- Inclined member- fabricated from two channels (C150X16) welded together back-to-back. The inclined member was erected with the vertical member at an angle of 45° and welded along the cross-section.

- Horizontal member- channel section (C200X21) welded with both the vertical and the inclined member.

As shown in Figure 4.4, each self standing bracing frame was connected to supporting-beams, which were fastened to the test floor, by 25 mm diameter high strength bolts. The bracing frames were fastened to the supporting beams through slotted holes allowing the bracing frames to be adjusted to the test beam. High strength cold-rolled round bars (25 mm diameter) were welded along the middle of each vertical member of the bracing frames to simulate knife edge guides permitting vertical deflections of test beam while preventing the LTB.

### 4.3.5 Loading System and Instrumentation

Figure 4.5[A] shows the loading system used in this investigation. This system consisted of an actuator having a maximum stroke of 500 mm (20 inch), a commercially available load cell (Type: C2M1C) having a maximum measuring capacity of 890 kN (200,000 lbs), a string-pot transducer having a maximum stroke of 500 mm (20 inch) attached between the load cell and the outer perimeter of the actuator. The displacement control test system used in this investigation also included a controller, function generator, 10V power supply and servo valve. The actuator-load cell assembly was attached to a horizontal cross beam, which was connected across two vertical reaction columns.

Figure 4.5[B] illustrates a schematic view of the hydraulic servo control system used in this investigation. As shown in this figure, the actuator was operated by a hydraulic pump (Model: RL-T06-2-E200). The hydraulic pump was operated at a maximum pressure of 10 MPa (1500 psi). A servo valve (Model: A076-2630) was installed between the actuator and the hydraulic pump to control the hydraulic actuator. A MTS 406 controller was used to control the servo valve. A MTS 410 digital function generator was used to create the control signal. Since the test was conducted under a monotonically increasing downward displacement, a linear function generated by the 'ramp' mode of the MTS 410 function generator was used as the input signal to control the movement of the actuator at a desired rate 0.025 mm/sec. The required amount of the movement of the actuator was modulated by a string-pot transducer (Model: PT101-0020-111-1110) connected between the actuator and the load cell (see Figure 4.5[B]).

Figure 4.6 shows the locations of the instrumentation attached to the test beams. The instruments included string-pots [SP], Linear Varying Displacement Transducers (LVDTs) and high elongation capacity strain gages (Vishay Micro-Measurements & SR-4 type). There were a total of seven string-pots used, in which five of them were placed along the flange-web intersection of the tension flange in the mid span region (see Figure 4.6). These five string pots were placed symmetrically about the center line of the test beam in a vertical plane. SP-1 and SP-5 were placed directly below the loading points while SP-3 was placed at the mid span of the test beam. In addition, SP-2 and SP-4 were placed at quarter points within the uniform moment region as shown in Figure 4.6. The readings obtained from SP-1 and SP-2 were used to establish the load point rotation at a loading point towards A-end while SP-4 and SP-5 were used to establish such rotations towards B-end. A pair of string pots [SP-6 and SP-7] were used to measure the beam end rotation at the roller end (see Figure 4.6). The rotations can be calculated as the difference in displacement between the respective pair of string pots divided by the distance between them.

Five LVDTs were used as shown in Figure 4.6. LVDT-1 and LVDT-2 measured the end rotation at A-end of the test beam. The rotations can be calculated as the difference in displacement between both LVDTs divided by the distance between them. LVDT-5 was used to capture any possible slippage of the cross beam connected across the two reaction columns during the initial stages of loading. LVDT-3 and LVDT-4 were used to monitor the out-of-plane movement of the compression flange with respect to the tension flange at the center of the midspan. The readings obtained from LVDT-3 and LVDT-4 were used to establish the load at which local buckling initiated. It is realized that the method adopted in this investigation to capture the load at which local buckling occurs may not be ideal since local buckling may initiate anywhere within the uniform moment region. Nevertheless, no additional effort was made to monitor the local flange and/or web buckling during the experiments as it was beyond the scope of this investigation.

High elongation capacity strain gages (Vishay SR-4 type with a maximum capacity of 15% strain at room temperature) were attached to specimens A100-4, A70-2, A75-3 and

A75-B-1. The locations of the strain gages used on those beam specimens are as shown in Figure 4.6. All strain gages were placed across the cross-section located at the center of the midspan region (Section A-A as seen in Figure 4.6). A total of five stain gages were used on beam specimen A100-4. Two gages were placed at the outer surfaces of the tension and compression flanges along the flange-web intersection while the remaining three gages were positioned at the middle web and 60 mm away from the middle web towards the tension and compression flanges. A total of six strain gages were attached to each beam specimen A70-2 and A75-3. The strain gage locations are shown in Figure 4.6 including the additional strain gage, which was placed in the vicinity of hole in the tension flange (25 mm away from the center of the hole). Beam specimen A75-B-1 was instrumented with seven strain gages, including two additional strain gages placed in the vicinity of the holes in the tension and compression flanges (25 mm away from the center of the hole). The strain gages were attached at these locations for the following reasons;

- to monitor spread of plastification as the specimen was loaded well into its inelastic range.
- to establish the strain demand on the tension flange having no holes (solid flange) and on the tension flange having holes in this investigation.
- to assess the effect of holes on flange-web interaction.
- to verify the location of the neutral axis when a beam section had holes in its tension flange only, since the section is no longer symmetric about the neutral axis of the gross cross-section.

## 4.4 Test Procedure

Figure 4.7 shows a photograph of the test setup. This figure shows how the test beam, transfer beam and the actuator-load cell assembly were arranged within the loading frame and bracing frames. All beam specimens were tested under a monotonically increasing downward vertical displacement. Once the beam specimen was placed in the testing apparatus, it was centered with respect to the vertical axis passing through the center of the actuator-load cell assembly in the longitudinal direction. The beam specimen was also centered laterally with respect to the bracing frames and the vertical axis of the combined actuator-load cell assembly. After centering the test beam within the test frame, first the bracing frames were moved so that they come into contact with the flange tips of the beam specimen and then, they were tightened with the support beams at the bottom (see Figure 4.7). The transfer beam was then, placed on the rollers spaced at the center-to-center distance of 750 mm and was adjusted to laterally center it with respect to the vertical axis of the combined actuator-load cell assembly. Each bracing frame was tied with a 25 mm diameter tie rod passing through the flanges of the vertical member of the bracing frame to provide additional rigidity to the braced frame.

The test specimen was initially preloaded under displacement control. The beam specimen was preloaded within its elastic limit to ensure that the instrumentations functions properly and to confirm proper seating of the test beam in the testing apparatus. If the beam specimen was found to be improperly seated then, the seating was adjusted and the instrumentations reset. Now the test beam is ready to be loaded. A constant loading rate of 0.025 mm/sec was maintained throughout the test. The test beam was loaded until well past the peak load and until the load dropped below the peak load. The theoretical load carrying capacity of the test beam was known. Often the peak load is higher than this theoretical capacity. Usually, the beams were continued to be loaded until the load dropped below this theoretical capacity. The beam specimens that failed as a result of net section fracture through the flange holes were concluded as soon as a sudden drop in loading occurred.

## 4.5 Sample Test Results

In order to evaluate and analyze the performance of the test specimens having flange holes, the following responses were established from the measurements recorded during the tests;

(a) Load versus midspan deflection ( $P$ vs. $\Delta$ )

The load ( $P$ ) and the midspan deflection ( $\Delta$ ) were obtained directly from the load cell and the string-pot [SP-3] attached to the center of the test beam.

(b) Moment versus average rotation at loading points ( $M$ vs. $\theta$ )

The measured load can be converted into a midspan moment as, $M = (P/2)L_s$, where $L_s$ is the shear span (a distance between load point and reaction point). The rotation at the loading point (in radians) towards A-end of the test beam was established as the difference in displacement between string-pots SP-1 and SP-2 divided by the distance between them. Similarly, the rotation at the loading point towards B-end of the test beam was computed from the measurements taken using SP-4 and SP-5 divided by the distance between them (see Figure 4.6). The average of these two rotations provided the loading point rotation ($\theta$).

(c) Moment versus average beam end rotation ($M$ vs. $\theta_e$)

The beam end rotation at A-end was established as the difference in displacement between LVDT-1 and LVDT-2 divided by the spacing between them. Similarly, the beam end rotation at B-end of the test beam was established from the measurements taken using SP-6 and SP-7 divided by the spacing between them. The average of these two rotations was considered as the beam end rotation ($\theta_e$).

(d) Load versus relative out-of-plane displacement of the compression flange ($P$ vs. $\delta$)

The load ($P$) was obtained as explained above. The relative out-of-plane movement of the compression flange to the tensions flange ($\delta$) was established using LVDT-3 and LVDT-4 placed at the center midspan of the test beam.

(e) Moment versus strain ($M$ vs. $\varepsilon$)

The strain measurements were obtained from strain gages attached to test beams.

### 4.5.1 Test Data Reduction

Figure 4.8[A] illustrates the moment-rotation relationship for beam specimens that exhibit ductile failure possessing substantial inelastic rotation. For such beams, unloading occurs only after significant local buckling of the compression flange. On the other hand,

Figure 4.8[B] shows the moment-rotation relationship for beams, failing primarily due to net-section fracture through the tension flange holes. Points A, B, C, D, E, F and G indicated in Figures 4.8[A] through 4.8[C] may be of engineering significance. Based on these points, the behavioral differences in responses of each beam specimens under consideration were analyzed and compared. Descriptions pertaining to each of the point of interest and how these points were established in this investigation are presented below;

**Point A** represents the proportional limit above which the moment is no longer proportional to the rotation (or the load is no longer proportional to the deflection). To be consistent, Point-A for each test, herein, was established using 0.1% offset method. That is, 0.1% of the elastic midspan deflection corresponding to the plastic load (0.1% of $\theta_p$) was drawn parallel to the initial slope, which was established using a linear regression analysis of the initial portion of the test results.

**Point B** is the point at which the calculated yield moment ($M_y$) is reached. The theoretical yield moment ($M_y$) was computed based on the average yield strength multiplied by the elastic section modulus established based on the measured cross-sectional dimensions ($M_y = S_g F_y$). The corresponding rotation at Point B is $\theta_y$. From the $M_y$ value, the corresponding yield load ($P_y$) can be calculated as, $P_y = 2M_y / L_s$. Note that the load applied by the actuator is double the reaction since the applied load was distributed at two equal point load in this test program. A midspan deflection corresponding to the yield load ($P_y$) is $\Delta_y$.

**Point C** represents the point at which the calculated plastic moment ($M_p$) is attained. The theoretical gross section plastic moment capacity ($M_p$) for each beam was calculated based on the average measured yield strength of the flange material ($F_y = 409$ MPa) multiplied by the plastic section modulus determined based on the measured cross-sectional dimensions ($M_p = Z_g F_y$). A measured rotation corresponding to the plastic moment ($M_p$) is $\theta_p^+$. The plastic load corresponding to the plastic moment can be calculated as, $P_p = 2M_p / L_s$. A measured deflection corresponding to the plastic load ($P_p$) is $\Delta_p^+$.

**Point D** is the point at which a maximum moment ($M_m$) is reached. The corresponding measured rotation is $\theta_m$. The maximum moment was obtained from the measured maximum load ($P_m$) as $M_m = P_m L_s / 2$. The measured midspan deflection corresponding to the maximum load is $\Delta_m$.

**Point E** represents the point at which the moment-rotation (or load-deflection) curve reaches the calculated plastic moment (or the plastic load) again on the descending branch. The corresponding rotation is $\theta_p^-$ (or the corresponding deflection is $\Delta_p^-$).

**Point F/G** relates the point at which sudden drop in load occurred as a result of net-section fracture through the tension flange holes ($\theta_f$).

Table 4.5 summarizes the calculated gross-section plastic moment ($M_{p_i}$) and the plastic load ($P_{p_i}$) for each beam specimen tested in this study. The $M_{p_i}$ was calculated based on the measured cross-sectional dimensions and the measured yield strength of the flange material ($F_y$=409 MPa). The midspan deflection ($\Delta_{p_i}$) corresponding to $P_{p_i}$ and the load point rotation ($\theta_{p_i}$) as well as beam end rotation ($\theta_{ep_i}$) corresponding to $M_{p_i}$ under ideal elastic-perfectly plastic behavior are also presented in Table 4.5. From the engineering mechanics principles, an elastic midspan deflection for a simply supported beam member subjected to two point load in the midspan can be established as

$$\Delta = \underbrace{\frac{PL_s}{48EI_g}(3L^2 - 4L_s^2)}_{flexural} + \underbrace{\frac{PL_s}{2A_wG}}_{shear} \tag{4.3}$$

where $\Delta$ is the midspan deflection in the elastic range, $P$ is the applied load, $L_s$ is the shear span, $L$ is the clear span, $E$ is the elastic modulus, $I_g$ is the second moment of area about the axis of bending, $A_w$ is the shear area ($dw$) and $G$ is the shear modulus. In order to establish a more accurate stiffness, especially for members whose shear span (length-to-depth ratio, $L_s / d = 1075/205 = 5.24 < 6$) is less than 6 such as those tested, the calculation must also consider its shear flexibility (Green 2000).

For the same scenario as described above, an elastic rotation corresponding to a moment, $M$, can be established as

$$\theta = \frac{ML_m}{2EI_g} \tag{4.4}$$

where $L_m$ is the midspan length. Similarly, an elastic rotation at the beam end is

$$\theta_e = \frac{M}{2EI_g}(L - L_s) \tag{4.5}$$

The values $\Delta_{pi}$, $\theta_{pi}$ and $\theta_{epi}$ were calculated using the sectional properties (as given in Table 4.2) established based on the measured cross-section dimensions and the measured material characteristics such as the yield strength, $F_y$=409 MPa, and the measured elastic modulus, $E$=215 GPa of the flange material (see Table 4.3).

A statistical analysis of these calculated values is also provided in Table 4.5. The average value of the plastic moment ($M_p$) was 177 kNm with a standard deviation of 1.3 kNm. The associated coefficient of variation (COV) was 0.7%. The average value of the plastic load ($P_p$) was 329 kN with a standard deviation of 2.6 kN. The associated COV was 0.8%. As presented in the fourth column of Table 4.5, a mean value of the midspan defection was 19.3 mm with a standard deviation of 0.1. The associated COV was 0.3%. A mean value of the rotation (at load point) was 0.0078 rad with a COV of 0.3%. A mean value of the end rotation was 0.0190 rad with a standard deviation of 0.0001 rad resulting in a COV of 0.3%. Since the COVs of each parameter were less than 1%, the averages of these parameters were used in the subsequent comparisons. For example, the average value of plastic moment capacity, $M_p$= 177 kNm, was considered as the reference plastic moment capacity.

In general, the comparison of overall behavior is conventionally performed in terms of the measured properties. However, in this thesis, the load-deformation behavior (or moment-rotation relationship) was normalized relative to the nominal section properties and the nominal yield strength value as given in the CISC Handbook (2007). The reasons being were that (1) in design stand point, the nominal values are readily available from steel design handbooks and (2) this test program involved one beam size obtained from the same heat ID. Thus, by knowing the ratio between the measured values and the nominal values (in terms of sectional properties and the strength properties), the overall load-deformation (or moment-rotation) behavior can be converted from one to another (nominal-to-measured or vise versa).

Table 4.5 presents the nominal values associated with the plastic moment ($M_{p-nom}$), the plastic load ($P_{p-nom}$). The corresponding midspan deflection ($\Delta_{p-nom}$), load point rotation ($\theta_{p-nom}$) and beam end rotation ($\theta_{ep-nom}$) are also provided in Table 4.5. The $M_{p-nom}$ was established based on the nominal yield strength of ASTM A992 steel, $F_y$ = 345 MPa, and the nominal plastic section modulus, $Z_g$ = 445X10$^3$ mm$^3$ for the W200X42 section (CISC 2007). The $P_{p-nom}$ was established as, $2\,M_{p-nom}\,/\,L_s$, where $L_s$=1075 mm. To establish the nominal midspan deflection and rotations, the following values were used; $L_m$=750 mm, $L$=2900mm, $A_w$ = 1476 mm$^2$, $I_g$=40.9X10$^6$ mm$^4$, $E$=200 GPa and $G$ = 77 GPa. The calculated plastic moment capacity-to-the nominal plastic moment capacity

($M_p / M_{p-nom}$) =177/154 ratio value was 1.15. This value is referred to as an over strength factor in seismic design (CISC 2007).

As seen in Figure 4.8[A], the ductility of a beam member in terms of rotation capacity can be established at two different stages; (1) corresponding to maximum moment and (2) total available rotation capacity. To be consistent with other research studies in the past (McDermott 1969, Lucky and Adams 1969, Green 2000, Sause et al., 2001 and Yakel et al., 2002), the rotation capacity of the beams specimens were established at measured plastic moment, $M_p$=177 kNm ($M_p$=1.15$M_{p-nom}$). The rotation capacity corresponding to a maximum moment is defined as, $R_m = (\theta_m - \theta_p)/\theta_p$ where $\theta_m$ is the rotation corresponding to $M_m$ and $\theta_p$ is the elastic rotation corresponding to $M_p$ under ideal elastic-perfectly plastic behavior. The total rotation capacity is defined as, $R_y = (\theta_p^- - \theta_p)/\theta_p$ where $\theta_p^-$ is the rotation corresponding to $M_p$ on the descending curve of the moment-rotation response.

### 4.5.2 Load versus Midspan Deflection - ($P$ Vs. $\Delta$)

In order to illustrate the typical results associated with this research program, the test results for solid beam specimen A100-3 are presented in this section. Figure 4.9 shows the test load versus the midspan deflection for the beam specimen A100-3. As seen in Figure 4.9 (enlarged portion of the figure), the load-midspan deflection relationship remained linear up to a load of 237 kN, which is the proportional load. Beyond this load level, a decrease in the slope of the load-midspan deflection response was observed. The average calculated yield load, $P_y$=295 kN (see Table 4.5), was reached at a midspan deflection of 18.6 mm. Though the slope of the load-midspan deflection relationship continued to decrease, the beam specimen was able to reach an average plastic load, $P_p$=329 kN (see Table 4.5). The corresponding midspan deflection was 21.6 mm. The load-deflection relationship softened more rapidly after reaching $P_p$, which can be seen in Figure 4.9 as a distinct flattening of the curve, as the cross-section in the critical span region has yielded completely at this load level. Nevertheless, due to the material strain hardening, the beam continued to carry additional load and eventually reached a maximum load of 397 kN. The corresponding midspan deflection was 192 mm. After the attainment of the maximum load, the beam specimen began to shed load gradually. The test load dropped to $P_p$=329 kN again on the descending branch of the load-deflection curve at a midspan deflection of 294 mm. Additionally, Figure 4.9 (enlarged portion) presents a linear relationship between the load and the midspan deflection for beam A100-3 established using a linear regression analysis as $P = 16.38\Delta$. Thus, the experimentally obtained stiffness, $(k_\Delta)_{exp}$=16.38 (kN/mm) and the calculated stiffness based on the engineering mechanics principles from Equation 4.3, $(k_\Delta)_{cal}$=17.1 (kN/mm). The percentage difference between the experimentally obtained initial stiffness and the calculated value was 4.2% for beam specimen A100-3.

Figure 4.10 shows the normalized load versus the normalized midspan deflection relationship. The load was normalized relative to the nominal plastic load $P_{p-nom}$ =286 kN and the midspan deflection was normalized with respect to, $\Delta_{p-nom}$= 17.5 mm (see Table 4.5).

### 4.5.3 Moment versus Rotation ($M$ vs. $\theta$)

Figure 4.11 shows the moment, $M$, versus rotation, $\theta$, relationship. As seen in the figure (enlarged portion), the relationship remained linear up to a proportional moment of 128 kNm. The corresponding rotation was 0.0053 radians. Beyond this limit, the flexural stiffness deteriorated slightly until the theoretical yield moment of 159 kNm was reached. The corresponding rotation was 0.0068 radians. As the moment increased, although the flexural stiffness decreased, the beam attained $M_p$=177 kNm (=1.15 $M_{p-nom}$). The corresponding rotation was 0.0076 radians. As the moment increased further, the beam continued to carry additional load until it reached a maximum moment of 214 kNm. The corresponding rotation was 0.0960 radians. After attaining the maximum moment, the beam unloaded gradually and reached $M_p$ again on the descending branch at a rotation of 0.1542 radians. Moreover, Figure 4.9 (enlarged portion) shows a linear relationship between the moment and the rotation response for beam A100-3 established using a linear regression analysis as $M = 24150\theta$. Thus, the experimentally obtained initial stiffness, $(k_\theta)_{exp}$=24150 (kNm). The calculated initial stiffness based on Equation 4.2,

$(k_\theta)_{cal}$=22704 (kNm). The theoretical initial stiffness was established based on the calculated sectional properties as provided in Table 4.2 and the measured material characteristics of the flanges as given in Table 4.3 ($F_y$=409 MPa and $E$=215 GPa). The percentage difference between the experimentally obtained value and the calculated value was 6.4% for beam specimen A100-3.

Figure 4.12 shows the normalized moment versus the normalized rotation response. The moment was normalized with respect to $M_{p-nom}$=154 kNm while the rotation was normalized with respect to $\theta_{p-nom}$=0.0071 radians (see Table 4.5). The total rotation capacity, $R_y$, for beam specimen A100-3 was calculated to be 20.5 (=21.7-1.15). The rotation capacity corresponding to $M_m$=214 kNm, $R_m$, was estimated to be 12.4 (=13.5-1.15) (see Figure 4.12).

### 4.5.4 Moment versus End Rotation ($M$ vs. $\theta_e$)

Figure 4.13 illustrates the moment ($M$) versus end rotation ($\theta_e$) relation for beam A100-3. The general description associated with the moment versus end rotation is similar to the moment versus rotation as explained above. The beam specimen reached $M_y$=159 kNm at an end rotation of 0.0177 radians and $M_p$=177 kNm at an end rotation of 0.0205 radians. The $M_m$=214 kNm was attained at an end rotation of 0.1645 radians. The beam specimen reached $M_p$=177 kNm (=1.15$M_{p-nom}$) again on the descending branch at an end rotation of 0.2476 radians. As seen in the enlarged portion of Figure 4.13, the experimentally obtained initial stiffness, $(k_{\theta e})_{exp}$=9185 (kNm). The calculated initial stiffness based on Equation 4.3, $(k_{\theta e})_{cal}$=9351 (kNm). Thus, the percentage difference between the experimental stiffness and the calculated value was 1.8% for beam specimen A100-3.

A plot of the normalized moment versus end rotation is shown in Figure 4.14. The moment was normalized relative to the nominal plastic moment capacity, $M_{p-nom}$=154 kNm and the end rotation was normalized relative to the nominal end rotation (under ideal elastic-perfectly plastic behavior) corresponding to the nominal plastic moment ($M_{p-nom}$=154 kNm) $\theta_{ep-nom}$=0.0172 radians (see Table 4.5).

### 4.5.5 Load versus Out-of-Plane Displacement of Compression Flange (CF) - ($P$ vs. $\delta$)

Figure 4.15 relates the load ($P$) versus the out-of-plane displacement of the compression flange at the center of the midspan ($\delta$). The lowest load at which local bulking of the compression flange initiates was established using a measurement of 2 mm displacement in the compression flange relative to the tension flange. As thus, for beam specimen A100-3, a load at which local buckling initiates may be identified as 355 kN (see Figure

4.15). From the experimental study by Adams et al (1964), they observed that local buckling of a beam member subjected to uniform moment seemed to occur at a maximum load level. Though beam specimen A100-3 reached the maximum load of 397 kN, the occurrence of local buckling was at 355 kN based on the method adopted. The reason for the lower load at which local bulking occurred may be attributed that the way the LVDTs were attached in this test program (between compression and tension flanges). This may possibly include any displacement of the tension flange as well as the compression flange as the beam deflected laterally causing a distorted nature of the cross-section in the midspan region. Note that a precise estimation of load at which local buckling initiates is beyond the scope of this investigation.

## 4.6 Summary

The ratio between the average calculated plastic moment ($M_p$) and the nominal plastic moment ($M_{p-nom}$) was 1.15. The average calculated rotation ($\theta_p$)-to-the nominal radiation ($\theta_{p-nom}$) ratio value was 1.1. The COVs of the calculated parameters established based on the measured dimensions (as given in Table 4.1) and measured material characteristics (as given in Table 4.2) of each beam specimen were less than 1% (see Table 4.5). This revealed that spread of the test data was considerably low. However, slight deviations between data associated with each individual member may be due to the factors such as (1) variations in the geometric dimensions (2) inhomogeneous material characteristics (3) variations in shear spans, etc.

Table 4.1: Nominal and Measured Cross-Sectional Dimensions of Beam Specimens

| W200X42 | | Average Measured Dimensions (mm) | | | | | | | |
|---|---|---|---|---|---|---|---|---|---|
| | | Tension Flange | | Compression Flange | | Web | | | Beam Length |
| | | *b* | *t* | *b* | *t* | *d* | *h* | *w* | *L* |
| Type (1) | Beam ID (2) | (mm) (3) | (mm) (4) | (mm) (5) | (mm) (6) | (mm) (7) | (mm) (8) | (mm) (9) | (mm) (10) |
| Nominal Cross-Section Dimensions | | **166** | **11.8** | **166** | **11.8** | **205** | **181.4** | **7.2** | Nominal Beam Length (expected) =3050mm |
| Series-1 | **A100-1** | 168.2 | 11.0 | 167.5 | 11.3 | 205.0 | 182.7 | 7.3 | 3052 |
| | **A100-2** | 168.4 | 11.5 | 169.3 | 11.1 | 203.4 | 180.8 | 7.3 | 3049 |
| | **A100-3** | 169.7 | 11.2 | 167.1 | 11.3 | 203.8 | 181.3 | 7.6 | 3047 |
| | **A100-4** | 169.2 | 11.1 | 168.3 | 11.3 | 203.5 | 181.1 | 7.4 | 3049 |
| Series-2 | **A90-1** | 168.6 | 11.1 | 168.2 | 11.1 | 205.1 | 182.9 | 7.5 | 3050 |
| | **A85-1** | 169.4 | 11.1 | 168.3 | 11.4 | 203.5 | 181.0 | 7.4 | 3058 |
| | **A80-1** | 168.6 | 11.2 | 168.8 | 11.0 | 203.6 | 181.4 | 7.4 | 3050 |
| | **A75-1** | 168.8 | 11.2 | 169.1 | 11.0 | 203.4 | 181.2 | 7.3 | 3045 |
| | **A75-2** | 168.4 | 11.3 | 169.8 | 11.1 | 203.5 | 181.1 | 7.3 | 3050 |
| | **A75-3** | 169.1 | 11.1 | 168.5 | 11.5 | 203.4 | 180.8 | 7.2 | 3050 |
| | **A70-1** | 169.3 | 11.3 | 168.5 | 11.3 | 203.8 | 181.2 | 7.5 | 3057 |
| | **A70-2** | 168.7 | 11.3 | 169.7 | 11.1 | 203.7 | 181.3 | 7.5 | 3050 |
| | **A70-3** | 168.3 | 11.4 | 169.1 | 11.1 | 203.5 | 181.0 | 7.4 | 3046 |
| | **A60-1** | 168.3 | 11.2 | 168.3 | 11.1 | 204.5 | 182.2 | 7.7 | 3058 |
| | **A60-2** | 168.1 | 11.3 | 168.7 | 11.1 | 203.2 | 180.8 | 7.4 | 3050 |
| | **A60-3** | 169.0 | 11.0 | 168.3 | 11.4 | 203.7 | 181.3 | 7.4 | 3051 |
| | **A50-1** | 168.4 | 11.0 | 167.6 | 11.2 | 203.1 | 180.9 | 7.4 | 3050 |
| Series-3 | **A85-B-1** | 169.7 | 11.3 | 168.7 | 11.5 | 203.5 | 180.7 | 7.3 | 3050 |
| | **A75-B-1** | 169.7 | 11.2 | 168.7 | 11.3 | 203.6 | 181.1 | 7.3 | 3050 |
| | **A70-B-1** | 168.5 | 11.3 | 169.5 | 11.1 | 203.6 | 181.2 | 7.5 | 3044 |
| | **A60-B-1** | 169.5 | 11.3 | 168.4 | 11.4 | 204.2 | 181.5 | 7.7 | 3050 |
| Series-4 | **A85-F-1** | 168.1 | 11.2 | 168.9 | 11.2 | 203.8 | 181.4 | 7.4 | 3050 |
| | **A75-F-1** | 169.2 | 11.1 | 168.6 | 11.2 | 203.0 | 180.7 | 7.2 | 3050 |
| | **A70-F-1** | 168.7 | 11.3 | 169.2 | 11.2 | 204.4 | 181.9 | 7.4 | 3050 |
| | **A60-F-1** | 168.0 | 11.2 | 168.8 | 11.2 | 203.3 | 180.9 | 7.5 | 3049 |
| **Average** | | 168.8 | 11.2 | 168.6 | 11.2 | 203.7 | 181.3 | 7.4 | 3050 |

Table 4.2: Calculated Sectional Properties of Test Beams

| W200X42 | Calculated Sectional Properties Based on Measured Dimensions | | | |
|---|---|---|---|---|
| | $A$ | About Major Axis (X-X) | | |
| | | $I_g$ | $S_g$ | $Z_g$ |
| Nominal Section Properties | **5310** | **40.9** | **399** | **445** |
| Beam ID | ($mm^2$) | $10^6$ ($mm^3$) | $10^3$ ($mm^3$) | $10^3$ ($mm^3$) |
| (1) | (2) | (3) | (4) | (5) |
| **A100-1** | 5163 | 39.6 | 386 | 431 |
| **A100-2** | 5222 | 39.6 | 389 | 433 |
| **A100-3** | 5253 | 39.6 | 389 | 433 |
| **A100-4** | 5206 | 39.4 | 387 | 431 |
| **A90-1** | 5197 | 39.8 | 388 | 433 |
| **A85-1** | 5225 | 39.5 | 388 | 433 |
| **A80-1** | 5174 | 39.1 | 384 | 429 |
| **A75-1** | 5160 | 39.0 | 383 | 428 |
| **A75-2** | 5196 | 39.4 | 387 | 431 |
| **A75-3** | 5203 | 39.5 | 388 | 433 |
| **A70-1** | 5252 | 39.8 | 390 | 433 |
| **A70-2** | 5236 | 39.6 | 389 | 434 |
| **A70-3** | 5221 | 39.5 | 388 | 433 |
| **A60-1** | 5242 | 39.7 | 388 | 434 |
| **A60-2** | 5196 | 39.2 | 386 | 430 |
| **A60-3** | 5206 | 39.4 | 387 | 432 |
| **A50-1** | 5155 | 38.8 | 382 | 426 |
| **A85-B-1** | 5263 | 39.9 | 392 | 437 |
| **A75-B-1** | 5215 | 39.6 | 389 | 433 |
| **A70-B-1** | 5231 | 39.5 | 388 | 433 |
| **A60-B-1** | 5319 | 40.3 | 395 | 441 |
| **A85-F-1** | 5203 | 39.4 | 387 | 432 |
| **A75-F-1** | 5154 | 39.0 | 384 | 427 |
| **A70-F-1** | 5234 | 39.9 | 390 | 436 |
| **A60-F-1** | 5215 | 39.3 | 387 | 431 |
| **Average** | 5214 | 39.5 | 388 | 432 |

Table 4.3: Mechanical Characteristics of Beam Specimens

| Steel | Specimen ID | | Mechanical Characteristics | | | | | | | | |
|---|---|---|---|---|---|---|---|---|---|---|---|
| | | | $F_y$ (MPa) | $F_u$ (MPa) | $F_y/F_u$ | $\varepsilon_y$ | $\varepsilon_u$ | $\varepsilon_u/\varepsilon_y$ | $\varepsilon_{sh}$ | $E$ (GPa) | $\varepsilon_f$ (Over 200 mm) |
| (1) | (2) | | (3) | (4) | (5) | (6) | (7) | (8) | (9) | (10) | (11) |
| A992 | Flange coupons | F1 | 403 | 530 | 0.76 | 0.0022 | 0.1575 | 72 | 0.0130 | 211 | 0.2245 |
| | | F2 | 413 | 534 | 0.77 | 0.0022 | 0.1563 | 71 | 0.0123 | 219 | 0.2431 |
| | | F3 | 411 | 530 | 0.78 | 0.0023 | 0.1523 | 66 | 0.0136 | 215 | 0.2276 |
| | **$(\text{Flange})_{ave}$** | | **409** | **531** | **0.77** | **0.0022** | **0.1554** | **70** | **0.0130** | **215** | **0.2317** |
| | Closer to flange-web intersection | W1 | 460 | 561 | 0.82 | 0.0020 | 0.1059 | 53 | N/A | 198 | 0.1532 |
| | | W2 | 460 | 560 | 0.82 | 0.0020 | 0.1006 | 50 | N/A | 202 | 0.1595 |
| | **$(\text{Web})_{ave}$** | | **460** | **560** | **0.82** | **0.0020** | **0.1033** | **52** | **N/A** | **200** | **0.1564** |
| | Middle-web | W3 | 409 | 536 | 0.76 | 0.0022 | 0.1402 | 64 | 0.0135 | 205 | 0.2480 |
| | **$(\text{Web})_{ave}$** | | **409** | **536** | **0.76** | **0.0022** | **0.1402** | **64** | **0.0135** | **205** | **0.2480** |

Table 4.4: Chemical Composition of Beam Specimens

| Heat ID | Chemical Composition (%) - ASTM A992 Steel (extracted from mill certificate) | | | | | | | | | | | |
|---|---|---|---|---|---|---|---|---|---|---|---|---|
| | C | Mn | Si | P | S | V | Cr | Ni | Mo | Cu | Nb | Sn | **CEV** |
| **104846** | 0.112 | 1.200 | 0.190 | 0.021 | 0.013 | 0.044 | 0.160 | 0.015 | 0.021 | 0.039 | 0.005 | 0.042 | **0.390** |

Table 4.5: Nominal and Calculated Values Based on the Measured Dimensions and Material Characteristics

| Nominal Value ($F_{y-nom}$=345 MPa $E$=200 GPa) | $M_{p-nom}$ (kNm) | $P_{p-nom}$ (kN) | $\Delta_{p-nom}$ (mm) | $\theta_{p-nom}$ (rad) | $\theta_{e\,p-nom}$ (rad) | $M_{y-nom}$ (kNm) | $P_{y-nom}$ (kN) |
|---|---|---|---|---|---|---|---|
| | 154 | 286 | 17.5 | 0.0071 | 0.0172 | 138 | 256 |
| **Beam ID** (1) | $M_{pi}$ (kNm) (2) | $P_{pi}$ (kN) (3) | $\Delta_{pi}$ (mm) (4) | $\theta_{pi}$ (rad) (5) | $\theta_{e\,pi}$ (rad) (6) | $M_{yi}$ (kNm) (7) | $P_{yi}$ (kN) (8) |
| **A100-1** | 176 | 328 | 19.2 | 0.0078 | 0.0189 | 158 | 294 |
| **A100-2** | 177 | 329 | 19.3 | 0.0078 | 0.0190 | 159 | 296 |
| **A100-3** | 178 | 330 | 19.3 | 0.0078 | 0.0190 | 159 | 295 |
| **A100-4** | 176 | 325 | 19.2 | 0.0078 | 0.0189 | 158 | 293 |
| **A90-1** | 177 | 329 | 19.1 | 0.0078 | 0.0189 | 159 | 294 |
| **A85-1** | 177 | 329 | 19.3 | 0.0078 | 0.0190 | 159 | 294 |
| **A80-1** | 175 | 326 | 19.3 | 0.0078 | 0.0190 | 157 | 293 |
| **A75-1** | 175 | 325 | 19.3 | 0.0078 | 0.0190 | 157 | 291 |
| **A75-2** | 176 | 329 | 19.3 | 0.0078 | 0.0190 | 158 | 296 |
| **A75-3** | 177 | 329 | 19.4 | 0.0078 | 0.0190 | 159 | 294 |
| **A70-1** | 177 | 331 | 19.2 | 0.0078 | 0.0189 | 160 | 297 |
| **A70-2** | 178 | 329 | 19.3 | 0.0078 | 0.0190 | 159 | 294 |
| **A70-3** | 177 | 331 | 19.4 | 0.0078 | 0.0191 | 159 | 296 |
| **A60-1** | 178 | 331 | 19.3 | 0.0078 | 0.0190 | 159 | 294 |
| **A60-2** | 176 | 326 | 19.3 | 0.0078 | 0.0190 | 158 | 293 |
| **A60-3** | 177 | 330 | 19.4 | 0.0078 | 0.0191 | 158 | 295 |
| **A50-1** | 174 | 324 | 19.3 | 0.0078 | 0.0190 | 156 | 291 |
| **A85-B-1** | 179 | 333 | 19.4 | 0.0078 | 0.0190 | 160 | 299 |
| **A75-B-1** | 177 | 329 | 19.3 | 0.0078 | 0.0190 | 159 | 296 |
| **A70-B-1** | 177 | 329 | 19.3 | 0.0078 | 0.0190 | 159 | 294 |
| **A60-B-1** | 180 | 335 | 19.2 | 0.0078 | 0.0190 | 162 | 300 |
| **A85-F-1** | 177 | 328 | 19.3 | 0.0078 | 0.0190 | 158 | 294 |
| **A75-F-1** | 175 | 325 | 19.4 | 0.0078 | 0.0190 | 157 | 292 |
| **A70-F-1** | 178 | 330 | 19.2 | 0.0078 | 0.0189 | 160 | 296 |
| **A60-F-1** | 176 | 328 | 19.3 | 0.0078 | 0.0190 | 158 | 295 |
| **Mean** | **177** | **329** | **19.3** | **0.0078** | **0.0190** | **159** | **295** |
| **Standard Deviation** | 1.3 | 2.6 | 0.1 | 0.0000 | 0.0001 | 1.1 | 2.2 |
| **COV (%)** | 0.7 | 0.8 | 0.3 | 0.3 | 0.3 | 0.7 | 0.8 |
| **Max** | 180 | 335 | 19.4 | 0.0078 | 0.0191 | 162 | 300 |
| **Min** | 174 | 324 | 19.1 | 0.0178 | 0.0189 | 156 | 291 |

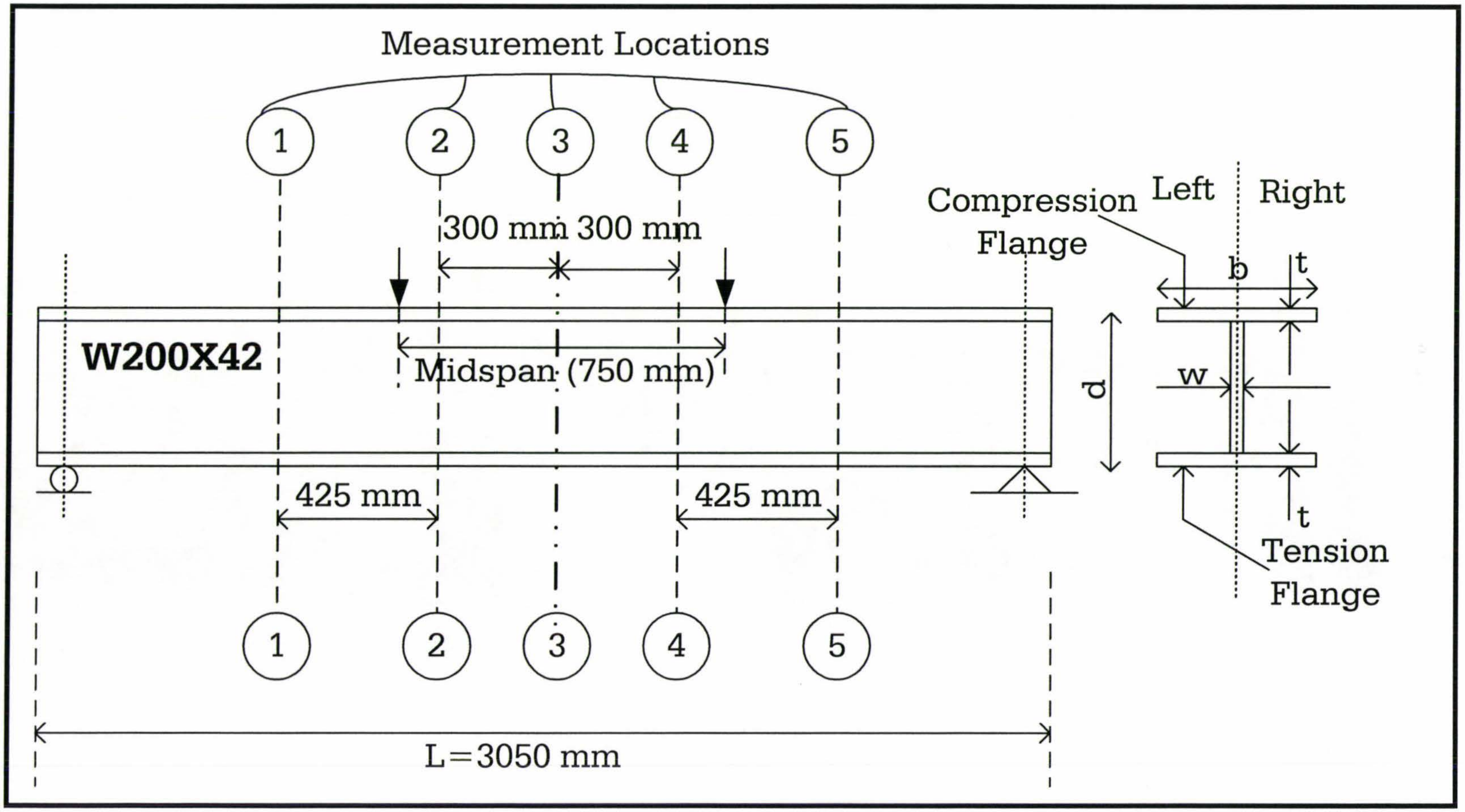


Figure 4.1: Locations of Cross-Sectional Measurements

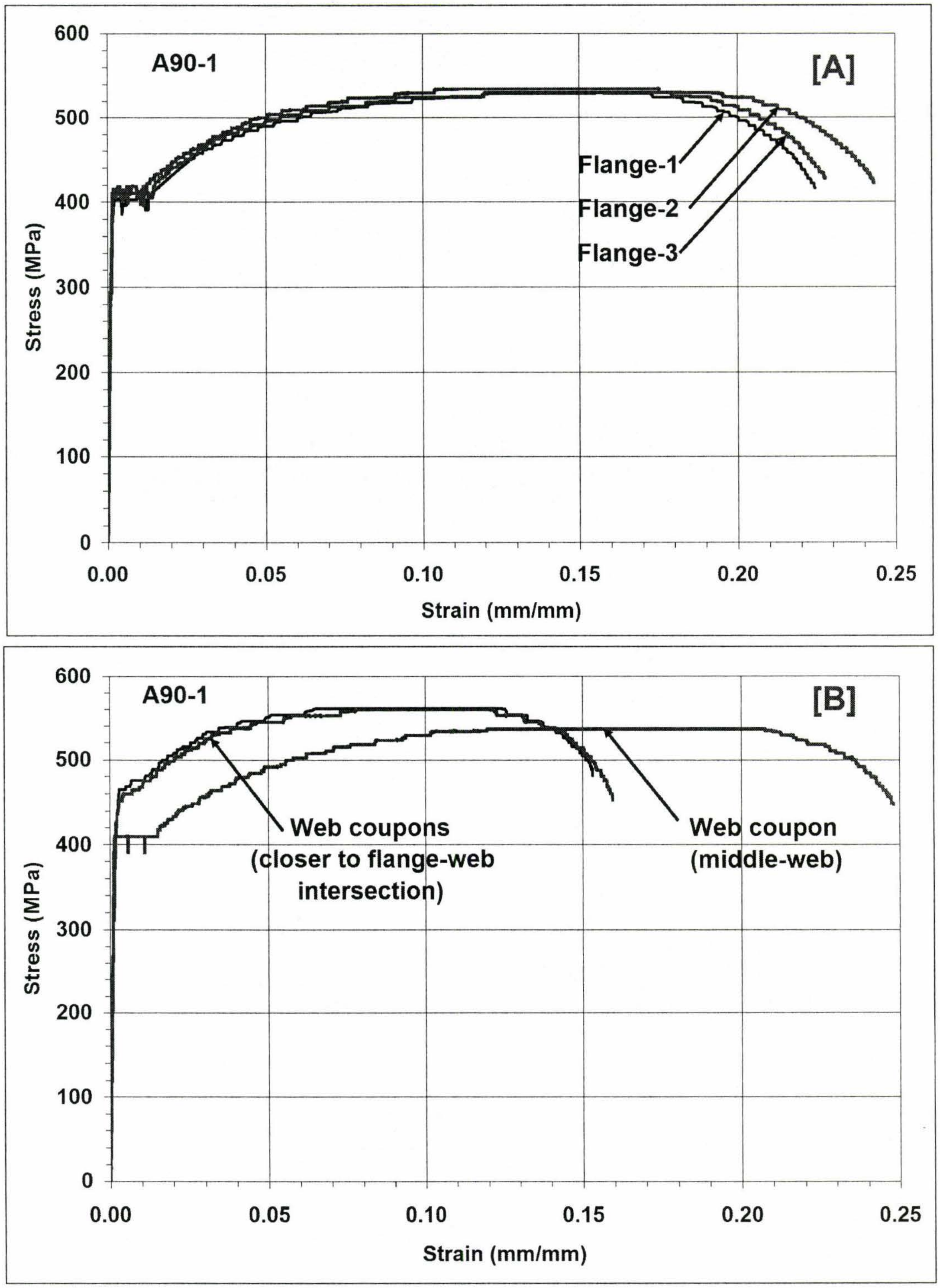


Figure 4.2: Stress-Strain Relationship of Flange and Web Coupons Obtained from Beam Specimen A90-1

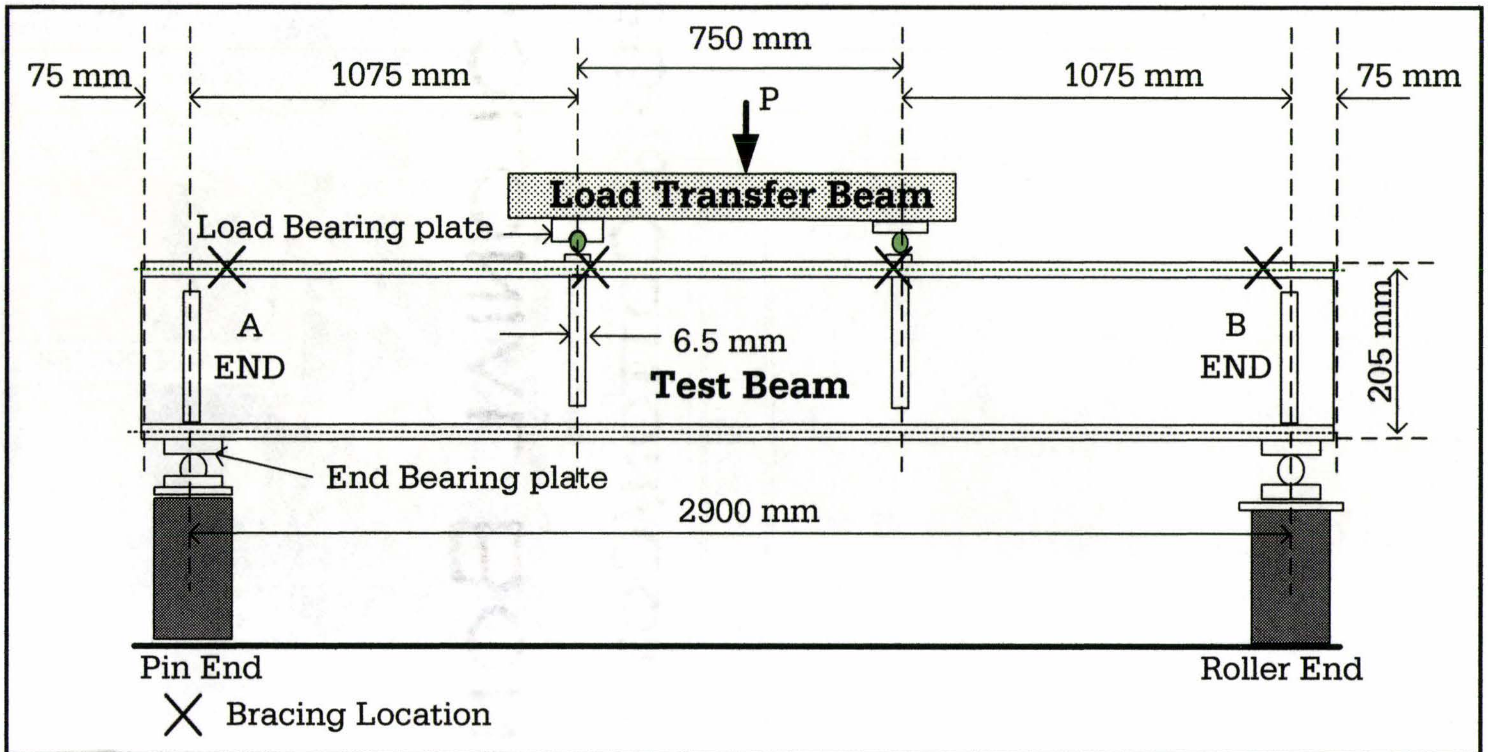


Figure 4.3: Schematic View of Test Setup

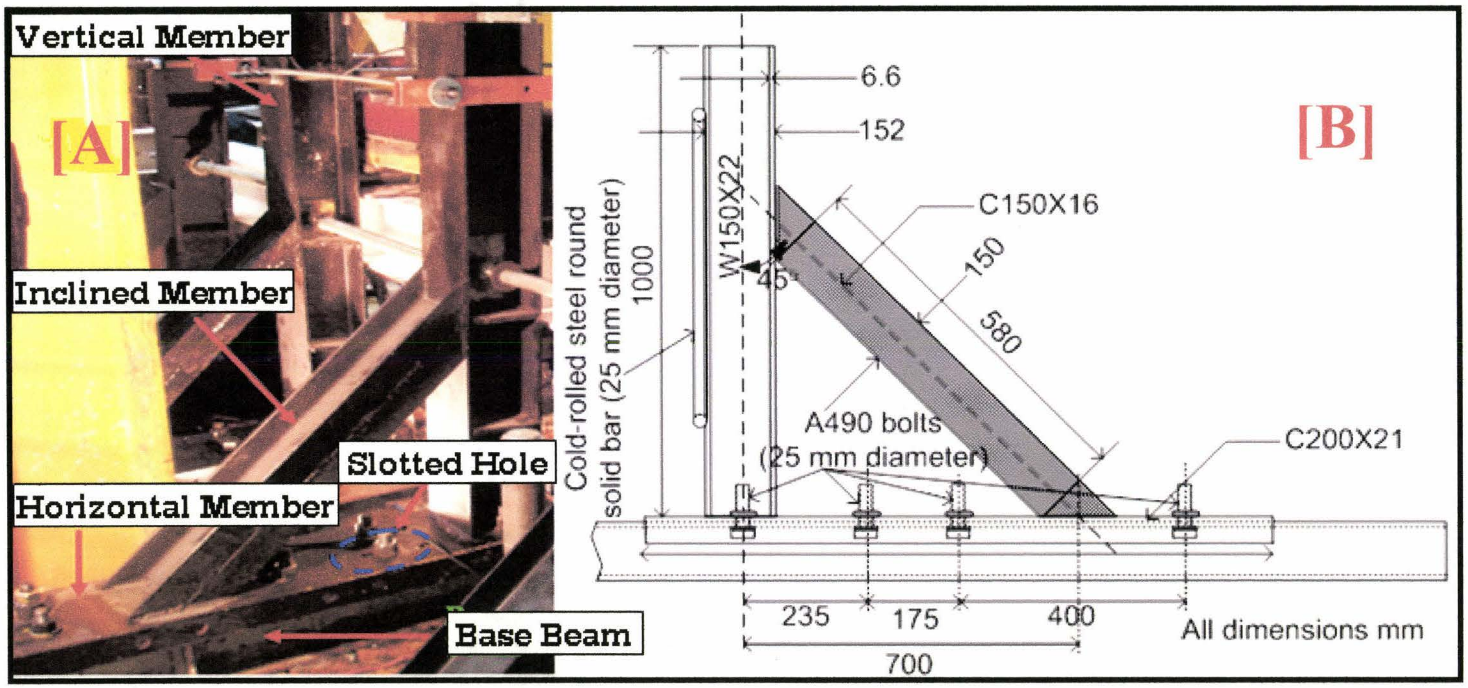


Figure 4.4: Lateral Bracing System [A] Photograph Image of Lateral Bracing System and [B] Schematic View of Lateral Bracing System

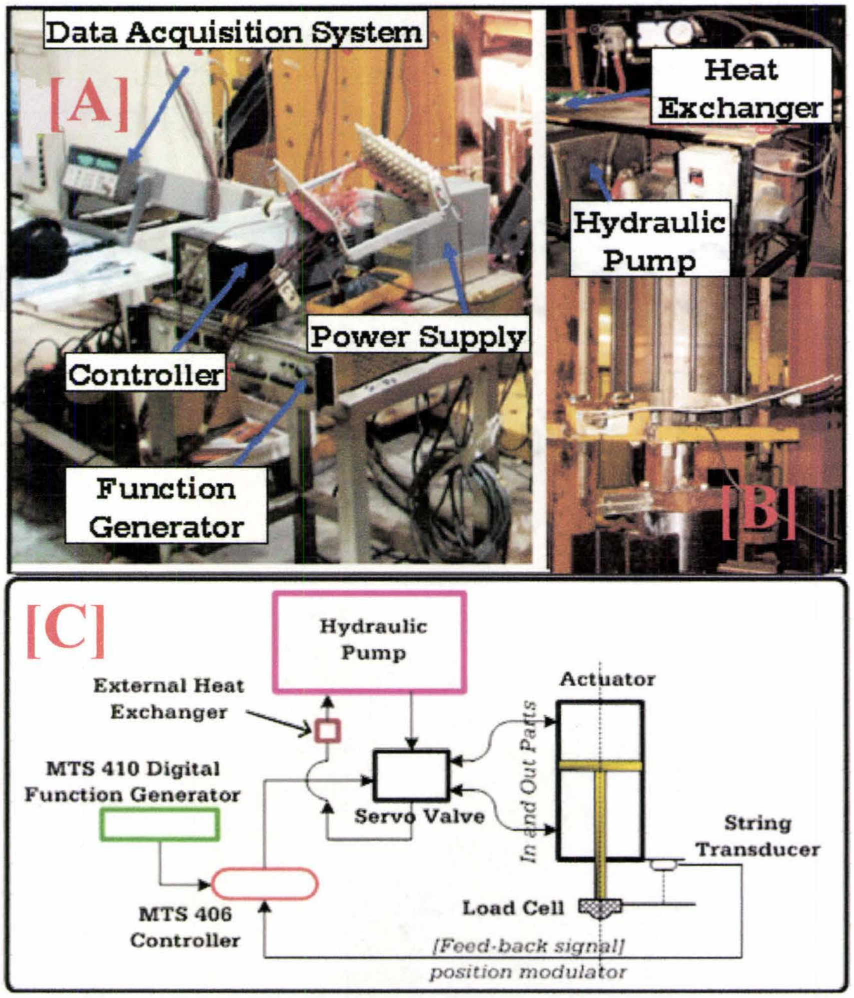


Figure 4.5: Component of Loading System [A] Data Acquisition System
[B] Hydraulic System and [C] Schematic View of Loading System

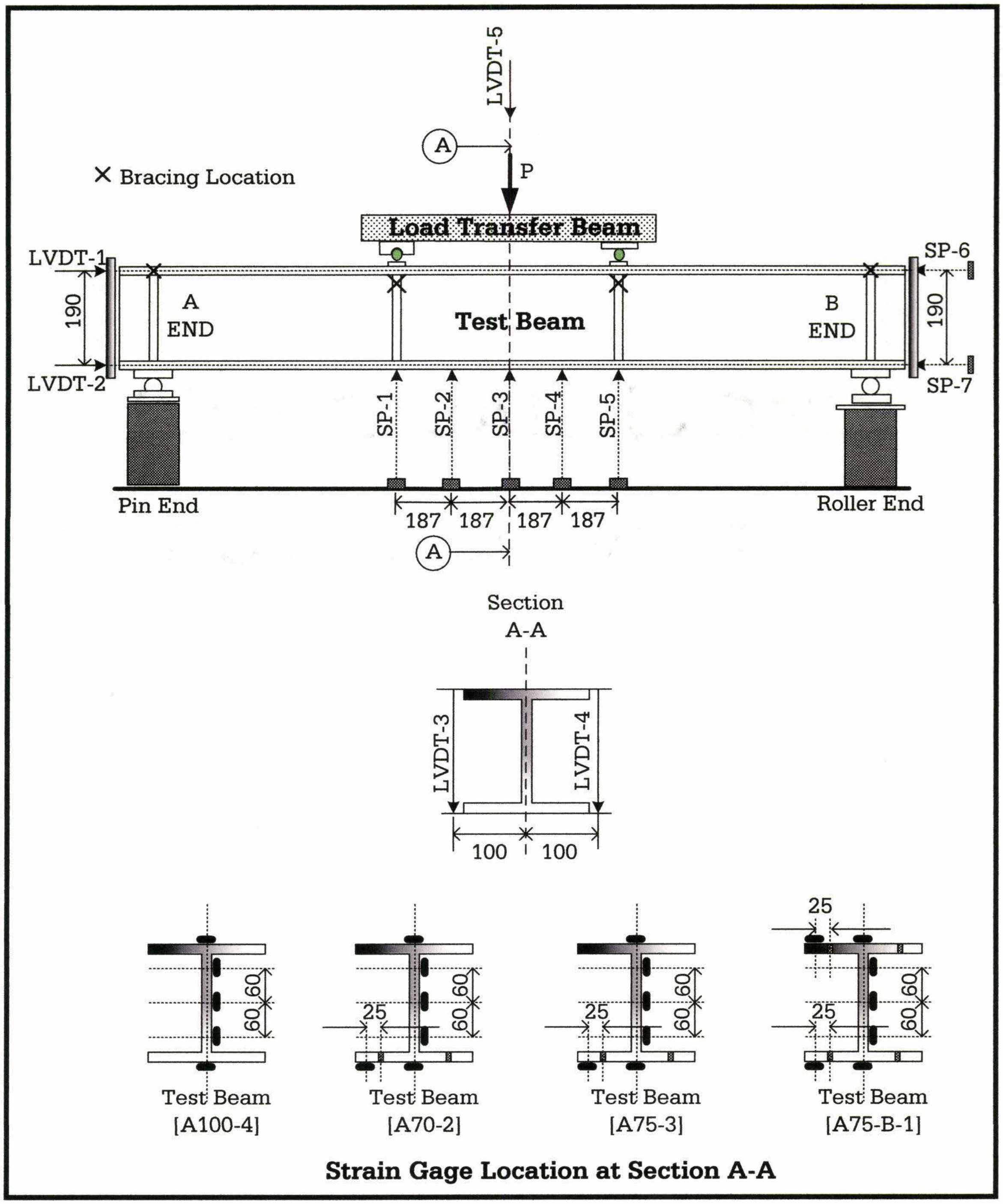


Figure 4.6: Test Specimen Instrumentation

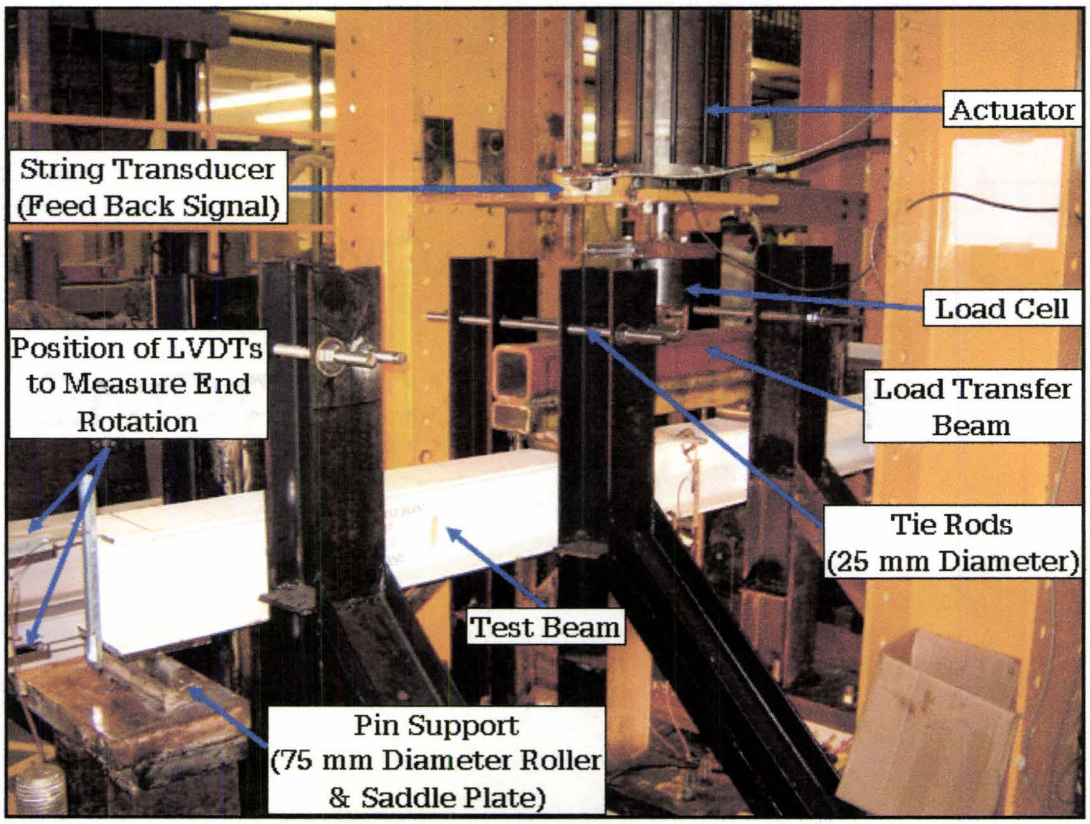


Figure 4.7: Photograph Image of Test Setup

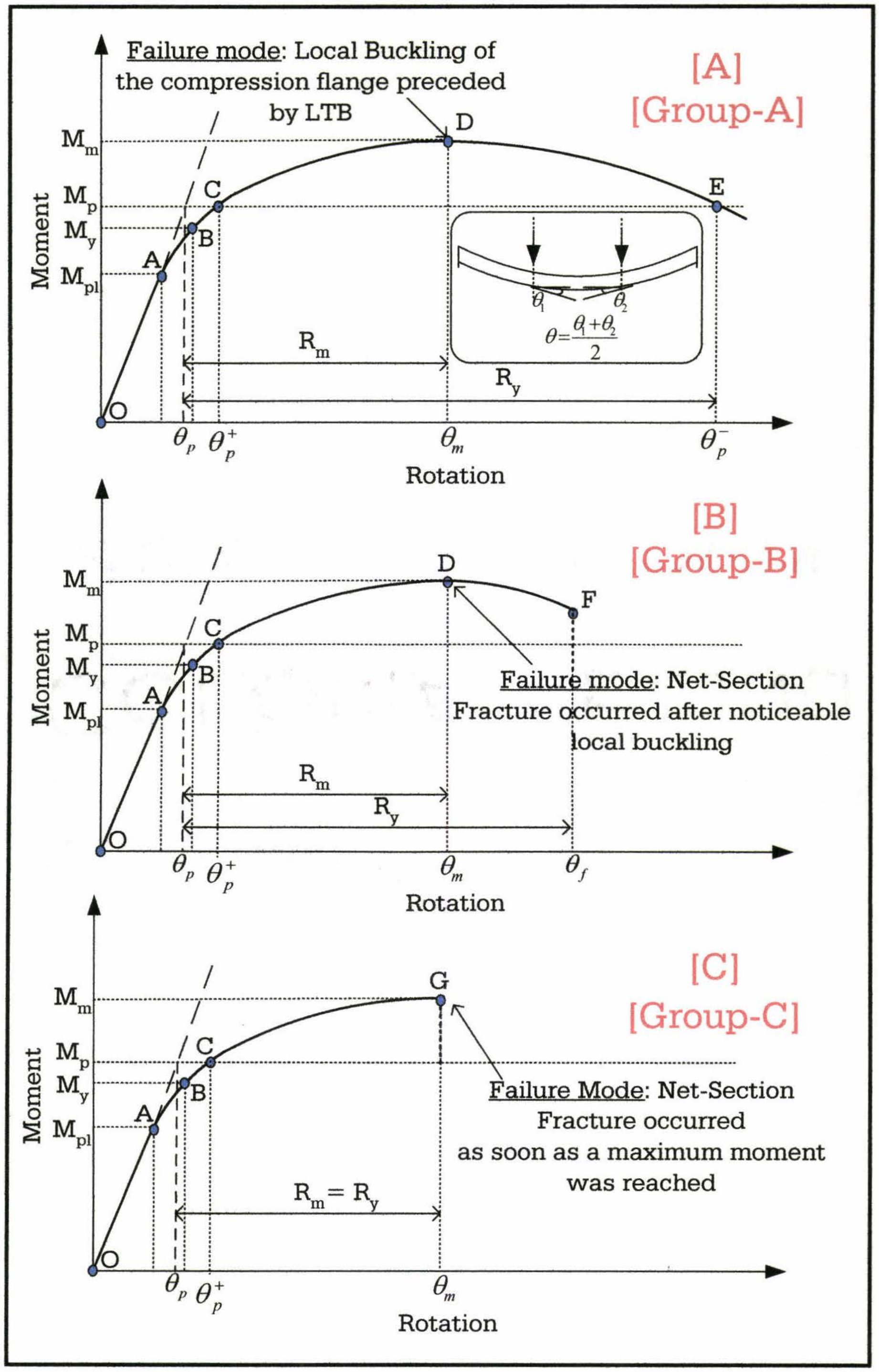


Figure 4.8: Typical Variation of Moment-Rotation Relationship

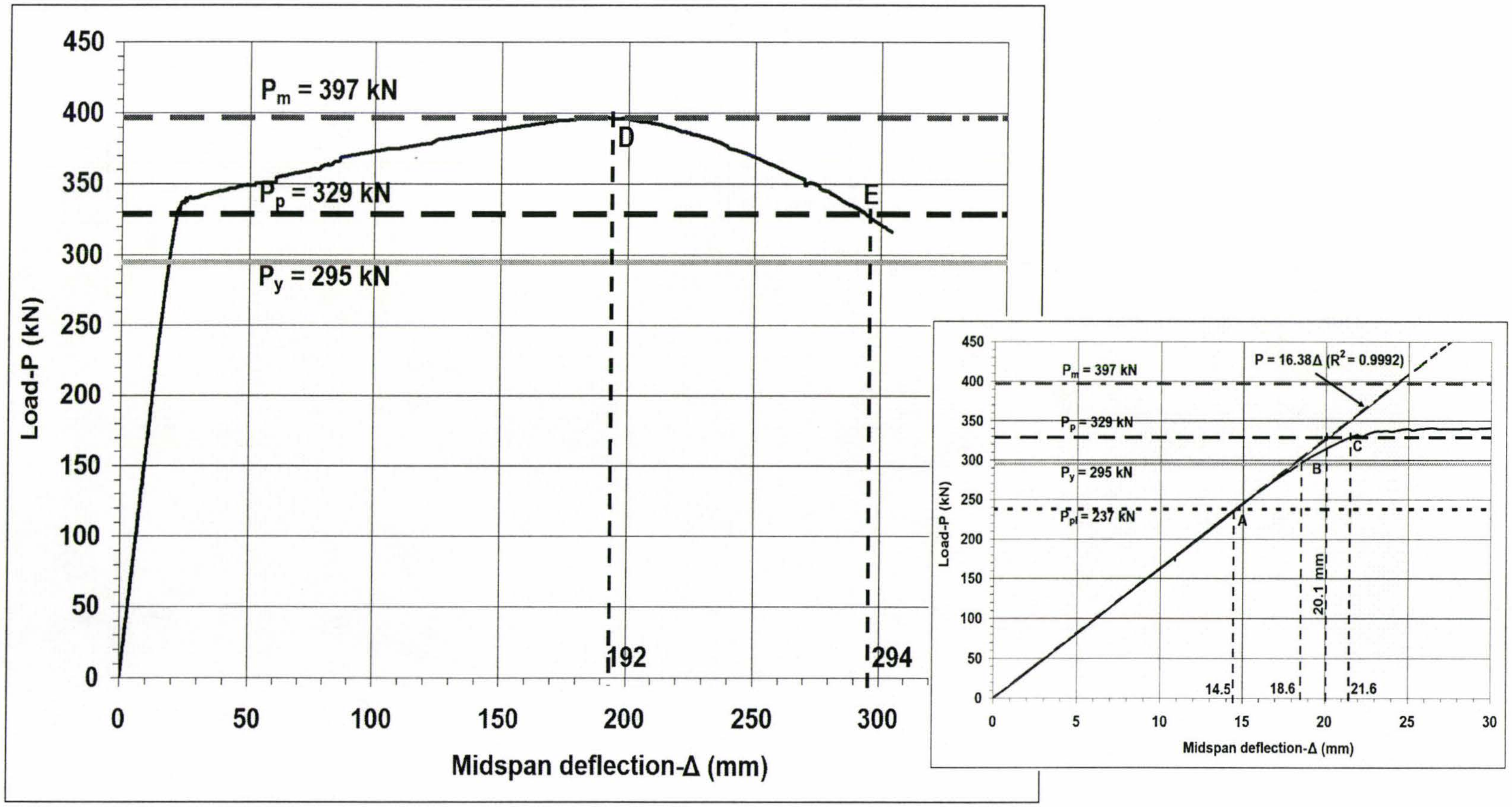


Figure 4.9: Load versus Midspan Deflection for Beam A100-3

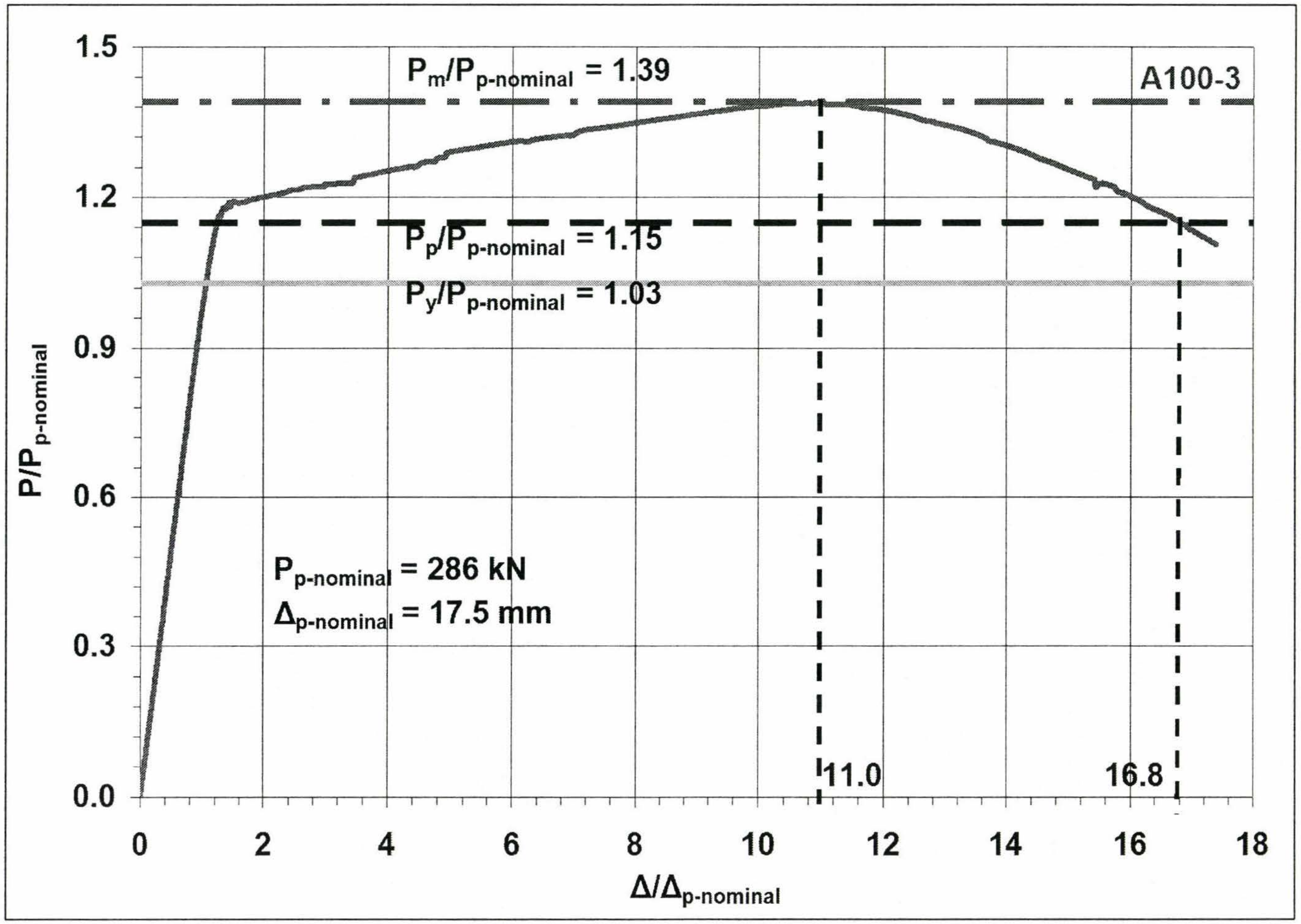


Figure 4.10: Normalized Load versus Midspan Deflection for Beam A100-3

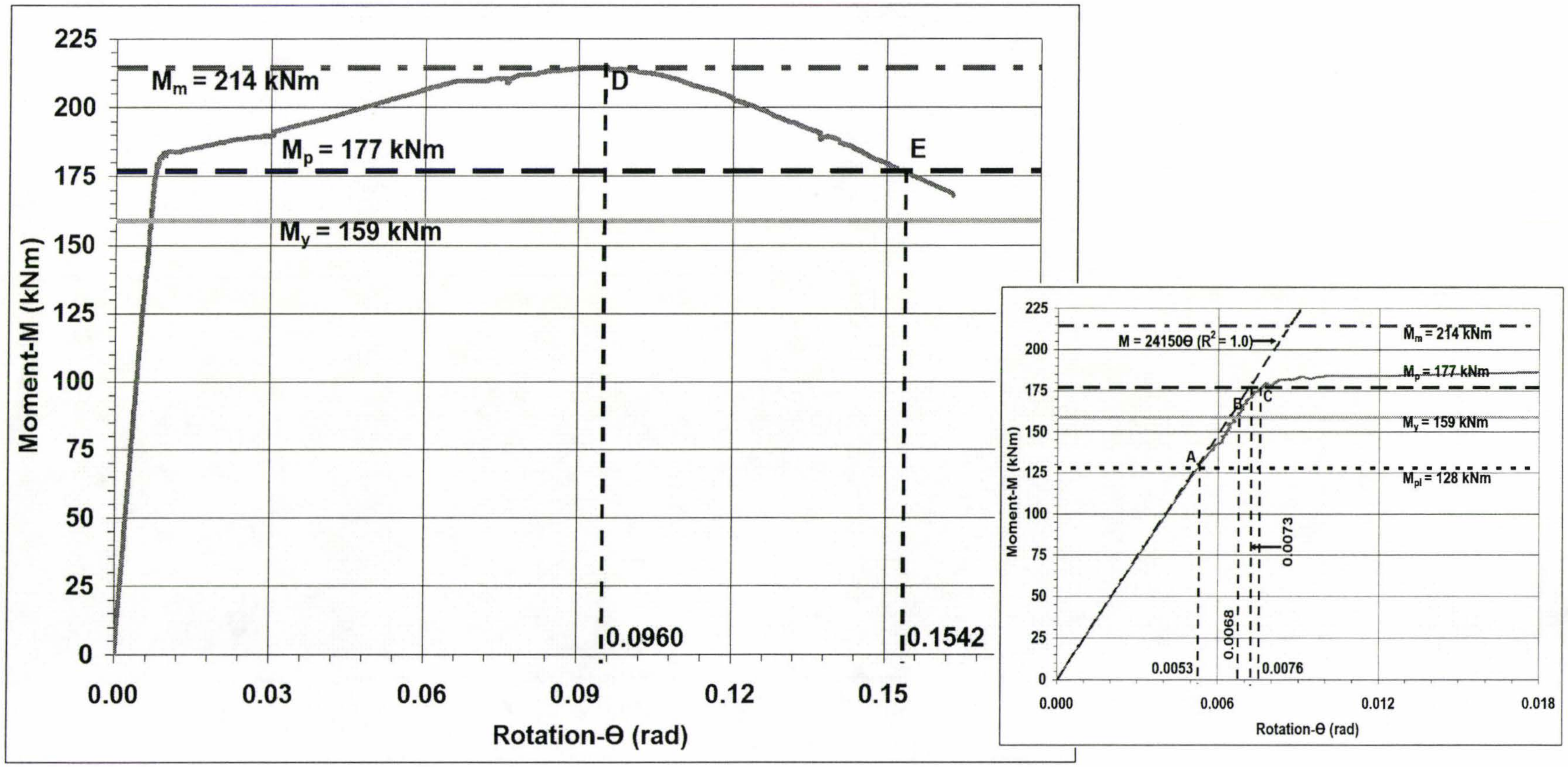


Figure 4.11: Moment versus Rotation for Beam A100-3

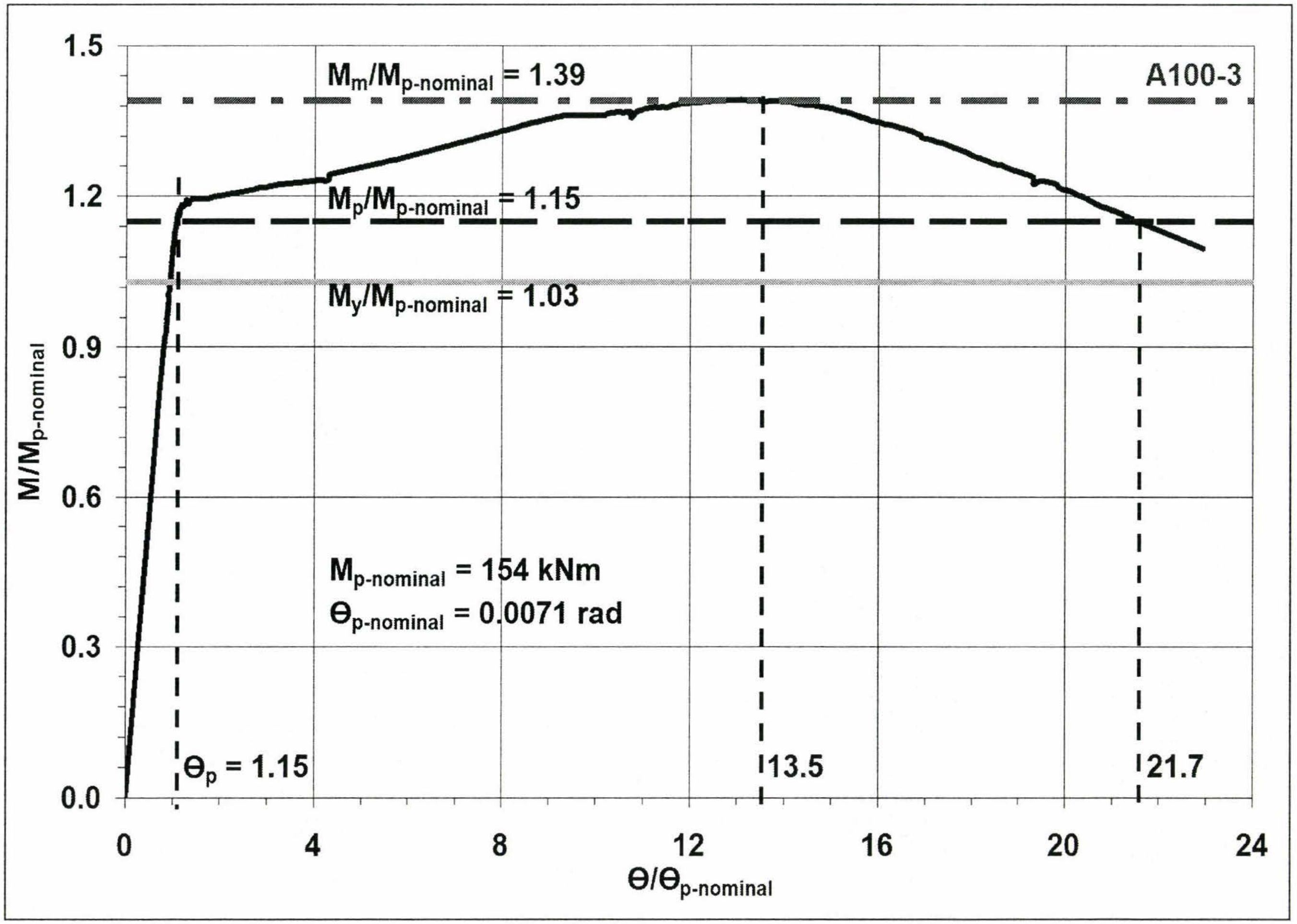


Figure 4.12: Normalized Moment versus Normalized Rotation for Beam A100-3

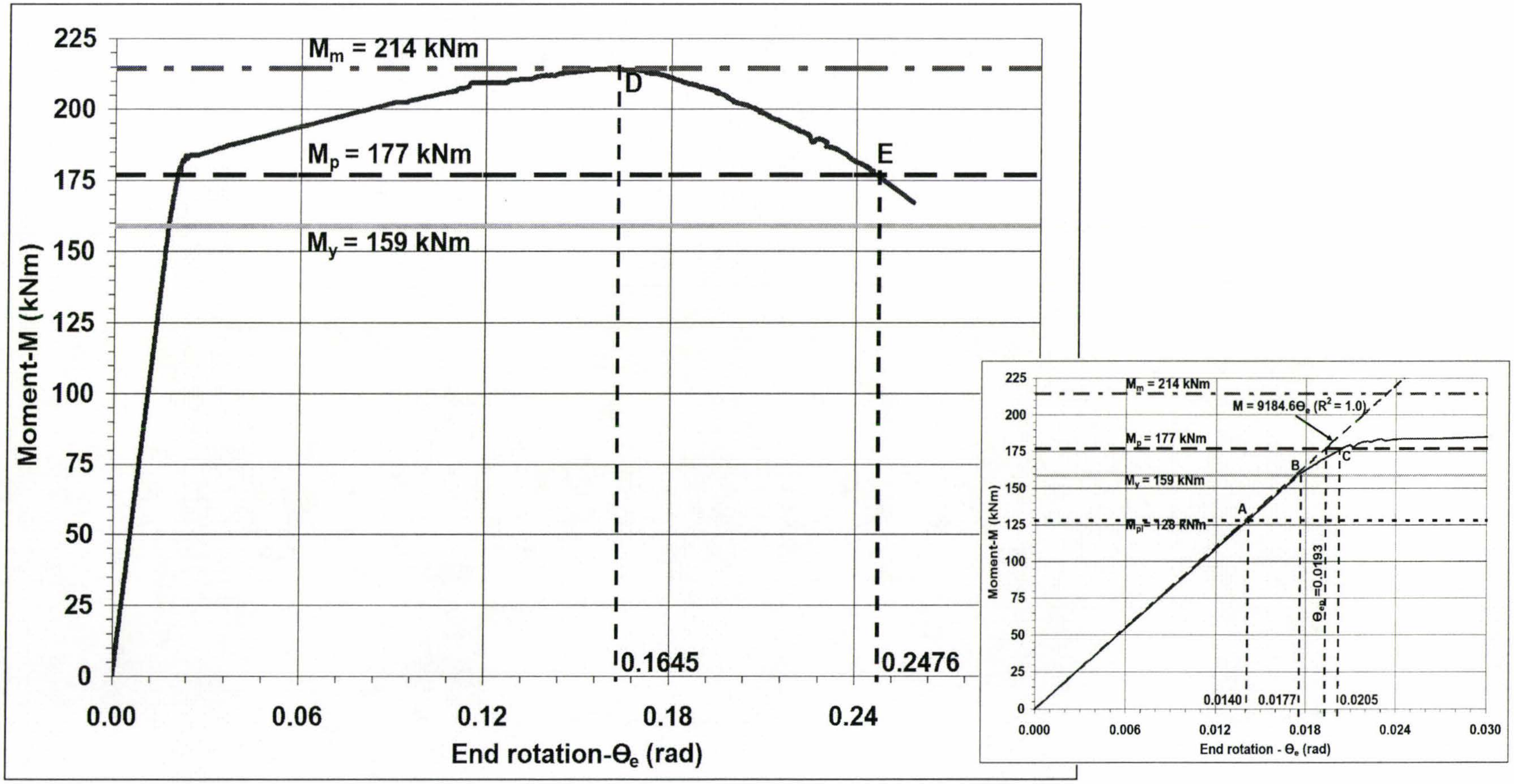


Figure 4.13: Moment versus End Rotation for Beam A100-3

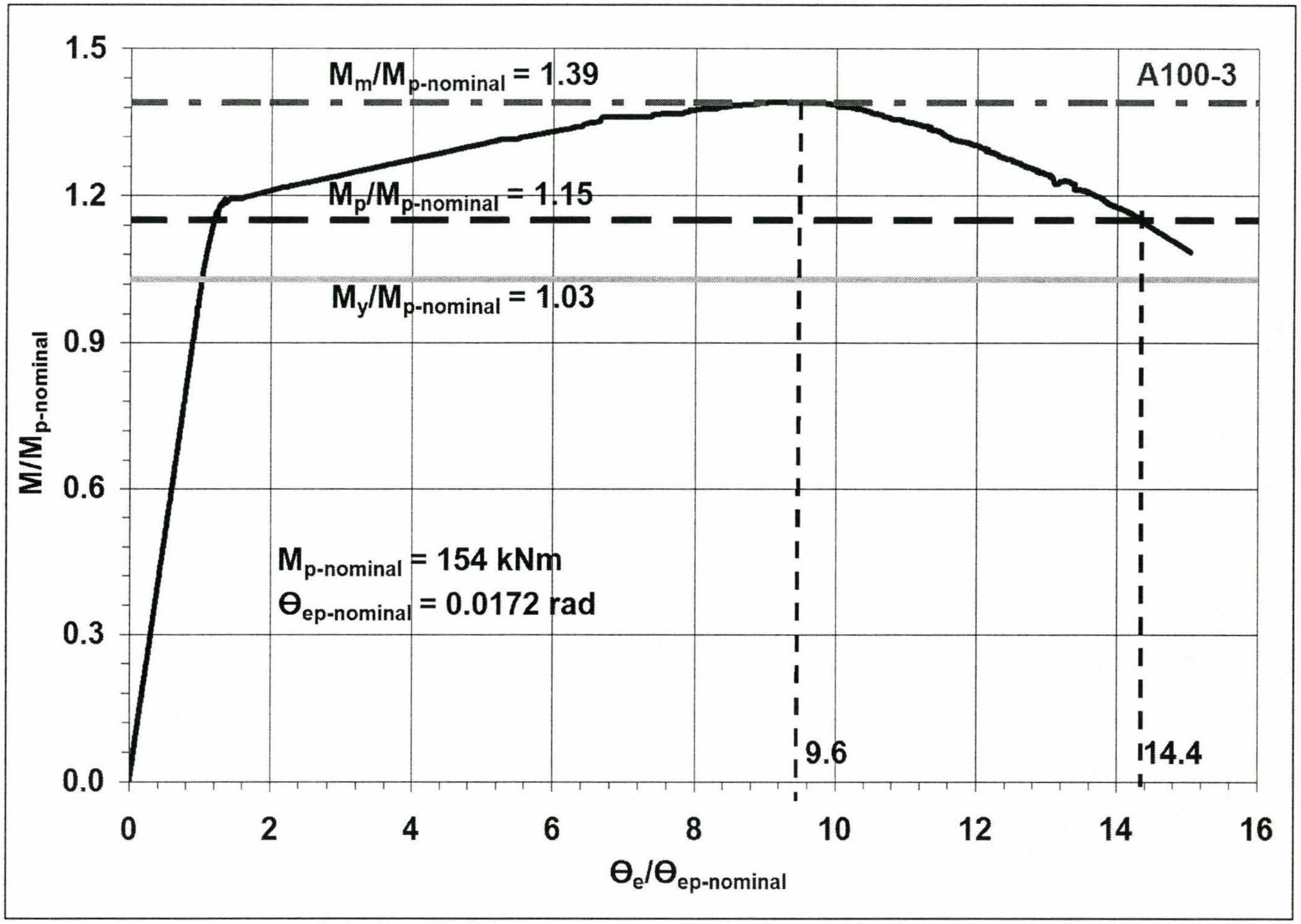


Figure 4.14: Normalized Moment versus Normalized End Rotation for Beam A100-3

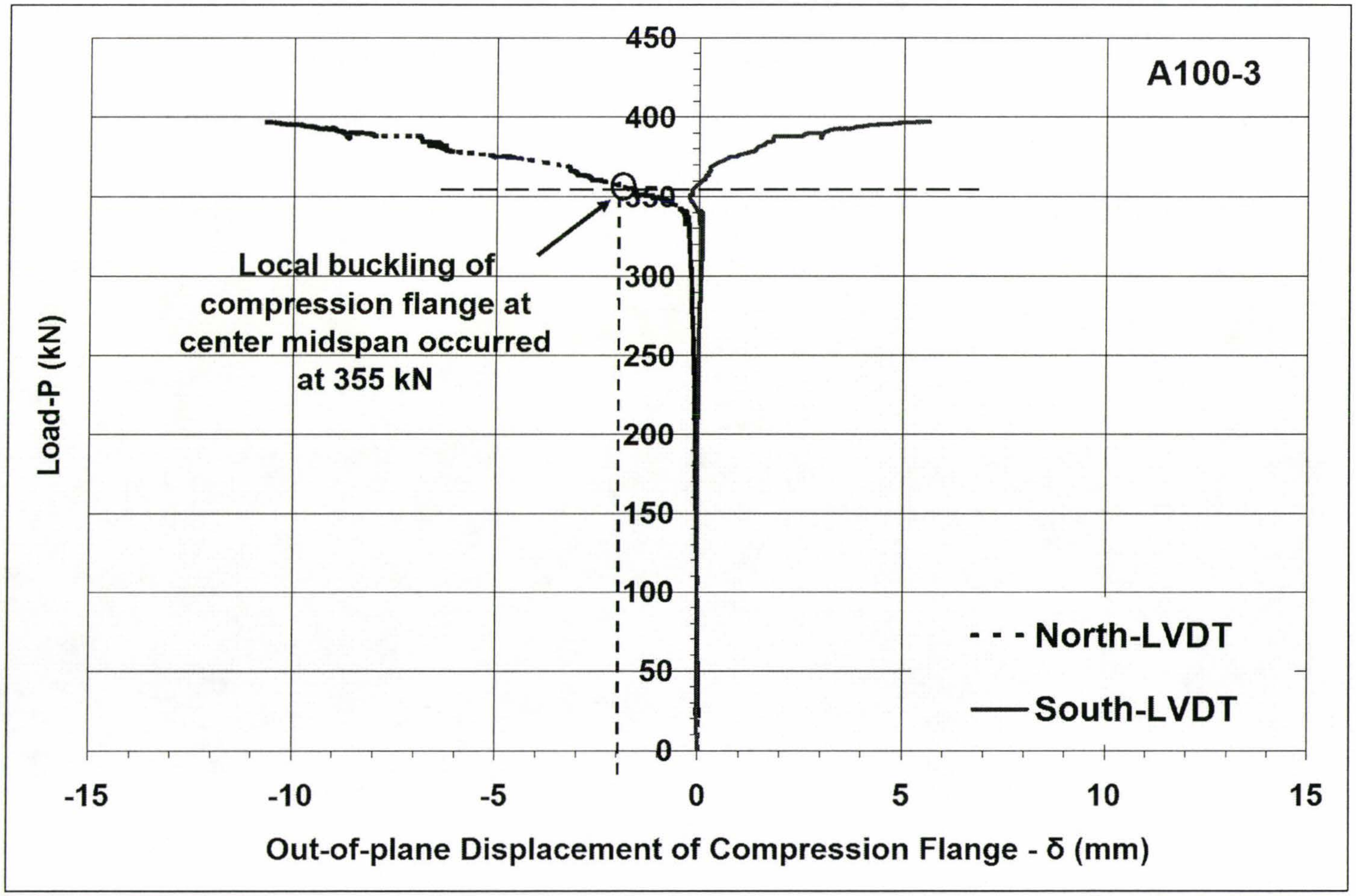


Figure 4.15: Load versus Out-of-Plane Displacement of CF Relative to TF for Beam A100-3

**Blank Page**

# CHAPTER: 5

# TEST RESULTS

## 5.1 Introduction

A total of twenty five W200X42 beams were tested under this program. The test matrix included 4-solid beams, 13-beams with open holes in the tension flange only, 4-beams with open holes in both flanges and 4-beams having fastener holes in both flanges. The bolts were sung tight and no surface preparation was performed during the installation of fasteners. The percentage of hole area to gross flange area ranged between 10% and 50%. The results from the instrumentation were plotted in accordance with the test data reduction procedure described in the previous chapter. The test results presented herein were normalized with respect to nominal values. For example, the moment ($M$) was normalized with respect to $M_{p-nom}$=154 kNm, and the load ($P$) was normalized with respect to $P_{p-nom}$= 286 kN. Similarly, the measured midspan deflection and rotations were normalized with respect to the corresponding nominal values as given in Table 4.6 ($\Delta_{p-nom}$=17.5 mm, $\theta_{p-nom}$=0.0071 rad and $\theta_{ep-nom}$=0.0172 rad). The experimental responses pertaining to each of the beam specimen presented in this chapter consist of;

- Normalized load versus midspan deflection ($P / P_{p-nom}$ vs. $\Delta / \Delta_{p-nom}$)

- Normalized moment versus load point rotation ($M / M_{p-nom}$ vs. $\theta / \theta_{p-nom}$)
- Normalized moment versus beam end rotation ($M / M_{p-nom}$ vs. $\theta_e / \theta_{ep-nom}$)
- Load versus out-of-plane displacement of the compression flange relative to the tension flange at the center midspan ($P$ vs. $\delta$)
- Normalized moment versus strain at the center midspan ($M / M_{p-nom}$ vs. $\varepsilon$) [for 4-beams only]

An experimental evaluation of the flexural behavior of all test beams in terms of strength and ductility is summarized. Based on these test results, a design method has been proposed to establish the flexural strength of steel I-beams having flange holes. A comparative analysis between the proposed design method and various international code methods (as described in Chapter 3) has been made. This chapter concludes with a summary based on the analysis of the proposed design method over the current CAN/CSA-S16.01 (CSA 2003) code method and three other international code methods.

## 5.2 Presentation of Experimental Results

As shown in Table 5.1, the test beams were lumped into three groups; Group A, Group B and Group C. This grouping was made based on (1) the overall variation of the moment-rotation (or load-midspan deflection) relationship and (2) the observed dominant failure mode. The general behavior with regards to the variation of the moment-rotation response was similar for all of the beam specimens in all groups until a maximum moment was reached. Beyond a maximum moment, however, the beam specimens categorized as Group A, exhibited ductile failure. The failure of Group A-specimens was mainly due to local buckling of the compression flange in the midspan region. The beam specimens falling into Group B failed as result of net-section fracture through the tension flange holes. However, such beams fractured after the formation of a local buckle in the compression flange, exhibiting a mixed failure mode. The beam specimens falling into Group C failed primarily due to net section fracture through the tension flange holes. The fracture on such beams occurred suddenly, without warning, as soon as a maximum load was reached.

Figures 5.1[A] through 5.25[A] illustrate the normalized load, $P / P_{p-nom}$, versus the normalized midspan deflection, $\Delta / \Delta_{p-nom}$, relationship for twenty five beam specimens, presented in the order as given in the second column of Table 5.2. The variation of load-deflection responses was linear until a proportional load was reached. Beyond this load level, perhaps due to the presence of residual stresses and stress concentration effects in the vicinity of hole region, the load-deflection curves softened gradually up to a yield load, $P_y$=295 kN (1.03 $P_{p-nom}$). As loading continued, although the load-deflection curve softened beyond the yield load, the beams were able to reach the gross-section plastic load, $P_p$=329 kN (1.15 $P_{p-nom}$). After reaching $P_p$, the load-deflection relation softened more rapidly since by then the cross-sections in the midspan region has yielded completely. This phenomena can be seen as a distinct flattening of the load-deflection responses from Figures 5.1[A] through 5.25[A], until a maximum load, $P_m$, was attained. Beyond the maximum load, the Group A-specimens (as given in Table 5.1), except A100-2, A80-1 and A75-B-1, began to shed load gradually and the plastic load was subsequently reached on the descending branch. Beam specimens A100-2, A80-1 and A75-B-1, however, unloaded rapidly. The Group A-specimens, except A80-1 and A75-B-1, exhibited a failure mode due to a combined lateral torsional buckling and local buckling in the midspan region. Beam specimens A80-1 and A75-B-1 exhibited a failure mode due to local buckling of the compression flange (no lateral deflection in the midspan region was noticed). The Group B-specimens exhibited a failure mode due to net section fracture which was preceded by local buckling of the compression flange. The Group C-specimens failed as a result of net section fracture as soon as a maximum load was reached.

Table 5.2 summarizes the tests results based on the load-midspan deflection relationships given in Figures 5.1[A] through 5.25[A]. This table presents the normalized values of the load and midspan deflection related to the points; point A, point B, point C, point D, point E, point F and point G ((as described in Chapter 4). The third column presents the proportional loads, $P_{pl}$, (point A), associated with each beam specimen tested. It was noted that the $P_{pl}$ reduced with increasing hole-to-gross flange area ratio ($\rho_h$). This may be due to early yielding of the flange material in the vicinity of hole region (stress concentration effects). The fourth and fifth columns give normalized midspan deflections corresponding to the calculated yield load, $P_y$=295 kN, and the normalized midspan deflections corresponding to the plastic load, $P_p$=329 kN, respectively. The sixth and seventh columns relate normalized maximum loads and the corresponding midspan deflections ($\Delta_m$), respectively, (point D). While the eighth column presents a normalized midspan deflection corresponding to the plastic load ($P_p$=329 kN) on the descending branch ($\Delta_p^-$), the ninth column provides the midspan deflections at fracture ($\Delta_f$). The tests on Group-A beam specimens were concluded as the load-deflection (or moment-rotation) curve dropped below the gross-section plastic load (or gross-section plastic moment) on the descending branch. Thus, the $\Delta_f$ is not available for such beams.

Figures 5.1[B] through 5.25[B] illustrate the normalized moment, $M / M_{p-nom}$, versus the normalized rotation, $\theta / \theta_{p-nom}$, responses pertaining to each beam specimen. The moment-rotation relationship showed a linear trend up to a proportional moment, $M_{pl}$. Beyond this moment, the flexural stiffness deteriorated gradually until the yield moment, $M_y$=159 kNm (1.03 $M_{p-nom}$), was attained. Although the flexural stiffness deteriorated rapidly beyond the yield moment, the beam specimens continued to carry additional load up to the gross-section plastic moment, $M_p$=177 kNm (1.15 $M_{p-nom}$). After reaching the plastic moment, although the flexural stiffness deteriorated more rapidly, the beams were able to attain a maximum moment, $M_m$. Beyond the maximum moment, the variation of moment-rotation responses were similar to the description as provided for the load-deflection relationship above.

Table 5.3 presents the test results based on the moment-rotation behavior. The third column gives the normalized proportional moments, $M_{pl}$. The fourth and fifth columns have the normalized rotations corresponding to the yield moment, $M_y$ = 159 kNm (1.03 $M_{p-nom}$), and the normalized rotations corresponding to plastic moment, $M_p$ = 177 kNm (1.15 $M_{p-nom}$), respectively. The sixth and seventh columns summarize a normalized maximum moment and the corresponding rotation for each beam tested. The eight and ninth columns provide a normalized rotation corresponding to the plastic moment, $M_p$ = 177 kNm (1.15 $M_{p-nom}$), again on the descending branch ($\theta_p^-$) and a normalized rotation at fracture ($\theta_f$), respectively.

Figures 5.1[C] through 5.25[C] show the normalized moment, $M / M_{p-nom}$, versus the normalized end rotation, $\theta / \theta_{p-nom}$. The description of general variation related to the moment-end rotation responses was similar to the moment versus rotation responses as described above (for the moment-midspan rotation relationship).

Table 5.4 summarizes the test results on the basis of the established moment versus end rotation relationships. Normalized end rotations corresponding to the yield moment,

$M_y$ = 159 kNm (1.03 $M_{p-nom}$), and the plastic moment, $M_p$ = 177 kNm (1.15 $M_{p-nom}$), are given in the fourth and fifth columns, respectively. Normalized end rotations established at maximum moments are presented in the seventh column. Normalized rotations at the plastic moment, $M_p$ = 177 kNm (1.15 $M_{p-nom}$), again on the descending branch and at fracture are provided in the eighth and ninth columns of Table 5.4, respectively.

Figures 5.1 [D] through 5.25[D] illustrate the load, $P$, versus the out-of-plane displacement, $\delta$, of the compression flange relative to the tension flange at the center midspan. Local buckling loads associated with the compression flange were established from each beam test and are summarized in Table 5.5. For Group A-specimens, except beams A80-1 and A75-B-1, the local buckling loads based on test measurements were found to be lower than the loads at which a wave type local buckle was visually observed during the tests. This may be because of the manner in which LVDT-3 and LVDT-4 were attached between the tension and compression flanges (see Figure 4.6 in Chapter 4). Note that the LVDT based measurements may possibly include any relative movement between the flanges as the beam specimens deformed laterally (due to lateral torsional buckling).

Figures 5.26 shows the normalized moment, $M / M_{p-nom}$, versus strain, $\varepsilon$, measured at various locations across a cross-section at the center midspan of beam specimens A100-4, A75-3, A70-2 and A75-B-1. As seen in the figure, the strains were recorded at the following locations; (1) outer surface of the tension flange closer to hole (25 mm away from the center of the hole); (2) outer surface of the tension flange at the flange-web junction; (3) web-closer to the tension flange (60 mm from the middle web); (4) middle web; (5) web-closer to the compression flange (60 mm from the middle web); (6) outer surface of the compression flange at the flange-web junction; and (7) outer surface of the compression flange closer to hole (25 mm away from the center of the hole). The strains recorded when the beam specimens reached the yield moment; $M_y = 159$ kNm ($1.03\,M_{p-nom}$), plastic moment, $M_p = 177$ kNm ($1.15\,M_{p-nom}$), and maximum moments are summarized in Table 5.6. As seen in the second column of Table 5.6, as beam specimen A100-4 reached $M_y = 159$ kNm ($1.03\,M_{p-nom}$), the outer surfaces of the tension and compression flanges nearly attained the yield strain of the flange material of 0.2% (measured). When beam A100-4 reached $M_p = 177$ kNm ($1.15\,M_{p-nom}$), the strain measurements, as seen in the sixth column of Table 5.6, indicated that the whole cross-section, except a portion at the middle web, has completely yielded. The strains at the maximum moment for beam A100-4 revealed that whole cross-sections in the midspan region, except the web portion closer to the neutral axis, experienced strains well above the onset of strain hardening strain of the flange material of 1.3% (see tenth column of Table 5.6). However, these strains were well below the strain corresponding to the tensile strength of the flange material (15.5%). This was because the flanges of solid flexural members cannot reach the ultimate strain since the failure of such beams may be triggered by local buckling (or combined with lateral torsional buckling) as soon as the compression flanges reached the onset of strain hardening strain (Haaijer and Thruliman, 1958).

As beam specimens A75-3, A70-2 and A75-B-1 reached $M_y = 159$ kNm ($1.03\,M_{p-nom}$), the strains measured adjacent to the hole region revealed that perhaps due to stress concentration the flange experienced strain well above the yield strain (0.2% of the flange material). Moreover, as beams A75-3 and A70-2 attained $M_p = 177$ kNm ($1.15\,M_{p-nom}$), the strain at the middle web was approximately 0.05%. This implied that no great deviation of the plastic neutral axis from the gross cross-section to the net cross-section has occurred. Conversely, a theoretical analysis indicates that a substantial movement of the neutral axis occurs due to holes of 25% (A75-3) and 30% (A70-2) to the gross flange area in the tension flange only. During the test some of the strain gages did not work properly or went out of range and are denoted herein as N/A in Table 5.6.

## 5.3 Comparison of Experimental and Calculated Initial Stiffnesses

Table 5.7 presents the experimentally determined stiffness based on the (1) load-midspan deflection responses $(k_\Delta)_{\exp}$ (2) moment-rotation responses $(k_\theta)_{\exp}$ and (3) moment-end rotation responses $(k_{\theta e})_{\exp}$. The experimentally obtained stiffness is the slope of the initial linear portion of the test data. The slope was determined by a regression analysis as noted in Chapter 4. Approximately 30% of test data prior to the calculated yield load was used for this linear regression analysis. As discussed previously in Chapter 4, the stiffnesses using Equations 4.3, 4.4 and 4.5 were also calculated based on the measured cross-sectional dimensions and the mechanical characteristics of the flange material. As summarized in the fourth column of Table 5.7, the $(k_\Delta)_{exp}/(k_\Delta)_{cal}$ varied from 0.87 and 1.03. The $(k_\theta)_{exp}/(k_\theta)_{cal}$ ranged between 0.98 and 1.16 (see the seventh column). The $(k_{\theta e})_{exp}/(k_{\theta e})_{cal}$ spanned between 0.94 and 1.09. This comparison indicated that a relatively good correlation existed between the experimentally determined stiffness and the calculated stiffnesses. The discrepancies between the experimentally obtained values and the calculated values may be attributed to various factors such as the presence of residual stresses, the presence of geometric imperfections, variations in mechanical characteristics, variations in geometrical dimensions, reaction frame flexibility and the accuracy of the measuring instruments, etc. (Green 2000).

## 5.4 Summary Test Results

### 5.4.1 Overview

Figure 5.27 compares the moment versus rotation responses of solid beams A100-1, A100-2, A100-3 and A100-4. As seen in this figure, the responses of four members were close to each other until a maximum moment was reached, although a slight variation did occur due to the inherent variablities; the presence of residual stresses, initial imperfections, inhomogeneous material characteristics, etc. After the attainment of maximum moment, beam specimens A100-1, A100-3 and A100-4 responded similarly in which the unloading occurred gradually with increasing rotation. The unloading of beam specimen A100-2, however, occurred rapidly. The unusual occurrence of rapid unloading may be attributed to fact that beam A100-2 buckled locally at one of the loading locations (towards B end) during the test.

Figure 5.28 compares the moment versus rotation response for the beam specimens having holes in the tension flange. The corresponding plot for solid beam A100-3 is also included in this figure. This was to illustrate how the presence of holes in the tension flange influenced the overall flexural behavior of beam members made of ASTM A992 steel. As can be seen in Figure 5.28, when holes were made on the tension flange in the critical moment (maximum moment) region, the responses of the beam members in terms of strength and ductility was considerably altered. A quantitative analysis of the impact on strength and member ductility due to the presence of flange holes will be provided in the following section of this chapter.

Figures 5.29 through 5.32 provide a comparison of the moment versus rotation behavior for the beam members having; (1) open holes in the tension flange; (2) open holes in both flanges; and (3) fastener holes in both flanges. The corresponding plot for solid beam A100-3 is also included in these figures to illustrate how the presence of holes under various scenarios influenced the overall behavior of flexural members. As seen in Figures 5.29 through 5.32, when holes occurred in both flanges the flexural strength was considerably reduced than a similar member having holes exclusively in the tension flange. However, when the holes contain fasteners of standard size the strength of the beam member was increased slightly over a similar member having holes in both flanges. It was also observed that the strength of beam members having holes exclusively in the tension flange and that of beam members having fastener holes in both flanges under similar condition were in close agreement (see Figures 5.29 through 5.32). Thus, it can be concluded from this observation that the use of fasteners of standard sizes could be partially effective in resisting the bending stresses in the compression region. Nevertheless, it was observed that the flexural behavior in terms of ductility, which is usually measured as a rotation capacity, was not improved as much as strength when holes were filled with fasteners of standard size (see Figure 5.29). This may be attributed to the fact that the presence of holes of any type, either open holes or fastener holes, will cause early yielding in the vicinity of hole region due to the presence of stress concentrations. As a result, the overall member ductility may be reduced.

Figure 5.33 shows photographic images taken in the midspan region of the test beams. As seen in the figure, the solid members exhibited a failure mode accompanying a large downward local buckle of the compression flange on one side and a permanent lateral deformation with a slight upward local buckle on the opposite side in the midspan region. Beam specimens A90-1, A85-1, A85-F-1 and A85-B-1 also experienced a similar failure mode as the solid members (see Figure 5.33). Holes in the tension flanges of these beams, however, stretched out in the longitudinal direction without causing necking across the flange width at the hole location. The failure mode associated with beam specimens A80-1 and A75-B-1 was primarily due to local buckling consisting of a downward local buckle on one side and upward local buckle on other side. No lateral deformation in the midspan region of beams A80-1 and A75-B-1 was observed. In beam specimens A85-B-1 and A75-B-1, holes in the compression flange squeezed in the longitudinal direction. That is, as shown in Figure 5.34[A], holes in the compression flange seemed to be a conical shape at the end of the test. As depicted in Figure 5.34[B], holes in the tension flanges of beams A80-1 and A75-B-1 stretched out in the longitudinal direction and necking was clearly visible on the tension flange across the hole location.

Beams A75 series, A70 series, A70-B-1 and A75-F-1 experienced a failure mode consisting of local buckling of the compression flange followed by net-section fracture through holes in the tension flange. However, beams A60 series, A50-1, A60-B-1, A70-F-1 and A60-F-1 fractured suddenly through holes in the tension flange as soon as they reached a maximum load. In all cases considered, a substantial amount of yielding occurred in the midspan region which was observed by flaking of whitewash, which was applied prior to the test.

### 5.4.2 Strength of Beams Based on Test Results

Table 5.8 summarizes the followings; (1) the nominal net-section fracture strength-to-nominal gross-section yield strength ratio ($A_{fn}F_u / A_{fg}F_y$); (2) the maximum measured moment (including an average of identical tests) ($M_m$); and (3) the strength reduction (in percentage) with respect to the solid beams. The nominal net-section fracture strength ($A_{fn}F_u$) and the nominal gross-section yield strength ($A_{fg}F_y$) were calculated based on the measured ultimate and yield strengths of the flange material of 531 MPa and 409 MPa, respectively. The flexural strengths of the beam specimens, having $A_{fn}F_u / A_{fg}F_y \geq 1.0$, were not significantly affected due to holes in the flanges (see the fifth column of Table 5.8). Moreover, these beam specimens failed in ductile manner due to either a combined lateral torsional buckling and local buckling or mainly local buckling of the compression flange.

As presented in the fifth column of Table 5.8, the strength reduction increased as the size of holes increased, particularly for the cases where $A_{fn}F_u / A_{fg}F_y$<1.0. Thus, beam specimens A75 series and A70 series with the $A_{fn}F_u / A_{fg}F_y$ ratio value of 0.96 and 0.92, respectively, had a strength reduction of 2.3% and 4.7%, respectively. Furthermore, these specimens failed due to net-section fracture, which was preceded by local buckling. Therefore, beam specimens A75 series and A70 series did not experience a sudden failure, rather providing some warning of impending failure such as a wave type local buckle in the compression flange prior to fracturing. Assuming a reduction in strength within 5% range can be ignored from the design stand point, holes of approximately 30% to the gross flange area can be ignored in flexural strength calculations for beam specimens having holes either in the tension flange only or fastener holes in both flanges (see the fifth column of Table 5.8). It is pertinent to note that Kicinsky's study (1963) on a rolled beam made of ASTM A7 steel with $F_y / F_u$ ratio of approximately 0.5 indicated that no moment reduction occurred for fastener holes of 23% to the gross tension flange area. Douty and McGuire (1965) concluded based on their test results that no moment reduction occurred for beam specimens with 27% fastener holes to the gross flange area. The beam specimens in their study conformed to ASTM A7 steel with $F_y / F_u$ ratio of approximately 0.5 (see Chapter 2 for further details). Zahorsky (1994) conducted flexural tests on beam specimens made of Grade 50 steel with $F_y / F_u$ ratio of 0.73. Based on the test results, Zahorsky (1994) recommended that the holes of normal size up to 30% of the gross flange area can be ignored in calculating the cross-sectional strength of a flexural member. The test results presented in this thesis report was therefore, closely comparable to the past research studies for the cases where either open holes occur in the tension flange only or "snug tight" fastener holes exist in both flanges. Beam specimens A60 series ($A_{fn} F_u / A_{fg} F_y$=0.81<1.0) and A50-1 ($A_{fn} F_u / A_{fg} F_y$=0.67<1.0) showed a strength reduction of 9% and 17%, respectively. Also these specimens failed as a result of net-section fracture as soon as a maximum moment was reached (brittle failure).

Beam specimen A75-B-1 ($A_{fn} F_u / A_{fg} F_y$=0.96<1.0) having holes in both flanges had a strength 6.5% lower than the solid beam and 4.3% lower than a similar beam having holes exclusively in the tension flange (A75 series). Beam specimen A70-B-1 ($A_{fn} F_u / A_{fg} F_y$=0.91<1.0) had a strength 8% lower than the solid beam and 3.4% lower than a similar beam having holes in the tension flange only (A70 series). The strength reduction associated with beam specimen A60-B-1($A_{fn}F_u / A_{fg}F_y$=0.82 <1.0) was 10.3% lower than the solid beams and 1.5% lower than a similar member having holes in the tension flange only (A60 series). It was of interest to note that the strength reductions between beams A70-B-1 and A70 and between beams A60-B-1 and A60 decreased. This may be due to the fact that the larger holes cause early net-section fracture. Therefore, it may be concluded that the flexural strength was governed by the nature of failure such as fracture regardless of the presence of holes in the compression flange.

When holes contained "snug tight" fasteners of standard sizes, beam specimens A75-F-1, A70-F-1 and A60-F-1 had a strength reduction of 1.9%, 3.3% and 9.3%, respectively. It was noted that the flexural strength of the beams having holes in the tension flange only and that of similar beams having "snug tight" fasteners in both flanges were closer to each other (see the fifth column of Table 5.8). Therefore, it is concluded that the presence of fasteners in the compression flange was partially effective in resisting the flexural stresses.

### 5.4.3 Rotation Ductility of Beams Based on Test Results

Two different definitions of the "rotation capacity"; such as a rotation capacity at the maximum moment ($R_m$) and a total rotation capacity ($R_y$) were used to establish the ductility of a flexural member. Table 5.9 summarizes the $R_m$ and $R_y$ values determined from the moment versus rotation curve for each of the beam specimen considered. Table 5.9 also includes average rotation capacities for identical tests. Note that an average $R_y$ for the solid beam specimens was established based on the test results of A100-3 and A100-4 only, whereas an average $R_m$ was established using the test results of all four solid beams. As presented in the fifth and seventh columns of Table 5.9, the percentage reductions in $R_m$ and $R_y$ for each beam specimen were established relative to the corresponding average values of the solid beams.

As summarized in the fifth and seventh columns of Table 5.9, the rotation capacities were not influenced significantly due to holes in the tension flanges for the beam specimens having the $A_{fn}F_u / A_{fg}F_y \geq 1.0$ (for example A90-1, A85-1 and A80-1). Nevertheless, as the $A_{fn}F_u / A_{fg}F_y$ ratio decreased the percentage reductions in $R_y$ for beams A75 series, A70 series and A60 series and A50-1 increased from 19.9% to 77.2% (see the fifth column of Table 5.9). The percentage reduction associated with $R_m$ for beams A70 series, A60 series and A50-1 varied between 9% and 61%. When open holes occurred in both flanges, the reductions in $R_y$ for beam specimens A85-B-1, A75-B-1, A70-B-1 and A60-B-1 increased from 10.9% to 56.4%. The $R_m$ associated with beam A75-B-1, A70-B-1 and A60-B-1 was 20.3%, 26.8% and 25.2%, respectively, lower than the corresponding value of the solid beam.

When holes contained "snug tight" fasteners, the rotation capacities of the beam specimens were not significantly influenced provided that $A_{fn}F_u \geq A_{fg}F_y$. As the $A_{fn}F_u / A_{fg}F_y$ ratio decreased, the percentage reduction in $R_y$ for beam specimen A75-F-1, A70-F-1 and A60-F-1 increased from 28% to 60%. A similar trend of reduction in $R_m$ was observed varying between 4% and 31.7% for beams A75-F-1, A70-F-1 and A60-F-1. It can be noted that the strength and ductility of the beam specimens, whose failure was accompanied by the combined lateral torsional buckling and local buckling (for example A85-F-1), were considerably improved as the fasteners of standard sizes were inserted into the flange holes. This was not true, however, for the beam specimens, whose failure was due to net section fracture (brittle failure).

## 5.5 Evaluation of Experimental Results

This section presents an evaluation of the experimental results in terms of the moment capacity ($M_m$) of beam specimens having the flange holes (or flange fastener holes) of various diameters by comparing with the theoretical moment calculation; gross-section plastic moment ($M_p$) and net-section fracture moment ($M_{fn}$). The net-section fracture moment is defined as follows (Dexter and Altstadt, 2003):

$$M_{fn} = Z_n F_u \tag{5.1}$$

where $Z_n$ is the plastic section modulus of the net-section and $F_u$ is the measured ultimate strength of the flange material. When holes were made exclusively in the tension flange (or fastener holes occurred in both flanges), the plastic section modulus of the net-section, $Z_n$, was calculated based on the movement of the position of the neutral axis from the gross cross-section to the net cross-section (see Chapter 3-Equation 3.6).

However, the strain measurements made on the middle web of the beam specimens having holes in the tension flanges only (A75-3 and A70-2), indicated that the movement of the neutral axis from the gross cross-section to the net cross-section at the hole location was not significant throughout the test (see Figure 5.26). That is, the position of the neutral axis underwent negligible change. This may be attributed to the fact that the holes were made over a short length compared to the length of uniform moment span, the stress conditions do not change abruptly enough to allow a complete redistribution of stresses within this short length. Therefore, the neutral axis cannot move suddenly from the gross cross-section to the net cross-section at the hole location, unless raw of holes were made in a significant portion of the midspan region. Moreover, the material strain hardening will inhibit the movement of the neutral axis as stresses in the vicinity of hole region may be more than the yield stress when the beam specimen reaches its plastic moment capacity. However, the movement of the neutral axis at the holes location was considered (based on the ideal elastic-perfectly plastic material behavior) in this study as a conservative design approach.

The maximum moment, $M_m$, obtained experimentally and net-section fracture moment, $M_{fn}$, calculated using Equation 5.1 are summarized in Table 5.10. Also, the $M_m / M_p$,

$M_m / M_{fn}$ and $M_p / M_{fn}$ ratio values, where $M_p$=177 kNm, are tabulated in Table 5.10. All test beams including specimen A50-1, in which holes removed a maximum 48% of the gross flange area, had a maximum moment more than $M_p$. In other words, net section fracture failure did not limit the attainment of the full plastic moment capacity. As provided in the sixth column of Table 5.10, the $M_m / M_p$ ratio value decreased as the $A_{fn} F_u / A_{fg} F_y$ ratio value decreased. On the contrary, the $M_m / M_{fn}$ ratio value increased as the $A_{fn} F_u / A_{fg} F_y$ ratio value decreased (see seventh column of Table 5.10). Therefore, it can be concluded that the establishment of moment based on $M_{fn}$ would be more conservative than $M_p$ when larger holes exist in the tension flanges causing sudden failure due to net-section fracture (for example A50-1). Moreover, the $M_m / M_{fn}$ ratio values were within 10% for the beams with holes in the tension flange only or fastener holes in both flanges. However, when holes existed in both flanges (as high as 37% of the gross flange area), the $M_m / M_{fn}$ ratios were within 20% (see the seventh column of Table 5.10). This revealed that there was a reasonable margin between $M_m$ and $M_{fn}$ (about 20%).

As presented in Figure 5.34, the $M_p / M_{fn}$ ratio increased as the $A_{fn} F_u / A_{fg} F_y$ ratio decreased for three different scenarios considered; (1) open holes in tension flange only, (2) open holes in both flanges and (3) fastener holes in both flanges. As indicated in the figure, failure of the beam specimens having the $A_{fn} F_u / A_{fg} F_y$<1.0 was due to net-section fracture (brittle failure mode). On the other hand, the beam specimens having the $A_{fn}F_u / A_{fg}F_y$>1.0 failed as a result of the combined lateral trosional buckling followed by local buckling (ductile failure). Therefore, it can be suggested from this figure that a design check, analogous to the tension member provision as per the current CSA (2003) code, be made. In this design check (for flexural members having holes in the flange), the gross cross-section shall be designed for $M_p$ (lower if the compression flange or web limit states control) while establishing the $M_{fn}$ at the net-section. The lesser of these two values can be used as a design moment. Note that the discussions and conclusions made herein were based on the steel grade having the measured yield-to-ultimate strength ratio of 0.77. Thus, such conclusions may be appropriate for steel grades with $F_y / F_u$<0.85.

## 5.6 Comparison of Test Results with Various Code Provisions

In this section, various international code provisions dealing with the design moment calculation for flexural members having flange holes (or fastener holes) are briefly presented. The code based design moments are compared with the experimentally established maximum moment and theoretically obtained gross-section plastic moment.

Case 1: Open Holes in Tension Flange Only: Table 5.11 summarizes design moments established in accordance with five different code provisions as considered in Chapter 3. As discussed, the current CSA (2003) and the BS5950 (BSI 2001) provisions use the net-section calculation to establish the design moment for a flexural member having open holes in the flanges. That is, the design moment, $M_d = Z_n F_y$, where $Z_n$ is the plastic section modulus of the net section and $F_y$ is the yield strength of the flange material. As per the current AISC-LRFD (2005), holes up to 23% to the gross flange area can be ignored for a steel grade having the $F_y / F_u$ ratio value of 0.77, such as the steel grade used in this study. Thus, beam specimens A90-1, A85-1 and A80-1 can be designed to carry the full plastic moment capacity, $M_p$=177 kNm. Based on the AISC-LRFD (2005), when holes result in removal of more than 23% of the gross flange area, the design moment will be calculated as, $M_d = Z_n F_y$. Note that the current AISC-LRFD (2005) does not seem to take into account the effects of open holes occurring exclusively in the tension flanges. The previous version of the AISC-LRFD (1999, however, ignores holes up to 7.6% of the gross flange area for a steel grade having the $F_y / F_u$=0.77. The AS4100 (SA 1998) permits holes up to 9.4% of the gross flange area for the beam material having the $F_y / F_u$ =0.77.

<u>Case 2: Open Holes in Tension and Compression Flanges</u>: the AISC-LRFD (2005) established higher moment relative to $M_p$ (=177 kNm) than the other code methods. Following the AISC-LRFD (2005), the AS4100 (SA 1998) permitted higher moment relative to $M_p$ than the CSA (2003) and the BS5950 (BSI 2001) codes. The ASIC-LRFD (1999) was more conservative over the other code methods.

Case 3: Fastener Holes in Tension and Compression Flanges: as discussed, the CSA (2003) code considers a 15% exemption for the effects of fastener holes. Thus, beam specimen A85-F-1 was exempted from the effects of holes and can be designed to carry its full plastic moment capacity, $M_p$. As presented in Table 5.11, the CSA (2003) allowed higher moment over the other codes considered. Following the CSA (2003), the BS5950 (2001) established higher moment relative to $M_p$ (=177 kNm). Following the BS5950 (2001), the AISC-LRFD (2005) allowed higher moment relative to $M_p$ (=177 kNm). Overall, the AISC-LRFD (1999) code was more conservative than the other code provisions.

Percentage reductions between the design moments, established based on five code methods, and the maximum measured moments are also presented in Table 5.11. For the beam specimens having open holes (9%-48% of the gross flange area) in the tension flanges only, the CSA (2003), the AISC-LRFD (2005), the BS5959 (BSI 2001) and the AS4100 (SA 1998) allowed, $M_d$ (on average) approximately 75% of $M_m$. For the similar case, however, the AISC-LRFD (1999) permitted $M_d$ (on average) approximately 60% of $M_m$. When open holes of 15%-37% to the gross flange area occurred in the both flanges, the $M_m$ (on average) was 30% more than $M_d$ established on the basis of the CSA (2003), the BS 5950 (BSI 2001) and AS 4100 (SA 1998). For the similar case, the $M_m$ (on average) was approximately 25% and 37% more than $M_d$ as per the AISC-LRFD (2005) and the AISC-LRFD (1999), respectively. Overall, the code based estimates were unnecessarily conservative when compared to the measured maximum moments.

## 5.7 Proposed Method for Flexural Members with Flange Holes

The variation of $M_p / M_{fn}$ ratio with $A_{fn}F_u / A_{fg}F_y$ ratio for the test beams is as shown in Figure 5.35. From this figure, it can be seen that the $M_p / M_{fn}$ ratio decreases as the $A_{fn}F_u / A_{fg}F_y$ ratio increases. As shown in Figure 5.36, the beam specimens having the $A_{fn}F_u / A_{fg}F_y \geq 1.0$ failed in ductile manner and in such cases, the $M_p / M_{fn} < 0.85$ (also see the eighth column of Table 5.10). However, the beam specimens having the $A_{fn}F_u / A_{fg}F_y < 1.0$ failed as a result of net-section fracture (brittle failure) and in such cases, the $M_p / M_{fn} > 0.85$. When holes occurred in both flanges, the beam specimens with the $A_{fn}F_u / A_{fg}F_y > 0.95$ failed due to local buckling of the compression flange (ductile failure) and in such cases the $M_p / M_{fn} < 1.0$. On the other hand, the beam specimens (holes occurred in both flange), having the $A_{fn}F_u / A_{fg}F_y < 0.95$, failed as a result of net section fracture and in such cases the $M_p / M_{fn} > 1.0$. In conclusion, the analysis of the experimental test results, therefore, indicated that limiting the stress in the tension flange to 0.85 $F_u$ provides a lesser probability of net-section fracture.

Based on the test results, a design procedure can be proposed, which is analogous to the design provision associated with a direct tension member. According to the clause 13.2 of the CAN/CSA-S16.01 (2003) standard, the nominal tensile resistance developed by an axial tension member shall be taken as the least of the gross-section yield strength ($A_g F_y$) or net-section fracture strength (0.85 $A_n F_u$). Similarly, for flexural members having flange holes, the nominal design moment at hole location can be established as follows:

- The gross cross-section, obviously, shall be designed to carry $M_p (= Z_g F_y)$ (or lower if other limit state such as web buckling/yielding controls).
- At hole location, the modified net-section fracture moment capacity be calculated, $M_{fnm}$ ($= 0.85\, Z_n F_u$).

If $M_p \leq M_{fnm}$, the effects of holes (or fastener holes) can be ignored, hence, the flexural member will be designed to carry its gross-section plastic moment capacity. Otherwise, the member will be designed to carry its modified net-section fracture moment capacity.

Table 5.12 summarizes the calculated proposed design moment ($M_{dp}$). This table also compares the $M_{dp}$ with the $M_p$ and with the $M_m$. As seen in the eighth column, the $M_p / M_{dp}$ ratio values varied between 1.0 and 1.24 for the case where open holes of 9%-48% to the gross flange area exits in the tension flange only. When open holes of 14%-37% to the gross flange area occurred in both flanges the $M_p / M_{dp}$ ratio values ranged between 1.03 and 1.32. For fastener holes of 15%-38% to the gross flange area existed in both flanges, the $M_p / M_{dp}$ ratio values spanned from 1.0 to 1.13. The ninth column of Table 5.12 presents the $M_m / M_{dp}$ ratio values for the beam specimens considered. For open holes of 9%-48% to the gross flange area occurred in the tension flanges only, the $M_m / M_{dp}$ ratios ranged between 1.21 and 1.25 with an average margin of 1.23. However, when open holes of 14%-37% to the gross flange area existed in both flanges, the $M_m / M_{dp}$ ratios varied from 1.22 to 1.43 with an average margin of 1.33. The $M_m / M_{dp}$ ratio values for the beam specimens having open holes in the tension flange only and similar specimens with fastener holes in both flanges were closer to each other (see ninth column of Table 5.12). Therefore, calculation of design moments for flexural members having flange holes as per the proposed method had a substantial margin of safety (more than 20%) with respect to the maximum measured moment for all cases considered.

A comparative analysis between the design moment calculations as per the existing code methods and the proposed method is summarized in Table 5.13. The proposed method allowed a higher moment than the code methods considered. This revealed that the current code provisions, particularly the 15% rule used in the current CAN/CSA-S16.01 standard (CSA 2003), are unnecessarily conservative as compared to the proposed method developed based the experimental results in this study. Dexter and Altstadt (2003) also indicated that the 15% exemption rule and the other currently existing specifications are conservative. However, such conclusion may be valid for steel grades having $F_y / F_u$ <0.85.

Figure 5.37 shows the variation of normalized design moment, $M_d / M_p$, with increasing holes to the gross-flange area, $\rho_h$, in the tension flange only. As seen in Figure 5.37, the design moments in accordance with the proposed method and the AISC-LRFD (2005) code method were identical for holes upto 23% of the gross flange area ($A_{fn}F_u / A_{fg}F_y \geq 1.0$). However, beyond 23% ($A_{fn}F_u / A_{fg}F_y < 1.0$), the moment as per the proposed method allowed relatively higher value over all five different code based design moment under consideration. Figure 5.38 shows the variation of normalized design moment, $M_d / M_p$, with increasing holes to the gross-flange area, $\rho_h$, in both the tension and compression flanges. As seen in the figure, the proposed method was in close agreement with the AISC-LRFD (2005) code method. Moreover, the proposed method allowed slightly higher moment than the AS4100 (SA 1998) code method. Figure 5.39 illustrates the variation normalized design moment, $M_d / M_p$, with increasing fastener holes of the gross-flange area, $\rho_h$, in both the tension and compression flanges. In this case, the design moments in accordance with the proposed method and the AISC-LRFD (2005) code method were identical for holes less than 23% of the gross flange area ($A_{fn}F_u / A_{fg}F_y \geq 1.0$). However, beyond 23% ($A_{fn}F_u / A_{fg}F_y < 1.0$), the proposed method allowed slightly higher moment than the CSA (2003) code method and the BS5950 (BSI 2001) code method. In all cases under consideration, the AISC-LRFD (1999) code provision was excessively conservative. Overall, the prediction of design moment based on the proposed method for all three different cases under consideration was equal or grater than the code based design moments.

## 5.8 Summary

Based on the experimental results, the beam specimen having open holes of approximately 30% of the gross flange area in the tension flange only had a flexural strength of more than 95% of the solid beam (i.e., strength reduction was less than 5%). This was also true when the beam specimens had fastener holes in both flanges. However, when open holes occurred in both flanges, the strength reduction associated with beam specimens A85-B-1 and A75-B-1 were of 1.8% and 6.5%. Therefore, open holes of upto 20% to the gross flange area may be provided in both flanges to obtain a flexural strength of more than 95% of the solid beam. Moreover, the test results revealed that the 15% exemption rule as per the current CAN/CSA-S16.01 (CSA 2003) standard was more restrictive for steel grades having $F_y / F_u \leq 0.8$, such as used in this test program ($F_y / F_u = 0.77$). The experimental results were closely correlated with the current AISC-LRFD (2005) in establishing a threshold value based on the ratio between $A_{fn}F_u$ and $A_{fg}F_y$. A design method was proposed on the basis of experimental results obtained in this study. The proposed method was compared with various code methods as considered in Chapter 3.

Overall, the design moments calculated based on the proposed method allowed slightly higher design moments than the various code based estimations. The proposed method was analogous to the tension member provision as per the Clause 13.2 of the current

CAN/CSA-S16.01 specification (CSA 2003). The proposed method circumvented an unnecessary ambiguity regarding the type of hole (whether it is a plain hole or fastener hole) since it treats the effects flange holes in the same manner. In contrast, the clause 14.1 of the current CAN/CSA-S16.01 (CSA 2003) standard treats the effects of holes and fastener holes in a different manner, in which when holes occur in flanges the theoretical net-section calculation shall be adopted whereas, when fastener holes occurs, the 15% exemption rule shall be applied. Moreover, the proposed method, as opposed to the current CSA (2003) code provision, considered the mechanical characteristics of the steel grade in terms of yield-to-ultimate strength ratio values.

Table 5.1: Group of Beam Specimens Exhibiting Similar Failure Modes

| Description (1) | **Group A** (2) | **Group B** (3) | **Group C** (4) |
|---|---|---|---|
| Beam ID | A100-1,A100-2,A100-3,A100-4,A90-1,A85-1,A80-1,A85-B-1,A75-B-1 and A85-F-1 | A75-1,A75-2,A75-3,A70-1,A70-2,A70-3, and A75-F-1 | A60-1,A60-2,A60-3,A50-1,A70-B-1,A60-B-1, A70-F-1 and A60-F-1 |
| Observed Failure Mode | (LTB+LB)/LB | LB+TF | TF |
| Typical ( $M-\theta$ ) relation | As shown in Figure 4.8[A] | As shown in Figure 4.8[B] | As shown in Figure 4.8[C] |
| Number of specimens under each group | 10 | 7 | 8 |

Table 5.2: Summary Test Results Based on Load versus Midspan Deflection Relationship
[ $P_{p-nom}$ =286 kN and $\Delta_{p-nom}$ =7.5 mm]

| **Beam ID** (1) | **Associated Results** (2) | Point A | Point B | Point C | Point D | | Point E | Point F/G | **Failure Mode** (10) |
|---|---|---|---|---|---|---|---|---|---|
| | | $P_{pl} / P_{p-nom}$ (3) | $\Delta_y / \Delta_{p-nom}$ (4) | $\Delta_p^+ / \Delta_{p-nom}$ (5) | $P_m / P_{p-nom}$ (6) | $\Delta_m / \Delta_{p-nom}$ (7) | $\Delta_p^- / \Delta_{p-nom}$ (8) | $\Delta_f / \Delta_{p-nom}$ (9) | |
| **A100-1** | Figure 5.1[A] | 0.81 | 1.12 | 1.28 | 1.40 | 10.9 | N/A | N/A | L.T.B+L.B |
| **A100-2** | Figure 5.2[A] | 0.83 | 1.11 | 1.26 | 1.39 | 10.4 | 13.9 | | |
| **A100-3** | Figure 5.3[A] | 0.83 | 1.09 | 1.23 | 1.39 | 11.0 | 16.8 | | |
| **A100-4** | Figure 5.4[A] | 0.78 | 1.10 | 1.26 | 1.39 | 11.3 | 16.5 | | |
| **A90-1** | Figure 5.5[A] | 0.81 | 1.08 | 1.29 | 1.39 | 11.3 | 15.7 | N/A | L.T.B+L.B |
| **A85-1** | Figure 5.6[A] | 0.77 | 1.11 | 1.31 | 1.40 | 10.6 | 15.2 | | L.T.B+L.B |
| **A80-1** | Figure 5.7[A] | 0.79 | 1.11 | 1.35 | 1.38 | 10.0 | 14.6 | | L.B |
| **A75-1** | Figure 5.8[A] | 0.78 | 1.14 | 1.48 | 1.36 | 9.0 | N/A | 11.4 | L.B+T.F |
| **A75-2** | Figure 5.9[A] | 0.72 | 1.19 | 1.55 | 1.34 | 10.4 | N/A | 13.5 | |
| **A75-3** | Figure 5.10[A] | 0.79 | 1.15 | 1.51 | 1.36 | 10.0 | N/A | 13.4 | |
| **A70-1** | Figure 5.11[A] | 0.74 | 1.14 | 1.65 | 1.33 | 8.7 | N/A | 11.6 | L.B+T.F |
| **A70-2** | Figure 5.12[A] | 0.70 | 1.15 | 1.54 | 1.33 | 9.4 | N/A | 10.5 | |
| **A70-3** | Figure 5.13[A] | 0.70 | 1.14 | 1.60 | 1.31 | 8.5 | N/A | 11.0 | |
| **A60-1** | Figure 5.14[A] | 0.69 | 1.19 | 1.86 | 1.28 | 6.9 | N/A | 6.9 | T.F |
| **A60-2** | Figure 5.15[A] | 0.70 | 1.25 | 2.14 | 1.26 | 7.4 | N/A | 7.4 | |
| **A60-3** | Figure 5.16[A] | 0.71 | 1.20 | 1.77 | 1.27 | 6.7 | N/A | 6.7 | |
| **A50-1** | Figure 5.17[A] | 0.67 | 1.38 | 2.35 | 1.16 | 3.8 | N/A | 3.8 | T.F |
| **A85-B-1** | Figure 5.18[A] | 0.81 | 1.12 | 1.57 | 1.36 | 9.4 | 13.9 | N/A | L.T.B+L.B |
| **A75-B-1** | Figure 5.19[A] | 0.76 | 1.22 | 1.86 | 1.30 | 7.7 | 12.6 | N/A | L.B |
| **A70-B-1** | Figure 5.20[A] | 0.72 | 1.25 | 1.92 | 1.28 | 7.3 | N/A | 10.4 | L.B+T.F |
| **A60-B-1** | Figure 5.21[A] | 0.69 | 1.38 | 2.35 | 1.25 | 6.5 | N/A | 6.5 | T.F |
| **A85-F-1** | Figure 5.22[A] | 0.78 | 1.11 | 1.35 | 1.38 | 9.9 | 15.7 | N/A | L.T.B+L.B |
| **A75-F-1** | Figure 5.23[A] | 0.76 | 1.22 | 1.67 | 1.36 | 10.0 | N/A | 12.1 | L.B+T.F |
| **A70-F-1** | Figure 5.24[A] | 0.74 | 1.25 | 1.88 | 1.34 | 9.4 | N/A | 10.7 | L.B+T.F |
| **A60-F-1** | Figure 5.25[A] | 0.71 | 1.57 | 2.37 | 1.26 | 6.8 | N/A | 6.8 | T.F |

Table 5.3: Summary Test Results Based on Moment versus Rotation Relationship
[$M_{p-nom}$=154 kNm and $\theta_{p-nom}$ = 0.0071 rad]

| Beam ID (1) | Associated Results (2) | Point A $M_{pl} / M_{p-nom}$ (3) | Point B $\theta_y / \theta_{p-nom}$ (4) | Point C $\theta_p^+ / \theta_{p-nom}$ (5) | Point D $M_m / M_{p-nom}$ (6) | Point D $\theta_m / \theta_{p-nom}$ (7) | Point E $\theta_p^- / \theta_{p-nom}$ (8) | Point F/G $\theta_f / \theta_{p-nom}$ (9) |
|---|---|---|---|---|---|---|---|---|
| **A100-1** | Figure 5.1[B] | 0.81 | 1.01 | 1.30 | 1.40 | 13.3 | N/A | N/A |
| **A100-2** | Figure 5.2[B] | 0.83 | 0.98 | 1.10 | 1.39 | 14.0 | 18.8 | |
| **A100-3** | Figure 5.3[B] | 0.83 | 0.96 | 1.07 | 1.39 | 13.5 | 21.7 | |
| **A100-4** | Figure 5.4[B] | 0.78 | 0.94 | 1.12 | 1.39 | 13.0 | 22.7 | |
| **A90-1** | Figure 5.5[B] | 0.81 | 0.94 | 1.13 | 1.39 | 16.0 | 21.9 | N/A |
| **A85-1** | Figure 5.6[B] | 0.77 | 1.14 | 1.34 | 1.40 | 14.8 | 21.5 | |
| **A80-1** | Figure 5.7[B] | 0.79 | 1.11 | 1.38 | 1.38 | 13.2 | 20.0 | |
| **A75-1** | Figure 5.8[B] | 0.78 | 1.08 | 1.43 | 1.36 | 13.5 | N/A | 17.2 |
| **A75-2** | Figure 5.9[B] | 0.72 | 0.95 | 1.40 | 1.34 | 14.5 | N/A | 19.2 |
| **A75-3** | Figure 5.10[B] | 0.82 | 0.98 | 1.34 | 1.36 | 13.3 | N/A | 17.7 |
| **A70-1** | Figure 5.11[B] | 0.74 | 1.10 | 1.57 | 1.32 | 11.2 | N/A | 15.8 |
| **A70-2** | Figure 5.12[B] | 0.70 | 0.97 | 1.95 | 1.33 | 14.6 | N/A | 16.2 |
| **A70-3** | Figure 5.13[B] | 0.70 | 0.98 | 1.58 | 1.31 | 11.4 | N/A | 15.4 |
| **A60-1** | Figure 5.14[B] | 0.69 | 1.02 | 1.91 | 1.28 | 10.4 | N/A | 10.4 |
| **A60-2** | Figure 5.15[B] | 0.70 | 1.10 | 1.86 | 1.26 | 10.0 | N/A | 10.0 |
| **A60-3** | Figure 5.16[B] | 0.71 | 1.12 | 1.88 | 1.27 | 9.4 | N/A | 9.4 |
| **A50-1** | Figure 5.17[B] | 0.67 | 1.16 | 2.66 | 1.16 | 5.9 | N/A | 5.9 |
| **A85-B-1** | Figure 5.18[B] | 0.81 | 0.96 | 1.41 | 1.36 | 13.8 | 20.0 | N/A |
| **A75-B-1** | Figure 5.19[B] | 0.76 | 1.21 | 2.02 | 1.30 | 11.0 | 18.2 | N/A |
| **A70-B-1** | Figure 5.20[B] | 0.72 | 1.23 | 2.46 | 1.28 | 10.1 | N/A | 15.4 |
| **A60-B-1** | Figure 5.21[B] | 0.69 | 1.57 | 3.27 | 1.25 | 10.3 | N/A | 10.3 |
| **A85-F-1** | Figure 5.22[B] | 0.78 | 0.98 | 1.20 | 1.38 | 13.4 | 21.0 | N/A |
| **A75-F-1** | Figure 5.23[B] | 0.76 | 1.06 | 1.61 | 1.36 | 13.0 | N/A | 16.4 |
| **A70-F-1** | Figure 5.24[B] | 0.74 | 1.13 | 2.12 | 1.34 | 13.2 | N/A | 15.6 |
| **A60-F-1** | Figure 5.25[B] | 0.71 | 1.64 | 3.52 | 1.26 | 9.5 | N/A | 9.5 |

Table 5.4: Summary Test Results Based on Moment versus End Rotation Relationship
[$M_{p-nom}$ =154 kNm and $\theta_{ep-nom}$ = 0.0172 rad]

| **Beam ID** | **Associated Results** | Point A | Point B | Point C | Point D | | Point E | Point F/G |
|---|---|---|---|---|---|---|---|---|
| | | $M_{pl} / M_{p-nom}$ | $\theta_y / \theta_{ep-nom}$ | $\theta_p^+ / \theta_{ep-nom}$ | $M_m / M_{p-nom}$ | $\theta_m / \theta_{ep-nom}$ | $\theta_p^- / \theta_{ep-nom}$ | $\theta_f / \theta_{ep-nom}$ |
| (1) | (2) | (3) | (4) | (5) | (6) | (7) | (8) | (9) |
| **A100-1** | Figure 5.1[C] | 0.81 | 1.04 | 1.27 | 1.40 | 9.6 | N/A | N/A |
| **A100-2** | Figure 5.2[C] | 0.83 | 1.02 | 1.19 | 1.39 | 8.9 | 11.8 | |
| **A100-3** | Figure 5.3[C] | 0.83 | 1.03 | 1.19 | 1.39 | 9.6 | 14.4 | |
| **A100-4** | Figure 5.4[C] | 0.78 | 1.03 | 1.21 | 1.39 | 10.5 | 15.3 | |
| **A90-1** | Figure 5.5[C] | 0.81 | 1.01 | 1.21 | 1.39 | 9.9 | 13.7 | N/A |
| **A85-1** | Figure 5.6[C] | 0.77 | 1.04 | 1.22 | 1.40 | 9.6 | 13.3 | |
| **A80-1** | Figure 5.7[C] | 0.79 | 1.07 | 1.21 | 1.38 | 8.7 | 12.2 | |
| **A75-1** | Figure 5.8[C] | 0.78 | 1.07 | 1.22 | 1.36 | 7.7 | N/A | 9.4 |
| **A75-2** | Figure 5.9[C] | 0.72 | 1.06 | 1.34 | 1.34 | 9.1 | N/A | 11.4 |
| **A75-3** | Figure 5.10[C] | 0.79 | 1.09 | 1.33 | 1.36 | 8.8 | N/A | 11.6 |
| **A70-1** | Figure 5.11[C] | 0.74 | 1.15 | 1.53 | 1.32 | 7.5 | N/A | 9.5 |
| **A70-2** | Figure 5.12[C] | 0.70 | 1.09 | 1.69 | 1.33 | 7.9 | N/A | 8.6 |
| **A70-3** | Figure 5.13[C] | 0.70 | 1.10 | 1.46 | 1.31 | 7.3 | N/A | 9.3 |
| **A60-1** | Figure 5.14[C] | 0.69 | 1.13 | 1.69 | 1.28 | 5.6 | N/A | 5.6 |
| **A60-2** | Figure 5.15[C] | 0.70 | 1.16 | 1.78 | 1.26 | 6.0 | N/A | 6.0 |
| **A60-3** | Figure 5.16[C] | 0.71 | 1.15 | 1.75 | 1.27 | 5.5 | N/A | 5.5 |
| **A50-1** | Figure 5.17[C] | 0.67 | 1.29 | 1.89 | 1.16 | 3.4 | N/A | 3.4 |
| **A85-B-1** | Figure 5.18[C] | 0.81 | 1.10 | 1.52 | 1.36 | 8.1 | 11.4 | N/A |
| **A75-B-1** | Figure 5.19[C] | 0.76 | 1.13 | 1.56 | 1.30 | 6.6 | 9.9 | N/A |
| **A70-B-1** | Figure 5.20[C] | 0.72 | 1.15 | 1.58 | 1.28 | 5.7 | N/A | 8.3 |
| **A60-B-1** | Figure 5.21[C] | 0.69 | 1.25 | 2.01 | 1.25 | 5.1 | N/A | 5.1 |
| **A85-F-1** | Figure 5.22[C] | 0.78 | 1.06 | 1.29 | 1.38 | 8.5 | 13.0 | N/A |
| **A75-F-1** | Figure 5.23[C] | 0.76 | 1.13 | 1.45 | 1.36 | 8.4 | N/A | 9.8 |
| **A70-F-1** | Figure 5.24[C] | 0.74 | 1.19 | 1.59 | 1.34 | 7.7 | N/A | 8.8 |
| **A60-F-1** | Figure 5.25[C] | 0.71 | 1.36 | 1.96 | 1.26 | 5.5 | N/A | 5.5 |

Table 5.5: Established Load Corresponding to the Initiation of Local Buckling

| Beam ID (1) | Associated Results (2) | Compression Flange Local Buckling Load (kN) (3) |
|---|---|---|
| **A100-1** | Figure 5.1[D] | 370 |
| **A100-2** | Figure 5.2[D] | 370 |
| **A100-3** | Figure 5.3[D] | 355 |
| **A100-4** | Figure 5.4[D] | 355 |
| **A90-1** | Figure 5.5[D] | 365 |
| **A85-1** | Figure 5.6[D] | 355 |
| **A80-1** | Figure 5.7[D] | 360 |
| **A75-1** | Figure 5.8[D] | 355 |
| **A75-2** | Figure 5.9[D] | 348 |
| **A75-3** | Figure 5.10[D] | 355 |
| **A70-1** | Figure 5.11[D] | 345 |
| **A70-2** | Figure 5.12[D] | 348 |
| **A70-3** | Figure 5.13[D] | 350 |
| **A60-1** | Figure 5.14[D] | 340 |
| **A60-2** | Figure 5.15[D] | 335 |
| **A60-3** | Figure 5.16[D] | 342 |
| **A50-1** | Figure 5.17[D] | 330 |
| **A85-B-1** | Figure 5.18[D] | 365 |
| **A75-B-1** | Figure 5.19[D] | 350 |
| **A70-B-1** | Figure 5.20[D] | 335 |
| **A60-B-1** | Figure 5.21[D] | 345 |
| **A85-F-1** | Figure 5.22[D] | 350 |
| **A75-F-1** | Figure 5.23[D] | 345 |
| **A70-F-1** | Figure 5.24[D] | 340 |
| **A60-F-1** | Figure 5.25[D] | 335 |

Table 5.6: Summary of Strain Values

| Location (1) | $\varepsilon$ at $M_y(=0.91M_p)$ (%) | | | | $\varepsilon$ at $M_p$ (%) | | | | $\varepsilon$ at $M_m$ (%) | | | |
|---|---|---|---|---|---|---|---|---|---|---|---|---|
| | **A100-4** (2) | **A75-3** (3) | **A70-2** (4) | **A75-B-1** (5) | **A100-4** (6) | **A75-3** (7) | **A70-2** (8) | **A75-B-1** (9) | **A100-4** (10) | **A75-3** (11) | **A70-2** (12) | **A75-B-1** (13) |
| **1** (Tension flange-closer to hole) | -- | +0.56 | +0.96 | +0.79 | -- | +2.02 | +2.25 | +3.00 | -- | N/A | N/A | N/A |
| **2** (Tension flange-middle) | +0.21 | N/A | +0.55 | +0.60 | +0.43 | N/A | +1.67 | +1.69 | +3.98 | N/A | N/A | N/A |
| **3** (Web-closer to tension flange) | +0.12 | +0.25 | +0.30 | +0.35 | +0.26 | +0.58 | +1.08 | +0.98 | +2.78 | N/A | N/A | N/A |
| **4** (Web-middle) | +0.00 | +0.02 | +0.04 | +0.02 | +0.03 | +0.05 | +0.05 | +0.04 | +0.54 | N/A | +1.05 | +0.47 |
| **5** (Web- closer to compression flange) | -0.19 | -0.11 | -0.11 | -0.24 | -0.23 | -0.22 | -0.48 | -0.97 | -1.73 | -1.82 | -1.88 | -2.53 |
| **6** (Compression flange-middle) | -0.20 | -0.21 | -0.23 | -0.45 | -0.41 | -0.51 | -0.78 | -1.38 | -3.33 | N/A | -3.84 | -3.31 |
| **7** (Compression flange-closer to hole) | -- | -- | -- | N/A | -- | -- | -- | N/A | -- | -- | -- | N/A |

Table 5.7: Comparison of Experimentally Obtained Stiffness with Calculated Stiffness Based on Measured Values

| Beam ID | $k_\Delta = P/\Delta$ (kN/mm) | | | $k_\theta = M/\theta$ (kNm) | | | $k_{\theta e} = M/\theta_e$ (kNm) | | |
|---|---|---|---|---|---|---|---|---|---|
| | Theory (Calculated) | Test | Test/Theory | Theory (Calculated) | Test | Test/Theory | Theory (Calculated) | Test | Test/Theory |
| (1) | (2) | (3) | (4) | (5) | (6) | (7) | (8) | (9) | (10) |
| **A100-1** | 17.10 | 16.29 | 0.95 | 22704 | 24824 | 1.09 | 9321 | 9113 | 0.98 |
| **A100-2** | 17.06 | 15.67 | 0.92 | 22704 | 25742 | 1.13 | 9335 | 9505 | 1.02 |
| **A100-3** | 17.09 | 16.38 | 0.96 | 22704 | 24150 | 1.06 | 9350 | 9185 | 0.98 |
| **A100-4** | 16.93 | 16.96 | 1.00 | 22589 | 24528 | 1.09 | 9325 | 9208 | 0.99 |
| **A90-1** | 17.18 | 15.97 | 0.93 | 22819 | 25874 | 1.13 | 9383 | 8884 | 0.95 |
| **A85-1** | 17.04 | 15.16 | 0.89 | 22647 | 26800 | 1.18 | 9312 | 8840 | 0.95 |
| **A80-1** | 16.90 | 15.67 | 0.93 | 22417 | 25475 | 1.14 | 9206 | 9305 | 1.01 |
| **A75-1** | 16.81 | 16.05 | 0.95 | 22360 | 25426 | 1.14 | 9199 | 9020 | 0.98 |
| **A75-2** | 17.04 | 16.79 | 0.99 | 22589 | 23400 | 1.04 | 9257 | 8840 | 0.95 |
| **A75-3** | 17.00 | 16.29 | 0.96 | 22647 | 24332 | 1.07 | 9312 | 9877 | 1.06 |
| **A70-1** | 17.24 | 15.30 | 0.89 | 22819 | 25097 | 1.10 | 9349 | 9822 | 1.05 |
| **A70-2** | 17.04 | 15.16 | 0.89 | 22704 | 23838 | 1.05 | 9367 | 9404 | 1.00 |
| **A70-3** | 17.10 | 15.67 | 0.92 | 22647 | 25176 | 1.11 | 9279 | 9877 | 1.06 |
| **A60-1** | 17.18 | 15.45 | 0.90 | 22761 | 23449 | 1.03 | 9357 | 10161 | 1.09 |
| **A60-2** | 16.88 | 16.05 | 0.95 | 22475 | 26012 | 1.16 | 9260 | 9354 | 1.01 |
| **A60-3** | 17.03 | 15.67 | 0.92 | 22589 | 25797 | 1.14 | 9272 | 8884 | 0.96 |
| **A50-1** | 16.77 | 16.62 | 0.99 | 22245 | 24220 | 1.09 | 9137 | 9933 | 1.09 |
| **A85-B-1** | 17.19 | 15.82 | 0.92 | 22876 | 23896 | 1.04 | 9401 | 9877 | 1.05 |
| **A75-B-1** | 17.06 | 16.37 | 0.96 | 22704 | 26080 | 1.15 | 9335 | 9161 | 0.98 |
| **A70-B-1** | 17.06 | 15.52 | 0.91 | 22647 | 22999 | 1.02 | 9312 | 9020 | 0.97 |
| **A60-B-1** | 17.43 | 15.09 | 0.87 | 23105 | 25600 | 1.11 | 9493 | 9305 | 0.98 |
| **A85-F-1** | 16.97 | 15.67 | 0.92 | 22589 | 23740 | 1.07 | 9305 | 9404 | 1.01 |
| **A75-F-1** | 16.79 | 17.23 | 1.03 | 22360 | 24091 | 1.04 | 9199 | 9822 | 1.07 |
| **A70-F-1** | 17.18 | 15.45 | 0.90 | 22876 | 23284 | 1.02 | 9421 | 8840 | 0.94 |
| **A60-F-1** | 17.00 | 16.45 | 0.97 | 22532 | 25800 | 1.15 | 9250 | 9208 | 1.00 |

Table 5.8: Comparison of Test Results Based on Strength

| Beam ID (1) | $\left[\frac{A_{fn}}{A_{fg}}\right]$ (%) (2) | $\left[\frac{A_{fn}F_u}{A_{fg}F_y}\right]$ (3) | $M_m$ (Test) (kNm) (4) | | % Reduction Relative to $M_m$ of solid section (5) |
|---|---|---|---|---|---|
| **A100-1** | 100 | **1.30** | 215 | 214 (average) | 0.0 |
| **A100-2** | 100 | **1.30** | 214 | | |
| **A100-3** | 100 | **1.30** | 214 | | |
| **A100-4** | 100 | **1.30** | 214 | | |
| **A90-1** | 91 | **1.18** | 214 | 214 | 0.0 |
| **A85-1** | 85 | **1.10** | 215 | 215 | +0.5 |
| **A80-1** | 79 | **1.03** | 212 | 212 | -0.9 |
| **A75-1** | 74 | 0.96 | 210 | 209 (average) | -2.3 |
| **A75-2** | 74 | 0.96 | 206 | | |
| **A75-3** | 74 | 0.96 | 210 | | |
| **A70-1** | 71 | 0.92 | 204 | 204 (average) | -4.7 |
| **A70-2** | 71 | 0.92 | 205 | | |
| **A70-3** | 70 | 0.91 | 202 | | |
| **A60-1** | 62 | 0.81 | 197 | 195 (average) | -8.9 |
| **A60-2** | 62 | 0.81 | 194 | | |
| **A60-3** | 63 | 0.82 | 195 | | |
| **A50-1** | 52 | 0.67 | 178 | 178 | -16.8 |
| **A85-B-1** | 86 | **1.17** | 210 | 210 | -1.8 |
| **A75-B-1** | 74 | 0.96 | 200 | 200 | -6.5 |
| **A70-B-1** | 70 | 0.91 | 197 | 197 | -7.9 |
| **A60-B-1** | 63 | 0.82 | 192 | 192 | -10.3 |
| **A85-F-1** | 85 | **1.10** | 212 | 212 | -0.9 |
| **A75-F-1** | 74 | 0.96 | 210 | 210 | -1.9 |
| **A70-F-1** | 70 | 0.91 | 207 | 207 | -3.3 |
| **A60-F-1** | 62 | 0.81 | 194 | 194 | -9.3 |

Table 5.9: Experimentally Established Rotation Capacity

| Beam ID | $\left[\frac{A_{fn}}{A_{fg}}\right]$ (%) | $\left[\frac{A_{fn}F_u}{A_{fg}F_y}\right]$ | Rotation Capacity | | | | | |
|---|---|---|---|---|---|---|---|---|
| | | | $R_y$ | | % Reduction Relative to $R_y$ of Solid Beam | $R_m$ | | % Reduction Relative to $R_m$ of Solid Beam |
| (1) | (2) | (3) | (4) | | (5) | (6) | | (7) |
| **A100-1** | 100 | **1.30** | N/A | 21.1 (average) | 0.0 | 12.2 | 12.3 (average) | 0.0 |
| **A100-2** | 100 | **1.30** | 17.6 | | | 12.8 | | |
| **A100-3** | 100 | **1.30** | 20.6 | | | 12.4 | | |
| **A100-4** | 100 | **1.30** | 21.6 | | | 11.8 | | |
| **A90-1** | 91 | **1.18** | 20.8 | 20.8 | -1.4 | 14.8 | 14.8 | +20.3 |
| **A85-1** | 85 | **1.10** | 20.4 | 20.4 | -3.3 | 13.6 | 13.6 | +10.6 |
| **A80-1** | 79 | **1.03** | 18.8 | 18.8 | -10.9 | 12.1 | 12.1 | -1.6 |
| **A75-1** | 74 | 0.96 | 16.1 | 16.9 ( average) | -19.9 | 12.4 | 12.7 (average) | +3.2 |
| **A75-2** | 74 | 0.96 | 18.0 | | | 13.4 | | |
| **A75-3** | 74 | 0.96 | 16.5 | | | 12.2 | | |
| **A70-1** | 71 | 0.92 | 14.6 | 14.6 ( average) | -30.8 | 10.0 | 11.2 (average) | -8.9 |
| **A70-2** | 71 | 0.92 | 15.0 | | | 13.4 | | |
| **A70-3** | 70 | 0.91 | 14.2 | | | 10.2 | | |
| **A60-1** | 62 | 0.81 | 9.2 | 8.7 ( average) | -58.8 | 9.2 | 8.7 (average) | -29.3 |
| **A60-2** | 62 | 0.81 | 8.8 | | | 8.8 | | |
| **A60-3** | 63 | 0.82 | 8.2 | | | 8.2 | | |
| **A50-1** | 52 | 0.67 | 4.8 | 4.8 | -77.2 | 4.8 | 4.8 | -61.0 |
| **A85-B-1** | 86 | **1.17** | 18.8 | 18.8 | -10.9 | 12.6 | 12.6 | +2.4 |
| **A75-B-1** | 74 | 0.96 | 17.0 | 17.0 | -19.4 | 9.8 | 9.8 | -20.3 |
| **A70-B-1** | 70 | 0.91 | 14.2 | 14.2 | -32.7 | 9.0 | 9.0 | -26.8 |
| **A60-B-1** | 63 | 0.82 | 9.2 | 9.2 | -56.4 | 9.2 | 9.2 | -25.2 |
| **A85-F-1** | 85 | **1.10** | 19.8 | 19.8 | -6.2 | 12.2 | 12.2 | -0.8 |
| **A75-F-1** | 74 | 0.96 | 15.2 | 15.2 | -28.0 | 11.8 | 11.8 | -4.1 |
| **A70-F-1** | 70 | 0.91 | 14.4 | 14.4 | -31.8 | 12.0 | 12.0 | -2.4 |
| **A60-F-1** | 62 | 0.81 | 8.4 | 8.4 | -60.2 | 8.4 | 8.4 | -31.7 |

Table 5.10: Comparison of Maximum Moment and Net-Section Fracture Moment [ $M_p$ =177 kNm]

| **Beam ID** | $\left[\frac{A_{fn}}{A_{fg}}\right]$ **(%)** | $\left[\frac{A_{fn}F_u}{A_{fg}F_y}\right]$ | $M_m$ **(Test) (kNm)** | $M_{fn}$ $(Z_n F_u)$ **(Theory) (kNm)** | $\left[\frac{M_m}{M_p}\right]$ | $\left[\frac{M_m}{M_{fn}}\right]$ | $\left[\frac{M_p}{M_{fn}}\right]$ | **Observed dominant failure mode** |
|---|---|---|---|---|---|---|---|---|
| (1) | (2) | (3) | (4) | (5) | (6) | (7) | (8) | (9) |
| **A90-1** | 91 | **1.18** | 214 | 221 | 1.21 | 0.97 | **0.80** | **L.T.B+L.B** |
| **A85-1** | 85 | **1.10** | 215 | 214 | 1.22 | 1.01 | **0.83** | **L.T.B+L.B** |
| **A80-1** | 79 | **1.03** | 212 | 207 | 1.20 | 1.02 | **0.85** | **L.B** |
| **A75-1** | 74 | 0.96 | 210 | 200 | 1.19 | 1.05 | 0.88 | |
| **A75-2** | 74 | 0.96 | 206 | 200 | 1.17 | 1.03 | 0.88 | L.B+T.F |
| **A75-3** | 74 | 0.96 | 210 | 199 | 1.19 | 1.06 | 0.89 | |
| **A70-1** | 71 | 0.92 | 204 | 198 | 1.15 | 1.03 | 0.89 | |
| **A70-2** | 71 | 0.92 | 205 | 198 | 1.16 | 1.04 | 0.89 | L.B+T.F |
| **A70-3** | 70 | 0.91 | 202 | 197 | 1.14 | 1.03 | 0.90 | |
| **A60-1** | 62 | 0.81 | 197 | 187 | 1.11 | 1.05 | 0.95 | |
| **A60-2** | 62 | 0.81 | 194 | 184 | 1.10 | 1.06 | 0.96 | T.F |
| **A60-3** | 63 | 0.82 | 195 | 183 | 1.10 | 1.07 | 0.97 | |
| **A50-1** | 52 | 0.67 | 178 | 163 | 1.01 | 1.09 | **1.08** | T.F |
| **A85-B-1** | 86 | **1.17** | 210 | 204 | 1.19 | 1.03 | 0.87 | **L.T.B+L.B** |
| **A75-B-1** | 74 | 0.96 | 200 | 180 | 1.13 | 1.11 | 0.98 | **L.B** |
| **A70-B-1** | 70 | 0.91 | 197 | 173 | 1.11 | 1.14 | **1.02** | T.F |
| **A60-B-1** | 63 | 0.82 | 192 | 161 | 1.09 | 1.19 | **1.10** | T.F |
| **A85-F-1** | 85 | **1.10** | 212 | 214 | 1.20 | 0.99 | **0.83** | **L.T.B+L.B** |
| **A75-F-1** | 74 | 0.96 | 210 | 198 | 1.19 | 1.06 | 0.89 | L.B+T.F |
| **A70-F-1** | 70 | 0.91 | 207 | 197 | 1.17 | 1.05 | 0.90 | T.F |
| **A60-F-1** | 62 | 0.81 | 194 | 184 | 1.10 | 1.06 | 0.96 | T.F |

Table 5.11: Comparison of Code Based Design Moment with Maximum Measured Moment

| Beam ID (1) | $\left[\frac{A_{fn}}{A_{fg}}\right]$ (%) (2) | $\left[\frac{A_{fn}F_u}{A_{fg}F_y}\right]$ (3) | $M_m$ (kNm) (4) | Design Moment (kNm) CSA (2003) (5) | AISC-LRFD (2005) (6) | AISC-LRFD (1999) (7) | BS5950 (BSI 2001) (8) | AS4100 (SA 1998) (9) |
|---|---|---|---|---|---|---|---|---|
| **A90-1** | 91 | **1.18** | 214 | 169 (-21%) | **177** (-17%) | 143(-33%) | 169 (-21%) | 171 (-20%) |
| **A85-1** | 85 | **1.10** | 215 | 164 (-24%) | **177** (-18%) | 133 (-38%) | 164 (-24%) | 167 (-22%) |
| **A80-1** | 79 | **1.03** | 212 | 159 (-25%) | **177** (-17%) | 124 (-42%) | 159 (-25%) | 163 (-23%) |
| **A75-1,2,3** | 74 | 0.96 | 209 | 154 (-26%) | 154 (-26%) | 117 (-44%) | 154 (-26%) | 160 (-23%) |
| **A70-1,2,3** | 71 | 0.92 | 204 | 152 (-25%) | 151 (-26%) | 113 (-45%) | 152 (-25%) | 158 (-23%) |
| **A60-1,2,3** | 62 | 0.81 | 195 | 141 (-28%) | 141 (-28%) | 102 (-48%) | 141 (-28%) | 152 (-22%) |
| **A50-1** | 52 | 0.67 | 178 | 130 (-27%) | 130 (-27%) | 89 (-50%) | 130 (-27%) | 146 (-18%) |
| **A85-B-1** | 86 | **1.17** | 210 | 156 (-26%) | **177** (-16%) | 142 (-32%) | 156 (-26%) | 159 (-24%) |
| **A75-B-1** | 74 | 0.96 | 200 | 138 (-31%) | 155 (-23%) | 125 (-38%) | 138 (-31%) | 144 (-28%) |
| **A70-B-1** | 70 | 0.91 | 197 | 132 (-33%) | 147 (-25%) | 119 (-40%) | 132 (-33%) | 138 (-30%) |
| **A60-B-1** | 63 | 0.82 | 192 | 122 (-36%) | 132 (-31%) | 110 (-43%) | 122 (-36%) | 129 (-33%) |
| **A85-F-1** | 85 | **1.10** | 212 | **177** (-17%) | **177** (-17%) | 147 (-31%) | 168 (-21%) | 158 (-25%) |
| **A75-F-1** | 74 | 0.96 | 210 | 160 (-24%) | 155 (-26%) | 129 (-39%) | 153 (-27%) | 144 (-31%) |
| **A70-F-1** | 70 | 0.91 | 207 | 154 (-26%) | 147 (-29%) | 126 (-39%) | 152 (-27%) | 138 (-33%) |
| **A60-F-1** | 62 | 0.81 | 194 | 143 (-26%) | 130 (-33%) | 112 (-42%) | 139 (-28%) | 128 (-34%) |

The values within the brackets (--) indicate the percentage reduction in design moment relative to the measured maximum moment

Table 5.12: Comparison of Proposed Design Moment with Plastic Moment [ $M_p$ =177 kNm] and Maximum Moment

| Beam ID | $\left[\frac{A_{fn}}{A_{fg}}\right]$ (%) | $\left[\frac{A_{fn}F_u}{A_{fg}F_y}\right]$ | $M_m$ (Test) (kNm) | $M_{fn}$ (Calculated) (kNm) | **Proposed Design Moment (kNm)** $M_{fnm}$ (=0.85 $M_{fn}$) (kNm) | $M_{dp}$ (kNm) | $\left[\frac{M_p}{M_{dp}}\right]$ | $\left[\frac{M_m}{M_{dp}}\right]$ |
|---|---|---|---|---|---|---|---|---|
| (1) | (2) | (3) | (4) | (5) | (6) | (7) | (8) | (9) |
| **A90-1** | 91 | **1.18** | 214 | 220 | **187>** $M_p$ | $M_{dp}=M_p$ **=177** | **1.00** | 1.21 |
| **A85-1** | 85 | **1.10** | 215 | 214 | **182>** $M_p$ | $M_{dp}=M_p$ **=177** | **1.00** | 1.22 |
| **A80-1** | 79 | **1.03** | 212 | 208 | **177=** $M_p$ | $M_{dp}=M_p$ **=177** | **1.00** | 1.20 |
| **A75-1,2,3** | 74 | 0.96 | 209 | 200 | 170< $M_p$ | $M_{dp}=M_{fnm}$ =170 | 1.04 | 1.23 |
| **A70-1,2,3** | 71 | 0.92 | 204 | 196 | 167< $M_p$ | $M_{dp}=M_{fnm}$ =167 | 1.06 | 1.22 |
| **A60-1,2,3** | 62 | 0.81 | 195 | 184 | 156< $M_p$ | $M_{dp}=M_{fnm}$ =156 | 1.13 | 1.25 |
| **A50-1** | 52 | 0.67 | 178 | 168 | 143< $M_p$ | $M_{dp}=M_{fnm}$ =143 | 1.24 | 1.24 |
| **A85-B-1** | 86 | **1.17** | 210 | 202 | 172< $M_p$ | $M_{dp}=M_{fnm}$ =172 | 1.03 | 1.22 |
| **A75-B-1** | 74 | 0.96 | 200 | 179 | 152< $M_p$ | $M_{dp}=M_{fnm}$ =152 | 1.16 | 1.32 |
| **A70-B-1** | 70 | 0.91 | 197 | 171 | 145< $M_p$ | $M_{dp}=M_{fnm}$ =145 | 1.22 | 1.36 |
| **A60-B-1** | 63 | 0.82 | 192 | 158 | 134< $M_p$ | $M_{dp}=M_{fnm}$ =134 | 1.32 | 1.43 |
| **A85-F-1** | 85 | **1.10** | 212 | 214 | **182>** $M_p$ | $M_{dp}=M_p$ **=177** | **1.00** | 1.20 |
| **A75-F-1** | 74 | 0.96 | 210 | 200 | 170< $M_p$ | $M_{dp}=M_{fnm}$ =170 | 1.04 | 1.24 |
| **A70-F-1** | 70 | 0.91 | 207 | 195 | 166< $M_p$ | $M_{dp}=M_{fnm}$ =166 | 1.07 | 1.25 |
| **A60-F-1** | 62 | 0.81 | 194 | 184 | 156< $M_p$ | $M_{dp}=M_{fnm}$ =156 | 1.13 | 1.24 |

Table 5.13: Comparison of Proposed Design Moment with Code Based Design Moment

| Type of Test (1) | Beam ID (2) | $\left[\frac{A_{fn}}{A_{fg}}\right]$ (%) (3) | $\left[\frac{A_{fn}F_u}{A_{fg}F_y}\right]$ (4) | $M_{dp}$ (kNm) (5) | % Reduction between Plastic Moment Capacity [$M_p$=177 kNm] and Code Based Design Moment: CSA (2003) (6) | AISC-LRFD (2005) (7) | AISC-LRFD (1999) (8) | BS5950 (BSI 2001) (9) | AS4100 (SA 1998) (10) | % Difference between Plastic Moment Capacity [$M_p$=177 kNm] and Proposed Design Moment (11) |
|---|---|---|---|---|---|---|---|---|---|---|
| **Case-2** *[Beam test with holes in tension flange only]* | **A90-1** | 91 | **1.18** | **177** | 04 | **00** | 19 | 04 | 03 | **00** |
| | **A85-1** | 85 | **1.10** | **177** | 07 | **00** | 25 | 07 | 06 | **00** |
| | **A80-1** | 79 | **1.03** | **177** | 10 | **00** | 30 | 10 | 08 | **00** |
| | **A75-1,2,3** | 74 | 0.96 | 170 | 13 | 13 | 34 | 13 | 10 | **04** |
| | **A70-1,2,3** | 71 | 0.92 | 167 | 14 | 14 | 36 | 14 | 11 | **06** |
| | **A60-1,2,3** | 62 | 0.81 | 156 | 20 | 20 | 42 | 20 | 14 | **13** |
| | **A50-1** | 52 | 0.67 | 143 | 26 | 26 | 50 | 26 | 17 | **24** |
| **Case-3** *[Beam test with holes in both tension and compression flanges]* | **A85-B-1** | 86 | **1.17** | 172 | 12 | **00** | 20 | 12 | 10 | **03** |
| | **A75-B-1** | 74 | 0.96 | 152 | 22 | 12 | 29 | 22 | 19 | **16** |
| | **A70-B-1** | 70 | 0.91 | 145 | 25 | 17 | 33 | 25 | 22 | **22** |
| | **A60-B-1** | 63 | 0.82 | 134 | 31 | 25 | 38 | 31 | 27 | **32** |
| **Case-4** *[Beam test with fastener holes in both tension and compression flanges]* | **A85-F-1** | 85 | **1.10** | **177** | **00** | **00** | 17 | 05 | 11 | **00** |
| | **A75-F-1** | 74 | 0.96 | 170 | 10 | 12 | 27 | 13 | 19 | **04** |
| | **A70-F-1** | 70 | 0.91 | 166 | 13 | 17 | 29 | 14 | 22 | **07** |
| | **A60-F-1** | 62 | 0.81 | 156 | 19 | 26 | 37 | 21 | 28 | **13** |

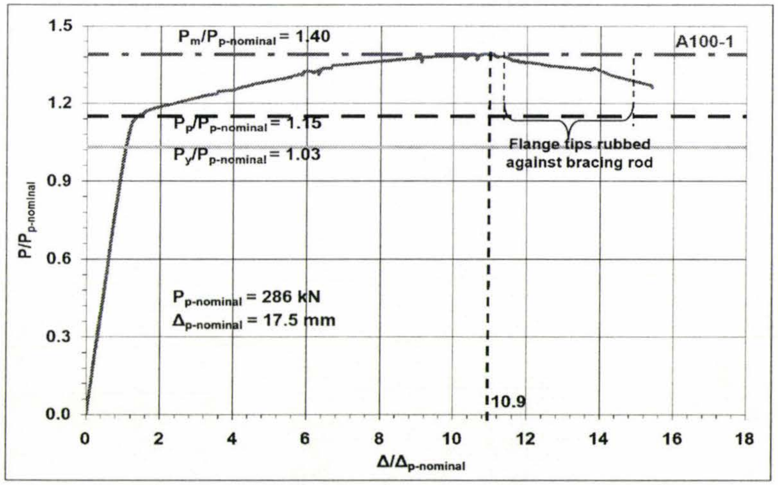


Figure 5.1[A]: Load versus Midspan Deflection for Beam A100-1

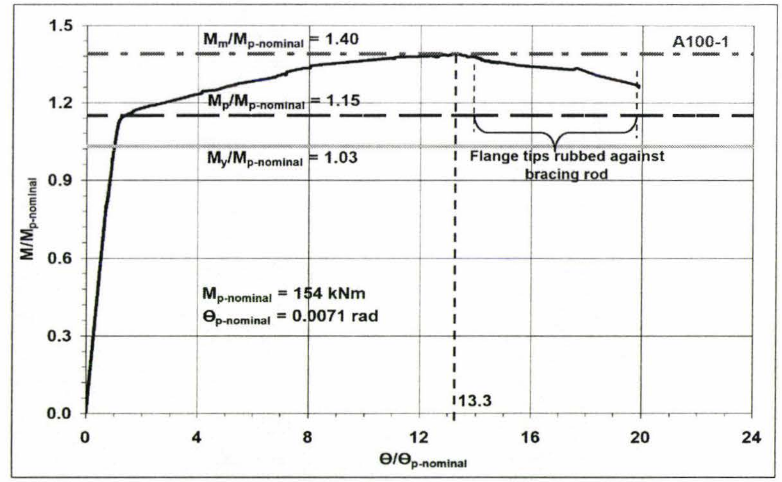


Figure 5.1[B]: Moment versus Rotation for Beam A100-1

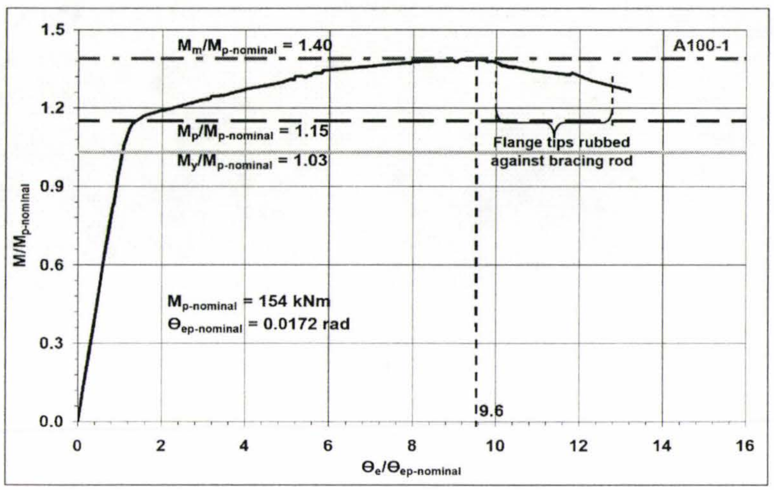


Figure 5.1[C]: Moment versus End Rotation for Beam A100-1

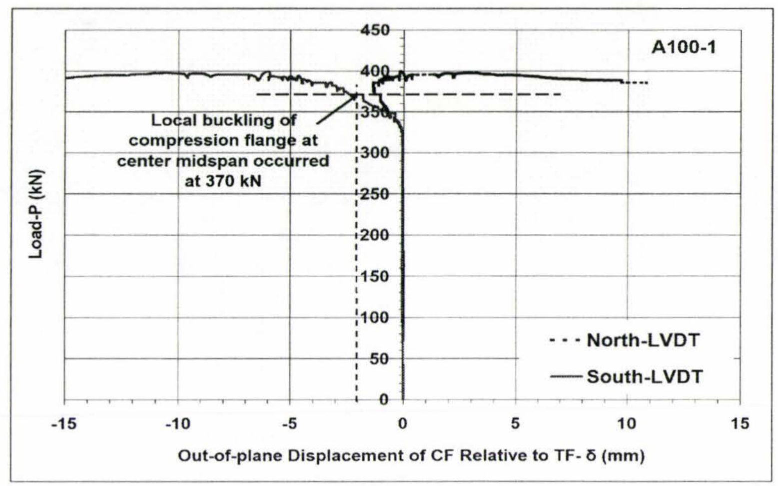


Figure 5.1[D]: Load versus Out-of-Plane Displacement of CF Relative to TF for Beam A100-1

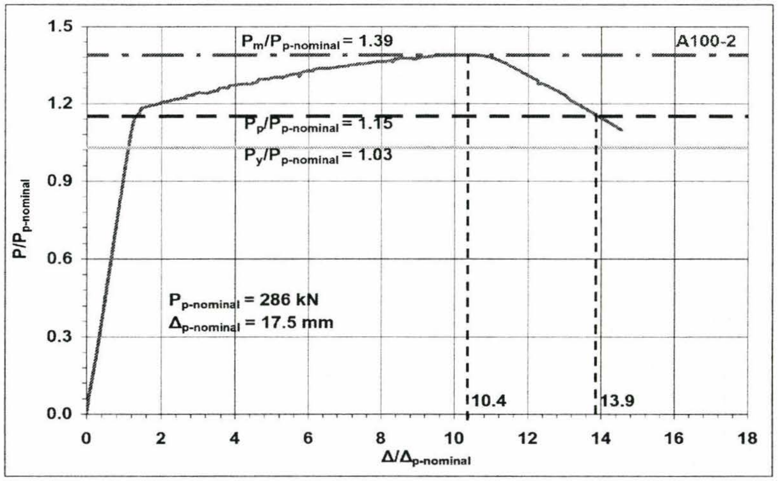


Figure 5.2[A]: Load versus Midspan Deflection for Beam A100-2

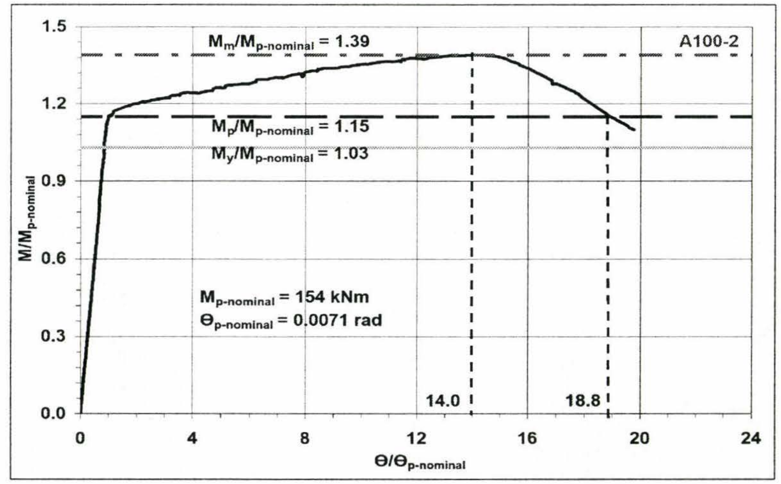


Figure 5.2[B]: Moment versus Rotation for Beam A100-2

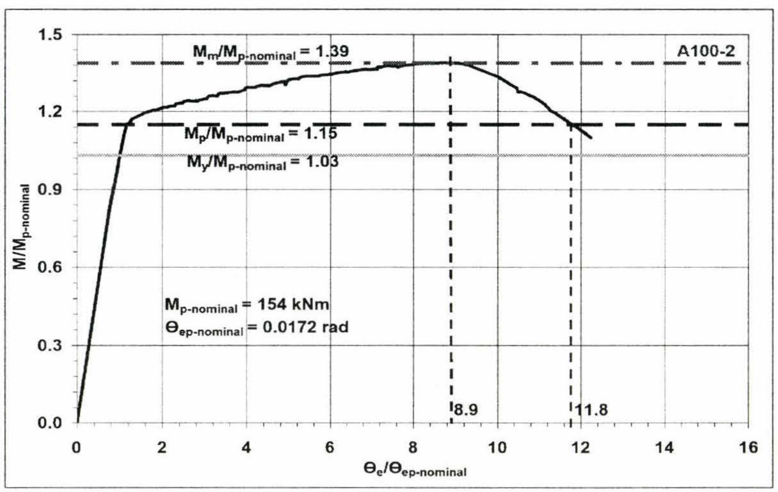


Figure 5.2[C]: Moment versus End Rotation for Beam A100-2

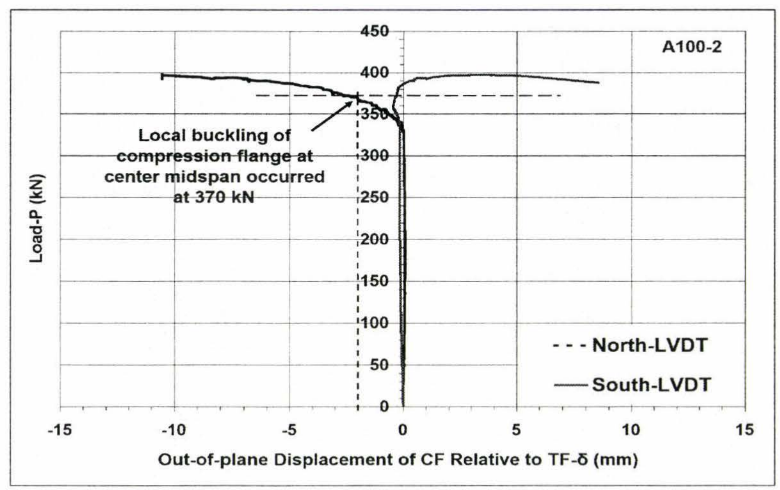


Figure 5.2[D]: Load versus Out-of-Plane Displacement of CF Relative to TF for Beam A100-2

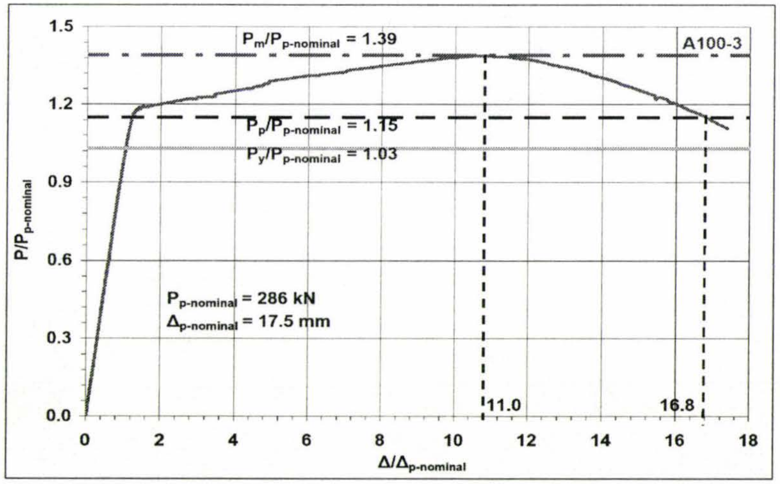


Figure 5.3[A]: Load versus Midspan Deflection for Beam A100-3

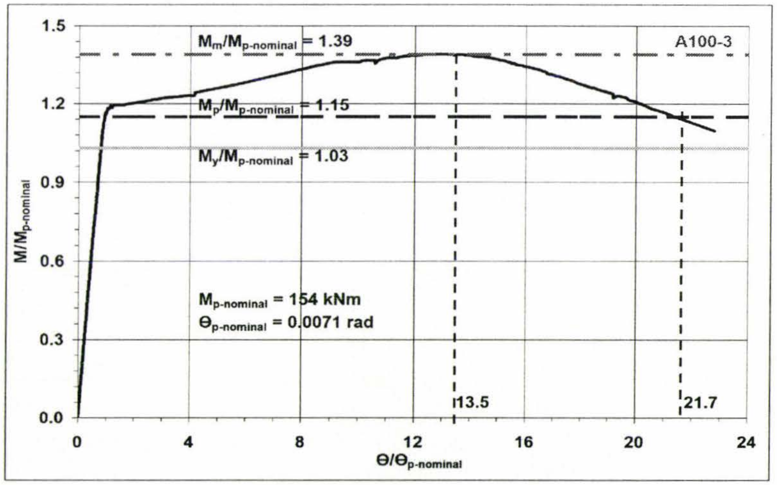


Figure 5.3[B]: Moment versus Rotation for Beam A100-3

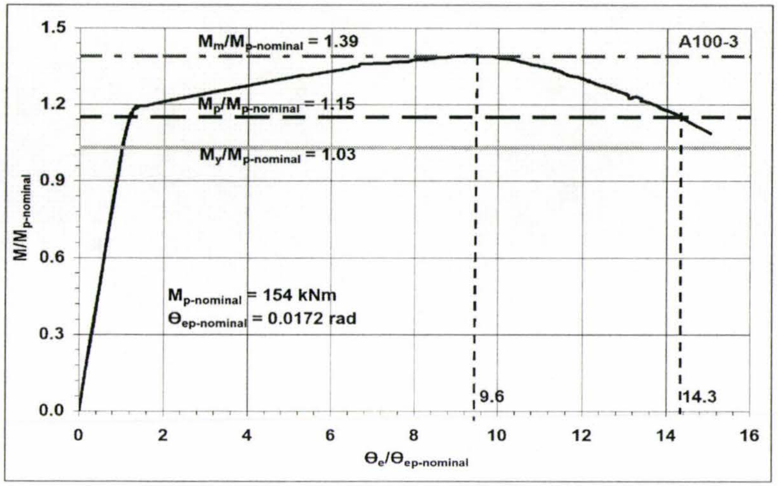


Figure 5.3[C]: Moment versus End Rotation for Beam A100-3

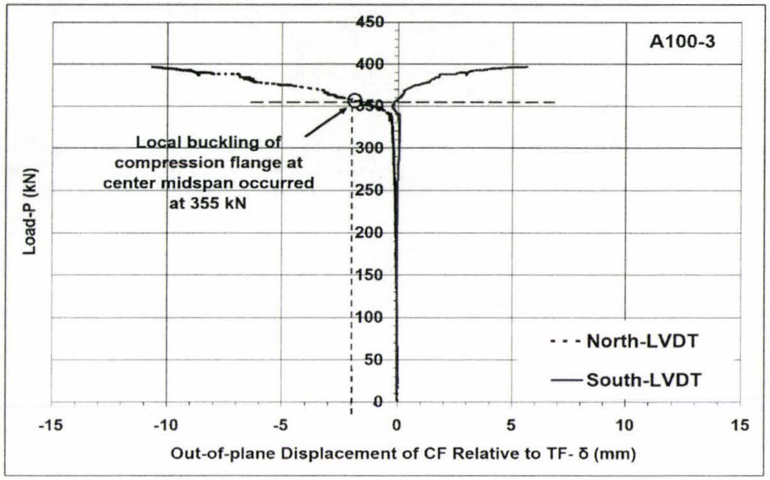


Figure 5.3[D]: Load versus Out-of-Plane Displacement of CF Relative to TF for Beam A100-3

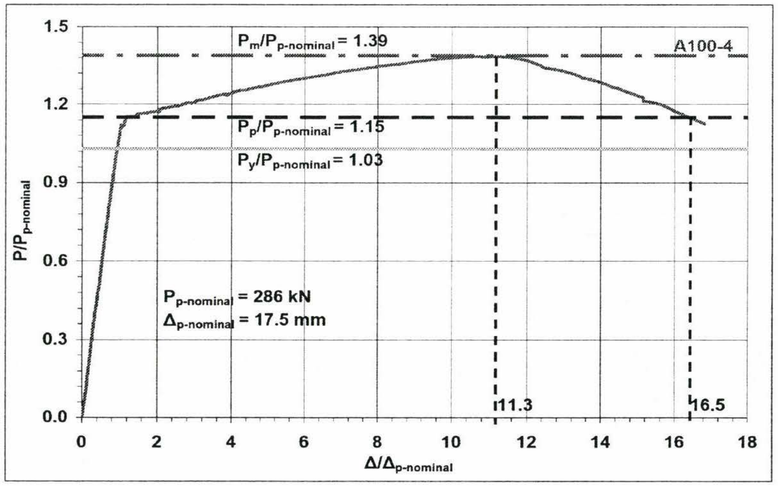


Figure 5.4[A]: Load versus Midspan Deflection for Beam A100-4

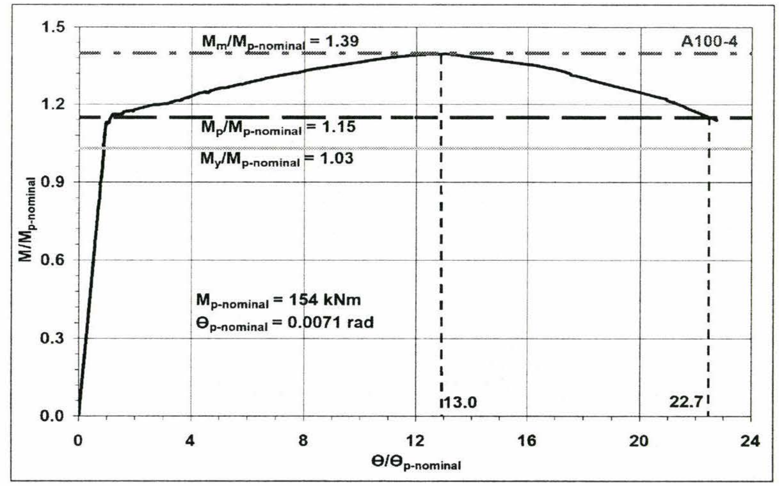


Figure 5.4[B]: Moment versus Rotation for Beam A100-4

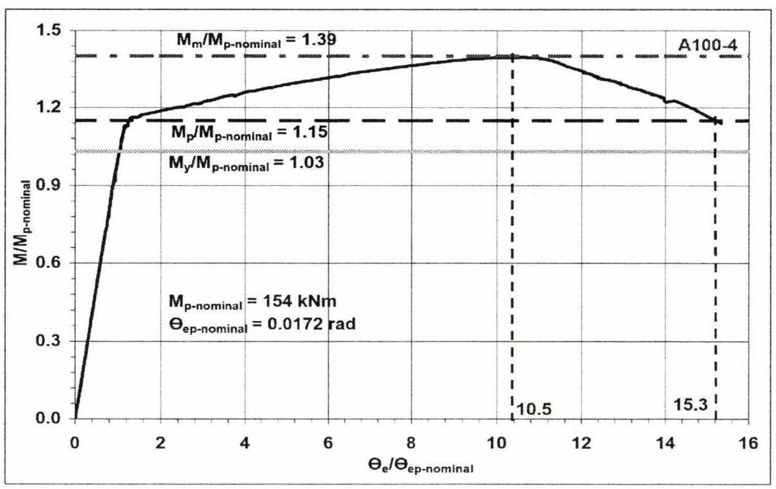


Figure 5.4[C]: Moment versus End Rotation for Beam A100-4

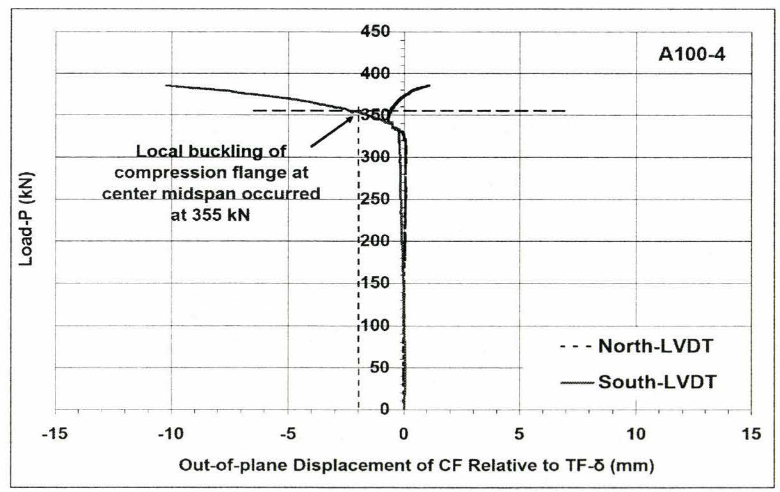


Figure 5.4[D]: Load versus Out-of-Plane Displacement of CF Relative to TF for Beam A100-4

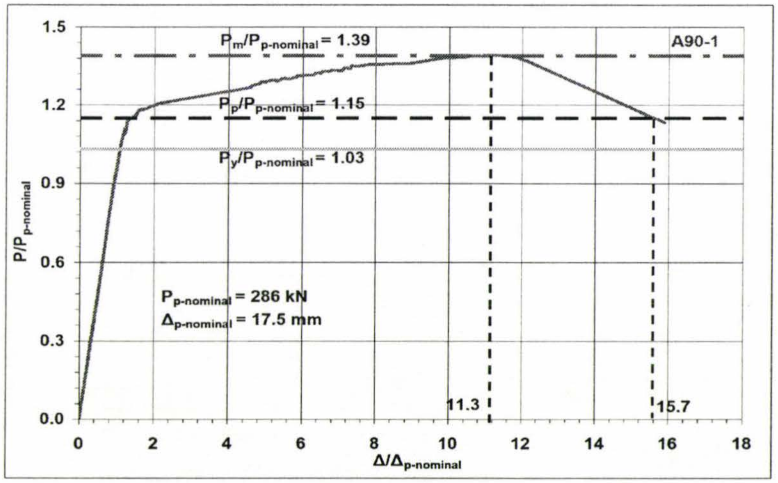


Figure 5.5[A]: Load versus Midspan Deflection for Beam A90-1

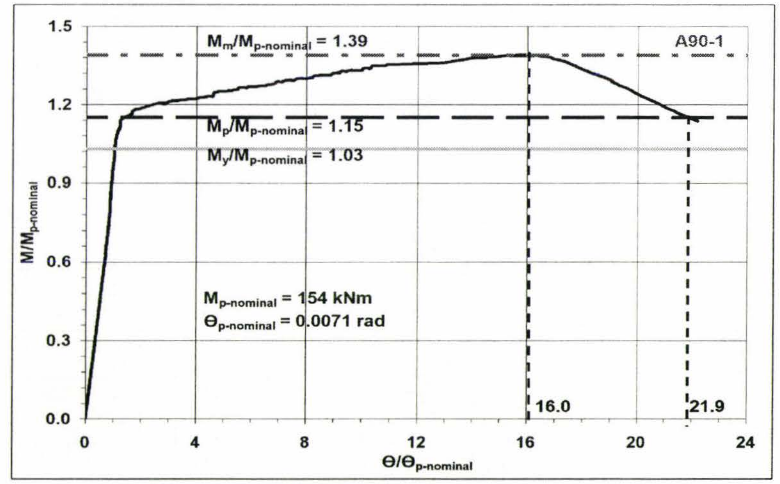


Figure 5.5 [B]: Moment versus Rotation for Beam A90-1

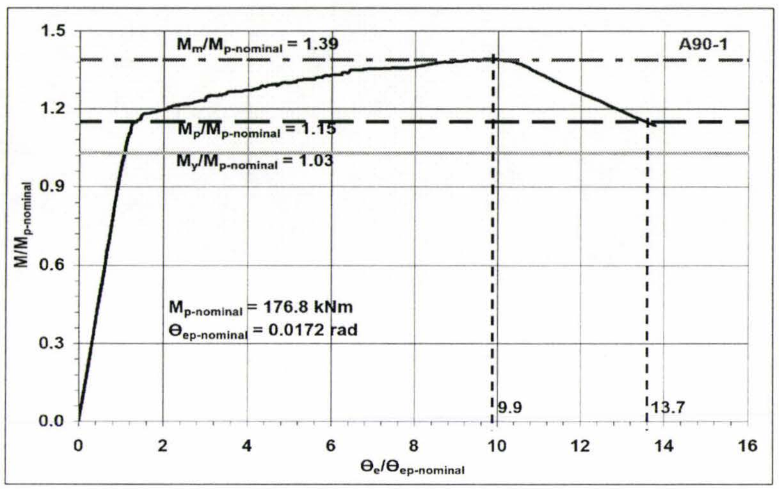


Figure 5.5[C]: Moment versus End Rotation for Beam A90-1

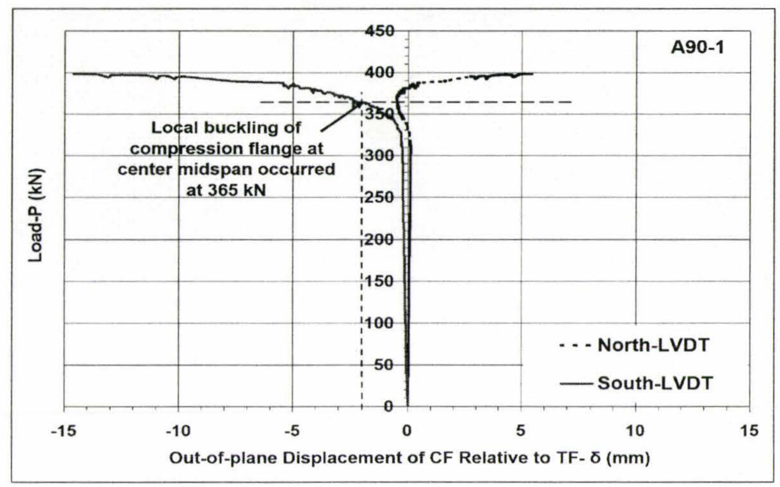


Figure 5.5[D]: Load versus Out-of-Plane Displacement of CF Relative to TF for Beam A90-1

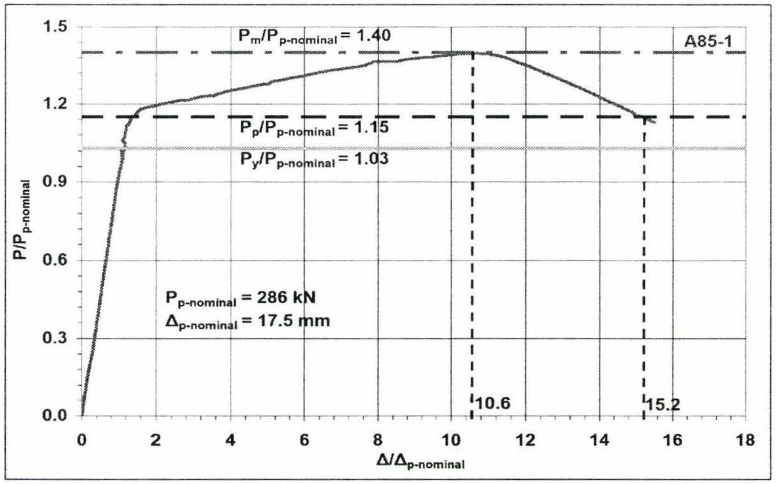


Figure 5.6[A]: Load versus Midspan Deflection for Beam A85-1

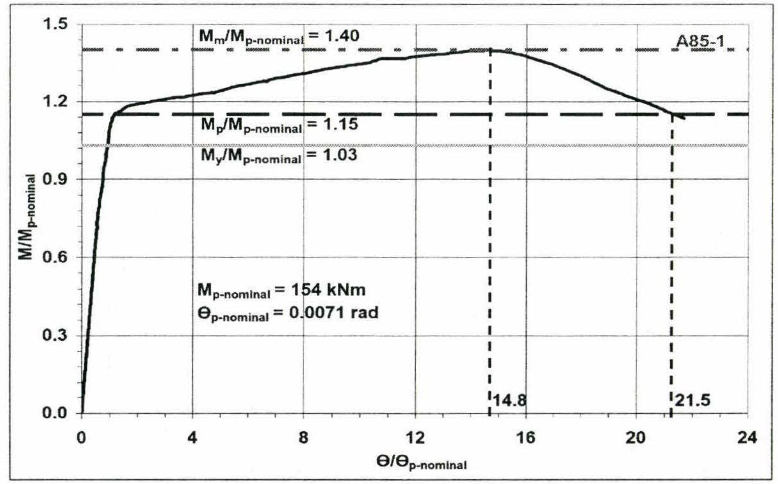


Figure 5.6[B]: Moment versus Rotation for Beam A85-1

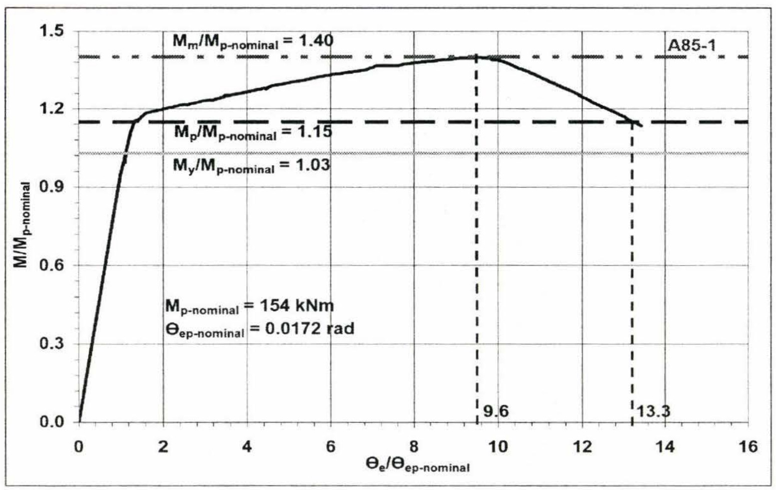


Figure 5.6[C]: Moment versus End Rotation for Beam A85-1

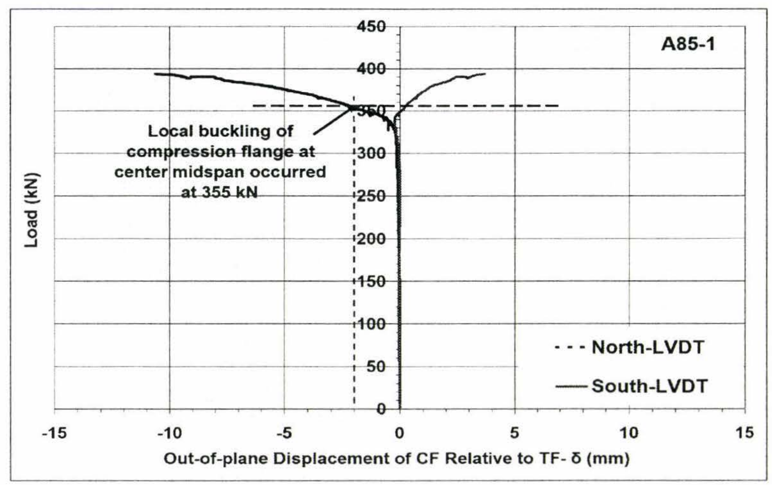


Figure 5.6[D]: Load versus Out-of-Plane Displacement of CF Relative to TF for Beam A85-1

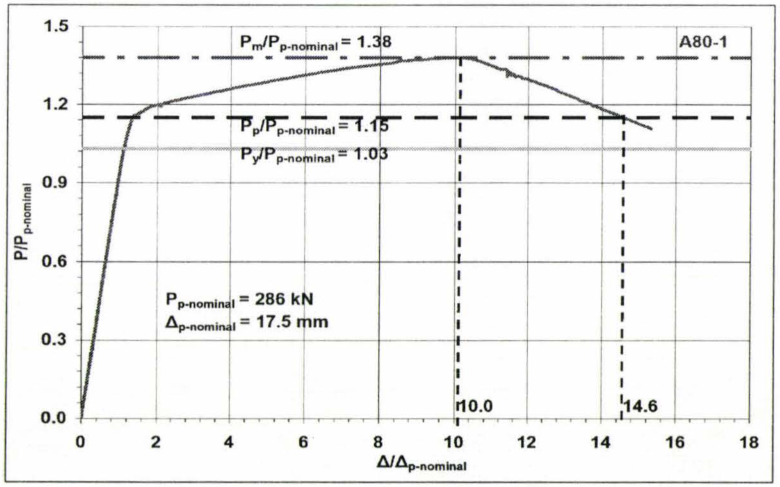


Figure 5.7[A]: Load versus Midspan Deflection
for Beam A80-1

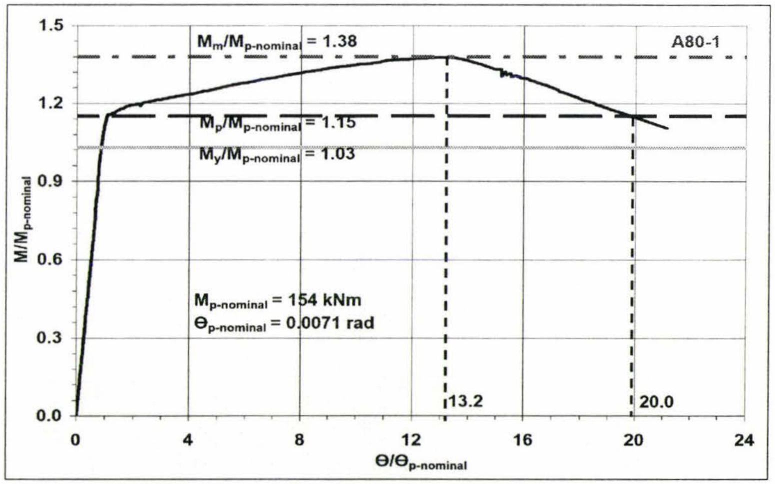


Figure 5.7[B]: Moment versus Rotation
for Beam A80-1

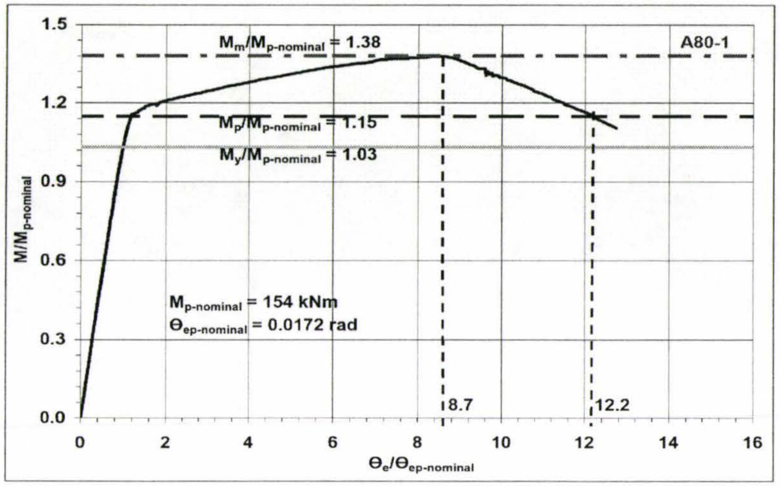


Figure 5.7[C]: Moment versus End Rotation
for Beam A80-1

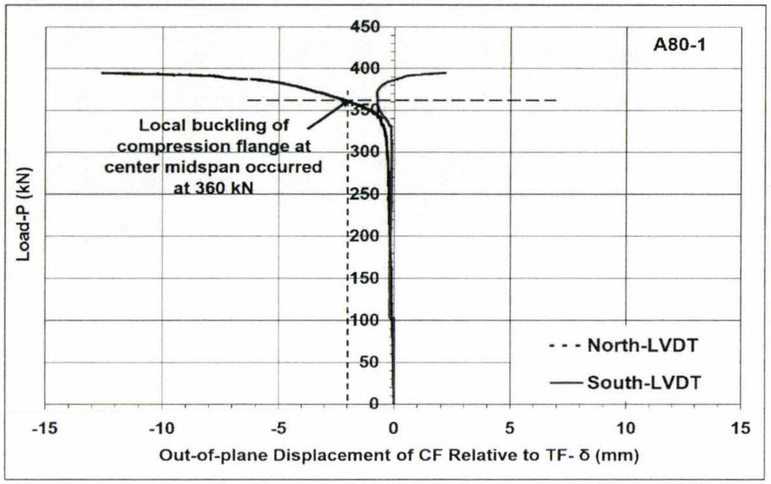


Figure 5.7[D]: Load versus Out-of-Plane Displacement
of CF Relative to TF for Beam A80-1

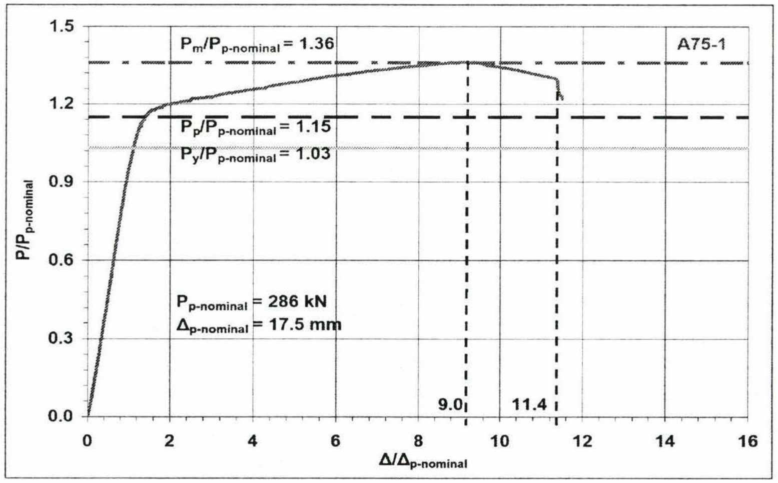


Figure 5.8[A]: Load versus Midspan Deflection for Beam A75-1

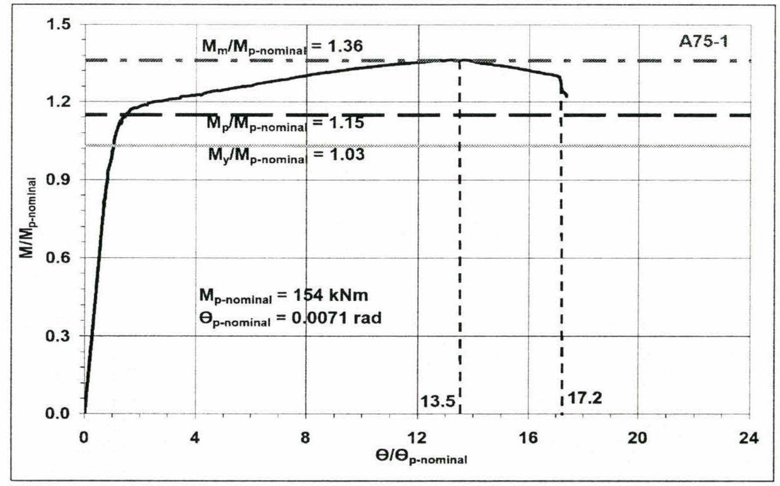


Figure 5.8[B]: Moment versus Rotation for Beam A75-1

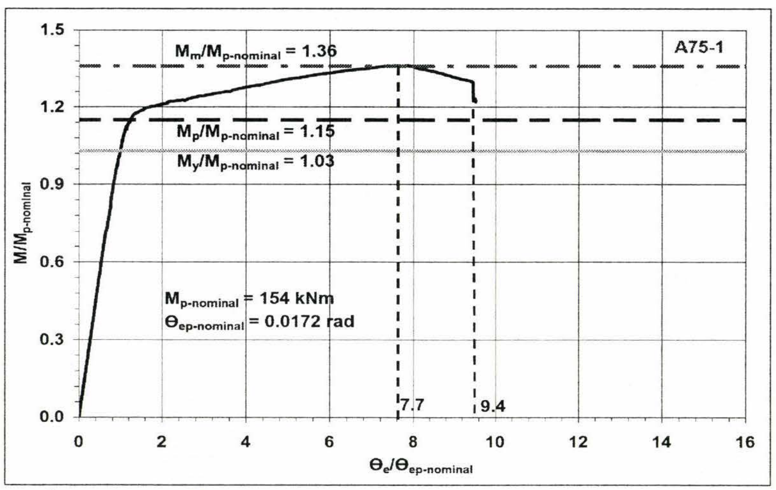


Figure 5.8[C]: Moment versus End Rotation for Beam A75-1

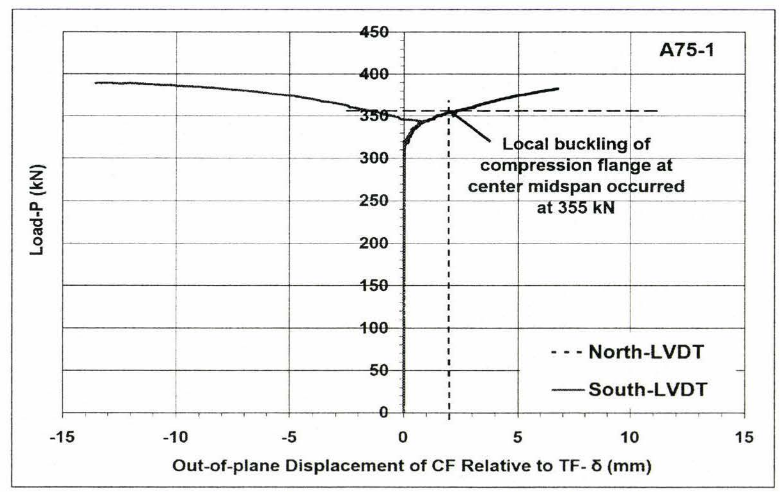


Figure 5.8[D]: Load versus Out-of-Plane Displacement of CF Relative to TF for Beam A75-1

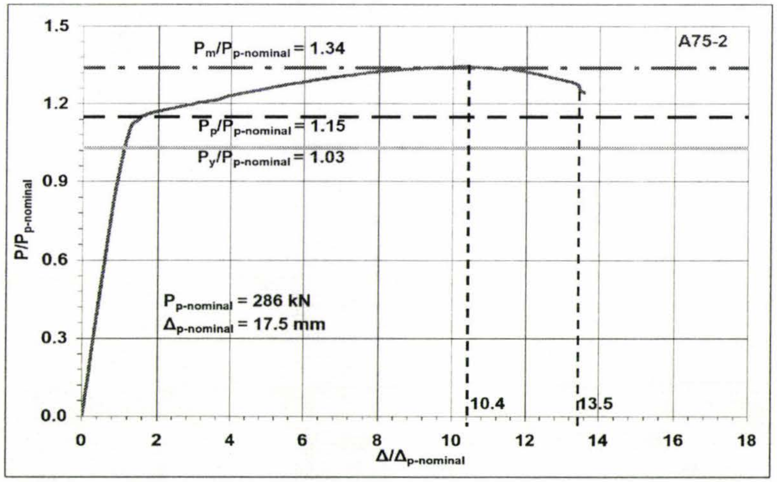


Figure 5.9[A]: Load versus Midspan Deflection for Beam A75-2

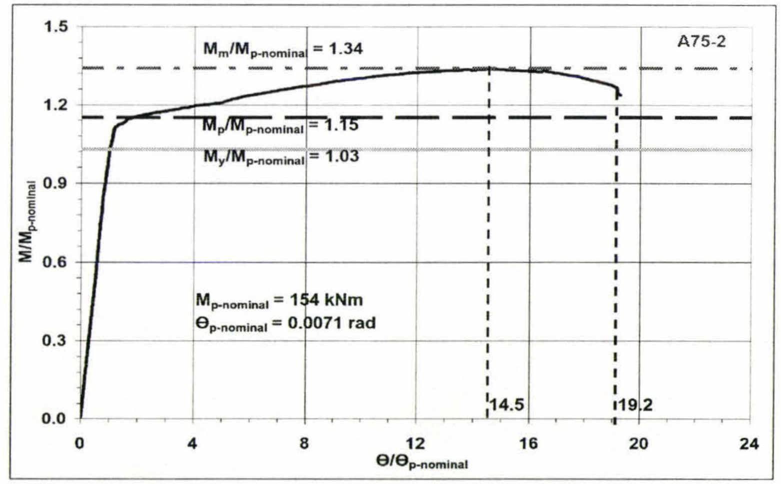


Figure 5.9[B]: Moment versus Rotation for Beam A75-2

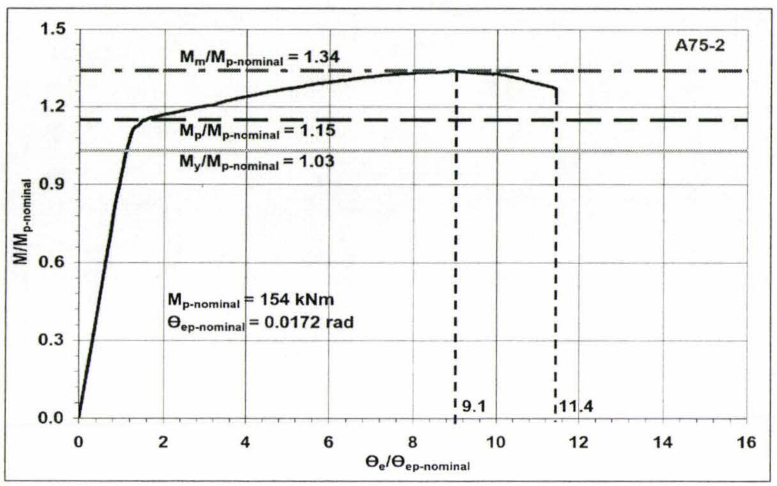


Figure 5.9[C]: Moment versus End Rotation for Beam A75-2

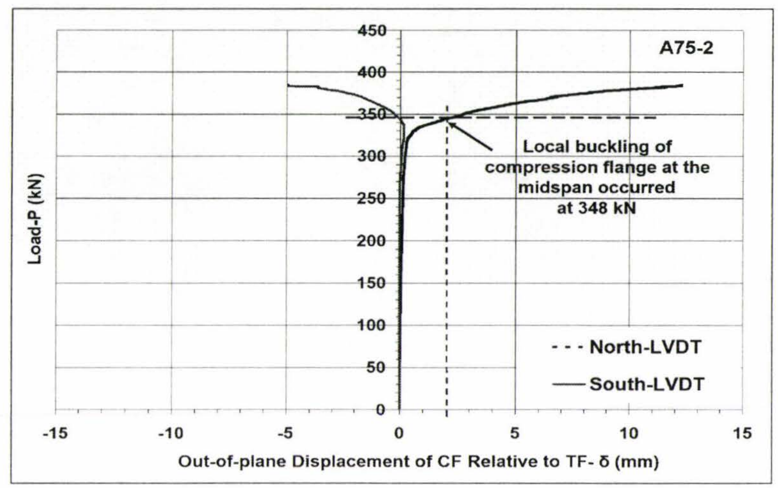


Figure 5.9[D]: Load versus Out-of-Plane Displacement of CF Relative to TF for Beam A75-2

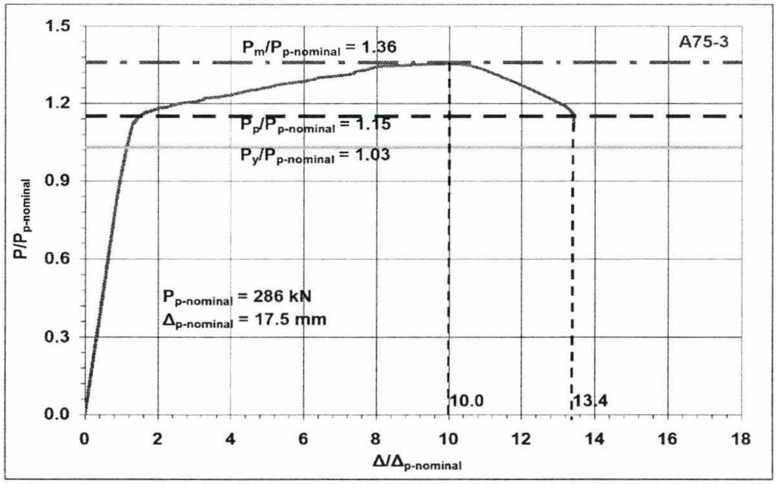


Figure 5.10[A]: Load versus Midspan Deflection for Beam A75-3

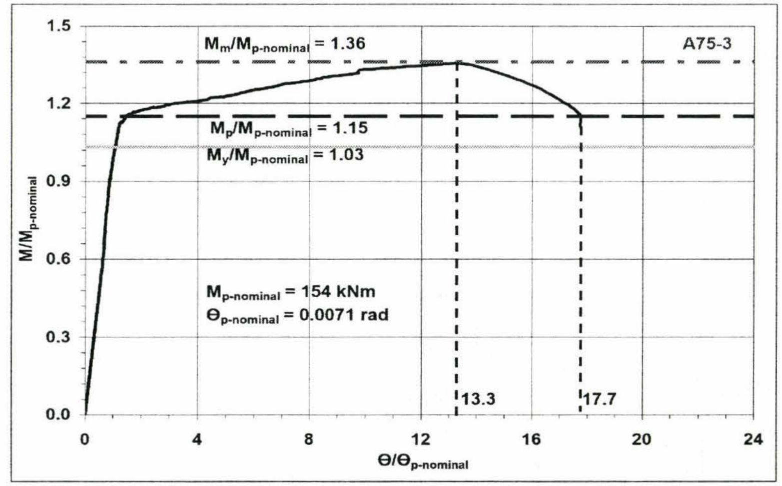


Figure 5.10[B]: Moment versus Rotation for Beam A75-3

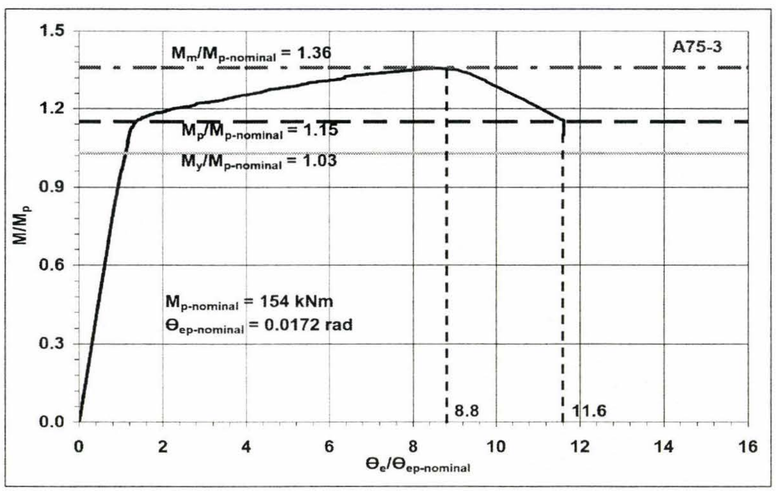


Figure 5.10[C]: Moment versus End Rotation for Beam A75-3

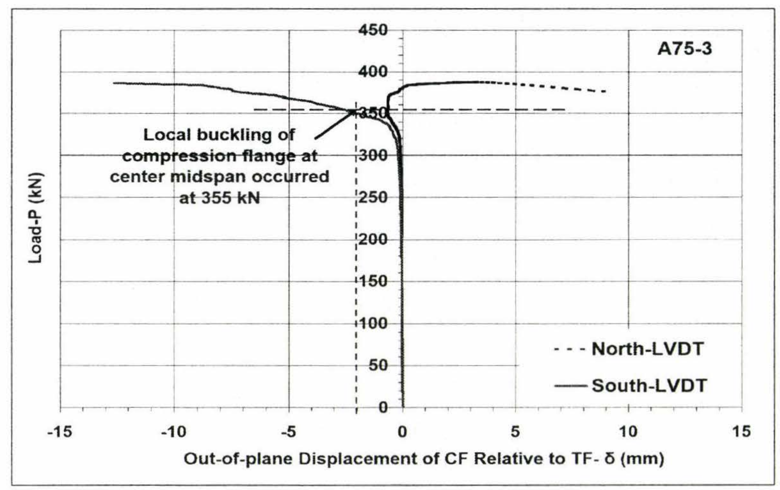


Figure 5.10[D]: Load versus Out-of-Plane Displacement of CF Relative to TF for Beam A75-3

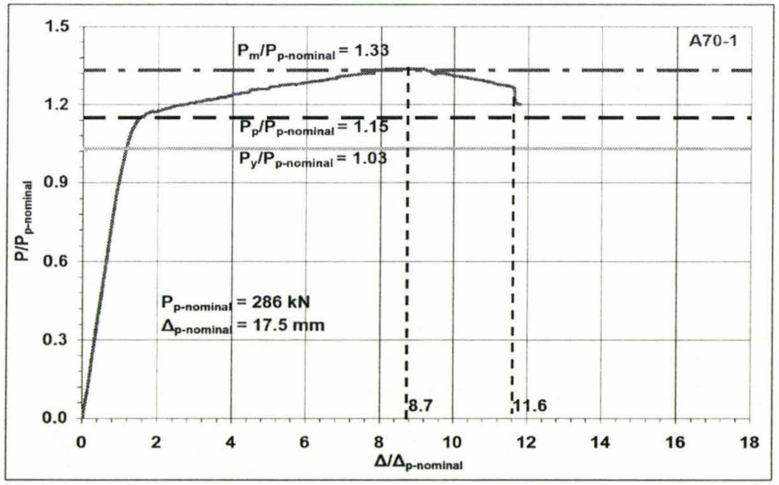


Figure 5.11[A]: Load versus Midspan Deflection for Beam A70-1

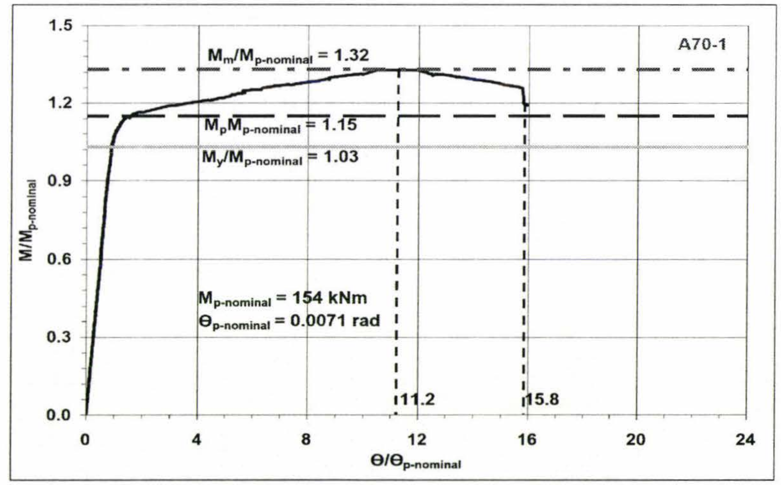


Figure 5.11[B]: Moment versus Rotation for Beam A70-1

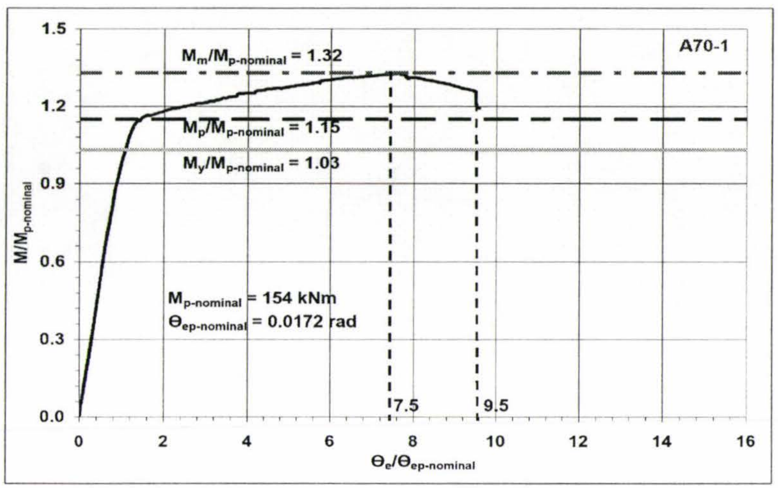


Figure 5.11[C]: Moment versus End Rotation for Beam A70-1

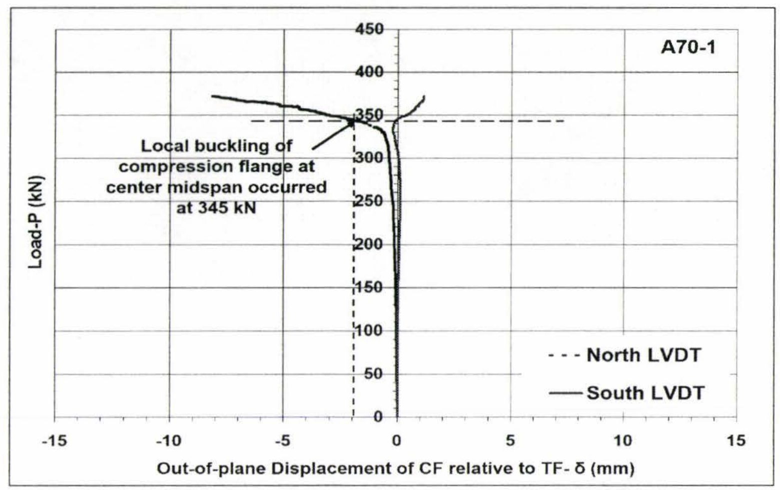


Figure 5.11[D]: Load versus Out-of-Plane Displacement of CF Relative to TF for Beam A70-1

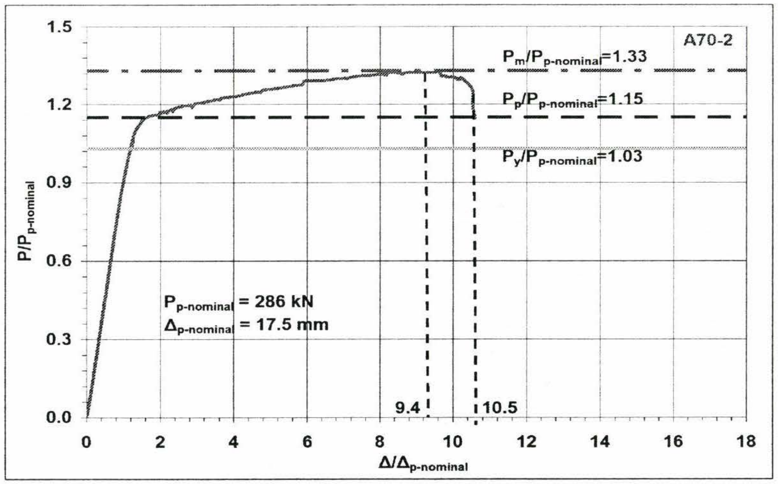


Figure 5.12[A]: Load versus Midspan Deflection for Beam A70-2

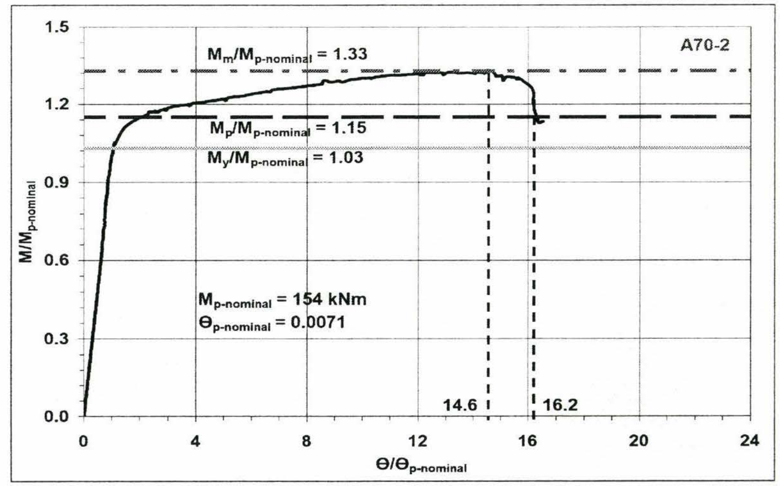


Figure 5.12[B]: Moment versus Rotation for Beam A70-2

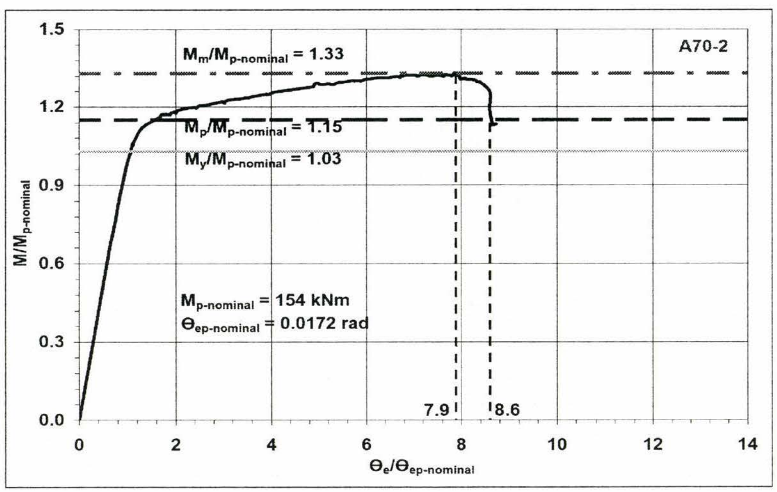


Figure 5.12[C]: Moment versus End Rotation for Beam A70-2

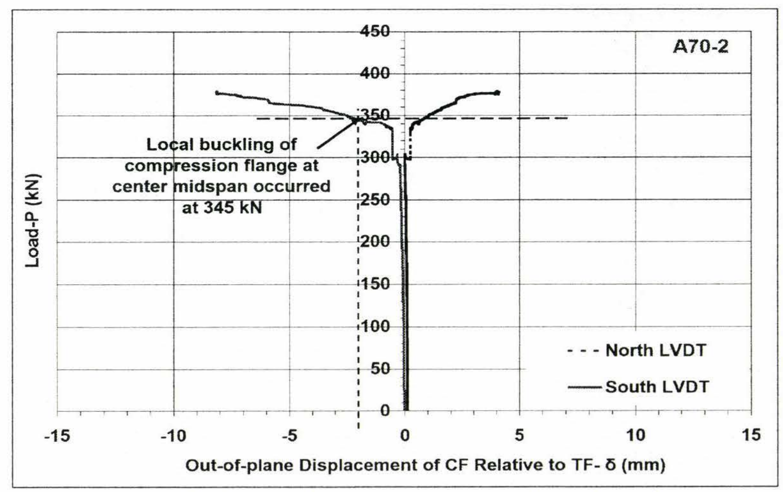


Figure 5.12[D]: Load versus Out-of-Plane Displacement of CF Relative to TF for Beam A70-2

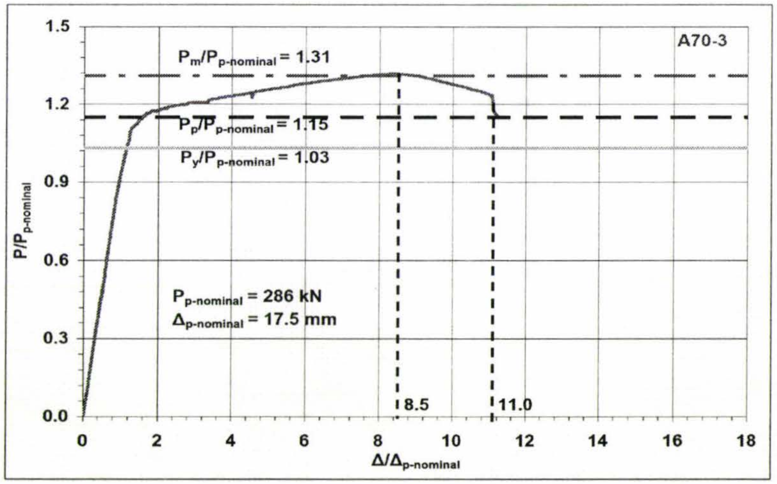


Figure 5.13[A]: Load versus Midspan Deflection for Beam A70-3

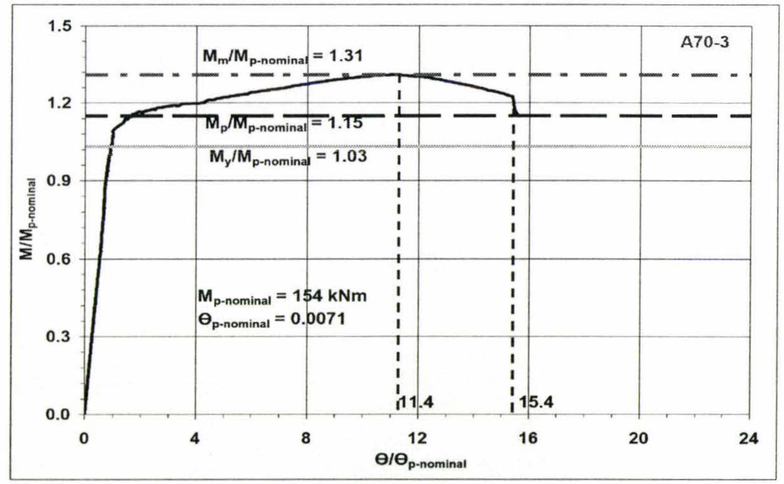


Figure 5.13[B]: Moment versus Rotation for Beam A70-3

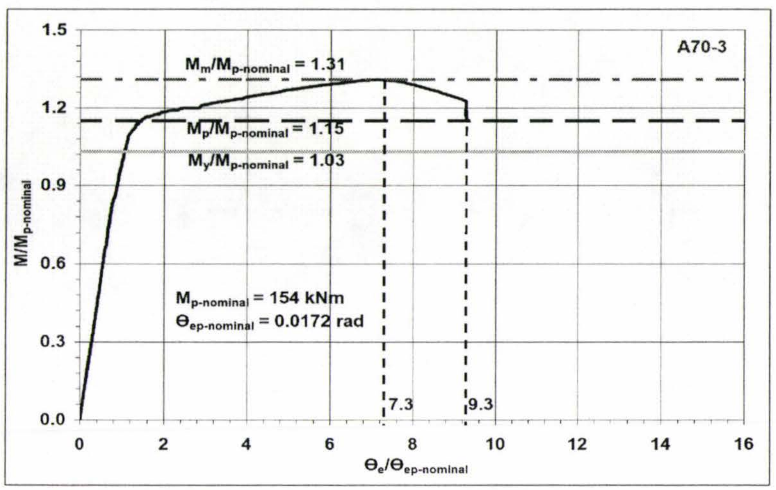


Figure 5.13[C]: Moment versus End Rotation for Beam A70-3

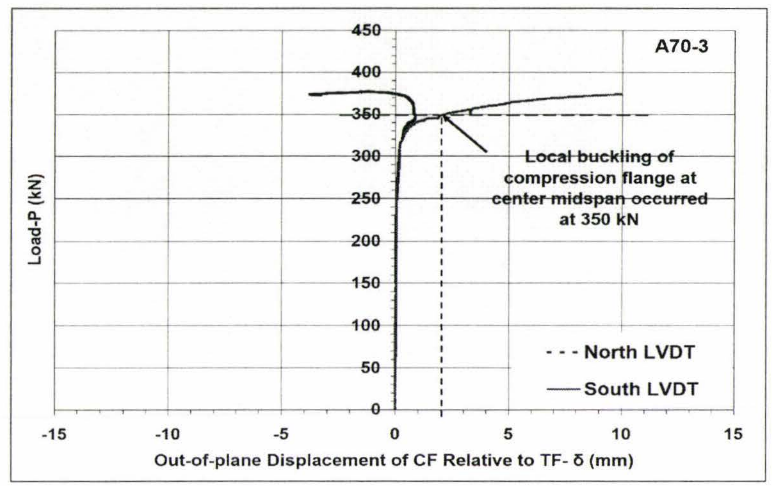


Figure 5.13[D]: Load versus Out-of-Plane Displacement of CF Relative to TF for Beam A70-3

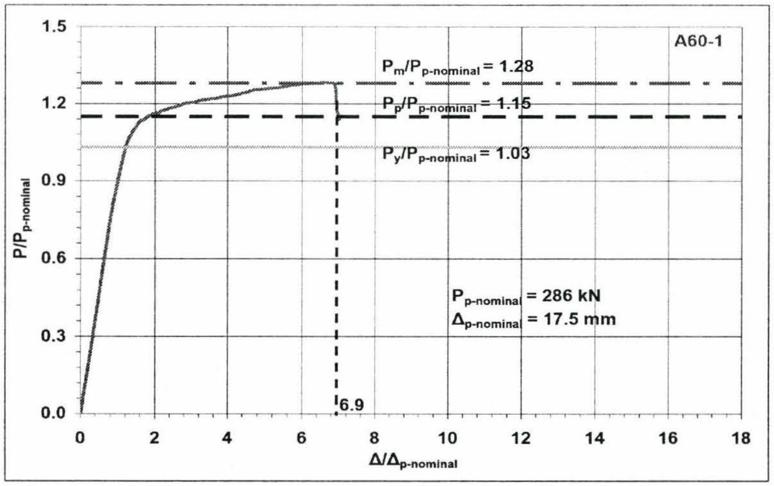


Figure 5.14[A]: Load versus Midspan Deflection for Beam A60-1

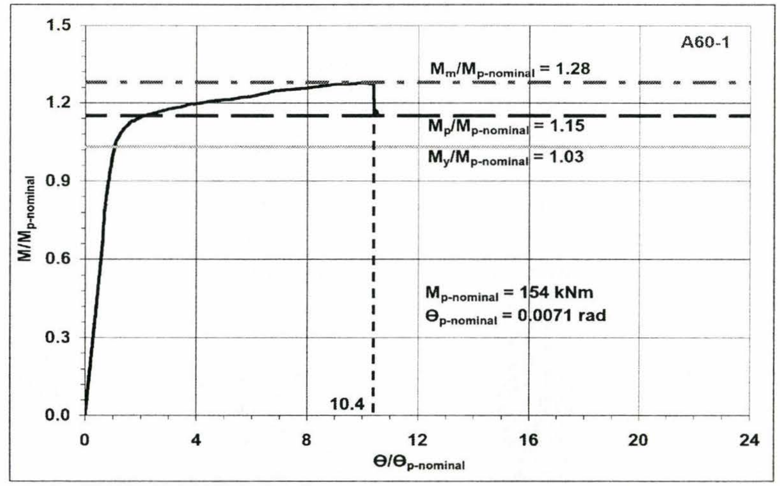


Figure 5.14[B]: Moment versus Rotation for Beam A60-1

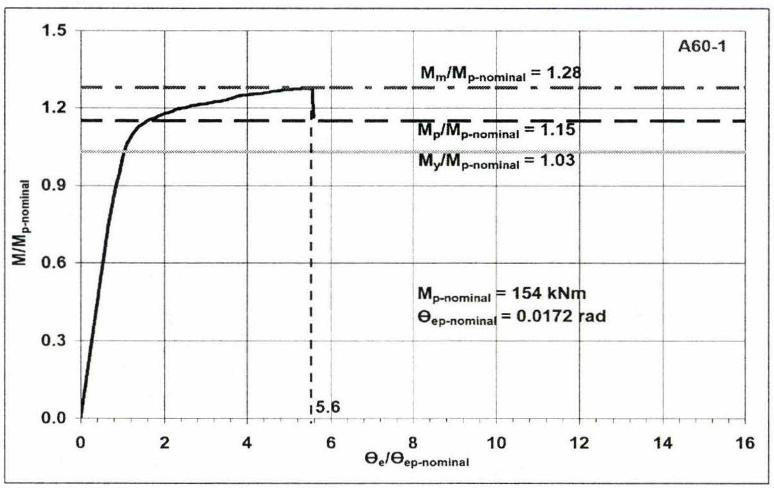


Figure 5.14[C]: Moment versus End Rotation for Beam A60-1

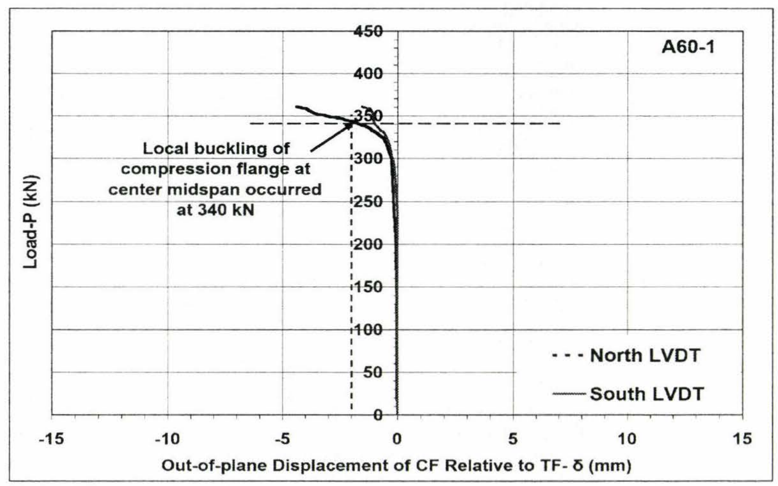


Figure 5.14[D]: Load versus Out-of-Plane Displacement of CF Relative to TF for Beam A60-1

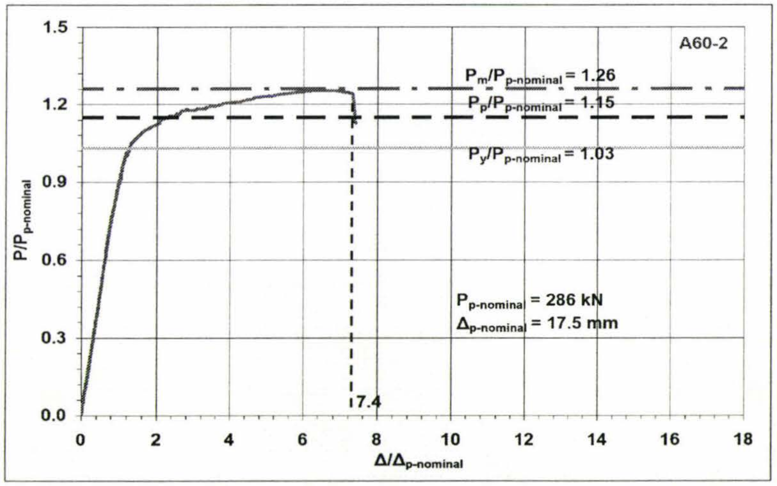


Figure 5.15[A]: Load versus Midspan Deflection for Beam A60-2

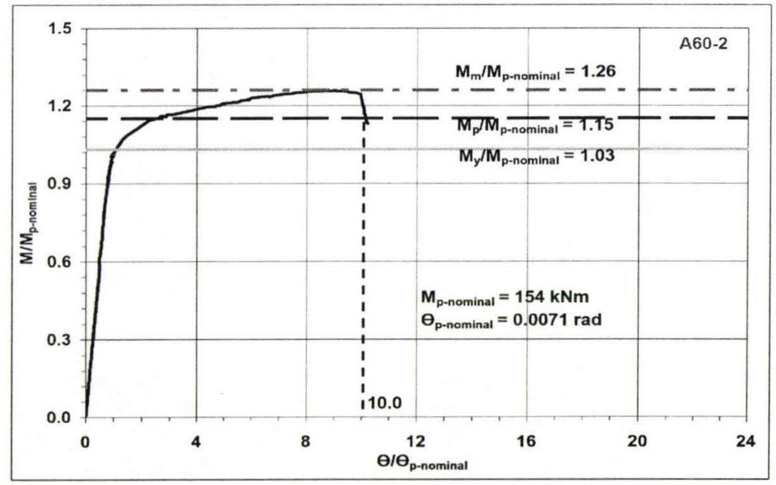


Figure 5.15[B]: Moment versus Rotation for Beam A60-2

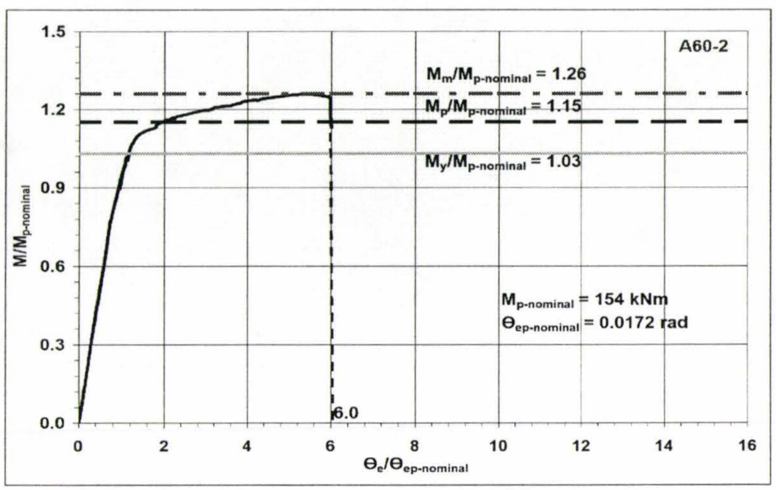


Figure 5.15[C]: Moment versus End Rotation for Beam A60-2

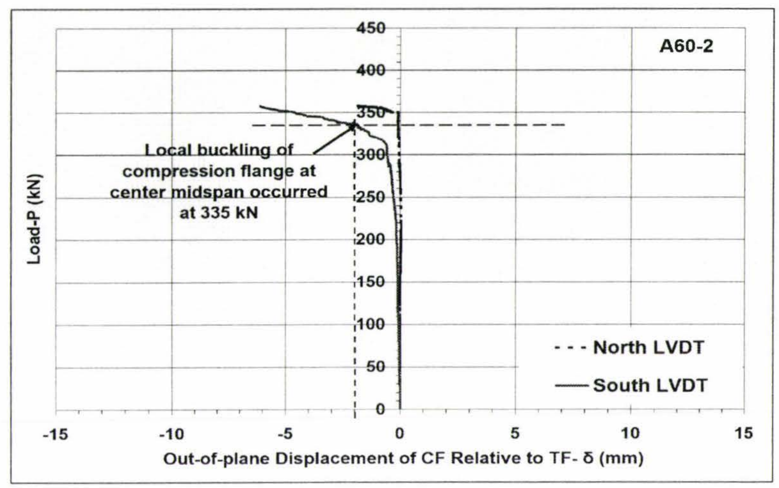


Figure 5.15[D]: Load versus Out-of-Plane Displacement of CF Relative to TF for Beam A60-2

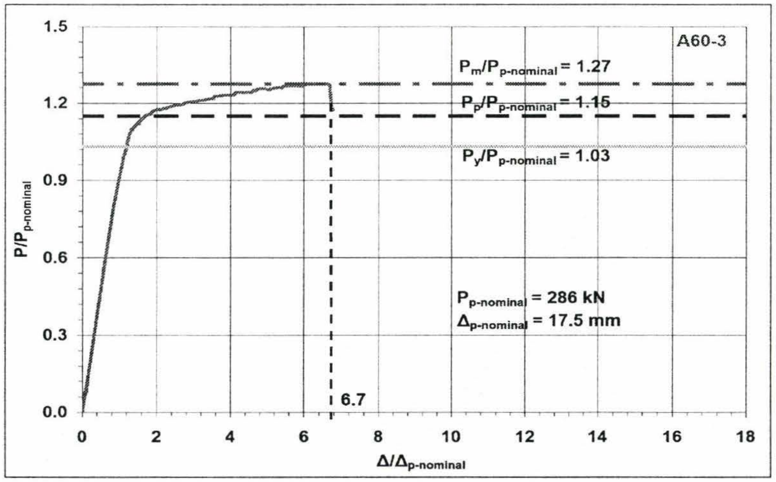


Figure 5.16[A]: Load versus Midspan Deflection for Beam A60-3

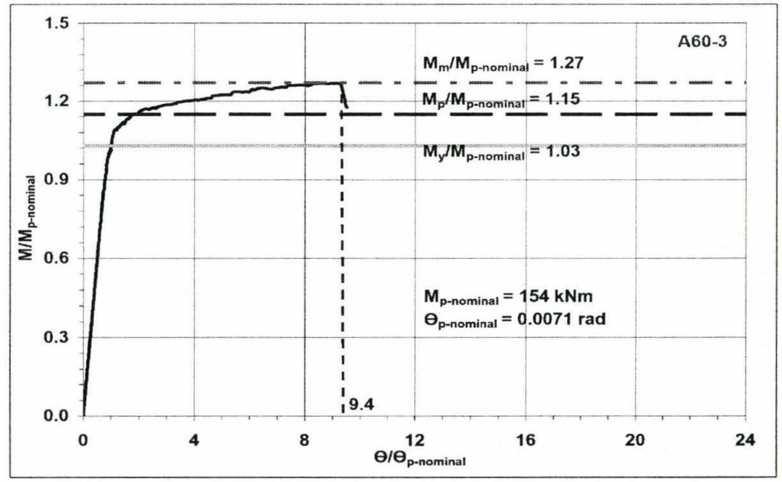


Figure 5.16[B]: Moment versus Rotation for Beam A60-3

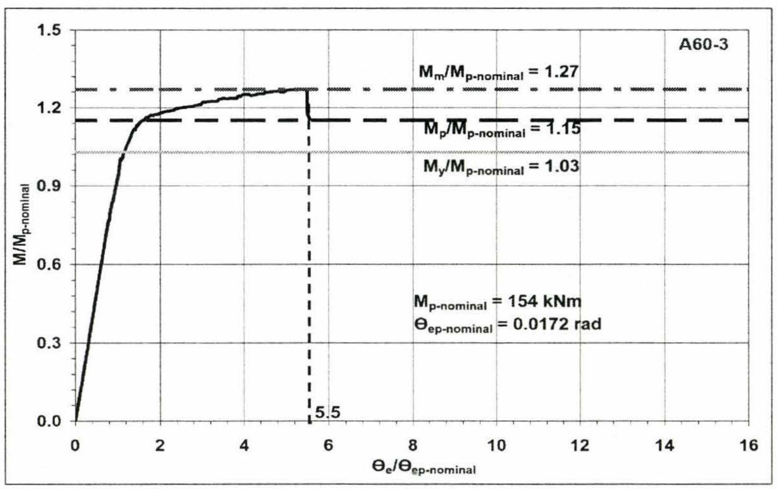


Figure 5.16[C]: Moment versus End Rotation for Beam A60-3

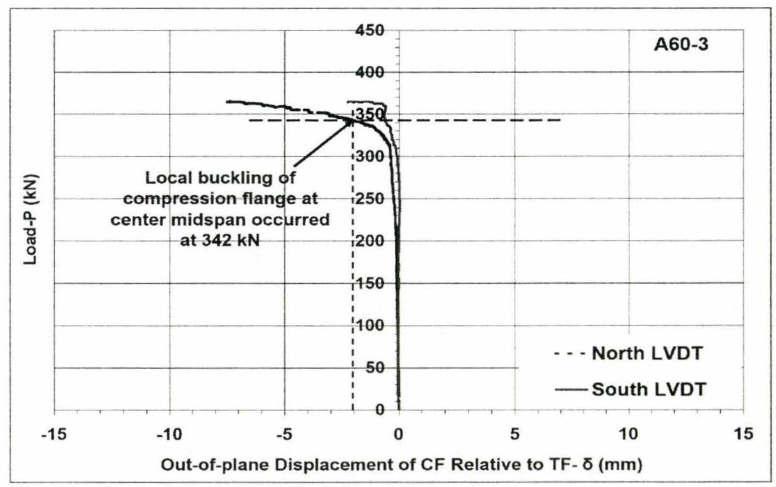


Figure 5.16[D]: Load versus Out-of-Plane Displacement of CF Relative to TF for Beam A60-3

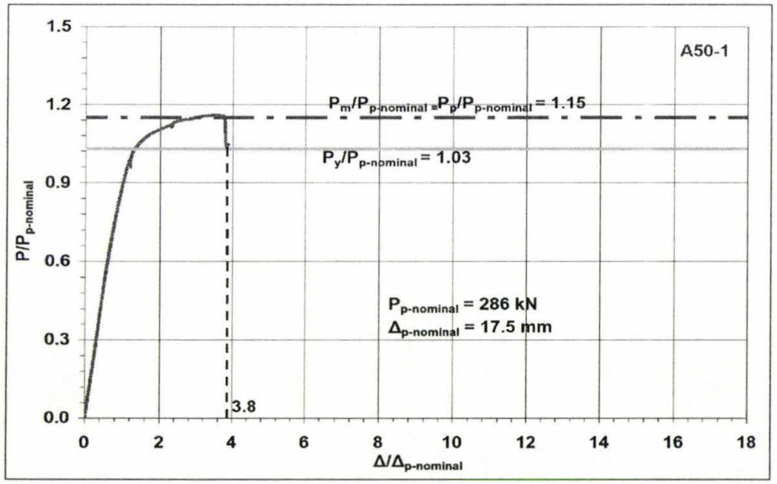


Figure 5.17[A]: Load versus Midspan Deflection for Beam A50-1

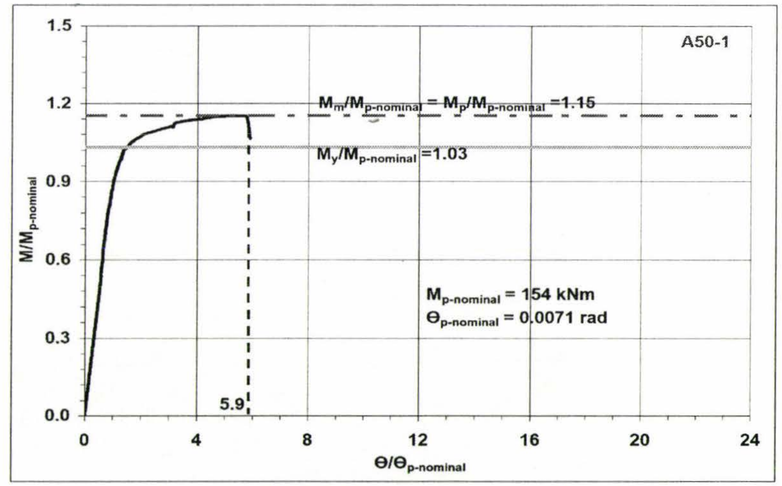


Figure 5.17[B]: Moment versus Rotation for Beam A50-1

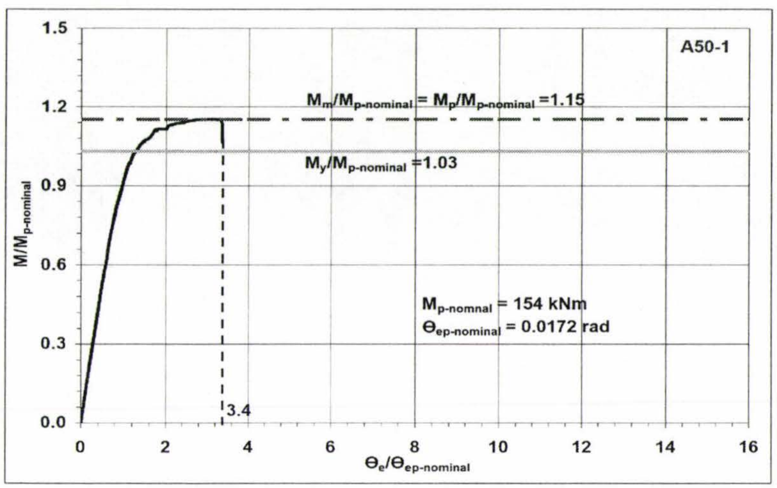


Figure 5.17[C]: Moment versus End Rotation for Beam A50-1

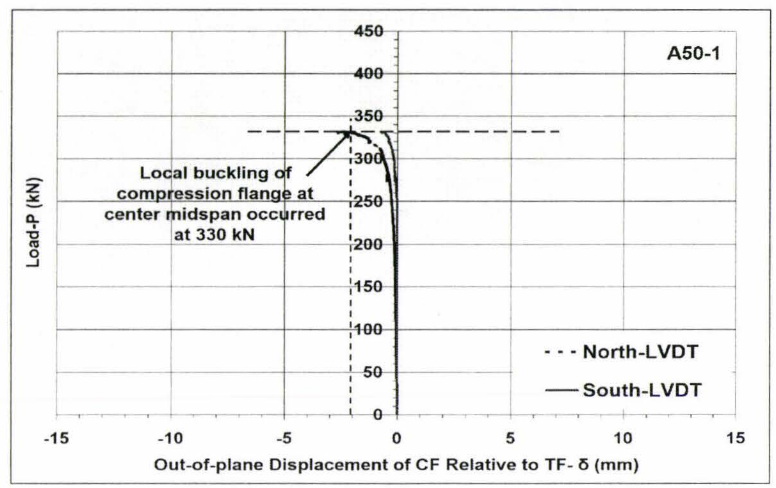


Figure 5.17[D]: Load versus Out-of-Plane Displacement of CF Relative to TF for Beam A50-1

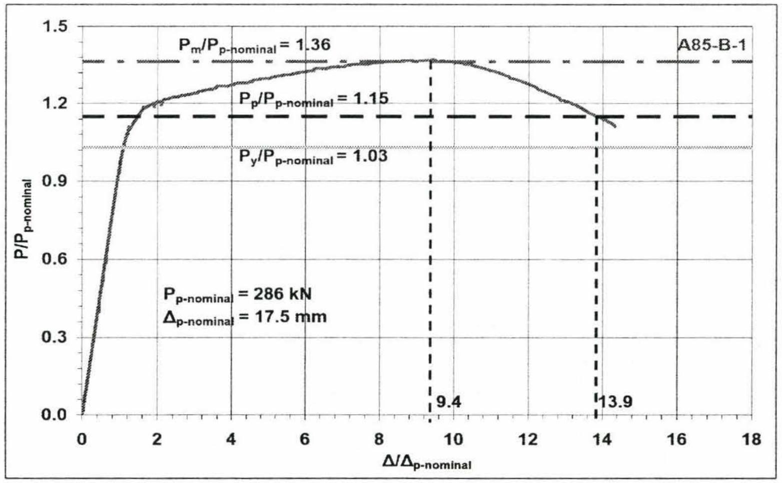


Figure 5.18[A]: Load versus Midspan Deflection for Beam A85-B-1

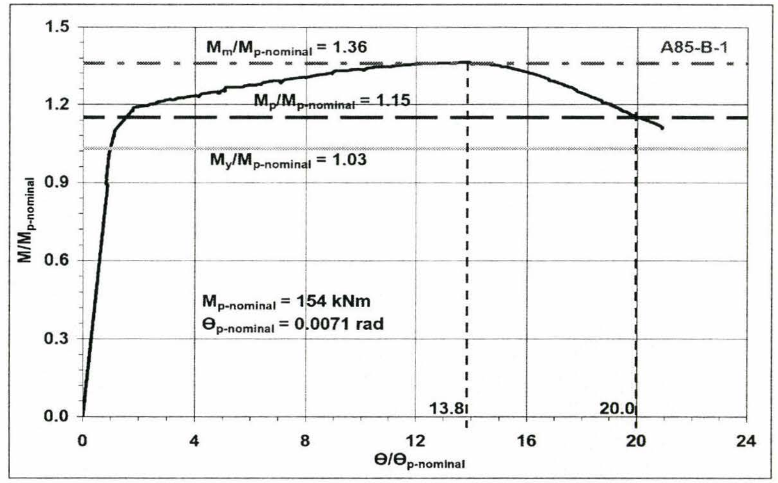


Figure 5.18[B]: Moment versus Rotation for Beam A85-B-1

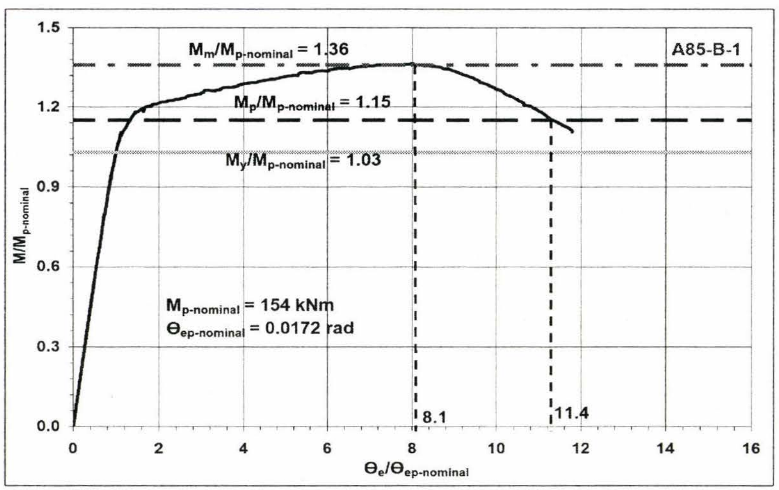


Figure 5.18[C]: Moment versus End Rotation for Beam A85-B-1

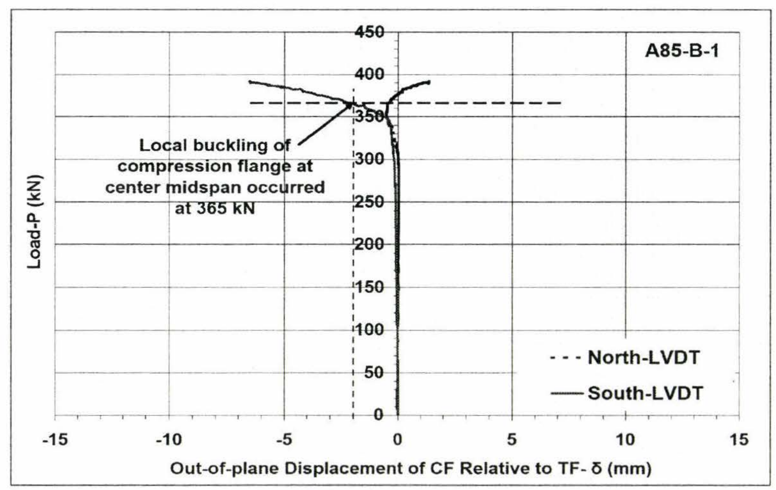


Figure 5.18[D]: Load versus Out-of-Plane Displacement of CF Relative to TF for Beam A85-B-1

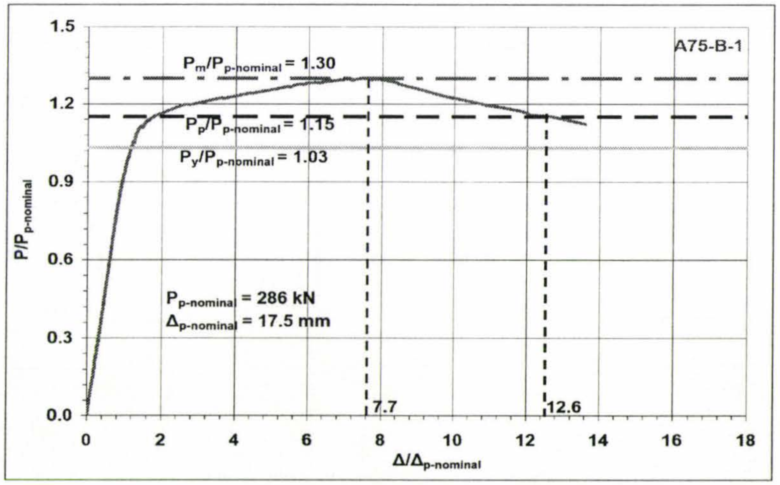


Figure 5.19[A]: Load versus Midspan Deflection for Beam A75-B-1

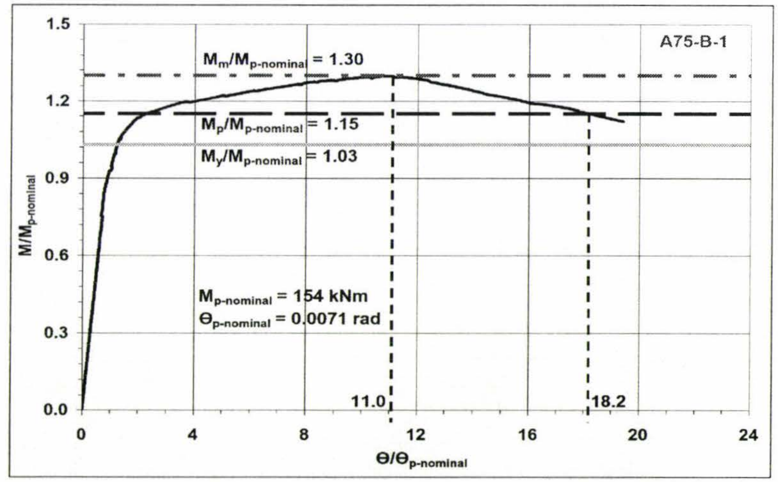


Figure 5.19[B]: Moment versus Rotation for Beam A75-B-1

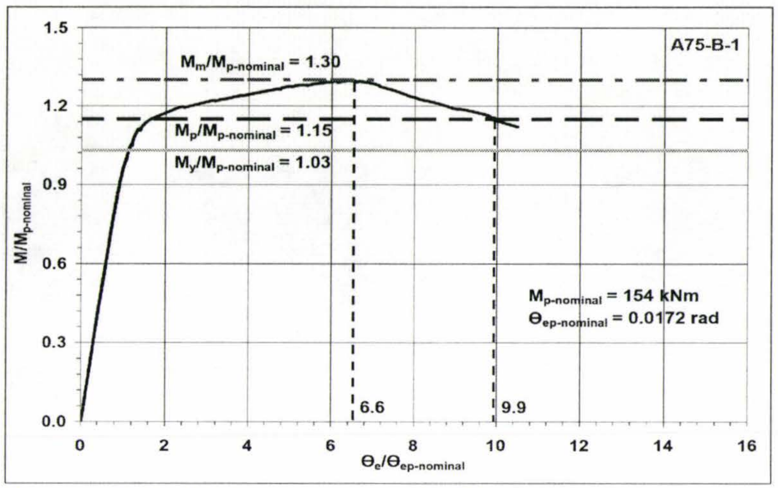


Figure 5.19[C]: Moment versus End Rotation for Beam A75-B-1

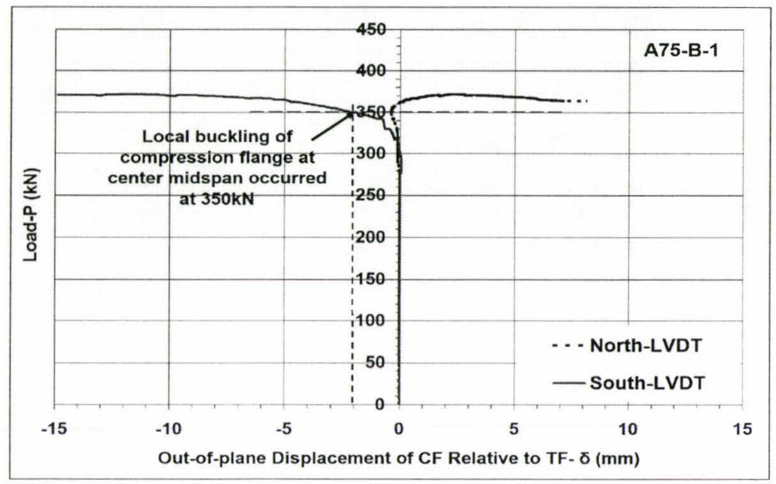


Figure 5.19[D]: Load versus Out-of-Plane Displacement of CF Relative to TF for Beam A75-B-1

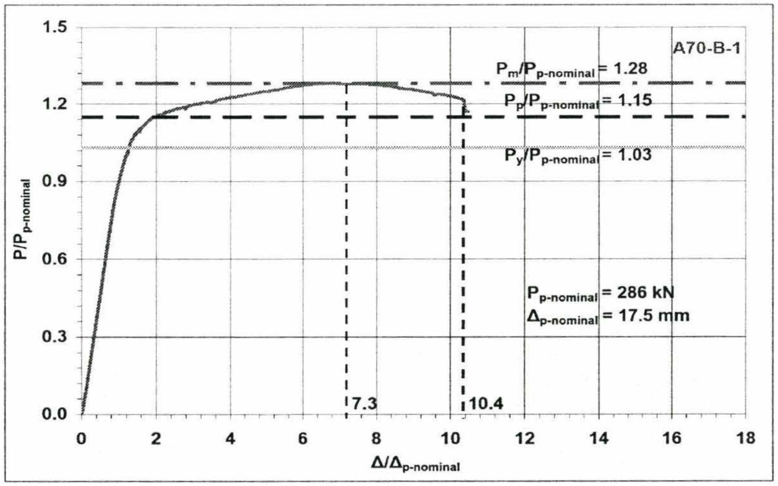


Figure 5.20[A]: Load versus Midspan Deflection for Beam A70-B-1

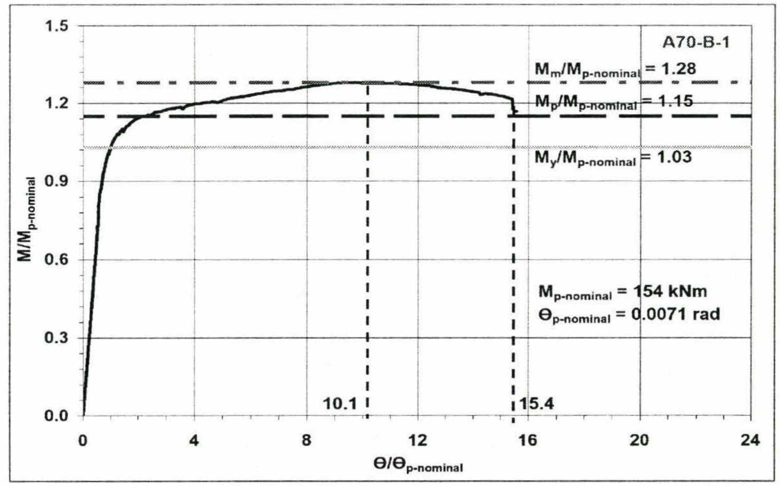


Figure 5.20[B]: Moment versus Rotation for Beam A70-B-1

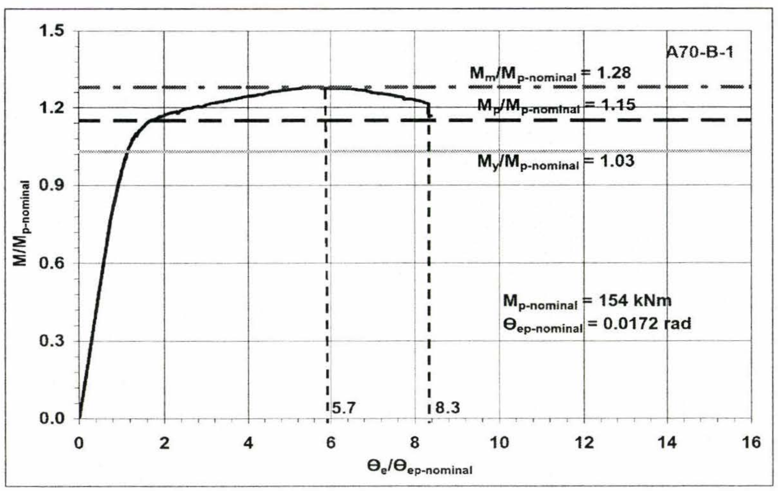


Figure 5.20[C]: Moment versus End Rotation for Beam A70-B-1

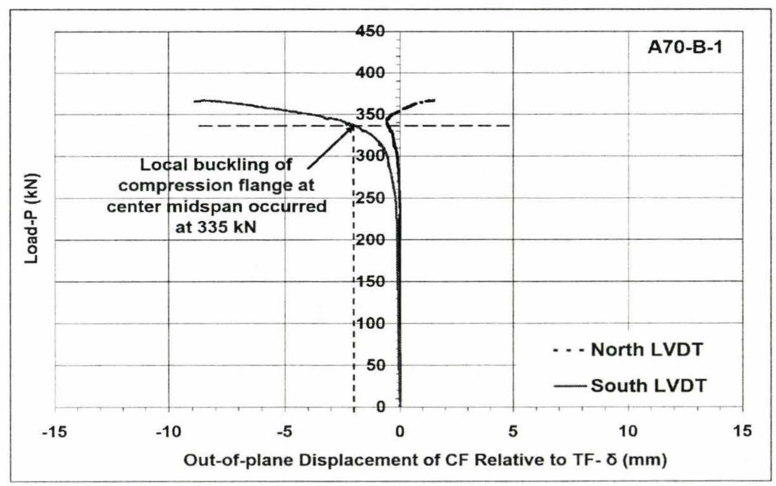


Figure 5.20[D]: Load versus Out-of-Plane Displacement of CF Relative to TF for Beam A70-B-1

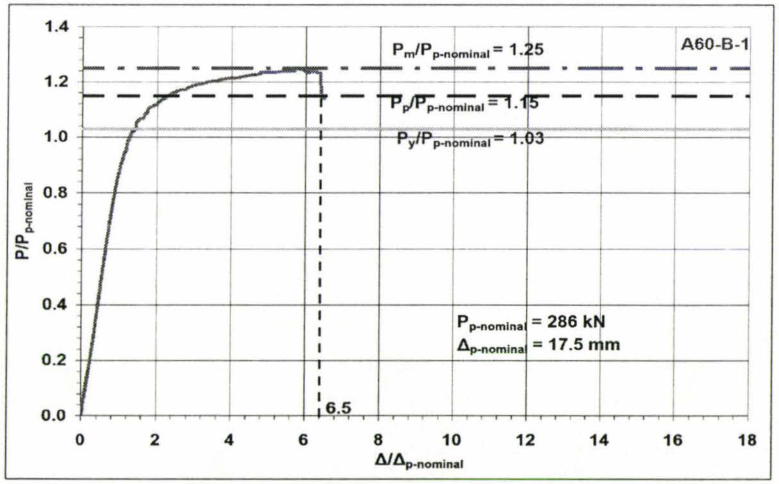


Figure 5.21[A]: Load versus Midspan Deflection for Beam A60-B-1

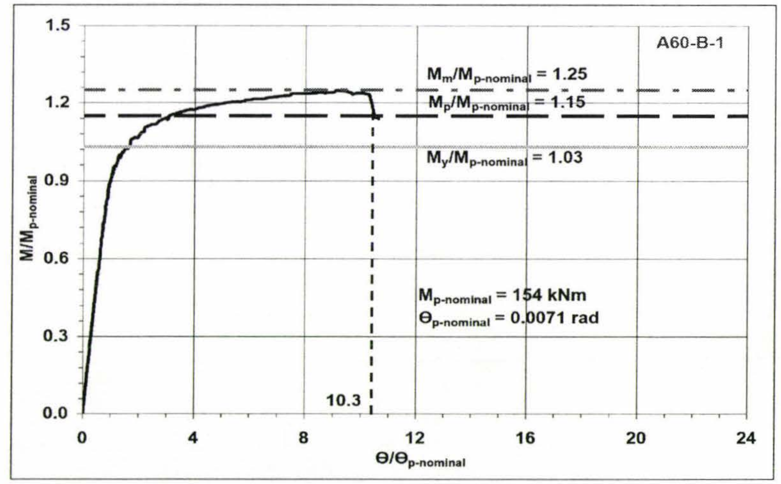


Figure 5.21[B]: Moment versus Rotation for Beam A60-B-1

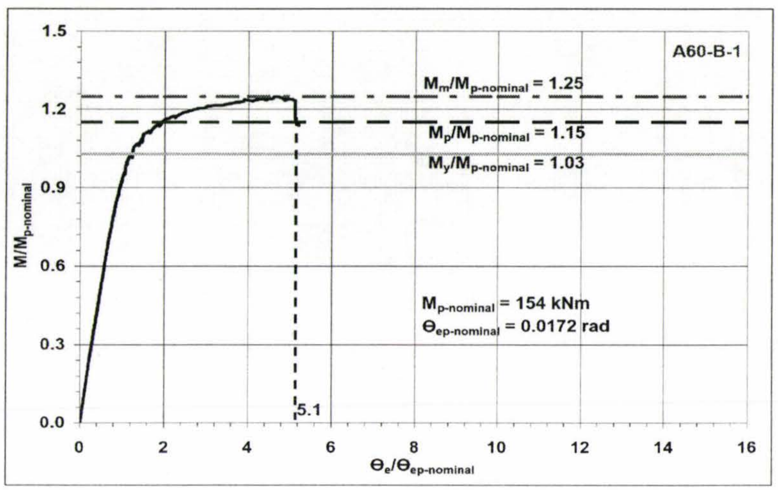


Figure 5.21[C]: Moment versus End Rotation for Beam A60-B-1

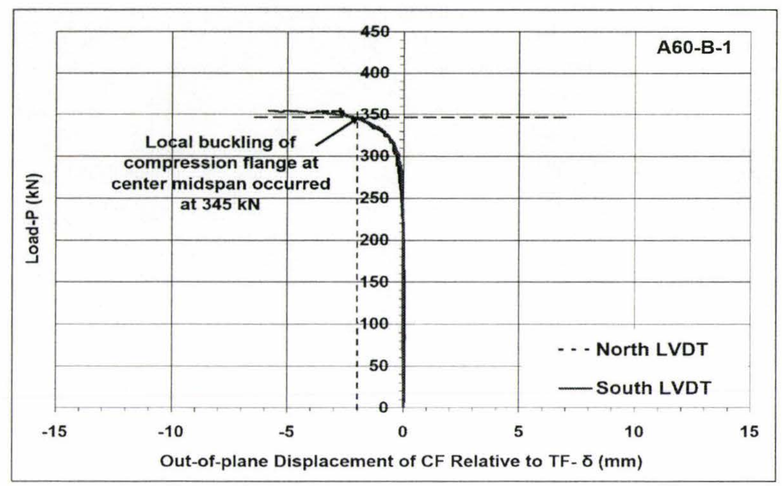


Figure 5.21[D]: Load versus Out-of-Plane Displacement of CF Relative to TF for Beam A60-B-1

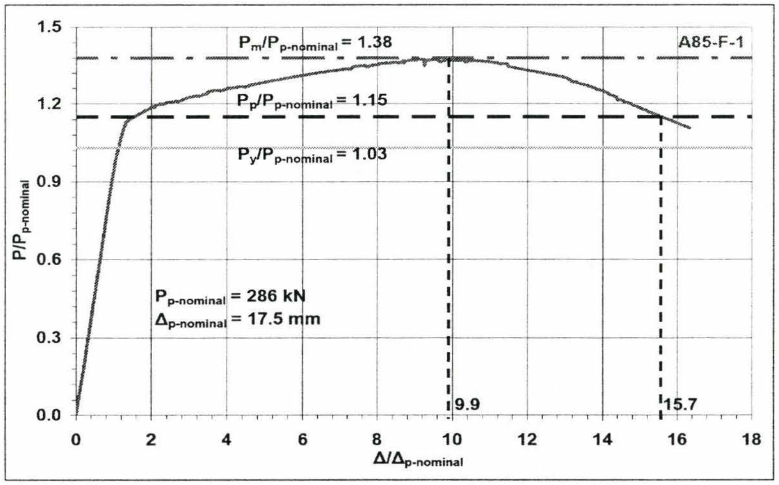


Figure 5.22[A]: Load versus Midspan Deflection for Beam A85-F-1

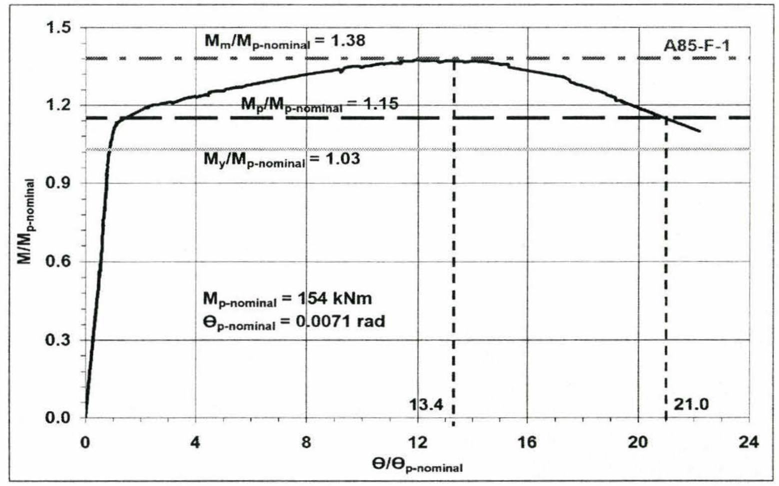


Figure 5.22[B]: Moment versus Rotation for Beam A85-F-1

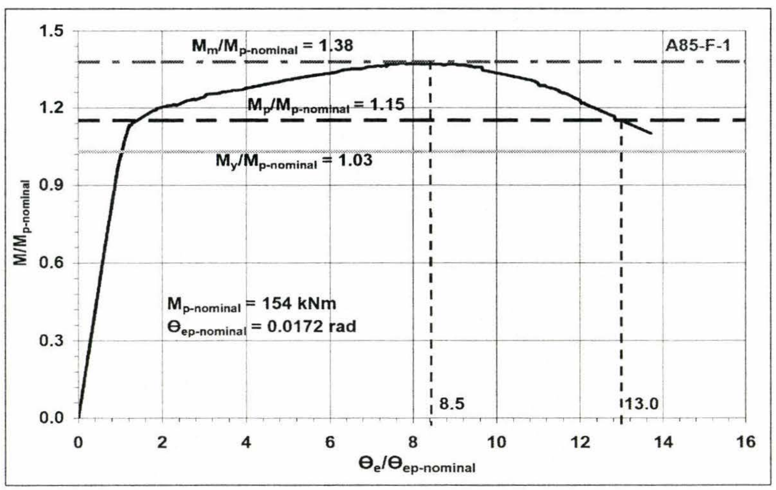


Figure 5.22[C]: Moment versus End Rotation for Beam A85-F-1

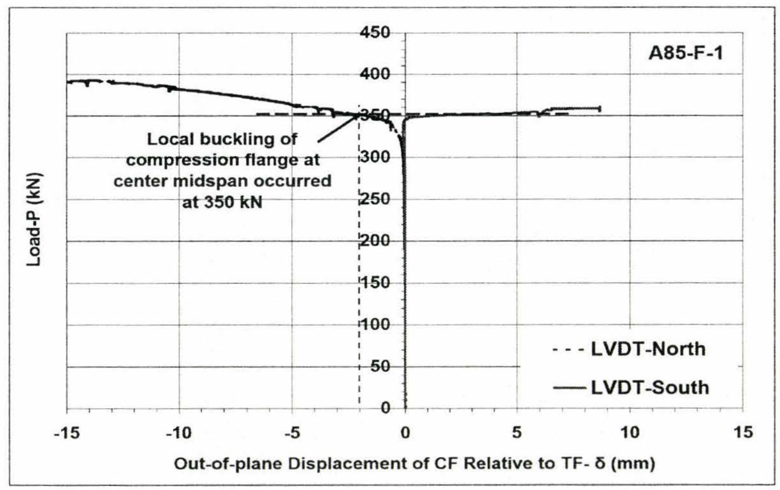


Figure 5.22[D]: Load versus Out-of-Plane Displacement of CF Relative to TF for Beam A85-F-1

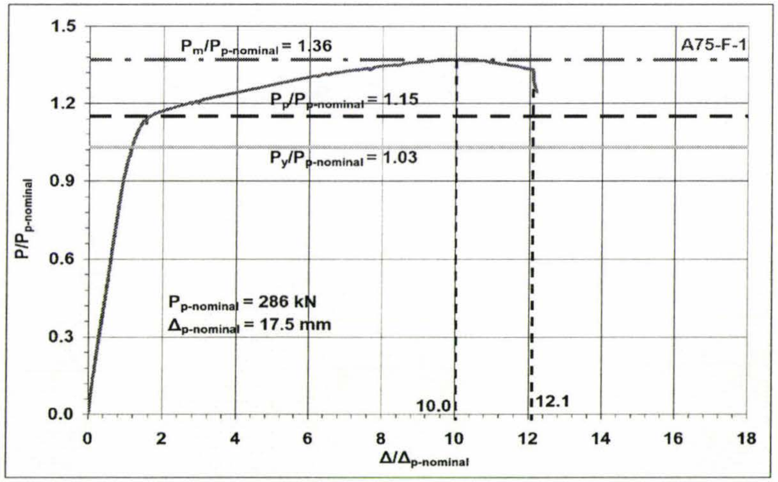


Figure 5.23[A]: Load versus Midspan Deflection for Beam A75-F-1

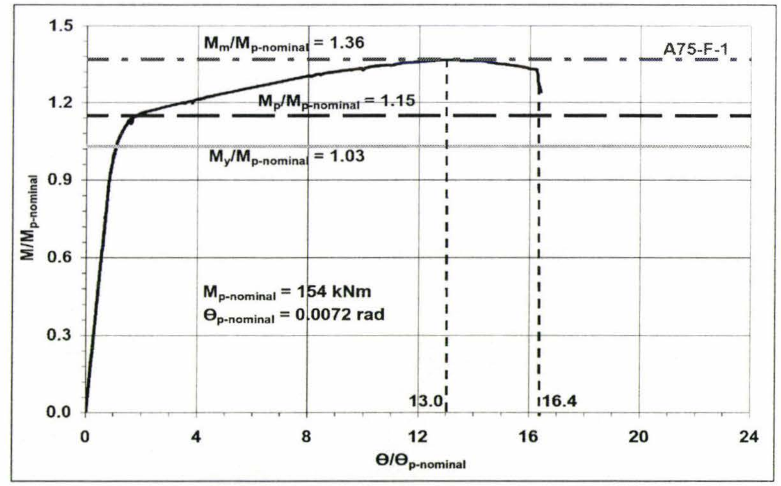


Figure 5.23[B]: Moment versus Rotation for Beam A75-F-1

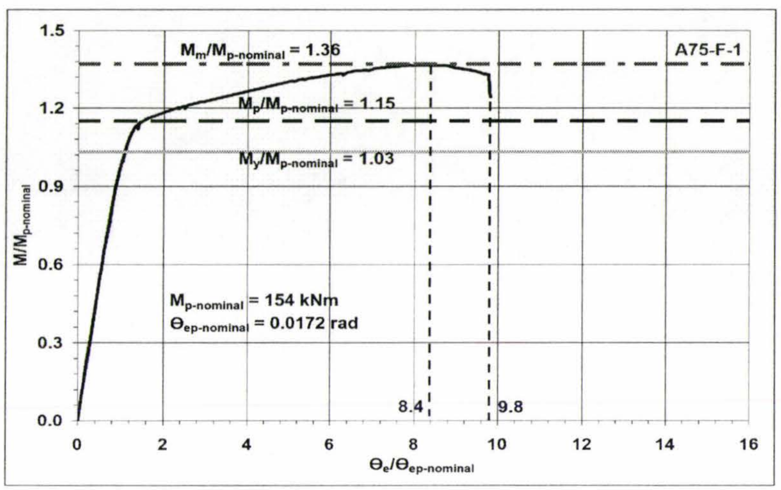


Figure 5.23[C]: Moment versus End Rotation for Beam A75-F-1

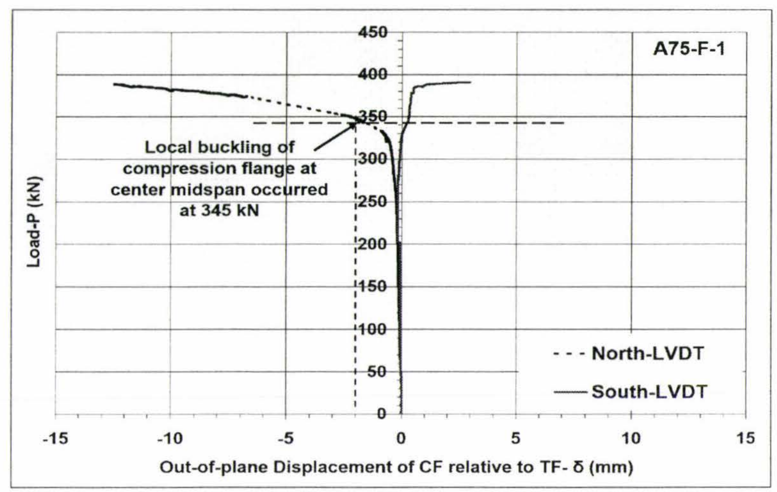


Figure 5.23[D]: Load versus Out-of-Plane Displacement of CF Relative to TF for Beam A75-F-1

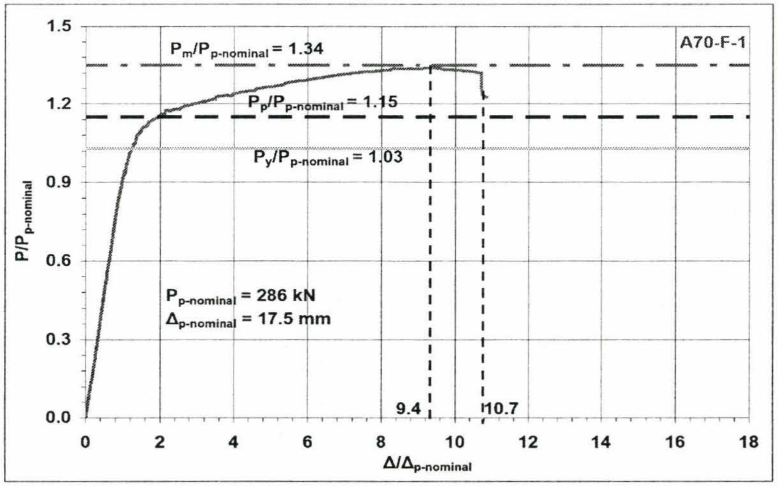


Figure 5.24[A]: Load versus Midspan Deflection for Beam A70-F-1

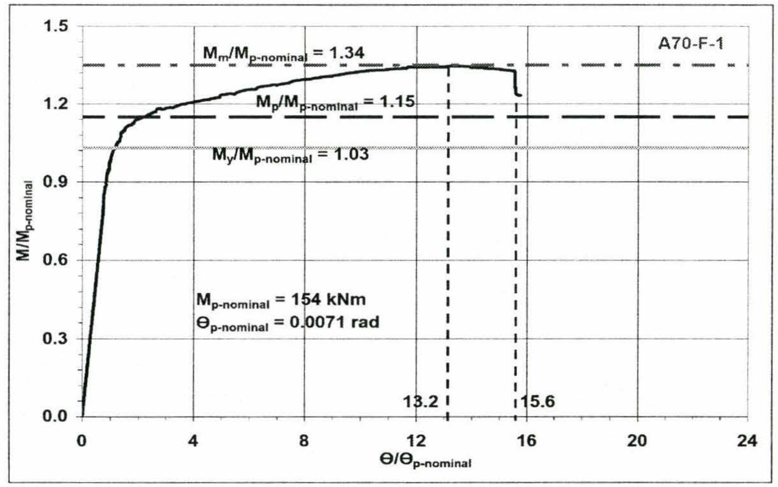


Figure 5.24[B]: Moment versus Rotation for Beam A70-F-1

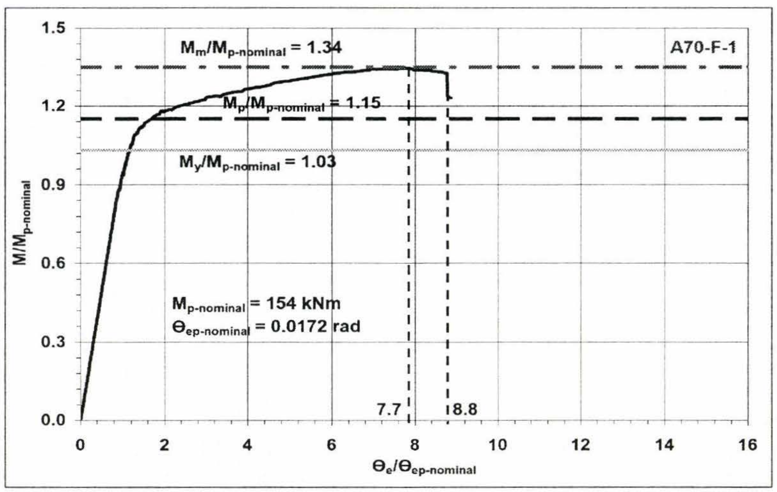


Figure 5.24[C]: Moment versus End Rotation for Beam A70-F-1

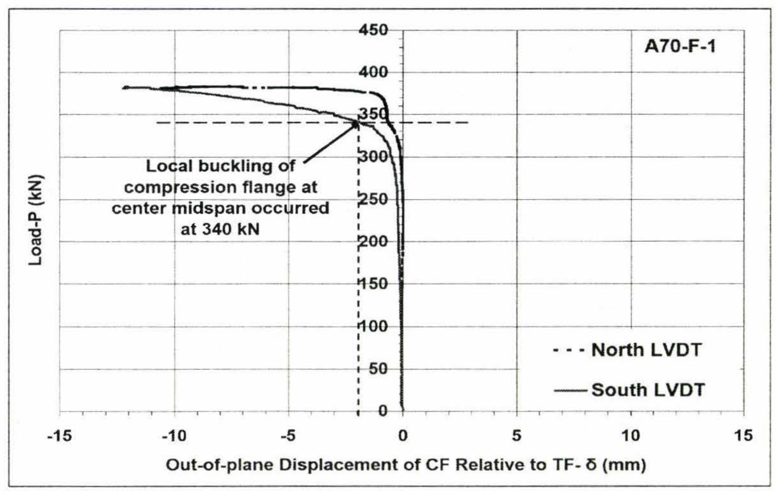


Figure 5.24[D]: Load versus Out-of-Plane Displacement of CF Relative to TF for Beam A70-F-1

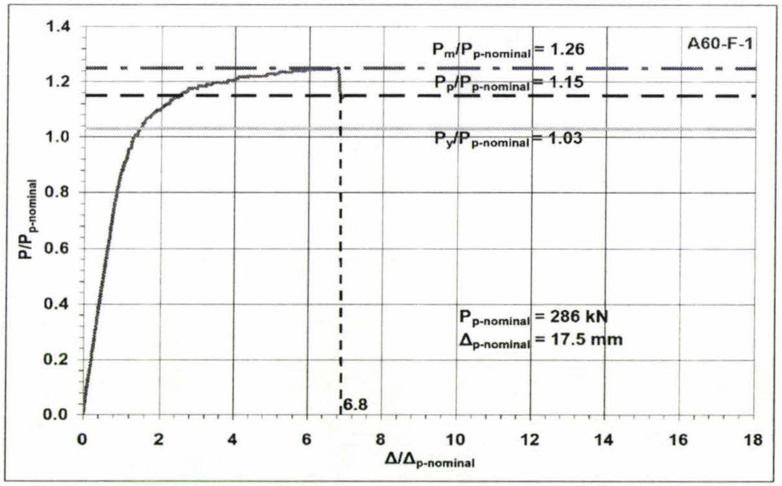


Figure 5.25[A]: Load versus Midspan Deflection for Beam A60-F-1

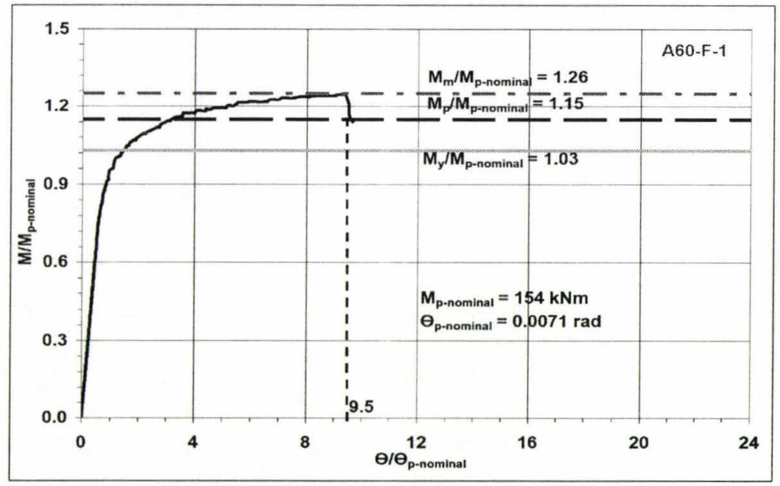


Figure 5.25[B]: Moment versus Rotation for Beam A60-F-1

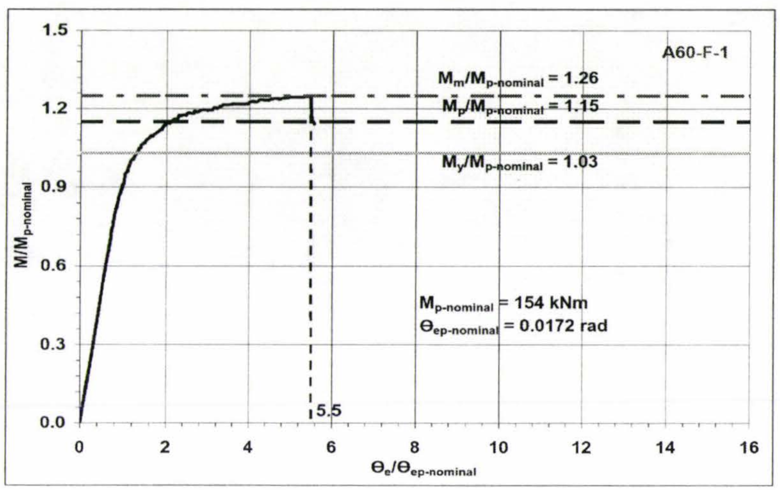


Figure 5.25[C]: Moment versus End Rotation for Beam A60-F-1

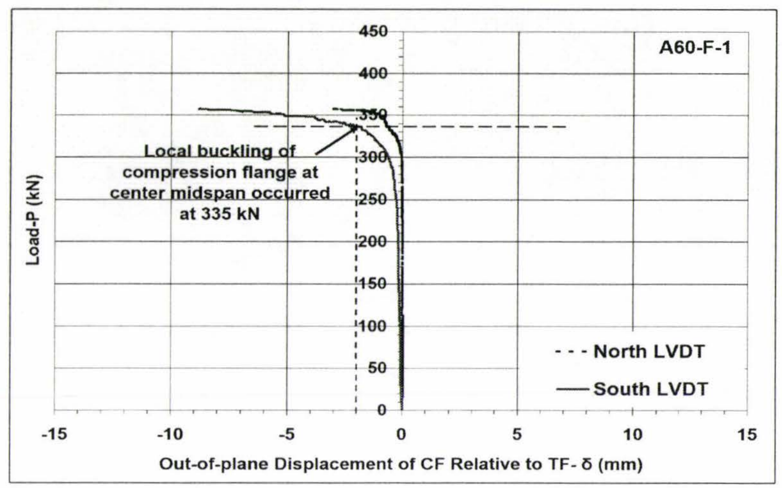


Figure 5.25[D]: Load versus Out-of-Plane Displacement of CF Relative to TF for Beam A60-F-1

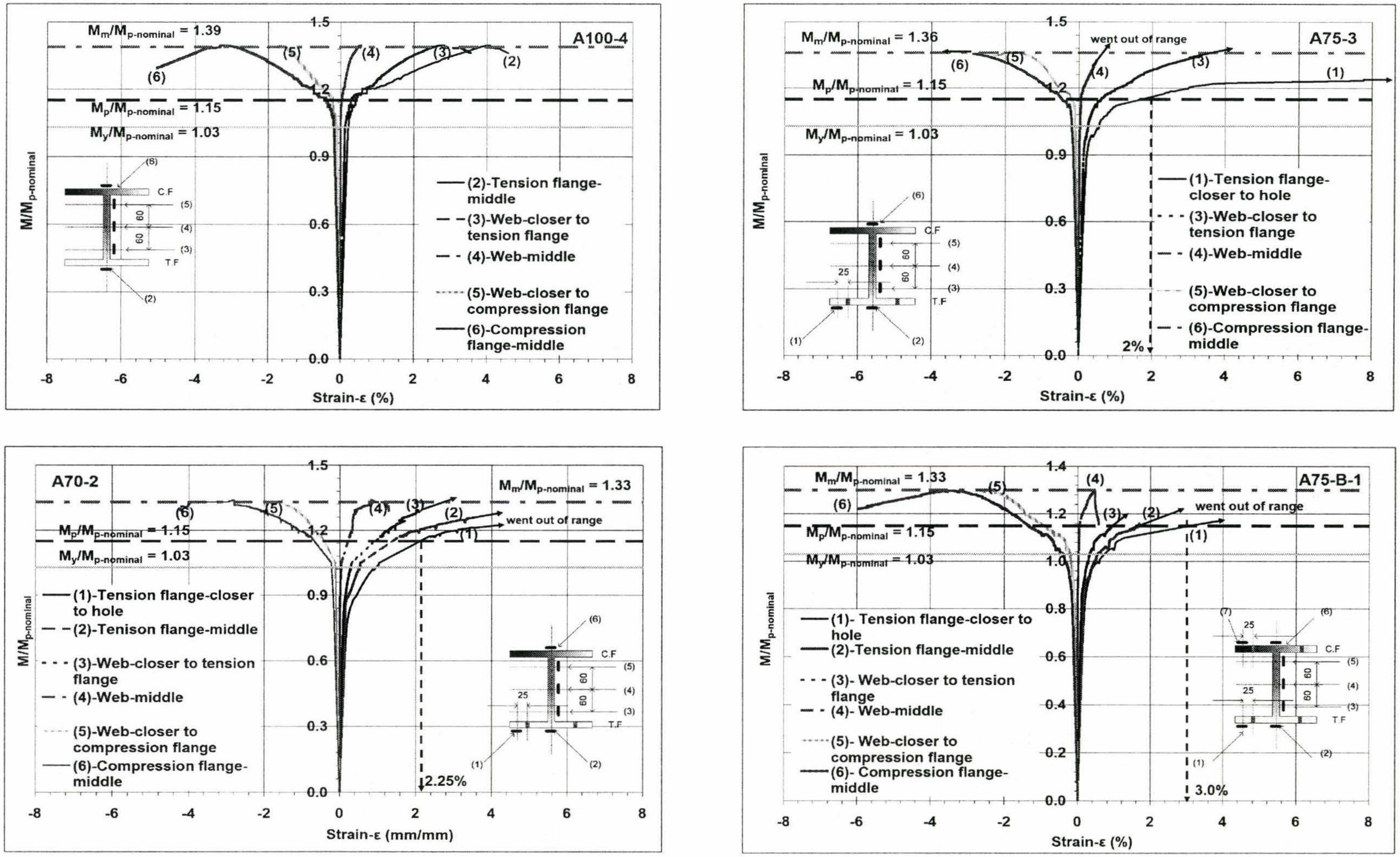

Figure 5.26: Moment versus Strain Variation for Beam Specimens A100-1, A75-3, A70-2 and A75-B-1

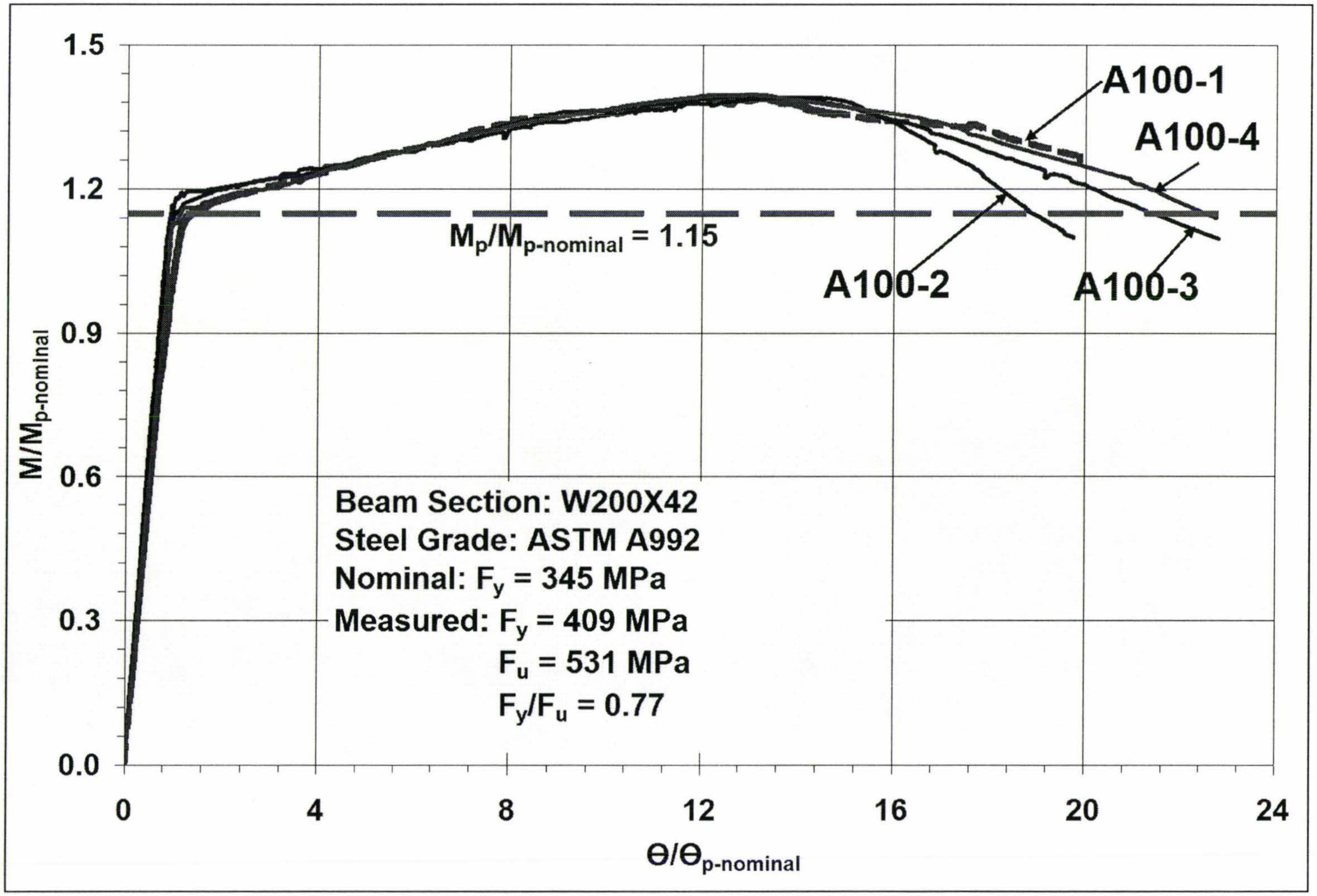


Figure 5.27: Comparison of Normalized Moment versus Normalized Average Load Point Rotation for Solid Beams A100-1, A100-2, A100-3 and A100-4

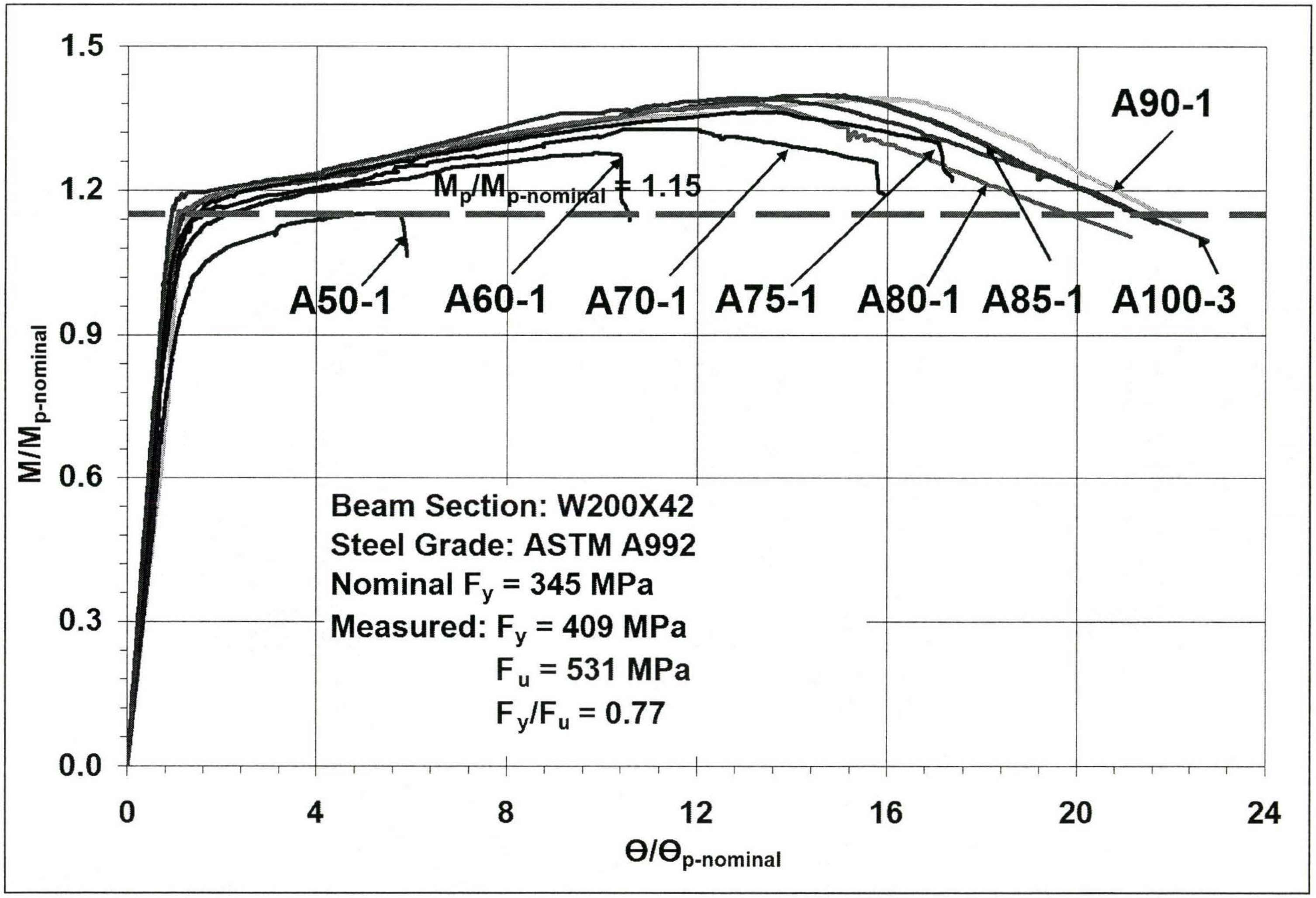


Figure 5.28: Comparison of Normalized Moment versus Normalized Average Load Point Rotation for Beams with Holes in Tension Flange Only

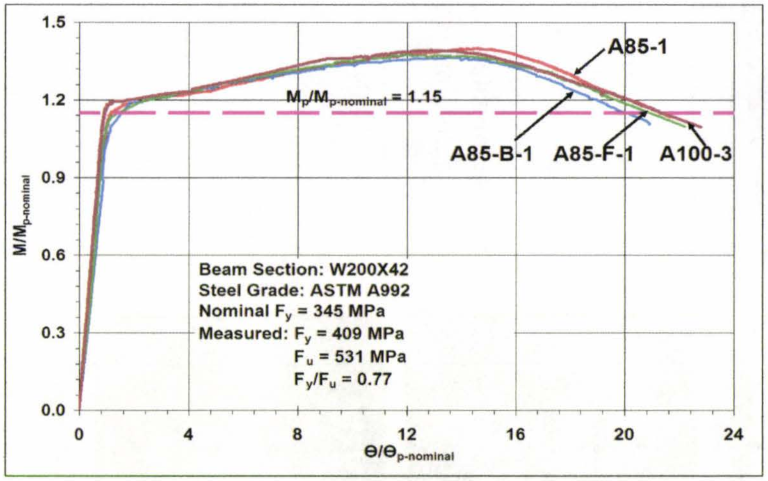


Figure 5.29: Comparison of Moment- Rotation Relationship for Beams A85-1, A85-B-1 and A85-F-1

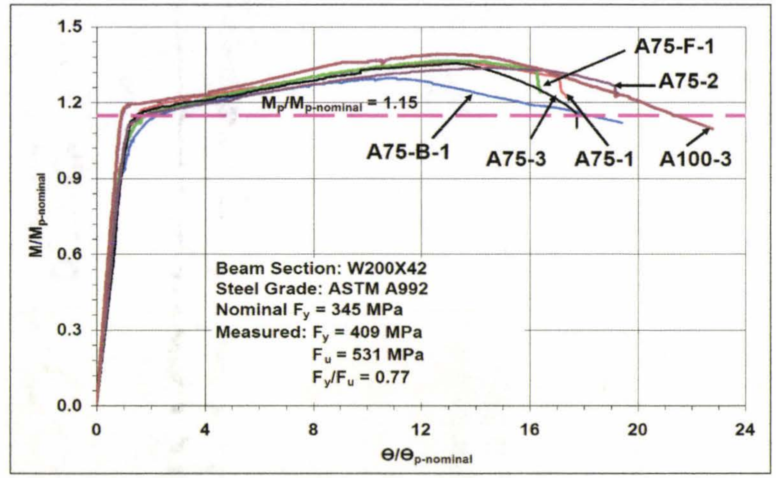


Figure 5.30: Comparison of Moment-Rotation Relationship for Beams A75-1-2-3, A75-B-1 and A75-F-1

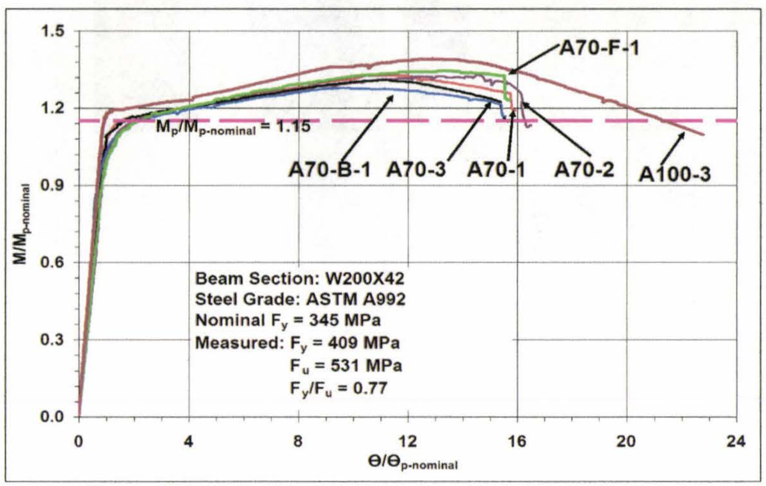


Figure 5.31: Comparison of Moment- Rotation Relationship for Beams: A70-1-2-3, A70-B-1 and A70-F-1

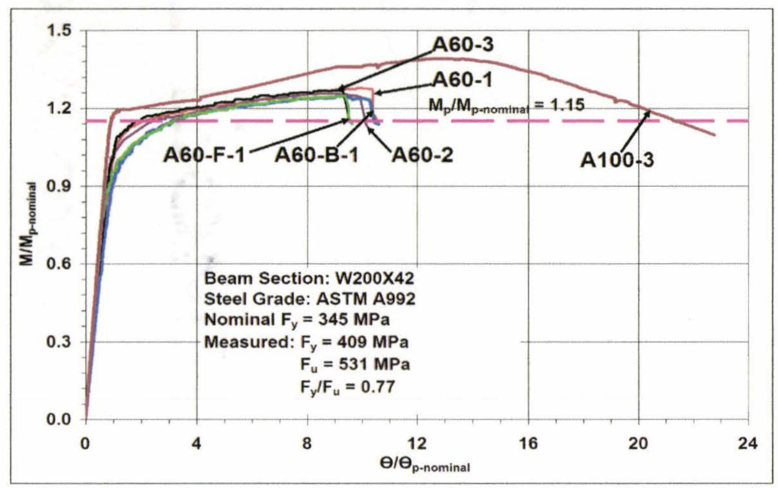


Figure 5.32: Comparison of Moment-Rotation Relationship for Beams: A60-1-2-3, A60-B-1 and A60-F-1

| Type of Test | Beam ID | Picture at Failure and Remarks | |
|---|---|---|---|
| **Case-1** *[Solid beam test]* | **A100-1**<br>**A100-2**<br>**A100-3**<br>**A100-4** | The failure pattern included a downward local flange buckle on one side and a permanent lateral deformation on the opposite side.<br> 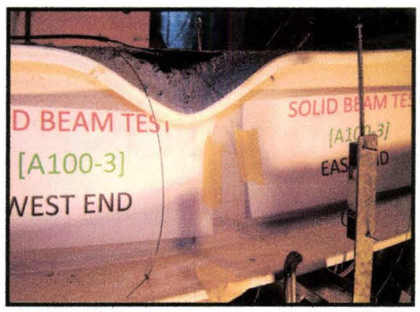 | 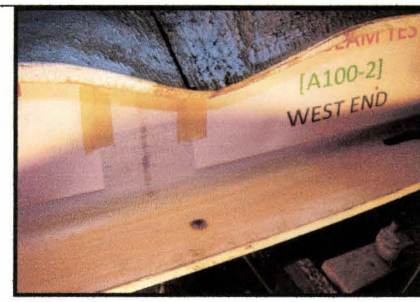  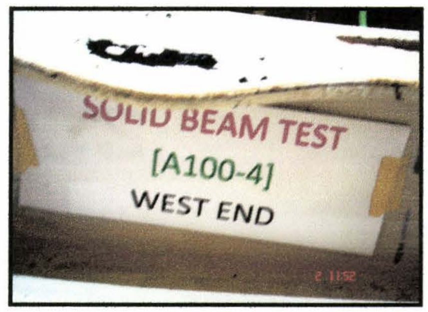  |
| **Case-2** *[Beam test with holes in tension flange only]* | **A90-1** |   | The failure pattern included a downward local flange buckle on one side and a permanent lateral deformation on the opposite side. Holes elongated slightly in the longitudinal direction |
| | **A85-1** |   | The failure pattern included a downward local flange buckle on one side and a permanent lateral deformation on the opposite side. Holes in the tension flanges elongated slightly in the longitudinal direction |

Cont.........

**A80-1**

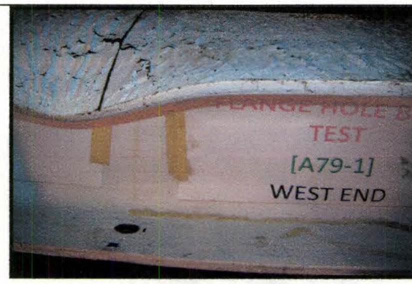


The failure was primarily due to a downward local flange buckle on one side and upward buckle on the opposite side. Holes in the tension flanges elongated in the longitudinal direction and necking at the holes location was visible

**A75-1**
**A75-2**
**A75-3**

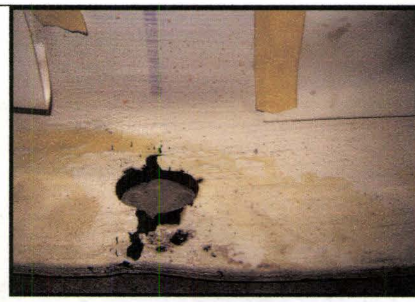

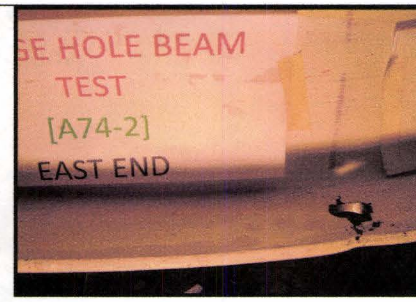



The specimens failed eventually by net-section fracture preceded by local buckle of the compression flange

**A70-1**
**A70-2**
**A70-3**


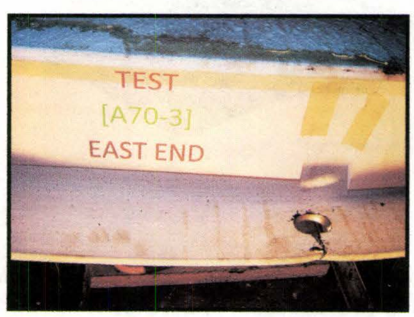


The specimens failed eventually by net-section fracture. Preceded by local buckling of the compression flange

Cont..........

**A60-1**
**A60-2**
**A60-3**

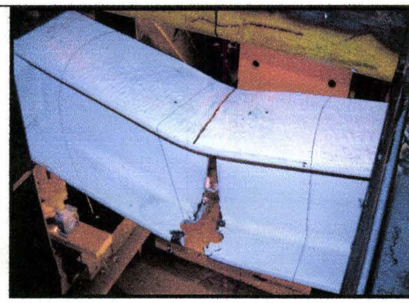

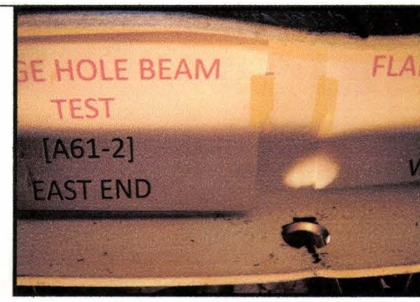



The specimens failed mainly as a result of net-section fracture.

---

**A50-1**


The specimen failed mainly as a result of net-section fracture.

---

**Case-3**
*[Beam test with holes in both tension and compression flanges]*

**A85-B-1**

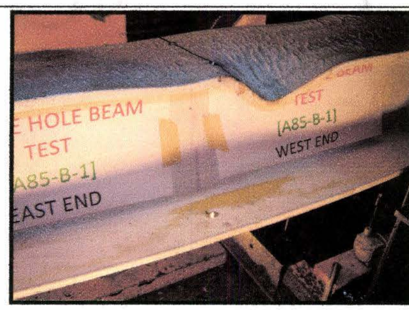


The failure pattern included a downward local flange buckle on one side and a permanent lateral deformation on the opposite side. Holes in the tension flange elongated slightly in the longitudinal direction.

**A75-B-1**

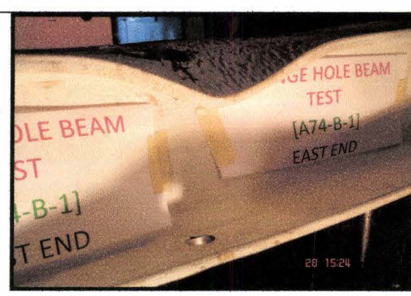


The failure of the specimen was primarily due to local flange buckling. Holes in the tension flange elongated in the longitudinal direction whereas, holes in the compression flange squeezed in the longitudinal direction.

Cont.........

Cont.........

| | | | |
|---|---|---|---|
| **Case-3** *[Beam test with holes in both tension and compression flanges]* | **A70-B-1** | 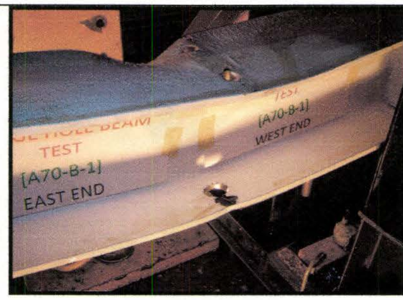  | The specimen failed eventually by necking followed by tension fracture. However, the tension fracture occurred after a noticeable downward local buckle in the compression flange in the mid-span region. |
| | **A60-B-1** | 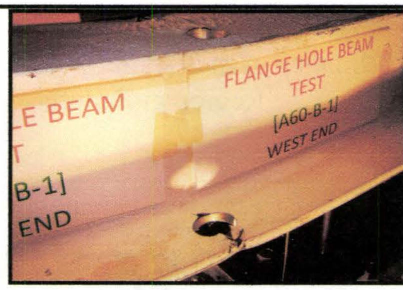  | The specimen failed primarily as a result of net-section fracture. |
| **Case-4** *[Beam test with fastener holes in both tension and compression flanges]* | **A85-F-1** | 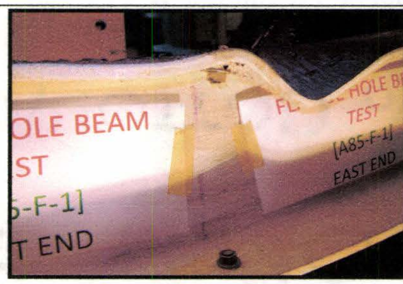  | The failure pattern included a downward local flange buckle on one side and a permanent lateral deformation on the opposite side |
| | **A75-F-1** | 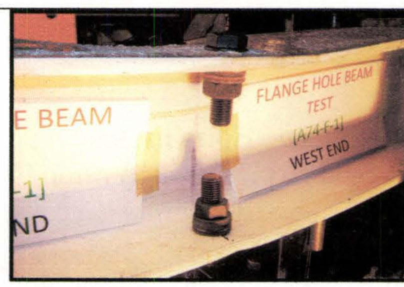  | The specimen failed eventually by net-section fracture preceded by local buckle of the compression flange |
| | **A70-F-1** | 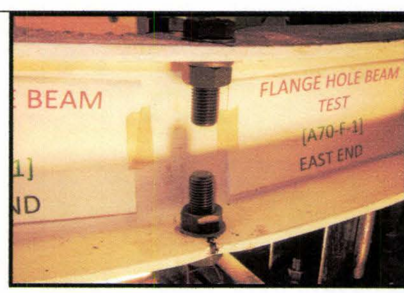  | The specimen primarily failed by net-section fracture. |

Cont.........

| | | |
|---|---|---|
| **A60-F-1** | 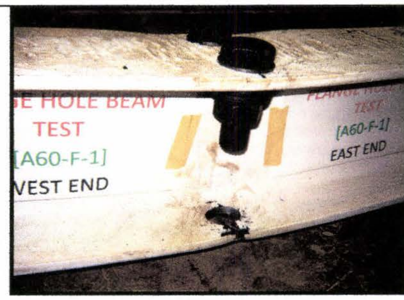  | The specimen primarily failed by net-section fracture. |

Figure 5.33: Photograph Images of the Beam Specimens in the Vicinity of Midspan Region at Failure

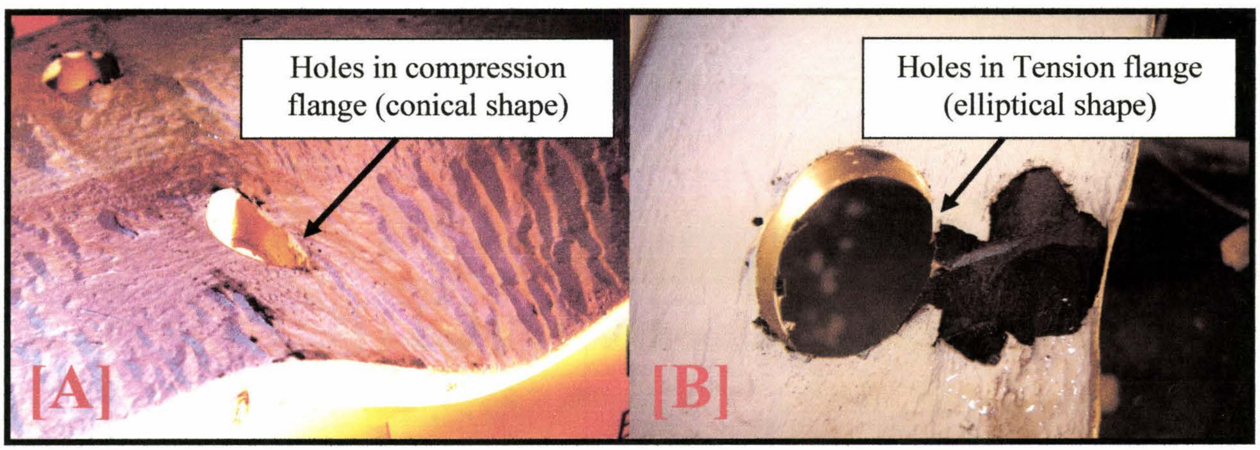


Figure 5.34: Deformation of Flange Holes in Bending [A] Holes in Compression Flange and [B] Holes in Tension Flange

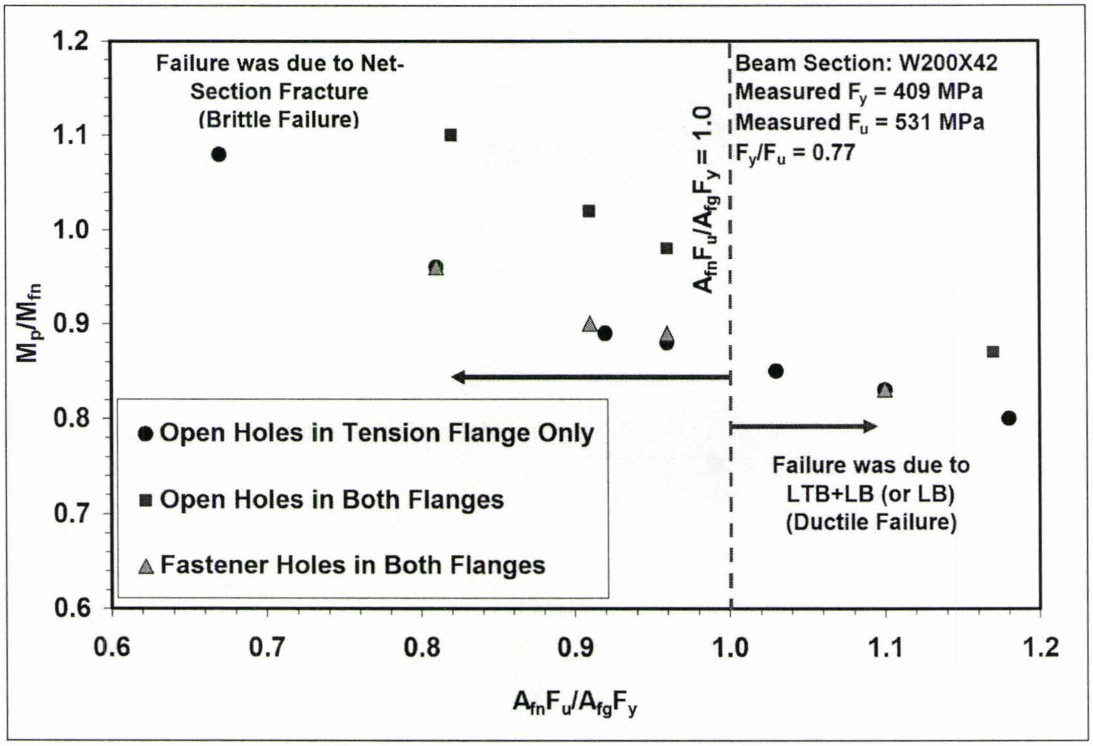


Figure 5.35: Graphical Illustration of the Variation of $M_p/M_{fn}$ versus $A_{fn}F_u/A_{fg}F_y$

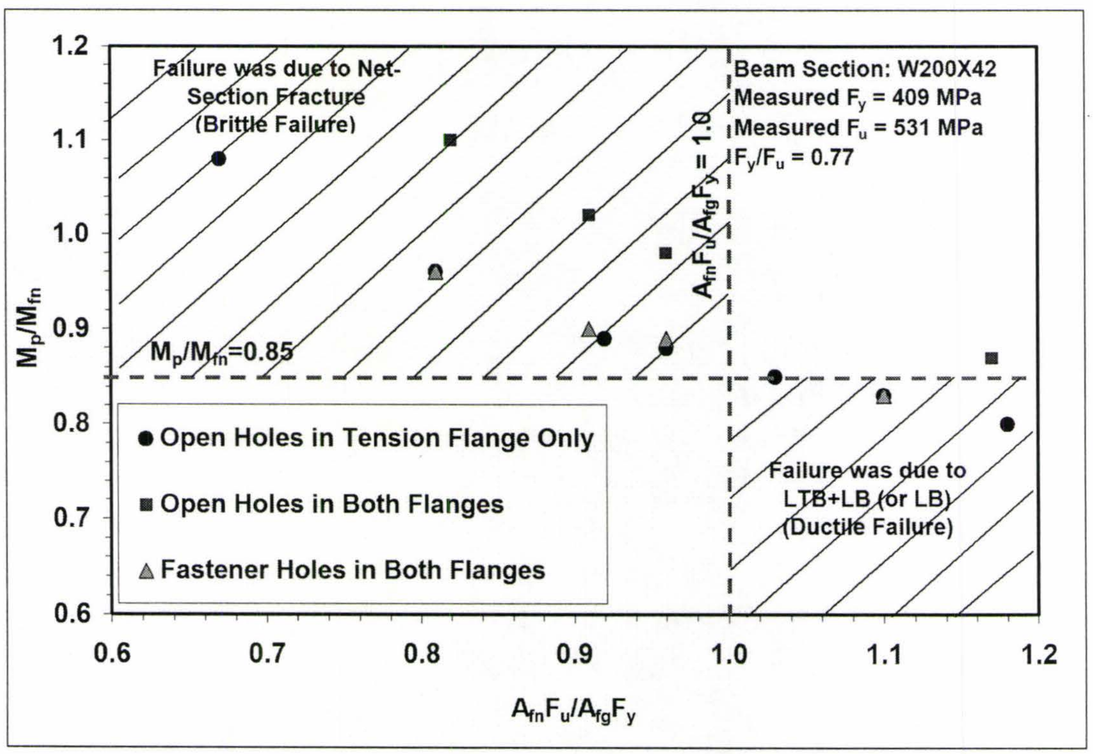


Figure 5.36: Graphical Illustration of Proposed Design Method

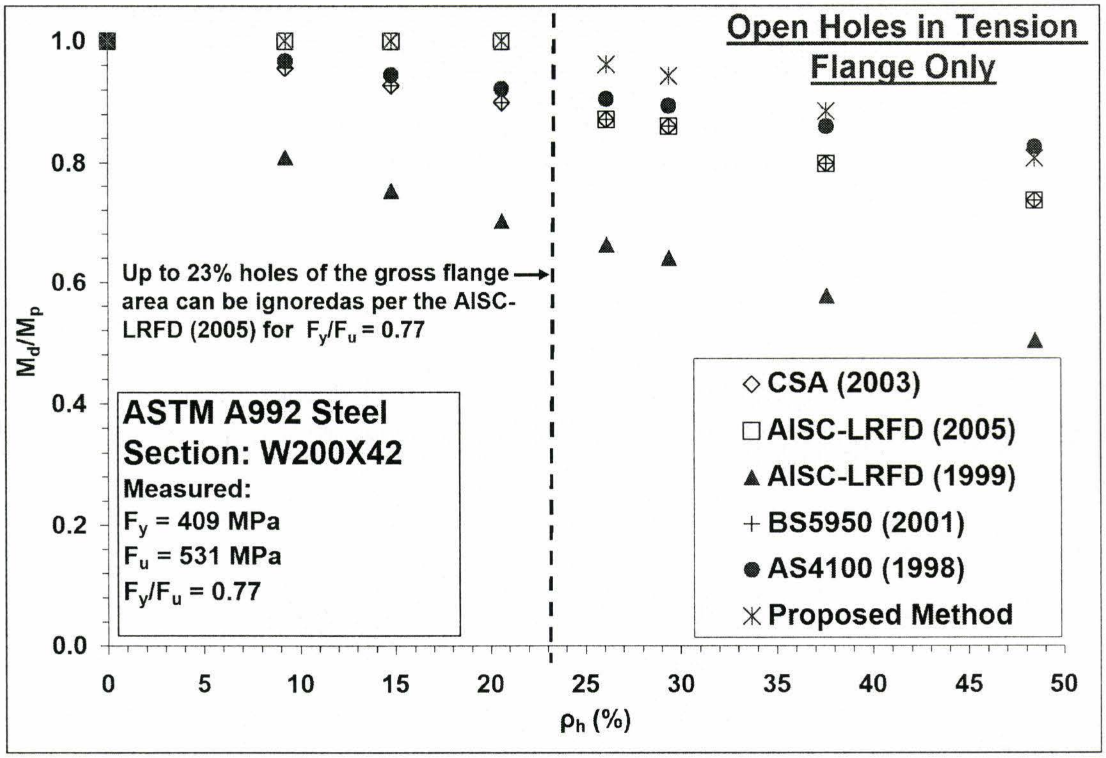


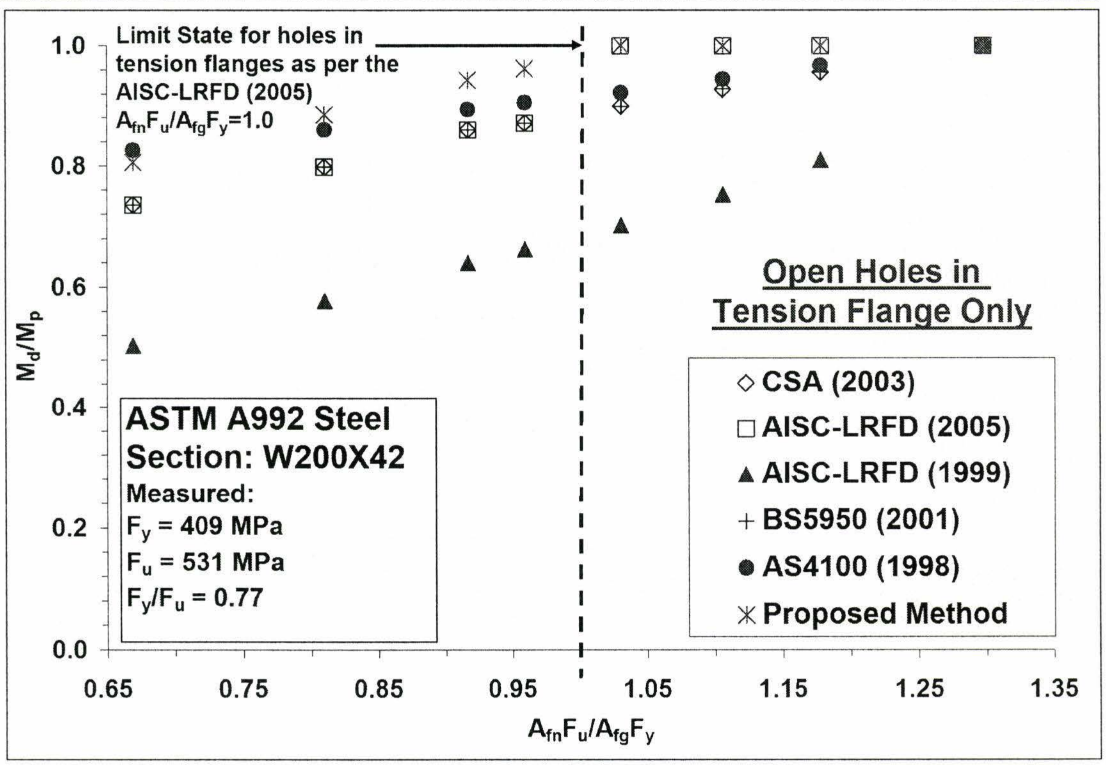


Figure 5.37: Variation of Design Moment Based on Different Code Provisions –Beams with Open Holes in Tension Flange Only

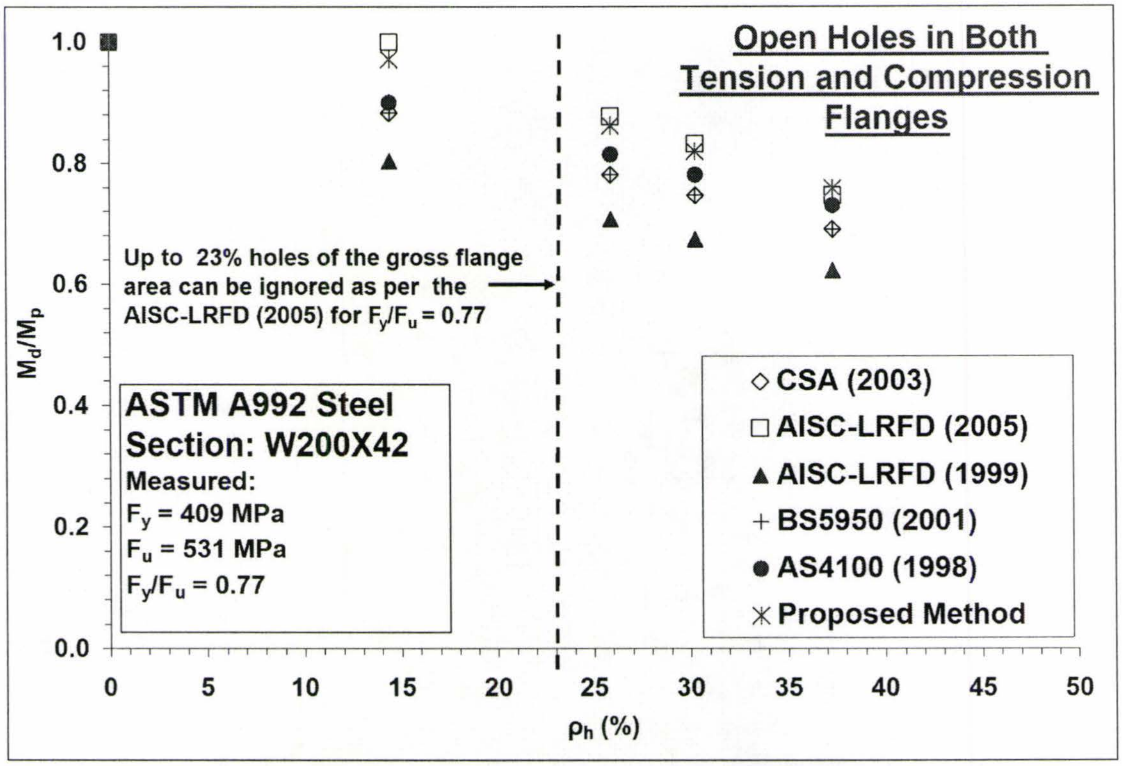


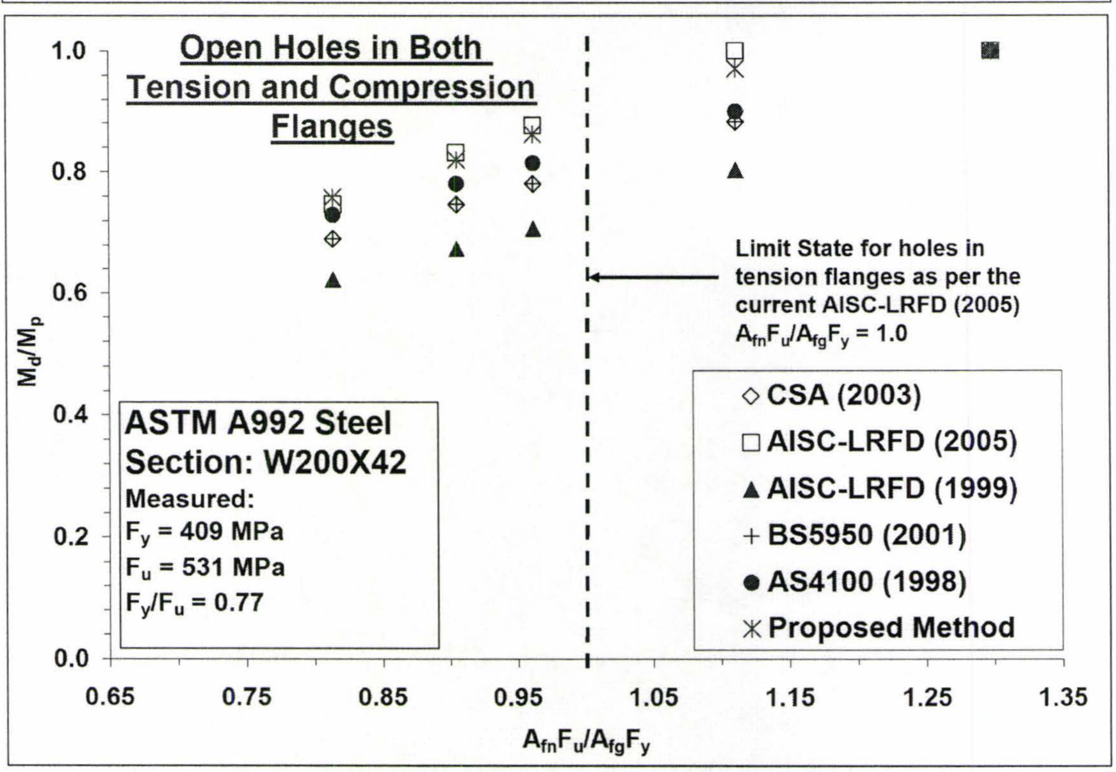


Figure 5.38: Variation of Design Moment Based on Different Code Provisions –Beams with Open Holes in Both Flanges

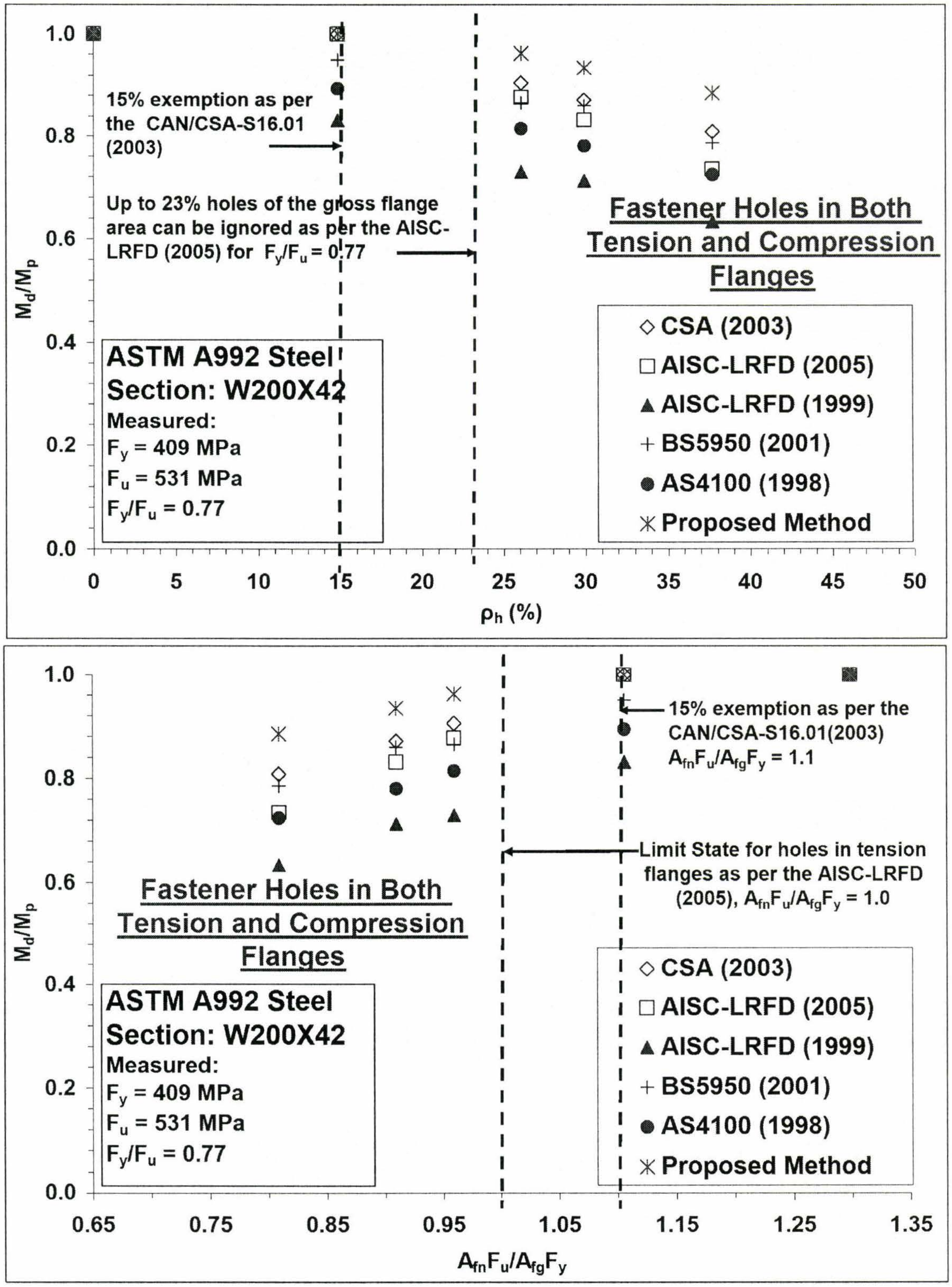


Figure 5.39: Variation of Design Moment Based on Different Code Provisions –Beams with Fastener Holes in Both Flanges

# CHAPTER: 6

# EXPERIMENTAL AND NUMERICAL STUDY OF DIRECT TENSION MEMBERS

## 6.1 Introduction

The objective of this part of the study presented in this chapter was to develop a material model that can capture the behavior of structural steel until fracture. In order to achieve the objective, the experimental and numerical analyses of steel coupons under direct tension loading were performed. The tensile coupons were obtained from wide flange beam sections made of two different steel grades; ASTM A992 steel and 350W steel. The overall stress-strain relationships of these coupons were experimentally established. The tests were simulated with Finite Element (FE) analyses by incorporating a material constitutive relation, which is expected to capture the behavior of the coupon up to fracture. The material constitutive relation was also used to predict the load-deformation behavior of coupons with a hole in the middle region subjected to direct tension loading. The FE results of these coupons were compared with the experimental results of similar samples. In this study, the commercially available ADINA 8.4 Version FE program (ADINA R&D 2007) was used for the finite element analyses.

## 6.2 Experimental Program

The tensile coupon experiments were performed on two different steel grades namely; ASTM A992 steel and the 350W steel. The ASTM A992 steel has been produced since 1997 under the description of "Enhanced A572 Grade 50" (Bjorhovde et al., 2001). More details pertaining to the material definition for the ASTM A992 steel can be found in Chapter 1. The 350W steel is the Canadian standard CSA G40.21 (CISC 2007) steel, which is equivalent to the older version of the ASTM A572 Grade 50 steel. The tensile coupons were cut along the rolling direction of the wide flange (WF) beam section W310X39 (W12X26). The dimensions of the tensile coupons were in accordance with ASTM A370-02 (ASTM 2002) specifications and recommendations. Figure 6.1 shows the dimensions of the tensile coupon used in this test program. The coupons contained a reduced width in order to ensure failure of the specimen within the reduced width. The expected failure was due to necking followed by fracture. Extensometers were attached within the reduced width. As shown in Figure 6.1, the gauge length used to calculate the coupon strain was 200 mm and the nominal width of the reduced region was 40 mm.

### 6.2.1 Test Matrix

A test matrix consisting of twenty eight coupons is presented in Table 6.1. Eight flange coupons and six web coupons were obtained from both the A992 steel section and the 350W steel section. In order to establish the mechanical characteristics of each steel grade, six solid coupons with three from the flanges and three from the webs of each steel grade were tested. The reason for conducting three solid tests from the flanges and webs of each steel grade was to verify the reliability of the test results.

The five coupons obtained from the section flanges of each steel grade were tested as perforated samples having different diameter holes in the middle region. These samples had the net area-to-gross area ($A_n / A_g$) ratio ranging from 0.9 to 0.5 in increments of 0.1. Three coupons obtained from the section webs of each steel grade were also tested with the $A_n / A_g$ ratio varying from 0.9 to 0.5 in increments of 0.2.

The average measured dimensions of each coupon tested are given in Table 6.1. The average width ($w$) and the average thickness ($t$) were established based on several measurements taken within the reduced cross-section. Such measurements were made using a micrometer having a resolution of 1/100 of a millimeter. The initial cross-sectional area was calculated based on these measured dimensions. Table 6.1 also summarizes the average hole diameters ($\phi$) for the perforated samples. In Table 6.1, A992-F1-1.0 and A992-W1-1.0 denote the flange and web coupons taken from the A992 steel section with the $A_n / A_g$ ratio of 1.0, respectively. Using such a name designation system, the remaining coupons used in this study can be identified.

### 6.2.2 Test Procedure

The tension coupon tests were performed using a Tinius Olsen machine with an axial load capacity set at 600 kN. The placement of a specimen in the testing machine is as shown in Figure 6.2. Prior to applying the load, the coupon specimen was aligned vertically and placed at the center position with respect to the grips of the machine's loading platforms. The coupon was gripped by applying a load well within the elastic limit. This was done to ensure that the coupon was correctly gripped. Next, the load was reduced to approximately 2 kN that may be required to grip the coupon steadily. At this stage, the coupon was considered ready for the tensile test.

As shown in Figure 6.2, two extensometers having gauge lengths of 200 mm and 50 mm, respectively, were attached on either face of the test coupon. The larger extensometer was used to acquire data to establish the overall engineering stress-strain curve of the coupon. The smaller extensometer was attached to collect data primarily within the elastic range since it has greater sensitivity in detecting elongations. The increase in sensitivity allowed a more accurate establishment of the initial modulus ($E$) and the proportional limit ($F_{pl}$). The smaller extensometer was detached shortly after the coupon reached its yield strength.

The coupons were tested at a loading rate of 0.5 mm/min in the elastic range. The loading rate was, however, increased to 2.5 mm/min in the strain-hardening range up to the ultimate loads. Beyond the ultimate loads, the loading rate was reduced to 0.5 mm/min up to fracture (Jaquess and Frank, 1999). A lower loading rate was applied in the strain softening region in order to minimize the influence of strain rate on the fracture. Previous studies have shown that higher strain rates result in lower fracture strains (Liu 2005).

Figure 6.3[A] shows the solid samples and the associated failure pattern at fracture. During the tests on solid samples, it was observed that the ductile fracture initiated from the middle part of the necked area. A similar nature of ductile fracture was also observed by Cabezas and Celentano (2004). Figure 6.3[B] shows the perforated samples and the associated failure patterns. As expected, the perforated samples fractured across the hole region.

### 6.2.3 Test Results - Solid Sample

Figures 6.4[A] through 6.4[D] show the experimental stress-strain relationships of the tensile coupons obtained from the flanges and webs of the A992 steel section and the 350W steel section. The engineering stress was established based on the applied load divided by the initial cross-sectional area. The engineering strain was calculated based on the elongation measured by an extensometer divided by the initial gauge length. As seen in Figures 6.4[A] and 6.4[C], the flange coupons of both steel sections strain hardened immediately after yielding. The web coupons of both steel sections exhibited a distinct yield plateau before strain hardening (see Figures 6.3[B] and 6.3[D]).

Table 6.2 summarizes the test results. Here, the comparison and discussion of the test results were made based on the average values. The average yield strength ($F_y$) and average ultimate strength ($F_u$) of the A992-flange coupons were calculated to be 445 MPa and 577 MPa, respectively, resulting in the $F_y / F_u$ ratio value of 0.77. The strains corresponding to the ultimate strength ($\varepsilon_u$) and at fracture ($\varepsilon_f$) were measured to be 13.8% and 21%, respectively. Note that the strains were established over the gauge length of 200 mm. The 350W-flange coupons had the $F_y$ and $F_u$ values of 428 MPa and 578 MPa, respectively, resulting in the $F_y / F_u$ ratio of 0.74. The $\varepsilon_u$ and $\varepsilon_f$ values associated with these coupons were 13.9% and 22%, respectively. The $F_y / F_u$ ratio value for the A992-flange coupon was 4% higher than that of the 350W-flange coupon.

The $F_y$ and $F_u$ values for the A992-web coupons were 409 MPa and 573 MPa, respectively, resulting in the $F_y / F_u$ ratio value of 0.71. These coupons reached the ultimate strength at the strain of 14.5% and fractured at the strain of 21%. The 350W-web coupons had the $F_y$ and $F_u$ values of 416 MPa and 582 MPa, respectively, resulting in the $F_y / F_u$ ratio value of 0.71. These coupons had $\varepsilon_u$ and $\varepsilon_f$ of 15.3% and 19.5%, respectively.

### 6.2.4 Test Results-Coupons With Middle Hole (Perforated Coupons)

Tension members can be uniformly stressed or non-uniformly stressed. Long tension members of constant cross-sectional area are uniformly stressed at regions away from the boundaries. However, often the members subjected to tension may not be uniform in practical applications. The behavior of tension members with holes is considerably different when compared to the behavior of similar solid members having uniform cross-section. Tension members having holes are non-uniformly stressed due to the stress concentration effects in the vicinity of hole region. Often failure as a result of net-section fracture is an undesirable failure mode. The presence of small local holes in a tension member (such as small bolt holes used for the connection of the member) causes early yielding around the holes so that the load-deflection behavior becomes non-linear. When holes are small compared to the gross cross-section, the member may reach the gross-section yield load ( $A_g F_y$ ). On the other hand, when holes are large, the member may fail prior to reaching the $A_g F_y$ due to fracture. Therefore, for yielding to occur in the gross area before fracturing through the net area, it is necessary that

$$A_n F_u > A_g F_y \tag{6.1}$$

or

$$A_n > Y A_g \tag{6.2}$$

where $Y$ is the yield ratio ( $F_y / F_u$ ). It can be seen from Equation 6.2 that for members of the same geometry with the same hole size, the yield ratio determines whether the gross area yields before fracture of the net area.

Table 6.3 summarizes the measured ultimate load ($P_u$), the $P_u / P_y$ ratio values, the ultimate stress across the net-section ($F_{un} = P_u / A_n$) and the strength ratios between the coupons having a middle hole and the solid samples ($F_{un} / F_u$). The gross section yield loads ($P_y$) for the flange and web coupons were established based on the measured cross-section area multiplied by the average measured yield strengths of the flanges and webs, respectively. The coupons having the $A_nF_u / A_gF_y \geq 1.0$ reached an ultimate load higher than $P_y (= A_gF_y)$. The coupons with the $A_nF_u / A_gF_y < 1.0$ fractured prior to reaching $P_y$. Furthermore, as summarized in the ninth column of Table 6.3, the ultimate strengths of perforated samples ($F_{un}$) were between 2%-8% higher than that of the solid samples ($F_u$). A similar observation was made by Fisher (1965). He explained that when holes occur in an axial tension member a free lateral contraction accompanying an axial extension cannot develop. This may result in a slightly higher strength for perforated samples when compared to that of the solid samples (Fisher 1965). As presented in the ninth column of Table 6.3, the strength ratios had no definite pattern (scatter). This may be due to various factors such as variations in material properties, geometric imperfections, hole making practices, etc. (Fisher 1965).

Table 6.4 compares the perforated sample test results with the unfactored design load calculated as per the clause 13.2 of the CSA (2003) standard. According to this clause, the unfactored tensile resistance developed by a direct member subjected to an axial tensile force shall be taken as the least of the gross-section yield load ($A_gF_y$) or the net section fracture load (0.85 $A_n F_u$). As seen in the sixth column of Table 6.4, the ultimate test loads were 20%-28% higher than the code predicted values. This is due to the code allowance of 85% of the tensile strength ($F_u$). The following section provides the development of material model, which is expected to capture the behavior of the coupons up to fracture, based on the experimental-numerical simulations.

## 6.3 Development of Material Model

### 6.3.1 Introduction

Figure 6.5 shows a typical engineering stress-strain relationship for a structural steel. In general, a standard uniaxial tensile test is considered to provide the basic tensile properties of a material in the range of small elastic-plastic deformations. The tensile test leads to the knowledge of the intrinsic stress-strain relation during its uniform loading history up to a certain point. In tensile testing, the uniform extension ceases when the load exceeds the maximum load, which is referred to as the ultimate load, $P_u$. At this stage, the specimen reaches its tensile strength ($F_u$) (see Figure 6.5). Beyond this limit, the material appears to strain soften due to necking of the sample. Once the specimen begins to 'neck', the distribution of stresses and strains become complex and the magnitude of such quantities become difficult to establish (Mackenzie et al., 1977).

### 6.3.2 Description of Regions

Figure 6.6 shows the stress versus strain relationship that is characteristic of many steels for structural applications. As seen in the figure, the stress-strain variation can be divided into five different regions as follows;

- Region-I (elastic range): during the initial stages of loading, stress varies linearly proportional to strain (up to a proportional limit). The stress at the proportional limit is typically established using the 0.01% strain offset method (Galambos 1998). Thus, the stress can be related to strain as

  $$0 < F_e \le F_{pl}; 0 < \varepsilon_e \le \varepsilon_{pl}; \qquad F_e = E\varepsilon_e \tag{6.3}$$

  where $F_e$ is the engineering stress, $\varepsilon_e$ is the engineering strain and $E$ is the initial elastic modulus.

- Region-II: represents a region from a proportional limit to the yield limit. In this region, the variation of stress-strain relationship can be idealized as

  $$F_{pl} < F_e \le F_y; \varepsilon_{pl} < \varepsilon_e \le \varepsilon_y; \qquad F_e = E_t\varepsilon_e \tag{6.4}$$

  where $F_y$ is the yield strength established based on the 0.2% offset method, $\varepsilon_y$ is the corresponding yield strain and $E_t$ is the tangent modulus $[E_t = (F_y - F_{pl})/(\varepsilon_y - \varepsilon_{pl})]$.

- Region-III: after the initiation of yielding, there may be a yield plateau. As the variation of stress is assumed to be constant along the yield plateau;

  $$\varepsilon_y < \varepsilon_e \le \varepsilon_{sh}; \qquad F_e = F_y \tag{6.5}$$

where $\varepsilon_{sh}$ is the strain at the onset of hardening. The ratio between $\varepsilon_{sh}$ and $\varepsilon_y$ is defined as, $m = \varepsilon_{sh} / \varepsilon_y$.

- Region-IV: at the end of yield plateau, strain hardening begins, with a subsequent increase in strength; $F_y < F_e \leq F_u; \varepsilon_{sh} < \varepsilon \leq \varepsilon_u$; $\qquad F_e = F_e(\varepsilon_e)$ (6.6)

  where $F_u$ is the ultimate strength.

The constitutive model requires the true stress-strain curve of the material in order to carry out the numerical analysis. The true stress versus the true strain relationship can be established directly from the engineering stress versus the engineering strain relationship as

$$\varepsilon_t = \ln(1 + \varepsilon_e) \tag{6.7}$$

$$F_t = F_e(1 + \varepsilon_e) \tag{6.8}$$

Equations 6.7 and 6.8 are valid up to onset of necking (ultimate strength). Equations 6.7 and 6.8 are derived based on two assumptions; (1) the stresses are uniform across the specimen and (2) material flows with negligible volume change. Since the stresses are no longer uniformly distributed over a gauge length beyond the onset of necking (i.e., strain localization begins after the onset of necking), these equations become invalid in the post ultimate strength range.

A power-law is often used to represent a flow curve relating true stress-strain relationship in the strain hardening region of a material (Holloman 1945 and Bruneau et al., 1998). Thus, the true stress-strain relation established from the engineering stress-strain relation (using Equations 6.7 and 6.8) was fitted with a power-law model by using a least square analysis.

- Region-V: represents the post ultimate strength behavior of the material. As explained the stresses and strains become more complex after the formation of necking, true stress-strain relation in this region cannot be established from a standard tensile test. Therefore, an-experimental-numerical methodology is helpful to derive the material behavior beyond onset of necking. The following section describes the related studies dealing with the establishment of true stress-strain relation after onset of necking.

## 6.4 Numerical Simulation of Tensile Test

### 6.4.1 Introduction

The accuracy and the validity of predicted global structural behavior and the associated failure mode depend on, in part, on the characterization of material behavior. The material behavior is generally established by means of uniaxial tensile testing. For ductile materials, however, specimen necking leads to the loss of homogeneous material response resulting from subsequent nonuniform deformation. This makes the local characterization difficult particularly for applications such as metal forming, analysis of bolted connections in a steel structure, analysis of corroded steel pipes, bulk forming operations (drawing, extrusion, and rolling) etc. In Finite Element (FE) modeling of such applications, understanding of the material behavior beyond necking up to fracture is needed. Data collected from a standard tensile test, however, would provide sufficient information pertaining to the material behavior up to the initiation of necking (see previous section). During the post necking stage, the standard tensile test would provide only an average stress-strain relation, which can seriously limit the use of FE models for large strain applications (Ling 1996). Since this study focuses on the effects of flange holes on the flexural behavior of steel beams including fracture, a characterization of the post ultimate strength behavior is needed together with numerical analyses to capture the local behavior at the flange hole locations.

### 6.4.2 A Literature Review – True Stress-Strain Relation in the Post Ultimate Strength Range (During Necking): Region-V

The tensile test is an important standard engineering procedure useful for characterizing relevant elastic and plastic variables related to the mechanical behavior of materials. Owing to the non-uniform stress and strain distributions existing at the neck for high levels of axial deformation, it has long been recognized that significant changes in the geometric configurations of the specimen have to be considered to properly describe the material response during the whole deformation process up to the fracture stage (Cabezas et al, 2003). Numerous approaches have been applied in the past to establish the true stress-strain relationship during necking (or in the post ultimate strength range). Early work on the uniaxial tension test by Bridgman (1952) quantified the multi-axial stress and strain distributions across the neck. The results suggested a uniform axial strain and a nonuniform axial stress across the specimen's neck. Bridgman's (1952) analysis employed classical methods to relate the local stresses and strains at the neck to the global load or average stresses. Bridgman's (1952) method requires continuous measurements associated with the reduction of diameter, which can be used to establish the necking curvature during the test. Thus, this method needs an advanced testing technique.

Zhang et al. (1994) proposed an alternative method to obtain the true stress-true strain relation in the post ultimate strength range (or during necking). In this method, the experimental tensile load-extension curve is considered as the target and the true stress-true strain relation is determined using an iterative method (trial and error). This iterative procedure is performed based on the FE analysis until the target is reached, within a tolerance. Although, this method was originally proposed for round samples, the concept of this method can also be applied to flat samples. The main advantage of this method is that the true stress-true strain data can be extracted from standard tensile test results without interrupting the test at different loads to establish profiles and dimensions at the neck. The main short coming of this method is that the entire stress-strain relation during necking is treated as unknown and iterations using a trial and error procedure are required for a series of strain intervals until good correlation with the post necking behavior of experimental results is attained. Thus, this method is computationally intensive and time-consuming.

Ling (1996) proposed a method based on a weighted-average method for determining uniaxial true tensile stress versus strain relation during necking for flat samples. The method requires identification of a lower and an upper bound for the true stress-strain function during necking and expresses the true stress-strain relation as the weighted average of these two bounds. According to Ling's (1996) method, a power-low fit, which represents strain hardening region of the flow curve, can be used to extrapolate the true-stress strain relation in the post ultimate strength region (Region-V). However, various studies on the numerical simulation of tensile specimens made of different alloys have indicated that the extrapolation of true stress-strain relation based on the power-law fit seems to underestimate the experimental stress-strain curve during necking (Ling 1996). On the other hand, for the same alloys, the true stress-strain relation established based on a linear hardening model has been found to overestimate the experimental curves during necking (Ling 1996). This observation was also supported by other researchers (by comparing the experimental and numerically obtained stress-strain curves) who have concluded that the strain hardening rate generally decreases with increasing true strain (Matic et al, 1988, Tvergaard 1993, Fukazawa and Butler, 1996, and Cabezas et al, 2004).

A linear hardening model, representing the variation of true stress ($F_t$)-true strain ($\varepsilon_t$) relation beyond the onset of necking can be given as

$$F_t = a_0 + a_1\varepsilon_t \tag{6.9}$$

where $a_0$ and $a_1$ are constants to be determined. These constants are determined using Considére Criterion (1885). That is, at onset of necking the following two relationships can be used;

$$F_t\big|_{\varepsilon=\varepsilon_{u,t}} = F_{u,t} \quad \& \quad \left.\frac{dF_t}{d\varepsilon_t}\right|_{\varepsilon=\varepsilon_{u,t}} = F_{u,t} \tag{6.10}$$

where $F_{u,t}$ and $\varepsilon_{u,t}$ are true stress value and true strain value corresponding to the onset of necking, respectively. Considering Equations 6.9 and 6.10, $a_0 = F_{u,t}(1-\varepsilon_{u,t})$ and $a_1 = F_{u,t}$. Hence, Equation 6.9 can be modified as; $F_t = F_{u,t}(1+\varepsilon_t - \varepsilon_{u,t})$. The $F_{u,t}$ and $\varepsilon_{u,t}$ are directly obtained from the tensile coupon test.

Since the lower and upper bounds for true stresses in the post ultimate strength region (Region-V) have been identified, Ling (1996) has proposed a better approximation on the true stress (in Region-V) by employing a weighted average of the power-law hardening (lower bound) and the linear hardening models (upper bound). Based on the weighted average method, the true stress-strain relation in the post ultimate strength region, Region-V) is related as

$$F_t = F_{u,t}\left[ w \underbrace{\left(\frac{\varepsilon_t^{\,n}}{n^n}\right)}_{Power-Law} + (1-w)\underbrace{(1+\varepsilon_t - \varepsilon_{u,t})}_{Linear-assumption} \right] \tag{6.11}$$

where $w$ is the unknown weight constant and ranges between $0 \le w \le 1$.

A suitable weight constant is established iteratively by numerical simulation of tensile test until a good correlation between the calculated and the experimental load extension curve is achieved. In other words, the experimental curve is considered to be a target curve and the numerical simulation of the sample coupon (using FE method) is performed using different $w$ until a good agreement is attained. It has been found experimentally that the largest error occurs immediately before fracture (Ling 1996). By comparing the experimental (stress and strain) values with those values obtained by FE simulation (calculated values) at fracture, a suitable weight constant will be established. The following section presents with regards to the FE modeling procedure employed in this research program.

### 6.4.3 Finite Element Modeling Procedure

The FE program ADINA 8.4 version (ADINA R&D 2007) was utilized to simulate the tensile test results. The test coupon was modeled using 4-node shell element with six degree of freedom per node (three translations and three rotations). The shell element can be employed to model thick and thin general shell structures and it accounts for finite strains by allowing changes in the element thickness (Bathe 1996). Therefore, they are suitable for large strain analyses involving inelastic deformation of material with nonzero effective Poisson's ratio (Bathe 1996). Also, this shell element can be efficiently used with plastic multi-linear material models for large-displacement/large-strain analyses (Cabezas et al., 2004). The shell element has 2x2 integration points in the mid surface (in r-s plane). Through the thickness of shell elements, 3 Gauss numerical integration points were employed (in t-direction).

The FE analysis incorporated both geometric and material non-linearities. The material properties used were a true stress and strain relationship derived from the engineering stress versus strain curve obtained from tension coupon tests up to the ultimate strength as shown in Figure 6.6. The von Mises yield criterion was used. The von Mises yield criterion can be interpreted physically as implying that plastic flow occurs when shear strain energy exceeds a critical value. This (von Mises) yield criterion is often used to estimate the yielding of ductile materials such as steels. A flow rule relates the plastic strain rates to the current stresses and the stress increments subsequent to yielding and a hardening rule specifies how yield condition is modified during the plastic flow. Since it is observed experimentally that metals such as steel obey the associated flow rule, ADINA metal plasticity model which is characterized as an associated flow plasticity model with isotropic hardening rule was employed in this study.

To capture highly localized strains and stresses that develop during necking, an additional point (point $E^1$ in Figure 6.6) was needed on the true stress versus strain curve beyond the ultimate stress (point $D^1$ in Figure 6.6). As discussed, the true stress-strain relation between point $D^1$ and $E^1$ as shown in Figure 6.6 was established using the weighted average method. An investigation on ductile fracture by Khoo (2000) indicated that the localized fracture strains for structural steel grade under uniaxial tensile load vary between 80% and 120%. Therefore, an equivalent fracture strain ( $\varepsilon_{f,t}$ ) of 100% was used in this study (i.e., true strain at point E[1] in Figure 6.6). Moreover, the use of maximum fracture strain of 100% can be thought of as an average value. It should be pointed out that it is unlikely that one can accurately determine the fracture strain through calculation or even through any conventional or standardize measurement techniques (Tseng 1990). At best the strain at fracture can be established by measuring the cross sectional area at fracture ( $A_f$ ) as

$$\varepsilon_{f,t} = \ln\left[\frac{A_g}{A_f}\right] \tag{6.12}$$

Based on Equation 6.12, true strain at fracture was estimated for the solid samples tested in this program. The calculated values ( $\varepsilon_{f,t}$ ) ranged between 65% and 75%. However, it was believed that the calculated values may be lower than the actual $\varepsilon_{f,t}$ since the cross-section at the fracture location was established after the test, by measuring the reduced width and the reduced thickness using a micrometer, which gives approximate $A_f$ . To establish the final area accurately, however, a more advanced technique must be employed to establish the final profile of the sample at the fractured location.

For a flat specimens, such as used in this study, subjected to an axial load, $P$ , necking occurs when $P$ reaches a maximum. Subsequently, the necking is spread over a length of the order of the width $b$ while the rest of the specimen remains prismatic as shown in Figure 6.7 (Bao 2004). This type of necking, which usually occurs in flat specimens, is known as diffuse necking. If diffuse necking continues, localized necking, which is also shown in Figure 6.7, may occur over a length of the order of the sheet thickness.

Figure 6.8 shows the FE model for a solid coupon sample. The model incorporated a geometric imperfection of a half sine wave along the gauge length (200 mm). The reason for selecting this type of imperfection was to simulate the variation of diffuse necking that may occur in the test sample. Maximum amplitude of 0.1% of the nominal width (40 mm) was used ($\delta_0 = 0.04$ mm). This value was chosen based on the geometric measurements made on the test specimens. It was noted that the all flange coupons had a maximum variation in the nominal width (40 mm) of less than 0.1%. Similarly, all web coupons (except 350W-W2-1.0 which had a slightly higher variation of 0.13%), were found to have a maximum imperfection of less than 0.1% of the nominal width (40 mm).

A fine mesh was introduced at the center of the sample for a length of 50 mm where the strain gradient is expected to be large. This length was selected since the diffuse necking spread over a length of the order of the width $b$ (= 40 mm). Models having meshes of 1 mm x 1 mm and 2 mm x 2 mm within the gauge length were analyzed to check the numerical convergence. The load-extension curves obtained for these two different meshes were found to be almost identical. Therefore, the mesh of 2 mm x 2 mm was considered to be adequate. Away from the center region (necking region), a coarse mesh was employed since the strain demand in such locations is considerably smaller than the regions where necking initiates. Here, a full model of the test sample was considered to compare the local and global behavior of the FE model with the test samples. In the FE model, one of the edges was fully restrained to simulate a rigid clamping action existing in the experiment. The loading edge was permitted to translate in the loading direction while restraining the remaining translations and rotations (see Figure 6.8).

A uniform displacement was applied in small incremental step. Initially, a prescribed increment of 0.15 mm was used. However, beyond the ultimate load, the ADINA FE program self-adjusted to find a suitable size of displacement to continue the loading until fracture due to a severe non-uniform distribution of stresses and strains during necking. The displacements at nodes, located 200 mm apart within the reduced width, were monitored at each load steps to evaluate the variation of the average engineering strain. The corresponding tensile load was established by summing the reactions at the loaded nodes. The resultant load was then, divided by the initial cross-sectional area to obtain the average engineering stress at each load step. This procedure was followed to simulate the experimental testing method used in this study, where a 200 mm gauge length extensometer was used to establish the overall variation of the average engineering strain.

## 6.5 FE Results

### 6.5.1 Solid Coupons

This section presents the numerical study of the mechanical behavior of the tension coupons obtained from the flanges and the webs of the A992 steel and the 350W steel. Owing to complex stress state that develops at the neck for high levels of axial deformation, an experimental-numerical methodology was followed to derive appropriate constitutive relations which characterize the material response. This section presents a detailed comparison between the experimental and numerical stress-strain curves for the standard tensile coupons. The analysis of necking phenomenon and the mechanism of ductile fracture at different loading stages is also discussed in this section. The material constitutive relations developed based on the experimental-numerical analysis of the standard coupons were used to establish the load-deformation behavior of perforated samples. A comparison between the test results and the FE results is made.

*A992-flange coupon*: Figure 6.9[A] shows the true stress-strain relation for the A992 flange coupon. This figure shows material constitutive relation derived using power law extrapolation, linear extrapolation and weighted average method with $w$=0.6. From this figure, one observes that there are two regions: [1] prior to onset of necking; and [2] during necking. The true stress-strain relation up to the onset of necking was directly obtained from the tensile test on flat coupons. The true stress-strain relation beyond onset of necking and up to fracture (Region-V) was established based on the weighted average method procedure (Ling 1996). Figure 6.9[B] shows a comparison between the experimental stress-strain curve and the numerically reproduced curve. In order to illustrate how a suitable weighting constant, $w$, can be chosen, three different values; $w$=1.0, $w$=0.6 and $w$=0.4 were considered in the numerical simulation. For $w$=1.0, representing the extrapolation of true stress-strain relation in Region-V solely by a power-law hardening model, the numerically reproduced curve was found to fall well below the experimental curve in the post ultimate strength region (see Figure 6.9[B]). However, for $w$=0.4, the numerically established curve was slightly above the experimental curve. Finally, a slightly larger value $w$=0.6 was used, which resulted in the calculated and the experimental stress-strain curves agreeing well.

In summary, when true stresses are underestimated, a material possesses less strain hardening than it should have. This insufficient strain hardening is directly reflected in the calculated load-extension curve, which falls below the test curve (target curve). On the other hand, if true stresses are overestimated, the material will have excessive strain hardening and the calculated curve falls above the test curve (target curve). Although a suitable weight constant ( $w$ ) that can reproduce the experimental stress-strain curve close enough needs to be established by trial and error approach, only a few trials were required to obtain a reasonable weighting constant.

*A992-web coupon*: Figure 6.10[A] shows the true stress-strain relation derived using $w$=0.5 (in Region-V). Figure 6.10[B] compares the test curves with the calculated curve. For $w$=0.5, the calculated curve had a good correlation with the target curve (experimental curve).

*350W-flange coupon*: Figure 6.11[A] shows the true stress-strain relation obtained using $w$=0.6 in the post ultimate strength region (Region-V). As discussed, the true stress-strain relation up to the onset of necking was directly obtained from the tensile test on flat flange coupons of 350W steel. As seen in Figure 6.11[B], the calculated (by numerical simulation) stress-strain curve reasonably agreed with the test curve (target curve) for $w$=0.6.

*350W-web coupon*: Figure 6.12[A] shows the material constitutive relation established based on the experimental-numerical simulation. As seen in Figure 6.13[B], the calculated curve had reasonably good correlation with the experimental curve for $w$=0.5.

In summary, the shape of the stress-strain curve after onset of necking (in the post ultimate strength range: Region-V) was determined by a trial-and-error method until the numerical calculation of the load and necking deformation corresponded well with the test data. The procedure associated with the development of material model is as follows; Step 1: establish the pre-necking true stress-strain curve directly from the experimentally obtained engineering stress-strain curve using Equations 6.7 and 6.8.

Step 2: use a power-law model fit to the true stress-strain curve in the strain hardening range (Region-IV), which is known as flow curve.

Step 3: establish the true stress-strain relation by assigning a weighting constant to interpolate the true stress-strain relation between the power-law extrapolation and the liner extrapolation of the true stress-strain relation in Region-V [Equation 6.11].

Step 4: perform numerical simulation with the true stress-strain curve obtained in Step 1 and in Step 3.

Step 5: compare the calculated load-displacement response (or stress-strain response) with the experiments and calculate the relative error at fracture point.

Step 6: adjust the true stress-strain curve in Region-V by using different weighting constant. `

Step 7: repeat Step 4 and Step 6 until the relative error becomes satisfactory. The relative error can be estimated by comparing the experimentally obtained stresses and strains at fracture with the corresponding values established numerically (see Table 6.5).

Based on the FE simulation of tensile tests in this study, the weighting constant $w$=0.6 and $w$=0.5 were close enough to reproduce the stress-strain curve established from the flanges and webs of both ASTM A992 steel and 350W steel, respectively. Table 6.5 summarizes the experimental as well as the calculated (using FE analysis) stresses and strains at fracture. The calculated stresses and strains were compared with the average experimental values of three samples at fracture. In FE models, a sudden drop in load occurred as a result of fracture as seen in the Figures 6.9[B] through 6.12[B]. This point was considered as a 'fracture point' and the corresponding stresses and strains were established. As presented in Table 6.5, the fracture stresses obtained by the FE method varied by a maximum 3% when compared to the corresponding experimental values. The fracture strain obtained by the FE method differed by a maximum 5% when compared to the corresponding experimental values. Since the calculated stresses and strains at fracture varied within 5% of the corresponding experimental values as well as the overall shape of the numerically reproduced stress-strain curve had a close agreement with that of experimentally obtained variation (see Figures 6.9[B] through 6.12[B]), the selected weighting constants, $w$=0.6 for flanges and $w$=0.5 for web coupons were reasonably close enough to reproduce the test curve (target curve).

### 6.5.2 Perforated Coupons

The FE analysis of the load-extension responses of perforated samples was carried out using the material constitutive relations developed based on the experimental-numerical simulation of standard coupons. Figure 6.13 compares the FE results with the test results for the perforated samples obtained from the flanges and webs of the A992 steel section. As seen in Figure 6.13, the calculated (using FE models) average stress-strain responses showed a reasonably good agreement with the test responses. Figure 6.14 compares the experimental results with the FE results for the perorated samples obtained from the flanges and webs of the 350W steel section. From this figure, one observes that the numerical simulation agreed well with the experimental results. As seen in the figure, the FE results had a reasonably good correlation with the experimental results.

Table 6.6 presents the experimentally and numerically obtained ultimate strength values for the perforated coupons. As indicated in the fifth column of Table 6.6, the FE results varied by less than 5% when compared to the experimental results.

## 6.6 Summary of FE Based Simulation Results

Figure 6.15 shows a representative FE model used to simulate the standard coupon test. This figure also illustrates the associated failure of the model due to necking followed by fracture. Figure 6.16 illustrates how the stresses and strains in a tensile sample varied from uniform stages to nonuniform stages beyond the onset of necking. As seen in this figure, the inward transverse displacement increased uniformly throughout the length during the earlier stages of deformation; up to the onset of necking. Beyond this point, the inward transverse displacement seemed to increase only locally at the necked cross-section. This phenomenon reveals that a highly localized deformation takes place beyond the onset of necking and thus, the stresses and strains present in the tensile samples are no longer uniform.

Figure 6.17 illustrates the evolution of plastic zones during the large deformation of the flange coupon of the A992 steel. As seen in this figure, the simulation indicated that at the final strain of approximately 100%, the necked region was largely strained whereas, farthest from the necked region, the specimen had only a very small strain of approximately 0.25%. One also observes from Figure 6.17 that at a strain of approximately 9%, the entire reduced region was strained plastically, whereas the wider ends remained elastic during the complete deformation history. When elongation increases further, a remarkable decrease of plastic zone is observed implying a sharp decrease in the load carrying capacity. However, at the final strain of approximately 100%, only the necked region of the tensile specimen remains plastic and all other parts have been unloaded elastically. A similar observation was made on the simulation of remaining coupons in this study. Moreover, it can be observed from Figure 6.17[C] that fracture in the FE model of the solid tensile sample occurred at the center of the sample where the maximum strain occurs.

Figure 6.18 shows the distribution of effective plastic strain at fracture for a tensile specimen with a hole in the middle. As seen in this figure, a maximum of approximately 100% strain occurred at the hole edge, which is perpendicular to the loading direction. Farthest from the hole region, the specimen unloaded elastically corresponding to an effective strain distribution of 0.04%. Moreover, the critical effective plastic strain of 100% occurred earlier in the perforated specimen than in the solid specimen due to the effects of stress concentration. Figure 6.19 compares the propagation of fracture observed in the experiment and in the FE simulation. As seen in Figure 6.19, the fracture propagated through the edges of hole perpendicular to the loading direction where a highly localized stress concentration occurs. A comparable failure pattern can be seen in the figure between the test sample and the numerically simulated sample.

Overall, a good correlation existed between the test samples and the FE models of the similar samples in terms of the load-elongation (or average stress-strain relation) behavior. The slight discrepancies between the test results and the FE results may be attributed to the following factors;

- The variations in the actual geometric imperfections present in the test sample and the assumed idealized geometric imperfections used in the FE model.
- The method of hole making practice may influence the material property adjacent to hole region, which was not taken into account in the FE simulation, i.e., the FE simulation assumed that the material was homogenous throughout a sample.
- Necking and its evolution are mainly governed by strain hardening. Accurately describing strain hardening was often critical in a numerical simulation
- The final elongation of the specimen may depend on other effects such as the applied strain rate and temperature. In the FE simulation, such factors were not taken into account.
- The variations in the effective critical plastic strain. Throughout the FE simulation, the effective critical plastic strain of 100% was assumed in this study.
- The use of constant Poison's ratio ($\nu$) of 0.3 in the FE model, however, Poison's ratio ($\nu$) of the test sample during deformation changes continuously (Liu 2005).

## 6.7 Conclusions

- The average yield strength of the flange coupons of the A992 steel was 4% higher than that of the 350W steel. The average ultimate strength of the flange coupons obtained from both steel grades was closer to each other. The A992 flange coupons had the average yield ratio 4% higher than the 350W steel. The average ductility ratio of the A992 flange coupons was approximately 9% lower than that of 350W steel.
- The ductility of axial tension members was greatly reduced when the net section fracture strength ( $A_n F_u$ ) was lower than the gross section yield strength ( $A_g F_y$ ).
- A suitable weighting constant ($w$) that can closely reproduce the experimental stress-strain relationship of standard coupons, can be obtained in a few trials.
- The power-law relations established in the strain hardening region of the flanges of A992 and 350W steel sections exhibited a close agreement to each other, although slight variations did occur. A weighting constant, $w = 0.6$, was established to predict the post necking behavior of the flanges of these steels (see Figures 6.9 and 6.11).
- The webs of these steel sections exhibited a similar power law relationship in the strain hardening region. However, a weighting constant, $w = 0.5$, was used to establish the post necking behavior of the web of the A992 and 350W steel sections (see Figures 6.10 and 6.12)

- By employing proper FE modeling of a standard tensile coupon, the load-elongation behavior up to fracture can be numerically reproduced.
- The developed material constitutive relation based on the experimental-numerical simulation provided a good load-deformation behavior of perforated samples.
- In all calculated stress-strain curves for the standard coupons, the stresses and strains at fracture differed by less than 5% when compared to the corresponding results from the experiment.
- The material models developed from the numerical simulation of the standard coupons was able to predict the load deformation behavior of perforated coupons in reasonably well, although slight variations did occur at the final elongations.

Table 6.1: Measured Dimensions of Tensile Coupons

| **Specimen ID** (1) | $t$ (mm) (2) | $w$ (mm) (3) | **Hole Diameter** $\varphi$ (mm) (4) |
|---|---|---|---|
| | **Flange-A992** | | |
| **A992-F1-1.0** | 9.847 | 40.035 | 0.00 |
| **A992-F2-1.0** | 9.864 | 40.060 | 0.00 |
| **A992-F3-1.0** | 8.539 | 40.098 | 0.00 |
| **A992-F-0.9** | 9.771 | 40.039 | 4.06 |
| **A992-F-0.8** | 8.738 | 40.030 | 8.03 |
| **A992-F-0.7** | 8.585 | 40.064 | 12.07 |
| **A992-F-0.6** | 9.762 | 40.060 | 16.33 |
| **A992-F-0.5** | 8.606 | 40.149 | 19.94 |
| | **Web-A992** | | |
| **A992-W1-1.0** | 5.745 | 39.988 | 0.00 |
| **A992-W2-1.0** | 5.757 | 40.013 | 0.00 |
| **A992-W3-1.0** | 5.842 | 40.016 | 0.00 |
| **A992-W-0.9** | 5.740 | 40.060 | 4.06 |
| **A992-W-0.7** | 5.770 | 40.047 | 12.07 |
| **A992-W-0.5** | 5.800 | 40.060 | 19.99 |
| | **Flange-350W** | | |
| **350W-F1-1.0** | 8.721 | 40.081 | 0.00 |
| **350W-F2-1.0** | 9.868 | 40.157 | 0.00 |
| **350W-F3-1.0** | 8.729 | 39.992 | 0.00 |
| **350W-F-0.9** | 8.602 | 40.039 | 4.09 |
| **350W-F-0.8** | 9.940 | 40.162 | 8.03 |
| **350W-F-0.7** | 9.948 | 40.170 | 12.07 |
| **350W-F-0.6** | 8.653 | 39.984 | 16.33 |
| **350W-F-0.5** | 9.872 | 40.081 | 19.97 |
| | **Web-350W** | | |
| **350W-W1-1.0** | 5.791 | 40.064 | 0.00 |
| **350W-W2-1.0** | 5.732 | 40.030 | 0.00 |
| **350W-W3-1.0** | 5.711 | 40.026 | 0.00 |
| **350W-W-0.9** | 5.711 | 40.043 | 4.09 |
| **350W-W-0.7** | 5.740 | 40.009 | 12.07 |
| **350W-W-0.5** | 5.787 | 40.047 | 19.89 |

Table 6.2: Summary of Mechanical Characteristics of Tension Coupons

| Steel Grade | Specimen ID | Mechanical Properties | | | | | | | | | |
|---|---|---|---|---|---|---|---|---|---|---|---|
| | | $F_y$ (MPa) | $F_u$ (MPa) | $\frac{F_y}{F_u}$ | $F_{pl}$ (MPa) | $\varepsilon_y$ | $\varepsilon_u$ | $\frac{\varepsilon_u}{\varepsilon_y}$ | $\varepsilon_{sh}$ | $E$ (GPa) | $\varepsilon_f$ (over 200 mm) |
| (1) | (2) | (3) | (4) | (5) | (6) | (7) | (8) | (9) | (10) | (11) | (12) |
| A992 | **A992-F1-1.0** | 448 | 579 | 0.77 | 408 | 0.0022 | 0.1348 | 61 | N/A | 204 | 0.2041 |
| | **A992-F2-1.0** | 446 | 585 | 0.76 | 404 | 0.0022 | 0.1353 | 62 | N/A | 203 | 0.2106 |
| | **A992-F3-1.0** | 441 | 568 | 0.78 | 406 | 0.0022 | 0.1441 | 66 | N/A | 201 | 0.2100 |
| | **$(\text{Flange})_{ave}$** | **445** | **577** | **0.77** | **406** | **0.0022** | **0.1381** | **63** | N/A | **203** | **0.2082** |
| | **A992-W1-1.0** | 405 | 568 | 0.71 | 405 | 0.0020 | 0.1484 | 74 | 0.0156 | 202 | 0.2083 |
| | **A992-W2-1.0** | 417 | 591 | 0.71 | 417 | 0.0021 | 0.1456 | 73 | 0.0132 | 201 | 0.2023 |
| | **A992-W3-1.0** | 405 | 561 | 0.72 | 405 | 0.0020 | 0.1401 | 70 | 0.0154 | 202 | 0.2308 |
| | **$(\text{Web})_{ave}$** | **409** | **573** | **0.71** | **409** | **0.0020** | **0.1447** | **72** | **0.0148** | **202** | **0.2138** |
| 350W | **350W-F1-1.0** | 426 | 581 | 0.73 | 398 | 0.0020 | 0.1412 | 71 | N/A | 208 | 0.2282 |
| | **350W-F2-1.0** | 425 | 575 | 0.74 | 400 | 0.0020 | 0.1443 | 72 | N/A | 215 | 0.2083 |
| | **350W-F3-1.0** | 434 | 578 | 0.75 | 396 | 0.0020 | 0.1307 | 65 | N/A | 216 | 0.2240 |
| | **$(\text{Flange})_{ave}$** | **428** | **578** | **0.74** | **398** | **0.0020** | **0.1387** | **69** | N/A | **213** | **0.2202** |
| | **350W-W1-1.0** | 414 | 571 | 0.73 | 414 | 0.0021 | 0.1595 | 76 | 0.0160 | 198 | 0.2054 |
| | **350W-W2-1.0** | 412 | 593 | 0.69 | 412 | 0.0021 | 0.1392 | 66 | 0.0140 | 198 | 0.1771 |
| | **350W-W3-1.0** | 422 | 581 | 0.73 | 422 | 0.0020 | 0.1602 | 80 | 0.0158 | 207 | 0.2025 |
| | **$(\text{Web})_{ave}$** | **416** | **582** | **0.71** | **416** | **0.0021** | **0.1530** | **74** | **0.0153** | **201** | **0.1950** |

Table 6.3: Tensile Strength of Perforated Tensile Specimens

| Steel Grade (1) | Specimen ID (2) | Hole Diameter- $\varphi$ (mm) (3) | $\lfloor A_n / A_g \rfloor$ (%) (4) | $\lfloor A_n F_u / A_g F_y \rfloor$ (5) | Experimental Ultimate Load $P_u$ (kN) (6) | $\left[\frac{P_u}{P_y}\right]$ $(P_y = A_g F_y)$ (7) | Ultimate Stress- $F_{un}$ $(=P_u / A_n)$ (MPa) (8) | Strength Ratio $\left[\frac{F_{un}}{F_u}\right]$ (9) |
|---|---|---|---|---|---|---|---|---|
| **A992 (Flange)** $[F_y = 445MPa$ $F_u = 577MPa]$ | **A992-F-0.9** | 4.06 | 90 | **1.17>1.0** | 215.5 | **1.24** | 613 | 1.06 |
| | **A992-F-0.8** | 8.03 | 80 | **1.04>1.0** | 170.0 | **1.09** | 608 | 1.05 |
| | **A992-F-0.7** | 12.07 | 70 | 0.91<1.0 | 147.8 | 0.97 | 615 | 1.06 |
| | **A992-F-0.6** | 16.05 | 60 | 0.78<1.0 | 145.0 | 0.83 | 619 | 1.07 |
| | **A992-F-0.5** | 19.94 | 50 | 0.65<1.0 | 106.5 | 0.69 | 612 | 1.06 |
| **A992 (Web)** $[F_y = 409MPa$ $F_u = 573MPa]$ | **A992-W-0.9** | 4.04 | 90 | **1.26>1.0** | 121.2 | **1.29** | 587 | 1.02 |
| | **A992-W-0.7** | 12.07 | 70 | 0.98≈1.0 | 97.5 | **1.03** | 604 | 1.05 |
| | **A992-W-0.5** | 20.02 | 50 | 0.70<1.0 | 70.0 | 0.74 | 602 | 1.05 |
| **350W (Flange)** $[F_y = 428MPa$ $F_u = 578MPa]$ | **350W-F-0.9** | 4.09 | 90 | **1.22>1.0** | 190.0 | **1.29** | 614 | 1.06 |
| | **350W-F-0.8** | 8.03 | 80 | **1.08>1.0** | 195.5 | **1.14** | 612 | 1.06 |
| | **350W-F-0.7** | 12.07 | 70 | 0.94<1.0 | 170.2 | 0.99 | 608 | 1.05 |
| | **350W-F-0.6** | 16.33 | 59 | 0.80<1.0 | 127.0 | 0.86 | 621 | 1.08 |
| | **350W-F-0.5** | 19.99 | 50 | 0.68<1.0 | 122.0 | 0.72 | 615 | 1.07 |
| **350W (Web)** $[F_y = 416MPa$ $F_u = 582MPa]$ | **350W-W-0.9** | 4.09 | 90 | **1.26>1.0** | 122.3 | **1.29** | 595 | 1.02 |
| | **350W-W-0.7** | 12.07 | 70 | 0.98≈1.0 | 96.5 | **1.01** | 602 | 1.03 |
| | **350W-W-0.5** | 19.89 | 50 | 0.70<1.0 | 69.0 | 0.72 | 591 | 1.02 |

Table 6.4: Comparison of Test Results with Code Prediction [CAN/CSA-S16.01 (CSA 2003)]

| **Steel Grade** (1) | **Specimen ID** (2) | $\lfloor A_n F_u / A_g F_y \rfloor$ (3) | $\left\{ \frac{P_u}{A_g F_y} \right\}_{test}$ (4) | $\left\{ \frac{0.85 A_n F_u}{A_g F_y} \right\}_{CSA(2003)}$ (5) | $\left\{ \frac{P_u}{0.85 A_n F_u} \right\}_{\frac{test}{CSA(2003)}}$ (6) |
|---|---|---|---|---|---|
| **A992 (Flange)** | **A992-F-0.9** | **1.17>1.0** | 1.24 | 0.99 | 1.25 |
| | **A992-F-0.8** | **1.04>1.0** | 1.09 | 0.88 | 1.24 |
| | **A992-F-0.7** | 0.91<1.0 | 0.97 | 0.77 | 1.26 |
| | **A992-F-0.6** | 0.78<1.0 | 0.83 | 0.65 | 1.28 |
| | **A992-F-0.5** | 0.65<1.0 | 0.69 | 0.55 | 1.25 |
| **A992 (Web)** | **A992-W-0.9** | **1.26>1.0** | 1.29 | 1.07 | 1.21 |
| | **A992-W-0.7** | 0.98≈1.0 | 1.03 | 0.83 | 1.24 |
| | **A992-W-0.5** | 0.70<1.0 | 0.74 | 0.60 | 1.23 |
| **350W (Flange)** | **350W-F-0.9** | **1.22>1.0** | 1.29 | 1.03 | 1.25 |
| | **350W-F-0.8** | **1.08>1.0** | 1.14 | 0.92 | 1.24 |
| | **350W-F-0.7** | 0.94<1.0 | 0.99 | 0.80 | 1.24 |
| | **350W-F-0.6** | 0.80<1.0 | 0.86 | 0.68 | 1.26 |
| | **350W-F-0.5** | 0.68<1.0 | 0.72 | 0.58 | 1.24 |
| **350W (Web)** | **350W-W-0.9** | **1.26>1.0** | 1.29 | 1.07 | 1.21 |
| | **350W-W-0.7** | 0.98≈1.0 | 1.01 | 0.83 | 1.22 |
| | **350W-W-0.5** | 0.70<1.0 | 0.72 | 0.60 | 1.20 |

Table 6.5: Comparison of Stresses and Strains at Fracture

| Steel Grade (1) | Specimen ID (2) | Experiment: Stress @ fracture (MPa) (3) | | Experiment: Strain @ fracture (mm/mm) (4) | | FEM: Stress @ fracture (MPa) (5) | FEM: Strain @ fracture (mm/mm) (6) | $(Exp/FEM)_{stress\ @\ fracture}$ (7) | $(Exp/FEM)_{strain\ @\ fracture}$ (8) |
|---|---|---|---|---|---|---|---|---|---|
| A992 | A992-F1-1.0 | 480 | 477 (average) | 0.2162 | 0.2117 (average) | 486 | 0.2098 | 0.98 | 1.00 |
| | A992-F2-1.0 | 477 | | 0.2090 | | | | | |
| | A992-F3-1.0 | 474 | | 0.2100 | | | | | |
| | A992-W1-1.0 | 479 | 496 (average) | 0.2083 | 0.2130 (average) | 497 | 0.2168 | 1.00 | 0.98 |
| | A992-W2-1.0 | 526 | | 0.2023 | | | | | |
| | A992-W3-1.0 | 483 | | 0.2285 | | | | | |
| 350W | 350W-F1-1.0 | 487 | 488 (average) | 0.2195 | 0.2169 (average) | 489 | 0.2169 | 1.00 | 1.00 |
| | 350W-F2-1.0 | 487 | | 0.2072 | | | | | |
| | 350W-F3-1.0 | 490 | | 0.2240 | | | | | |
| | 350W-W1-1.0 | 499 | 527 (average) | 0.2054 | 0.1955 (average) | 511 | 0.2064 | 1.03 | 0.95 |
| | 350W-W2-1.0 | 550 | | 0.1771 | | | | | |
| | 350W-W3-1.0 | 531 | | 0.2041 | | | | | |

Table 6.6: Comparison of Experimental Test Results with FEM Prediction for Perforated Samples

| **Steel Grade** (1) | **Specimen ID** (2) | **Experimental Ultimate-stress** $F_u^{Exp} = \left( P_u / A_g \right)_{Exp}$ (MPa) (3) | **FEM Ultimate-stress** $F_u^{FEM} = \left( P_u / A_g \right)_{FEM}$ (MPa) (4) | $\left( F_u^{Exp} / F_u^{FEM} \right)$ (5) |
|---|---|---|---|---|
| **A992** | **A992-F-0.9** | 547 | 542 | 1.01 |
| | **A992-F-0.8** | 482 | 480 | 1.00 |
| | **A992-F-0.7** | 429 | 423 | 1.01 |
| | **A992-F-0.6** | 369 | 362 | 1.02 |
| | **A992-F-0.5** | 308 | 298 | 1.03 |
| | **A992-W-0.9** | 528 | 523 | 1.01 |
| | **A992-W-0.7** | 422 | 418 | 1.01 |
| | **A992-W-0.5** | 297 | 299 | 0.99 |
| **350W** | **350W-F-0.9** | 548 | 547 | 1.00 |
| | **350W-F-0.8** | 489 | 488 | 1.00 |
| | **350W-F-0.7** | 427 | 427 | 1.00 |
| | **350W-F-0.6** | 366 | 366 | 1.00 |
| | **350W-F-0.5** | 311 | 312 | 1.00 |
| | **350W-W-0.9** | 540 | 543 | 0.99 |
| | **350W-W-0.7** | 417 | 417 | 1.00 |
| | **350W-W-0.5** | 291 | 302 | 0.96 |

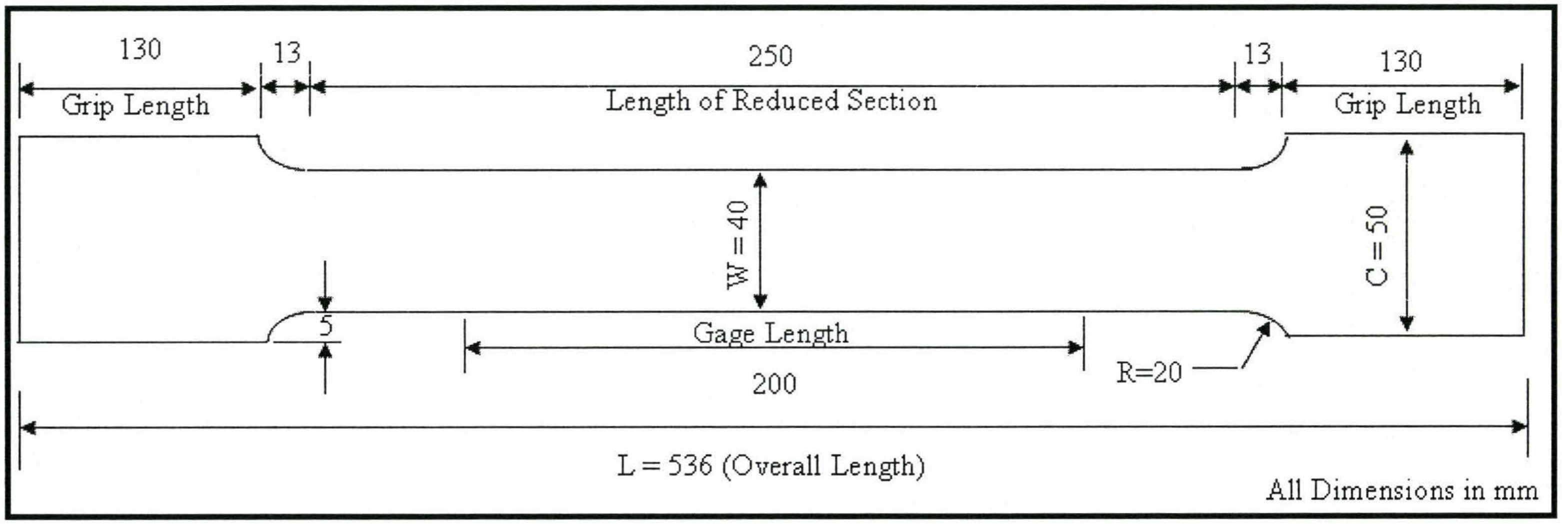


Figure 6.1: Dimensions of Tensile Coupon

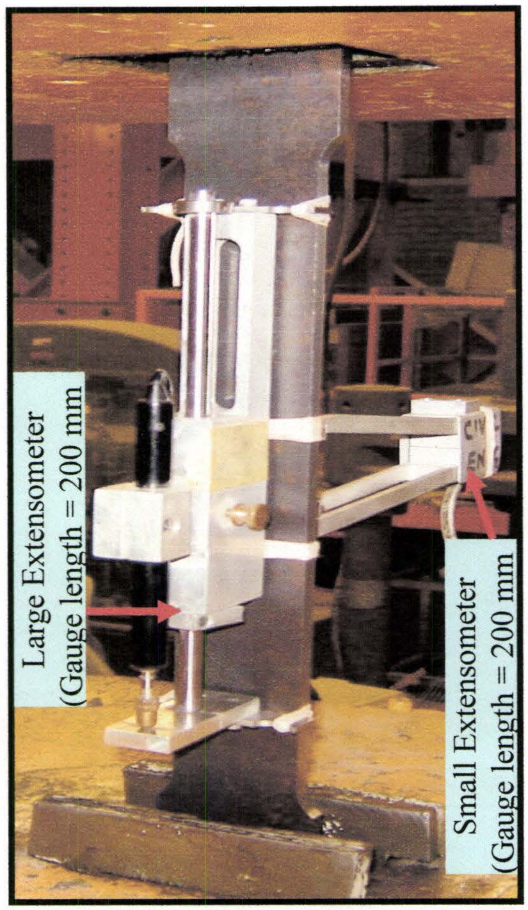


Figure 6.2: Test Setup

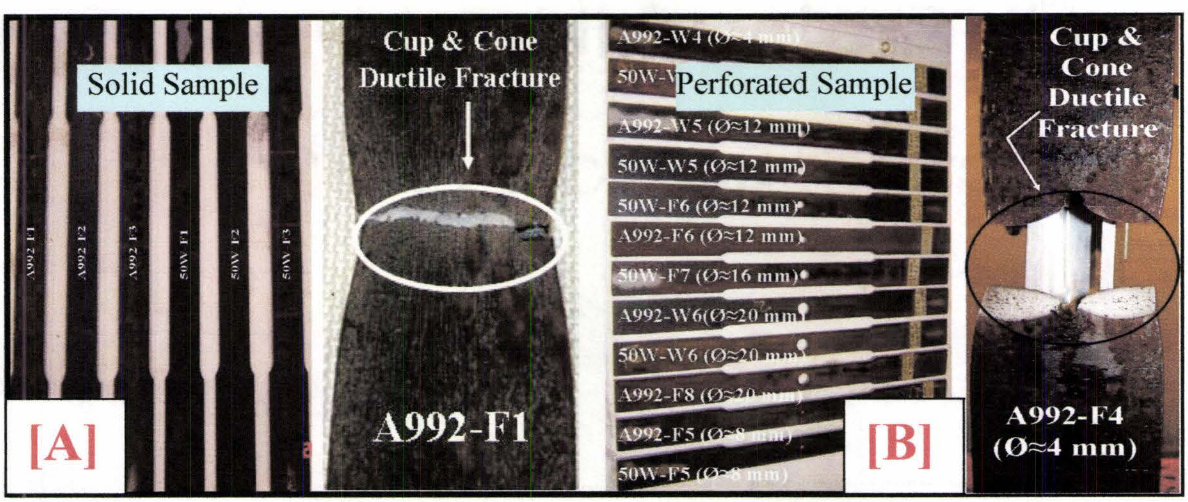


Figure 6.3: Specimens and Failure

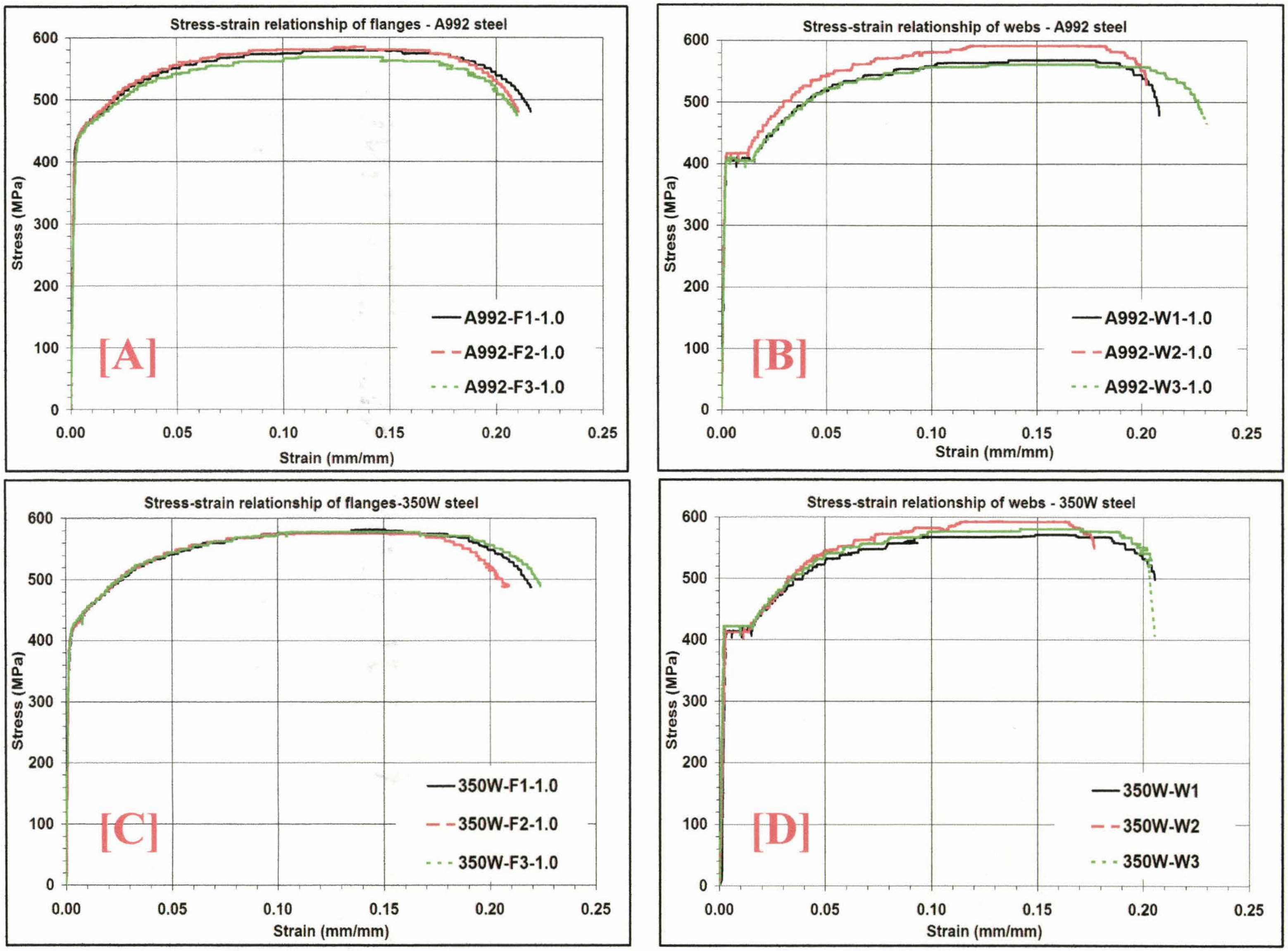


Figure 6.4: Experimental Stress-Strain Relationships [Over 200 mm Gauge Length]

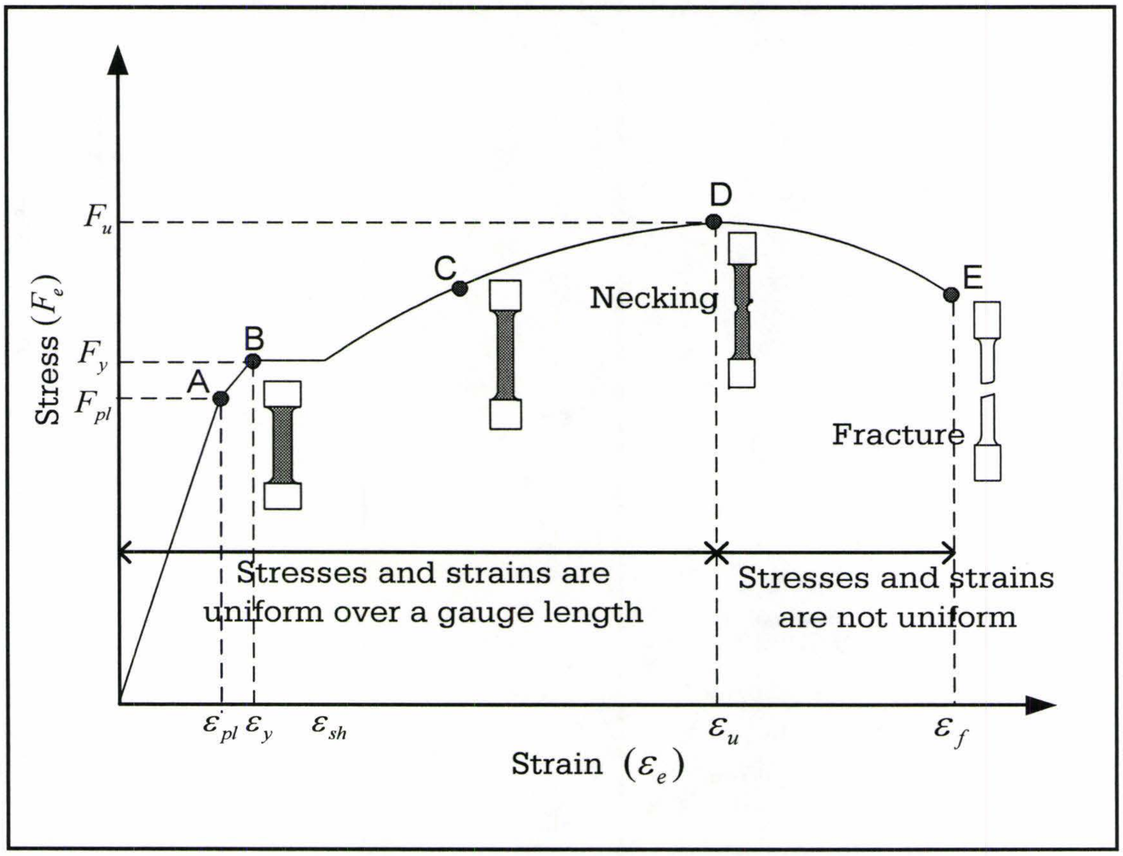


Figure 6.5: Typical Stress-Strain Behavior of Structural Steels

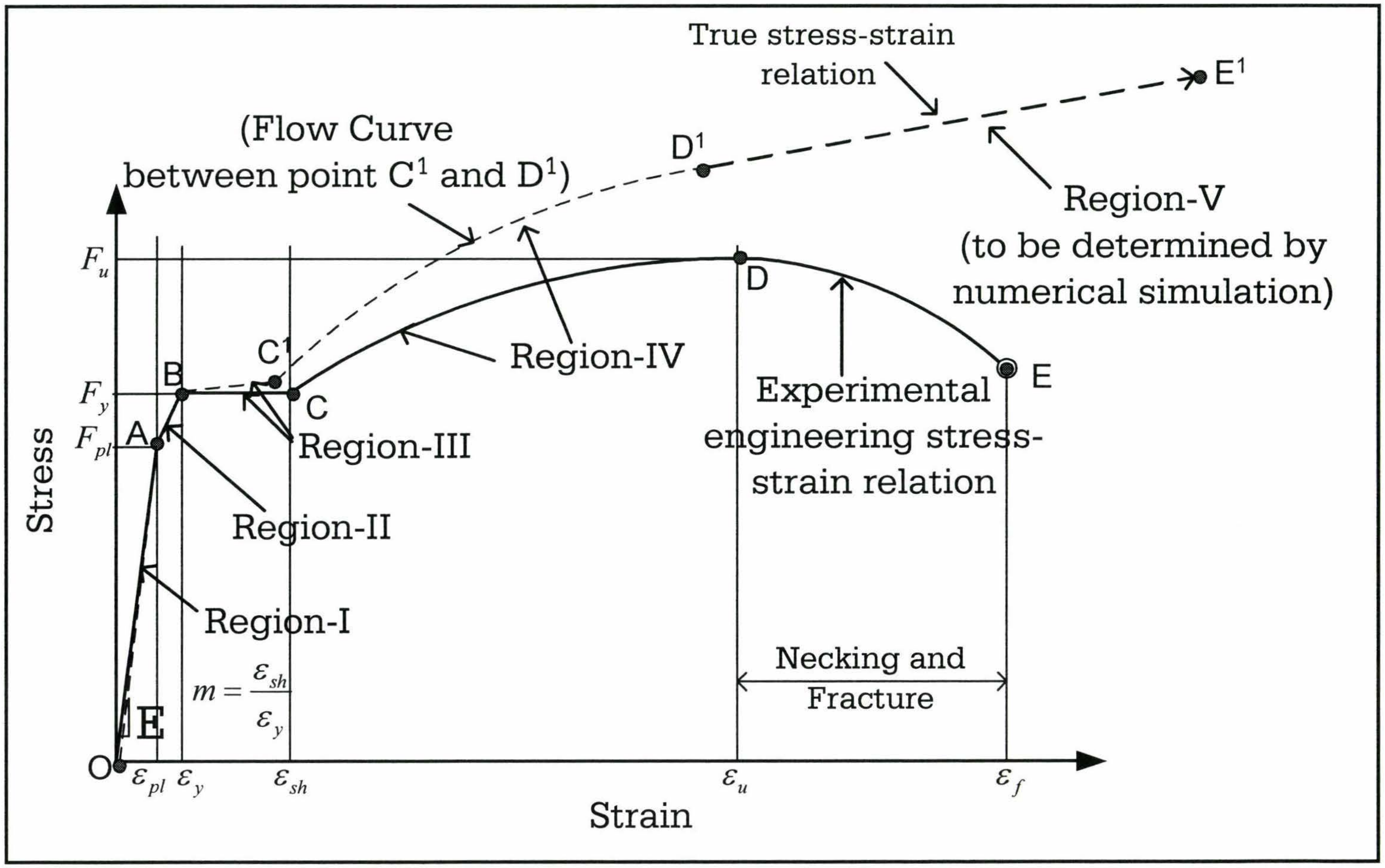


Figure 6.6: Material Model

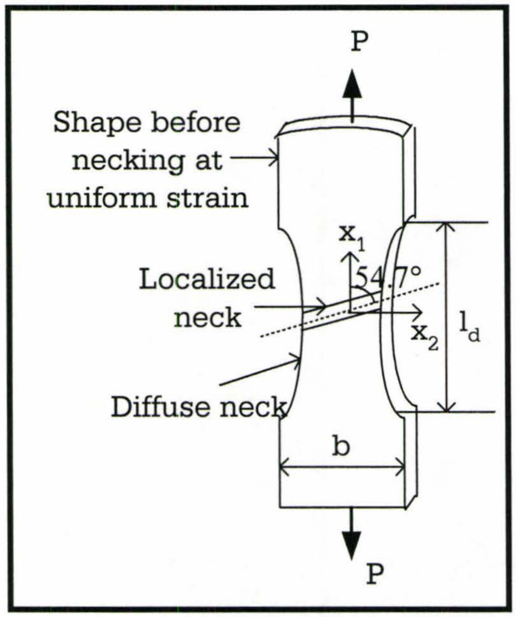


Figure 6.7: Tensile Necking in a Flat Specimen (Bao 2004)

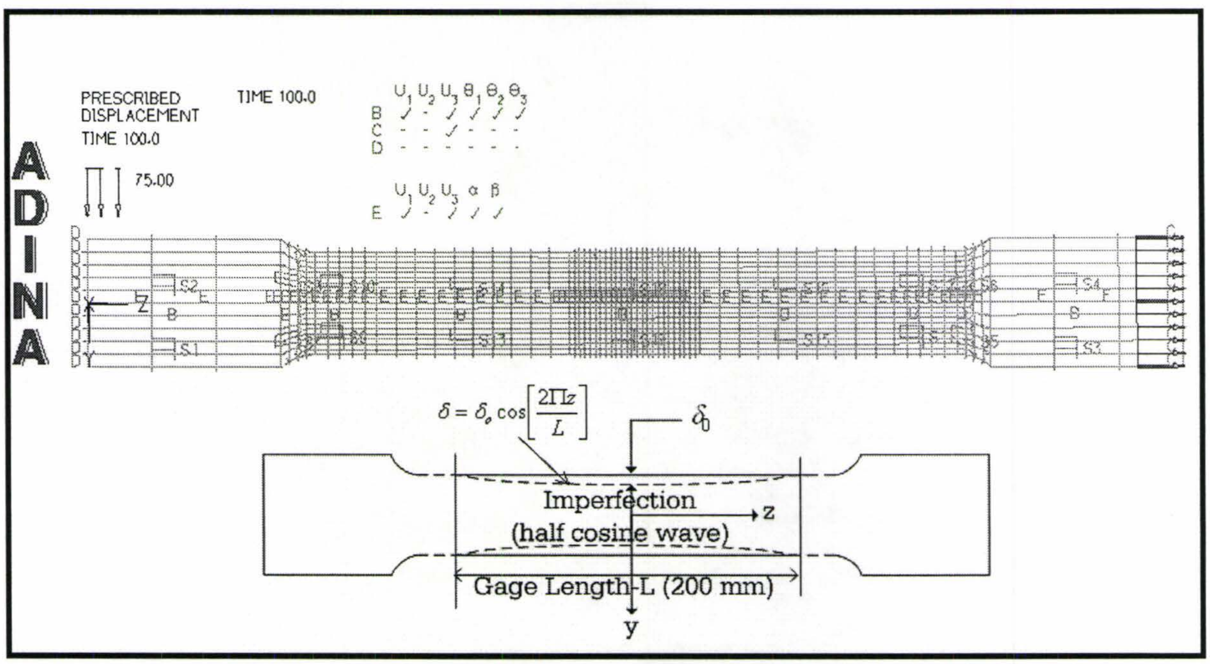


Figure 6.8: Finite Element Model for a Solid Coupon

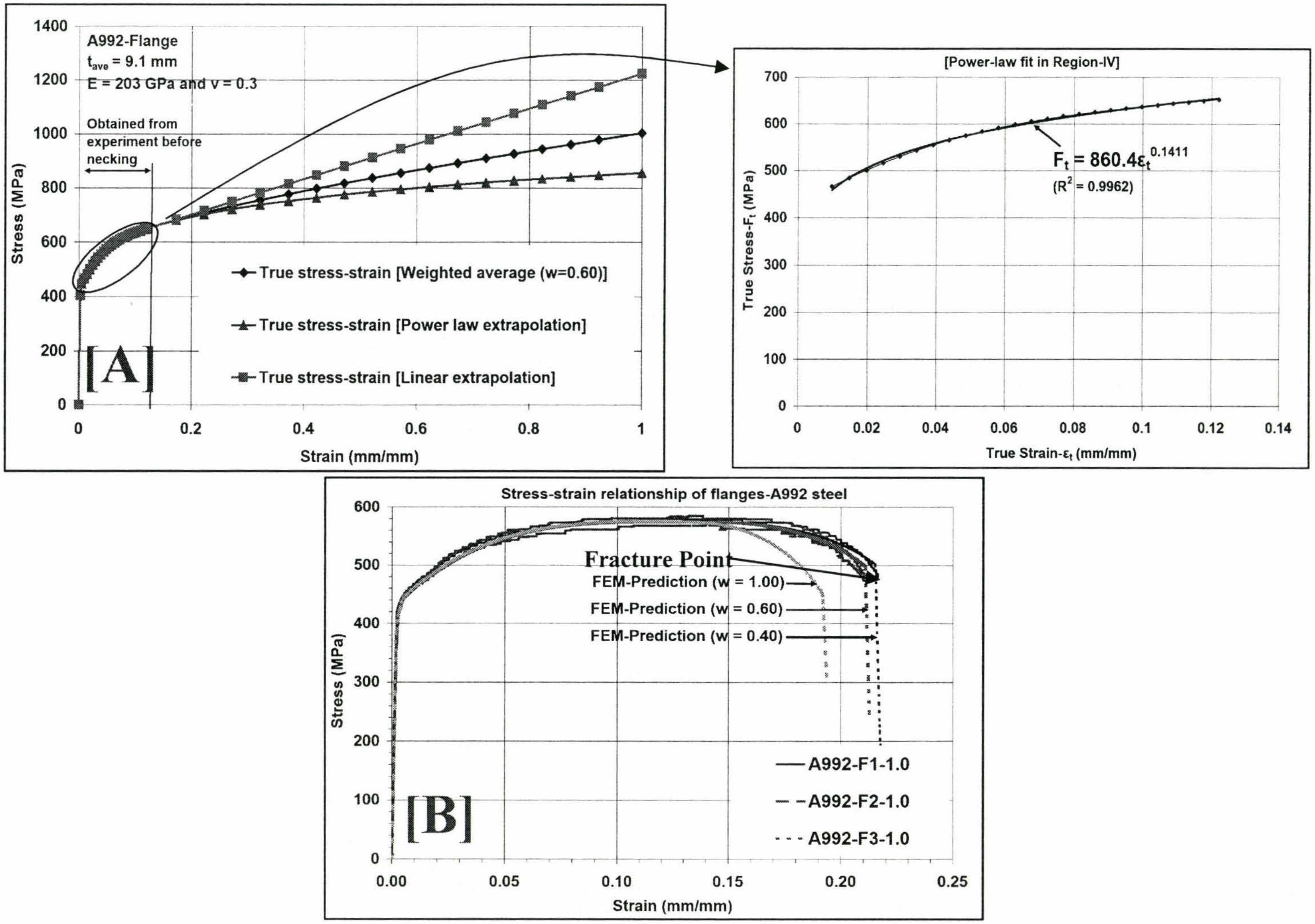


Figure 6.9: [A] Comparison of Experimental and Numerically Simulated Stress-Strain Relation and [B] Material Constitutive Relation up to Fracture for Flanges of A992 Steel

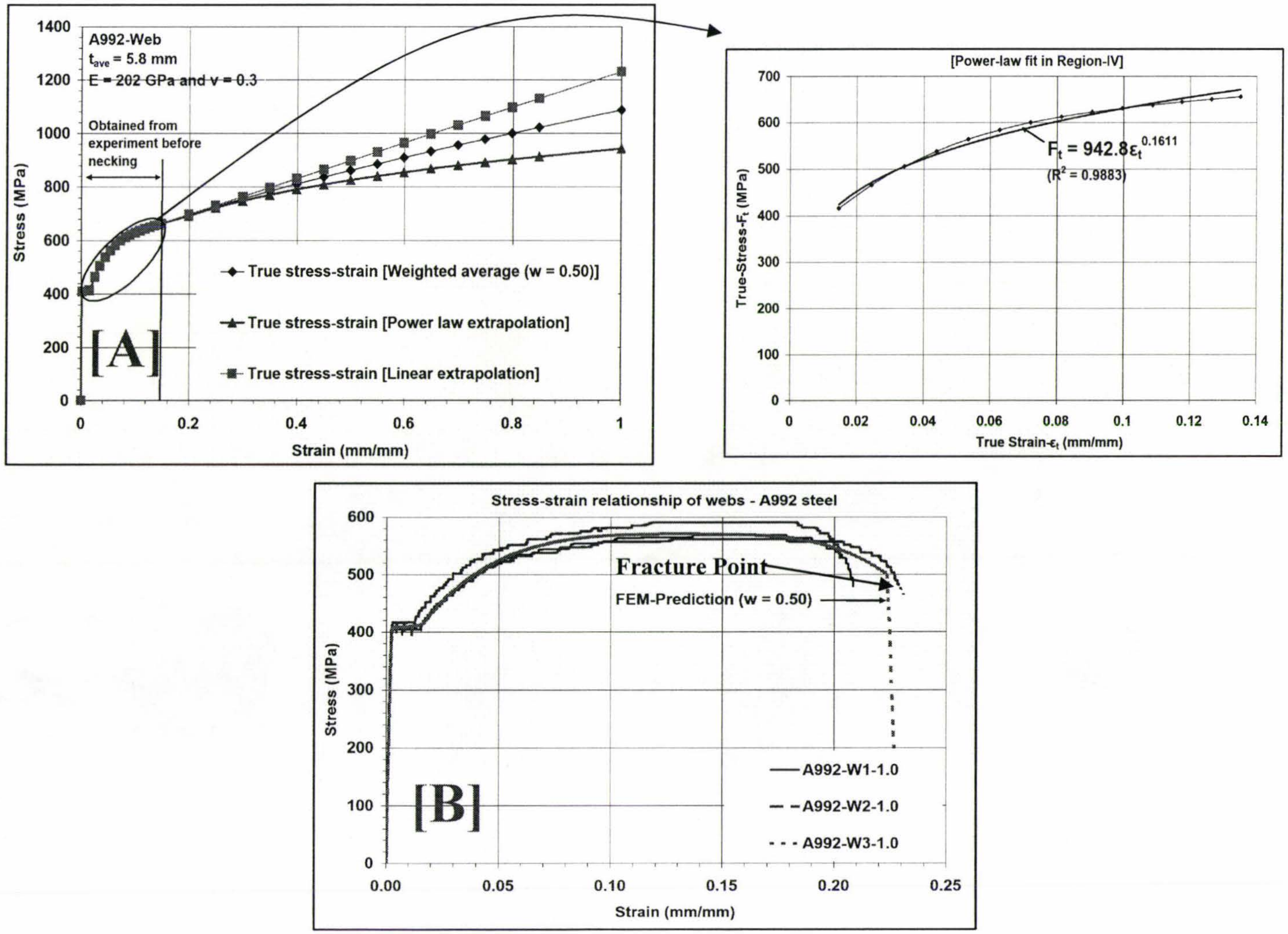


Figure 6.10: [A] Comparison of Experimental and Numerically Simulated Stress-Strain Relation and [B] Material Constitutive Relation up to Fracture for Webs of A992 Steel

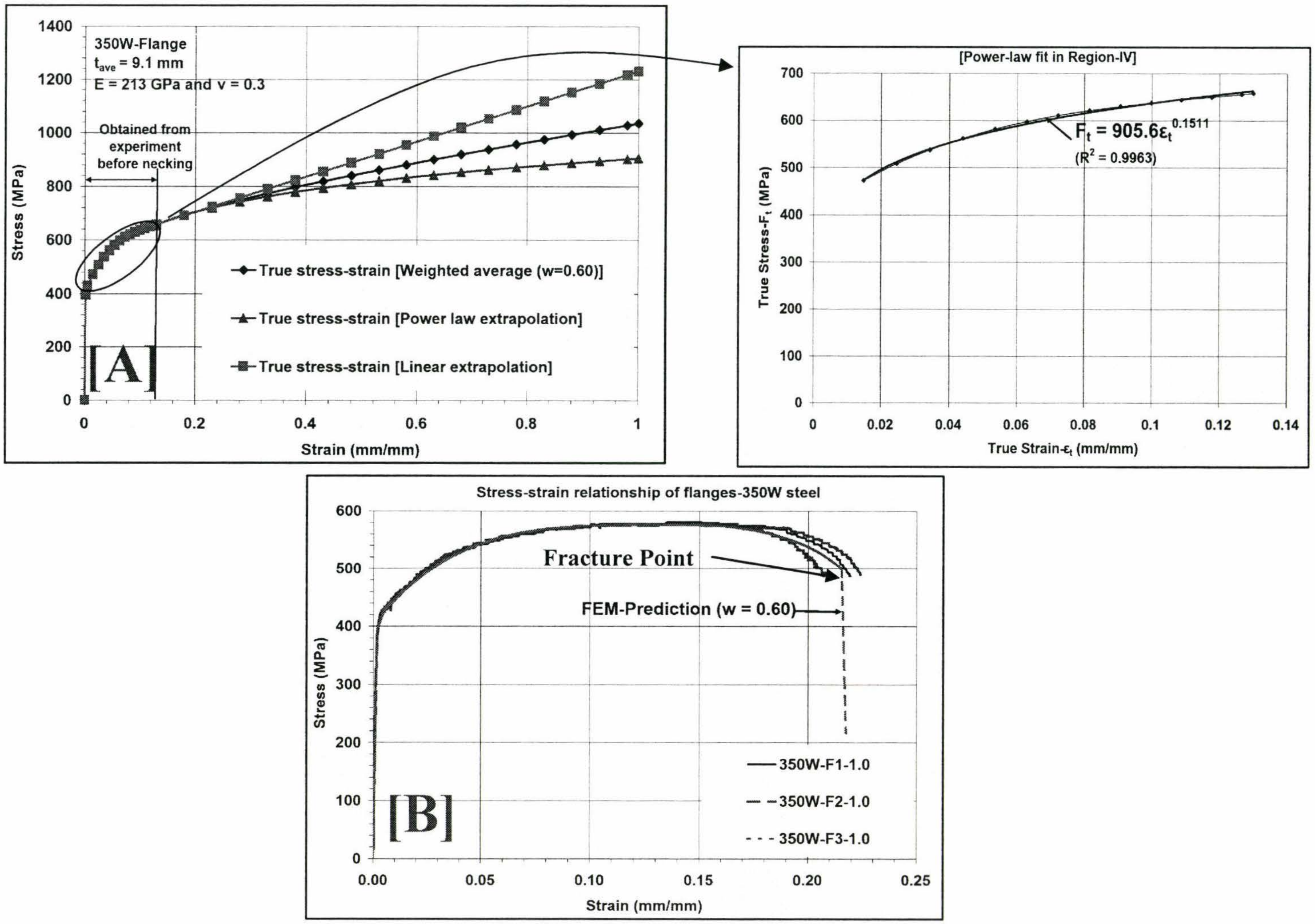


Figure 6.11: [A] Comparison of Experimental and Numerically Simulated Stress-Strain Relation and [B] Material Constitutive Relation up to Fracture for Flanges of 350W Steel

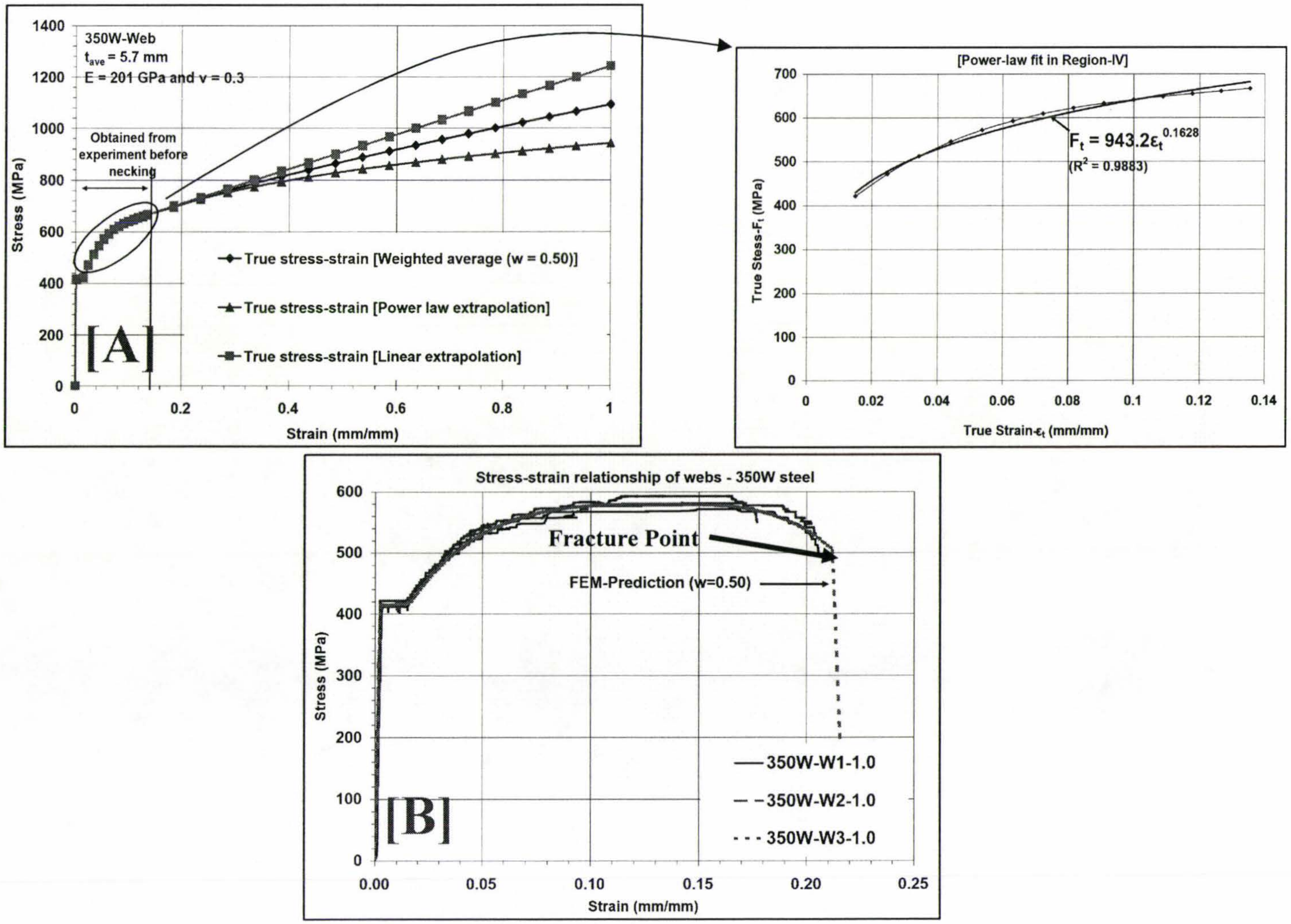


Figure 6.12: [A] Comparison of Experimental and Numerically Simulated Stress-Strain Relation and [B] Material Constitutive Relation up to Fracture for Webs of 350W Steel

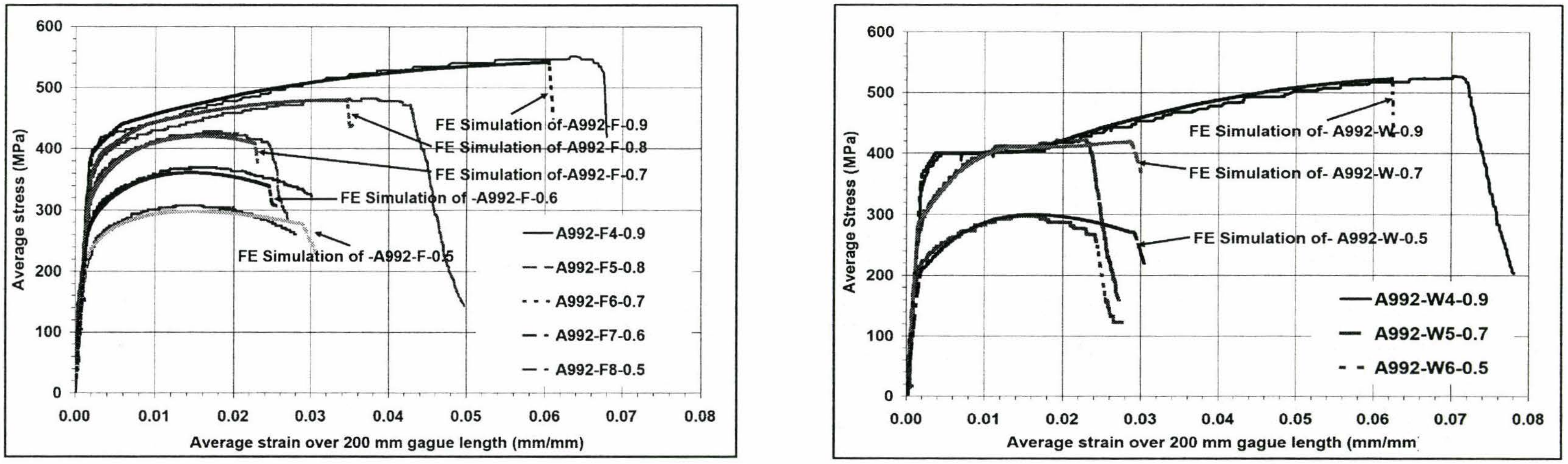


Figure 6.13: Comparison of Perforated Test Results with FE Results for A992 Steel

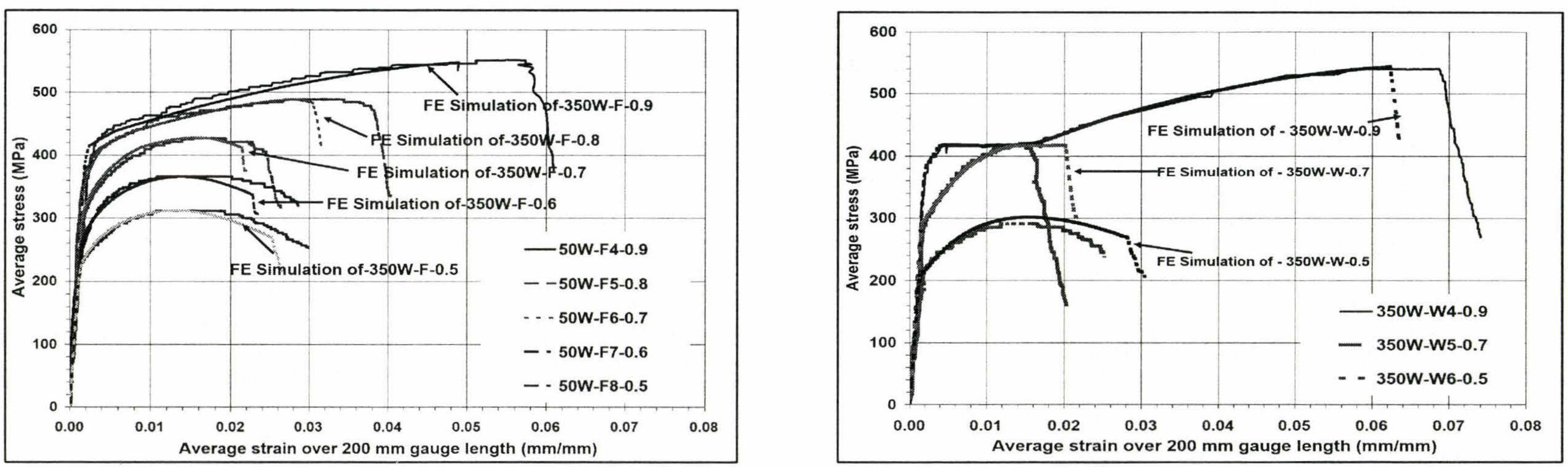


Figure 6.14: Comparison of Perforated Test Results with FE Results for 350W Steel

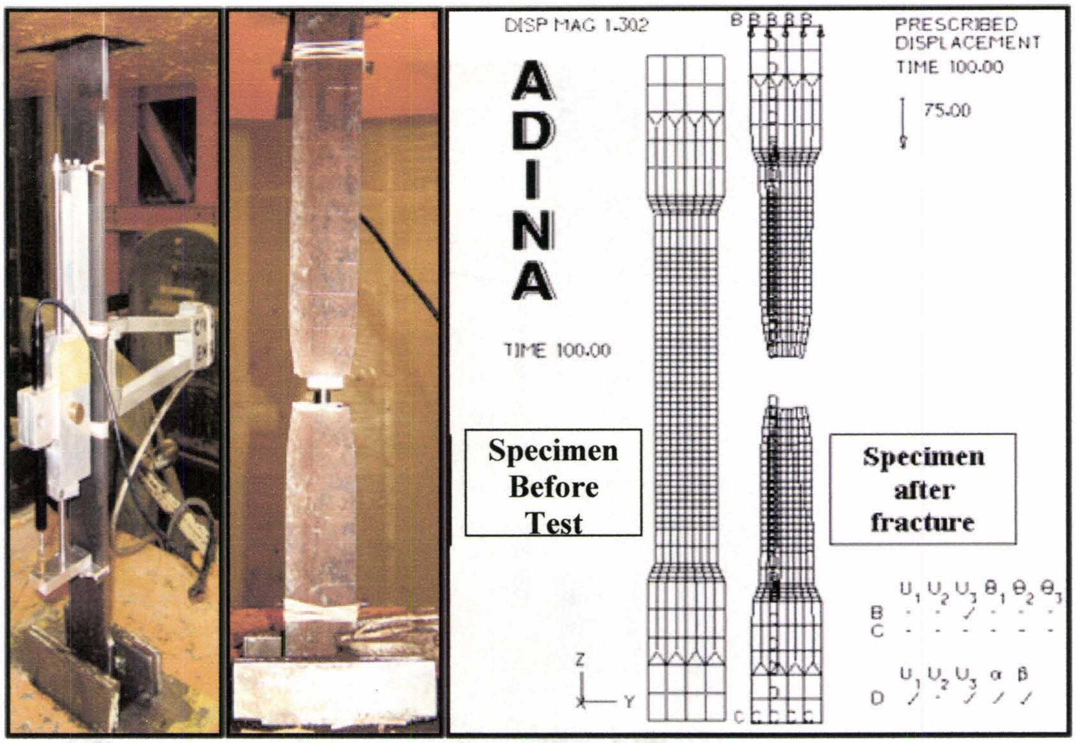


Figure 6.15: Comparison of Failure Pattern of Test Sample with FE Simulation Results

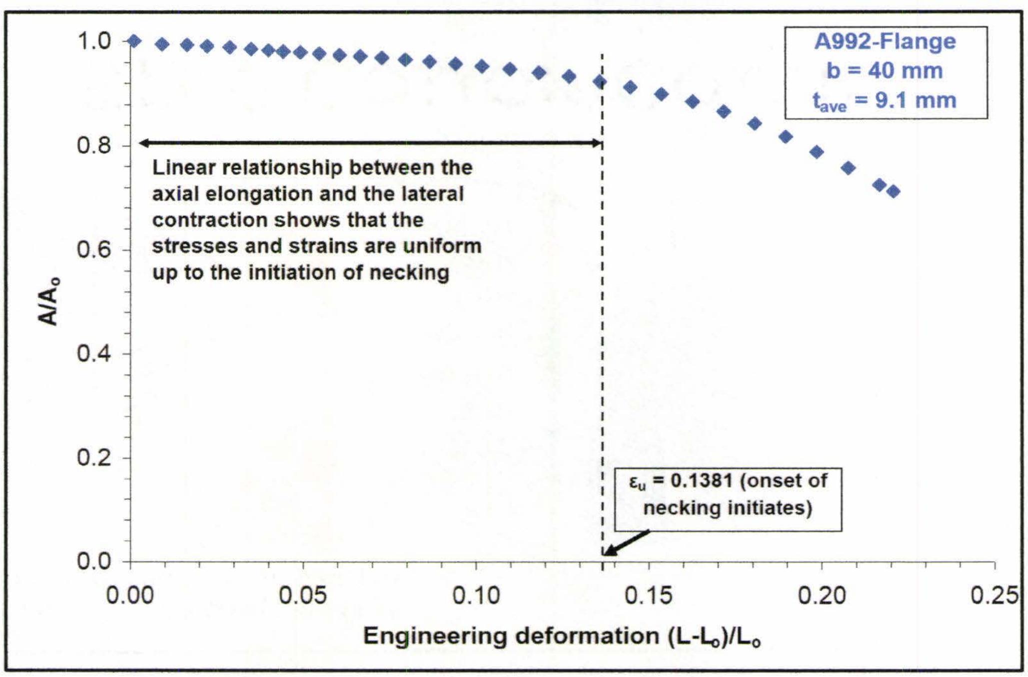


Figure 6.16: Variation of Transverse Area with Axial Deformation

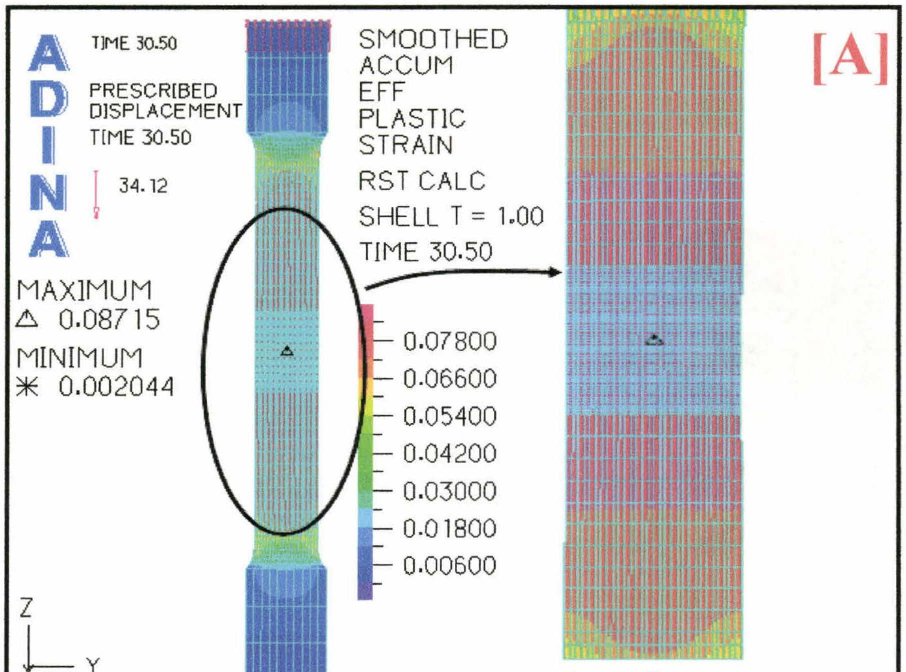


**Enlarged plastic zone prior to necking but, beyond yielding stage**

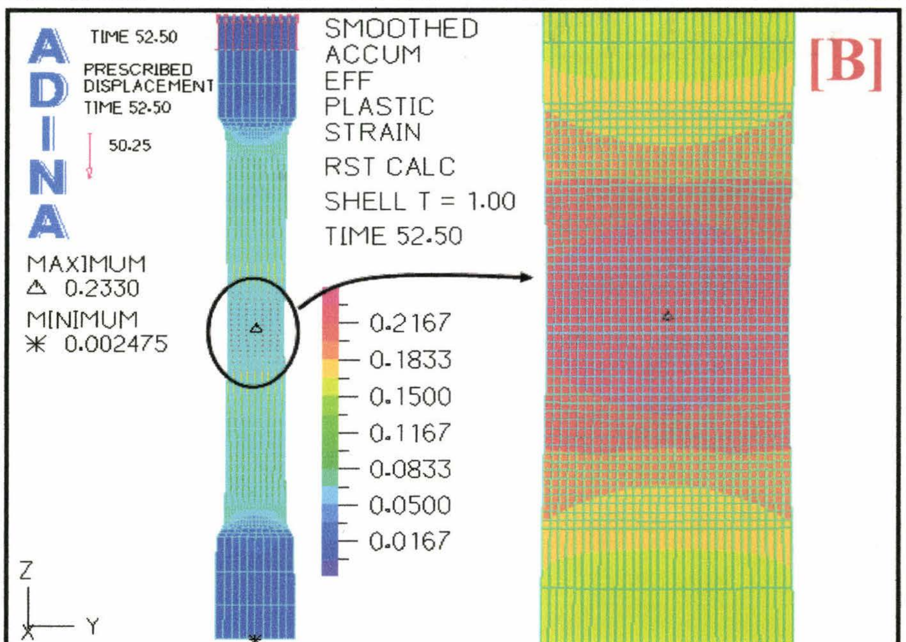


**Enlarged plastic zone between necking and fracture stage**

Cont…….

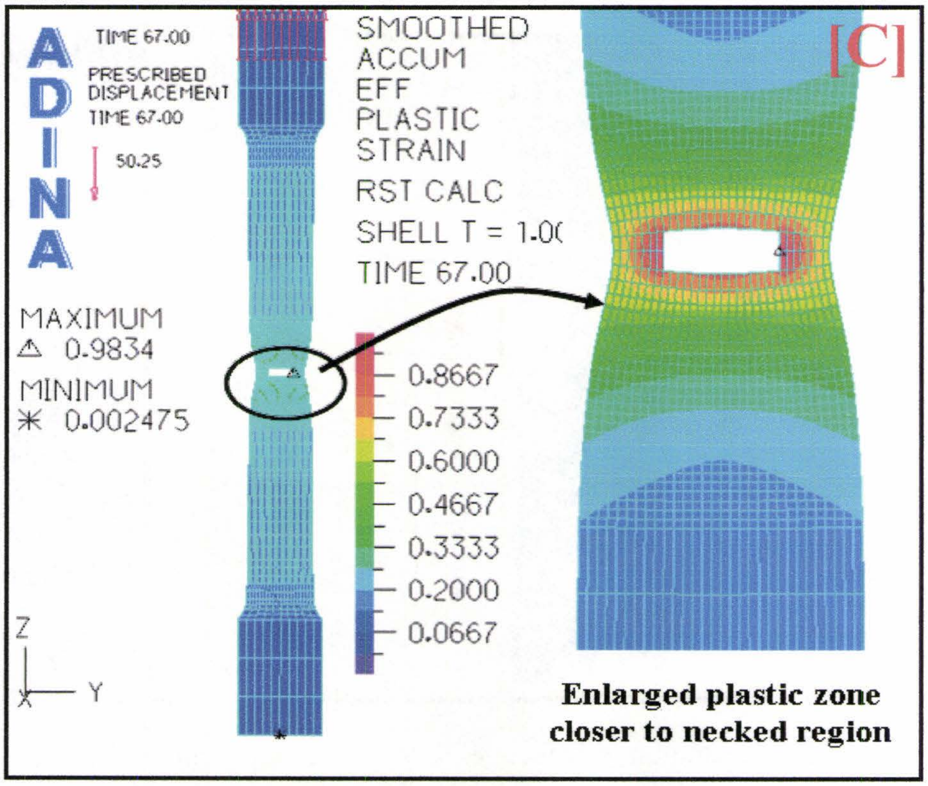


Figure 6.17: Plastification, Necking and Fracture of Solid Tension Coupons

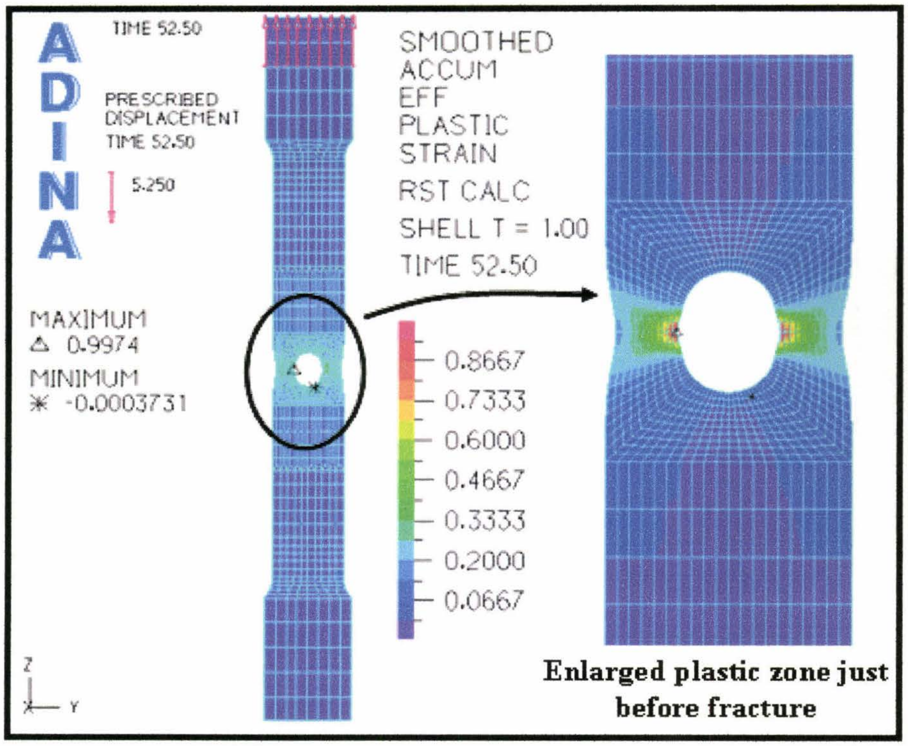


Figure 6.18: Distribution of Effective Plastic Strain in Perforate Sample Having ( $A_n$ / $A_g$ ) ratio of 0.8

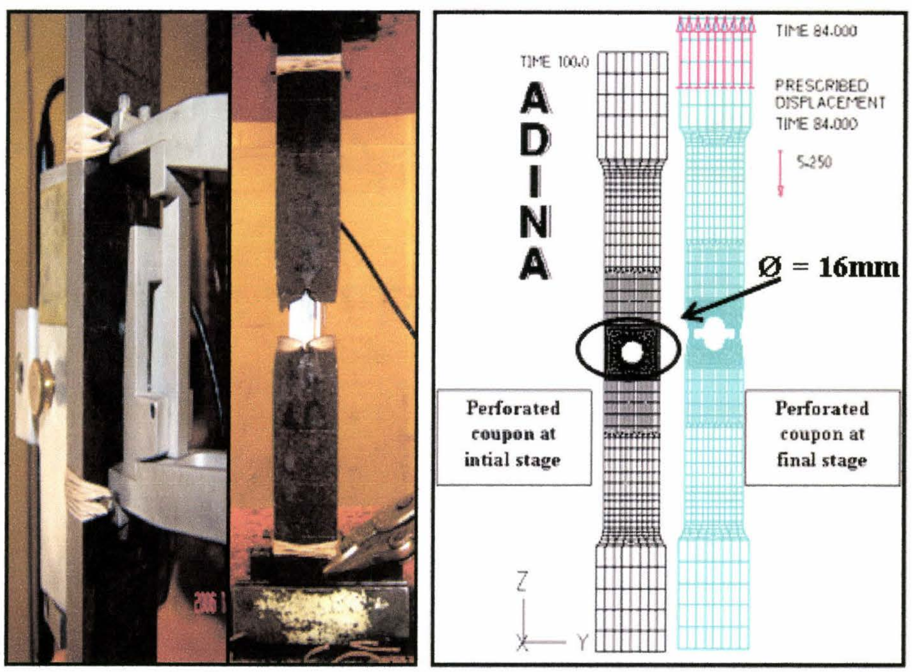


Figure 6.19: Comparison of Failure Pattern Observed in the Experiment and FE Simulation-Perforated Sample

# CHAPTER: 7

# FINITE ELEMENT ANALYSIS

## 7.1 Introduction

This chapter presents finite element modeling procedures associated with plate and beam analyses. These FE models were compared with the experimental results. The FE results were evaluated against the experimental results in terms of the global behavior (load-deflection) and the local behavior (local stresses and strains). This study was conducted using a commercially available ADINA FE program, version 8.4 (ADINA R&D 2007), which has capabilities for modeling geometric and material nonlinear effects. The factors contributing to discrepancies of the experimental and numerical results are discussed.

## 7.2 ADINA Options Used in This Study

The following ADINA options were utilized in this FE study;

Element Type: 4-node general purpose shell element was used. The theoretical formulation of the shell element can be found in various literatures (Ahmad et al., 1970 and Bathe 1996). A large number of researchers have demonstrated that shell elements are a suitable choice and sufficient for modeling the physical behaviour of I-shaped beams (White et al., 1993, Huang, 1994, Barth 1996, Earls and Shah 2000, Green et al., 2002, Greco and Earls 2003, Yang 2004, and Huns et al., 2006).

Material Models for Analysis of Steel Members: ADINA utilizes the incremental plasticity form of the elastic-plastic model, in which the increment of plastic strain is related to the state of stress and the stress increment (ADINA R&D 2007). Incremental models are formulated in terms of; a yield surface, a flow rule and a hardening rule. Of many material modeling options available in ADINA, an elastic-plastic constitutive model with von Mises yield surface, associative plastic flow rule and isotropic work hardening has been found to be suitable to represent the behavior of metals such as steels (Barth 1996 and Yang 2004).

Analysis Module Used: Since it is necessary to obtain equilibrium states in the unloading region, the ADINA non-linear static analysis module was employed. The load/displacement increment is generally established based on a pre-defined time function and time steps, which controls the variation of the load (or displacement) with time, for example; a linear variation. The increment size follows from accuracy and convergence criteria. Within each increment, the equilibrium equations are solved by means of the ADINA default Full Newton method. A sparse equations solver is employed in these analyses. Loads are applied to the specimen in a displacement control fashion that enforces a better conditioning of the tangent stiffness matrix when compared to the classical load-control procedure (Coelho et al., 2006).

## 7.3 FE Analysis of a Plate with a Hole

This portion of the study was performed (1) to establish mesh size that satisfactorily balances accuracy and computing resources (mesh convergence study) and (2) to establish the differences in load-deformation behaviours of a solid plate, a plate with a middle hole as well as a plate containing a fastener hole subjected to axial tension and axial compression loadings. In FE modeling, a finer mesh typically results in a more accurate solution. However, as a mesh is made finer, the computation time increases. Therefore, in any FE analyses, a mesh convergence study is performed to obtain an accurate solution with a mesh that is sufficiently dense and not overly demanding of computing resources.

The presence of a hole, which redistributes the membrane stresses in the plate, can cause significant changes in the deformation characteristics, and may also reduce the strength of such plate. This portion of the study analyzed the strength of plates subjected to axial loads. The main purpose of this analysis was to study the behavioural differences between the solid plate, plate with a hole and plate with a hole having a "snug tight" fastener. The behavior of such plates was established using the load versus axial deformation relationship. Note that the analysis of buckling behavior of slender plates having holes was beyond the scope of the study.

### 7.3.1 Problem Statement and Method of Analysis

Figures 7.1[A] and 7.1[B] illustrate the problem considered with regards to a simply supported plate having a concentric hole subjected to axial tension or compression. The plate was assumed to have the following dimensions; 400 mm long (a), 200 mm wide ($b$) and thickness ($t$) of 10 mm. Thus, a resulting plate slenderness ($b/t$) ratio is 20. The stress-strain behvaior of the plate was assumed to be a linear elastic-perfectly plastic material with the yield strength of 350 MPa. The elastic modulus and the Poisson's ratio for this material model were assumed to be 200 GPa and 0.3, respectively. As seen in Figure 7.1, the plate has a concentric hole of 22 mm diameter, in which a 20 mm (M20) fastener is placed. Practically, when a load is applied on a plate having this type connection, the plate will slip until bolts begin to bear against the hole edge. This type of connection is referred to as bearing type connection. To represent such type of connection, one edge of the bolt was assumed to be in contact with the corresponding edge of the hole at the beginning of the load. The plate portion on the other side of the single bolt line was idealized as a rest of the connection, and thus, the far end of the plate was fully supported (shaded area in Figure 7.1).

The plate was modeled using a 4-node shell element. Gauss numerical integration through the shell thickness was employed in this analysis. The size of the shell elements adjacent to the hole region was smaller than that of the elements on the rest of the plate region. Contact analysis with no friction effect was used to model the contact between the bolt and the hole edge. The bolt was modeled as a rigid target surface while the hole edge was modeled as a contactor surface. In these analyses, ADINA non-linear static analysis module was used. A uniform displacement was applied perpendicular to the short edge of the plate until the maximum displacement of 2.5 mm (maximum uniform strain of 0.005) was reached. For the solid plate and for plates with a concentric hole, the load was allowed to increase in small increments of 0.02 mm per step. The load increment in each step, for the plate with a bolt hole, was set to 0.01 mm, due to the use of contact surfaces.

### 7.3.2 Discussion of Results-Plate Analysis

Figures 7.2[A] and 7.2[B] show the load-deformation behavior (normalized axial stress versus axial strain) of a plate under tension and compression, respectively. These figures compare the load-deformation behavior of the following cases; [i] solid-plate, [ii] plate with a concentric hole, and [iii] plate with a fastener hole (smug tight bolt inside the hole). The average axial stress was defined as total tensile/compressive load divided by the plate's gross area (width x thickness). The axial stress was normalized with the yield stress of the plate material ( $F_y$=350 MPa). The average axial strain was established over the length of the plate between the loading edge and the plate's center line which passes through the center of the hole in this study. The axial strain was normalized with the yield strain. Since an idealized linear elastic-perfectly plastic material model with the yield strength of 350 MPa was used in this analysis, the solid-plate reached a maximum strength of 350 MPa. The corresponding yield strain was $1.75 \times 10^{-3}$

($F_y / E$=350/200,000=1.75x10$^{-3}$). It may be noted that, as expected, the load-deformation behavior of plates with no holes and plates with a concentric hole were similar under tension and under compression, particularly in the elastic range and at the ultimate load level. However, the behaviors of the plates having a hole with a fastener were different in tension and in compression. In tension, plates with fastener holes exhibited identical behavior as a plate with holes. However, in compression, the plates with fastener holes reached an ultimate strength of 343 MPa, which is 2% less than that of the solid plate. This may be due to the stress concentration effects in the vicinity of the hole region causing early yielding. The initial stiffness of the plate having fastener holes, subjected to compression load, was slightly higher than the initial stiffness value of 200 GPa used in the study, which may be primarily due to the bearing of the bolt on the near edge of the bolt hole.

Table 7.1 summarizes the finite element analyses based ultimate strength of plates having different size of holes (i.e., different $A_n / A_g$ ratio). The percentage strength reduction of a plate with fastener hole under tension increased with increasing bolt size. The percentage strength reduction under tension was approximately equal to the ratio of $A_h / A_g$ (i.e., hole area/gross area). However, the strength reduction in plates with fastener holes subjected to compression was considerably less. Largest reduction of 4% was observed for the plate having a 40 mm fastener hole ($A_n / A_g$=0.8).

## 7.4 Finite Element Analysis of Beam

In this phase, the test beams having flange holes discussed in Chapters 4 and 5 were modeled and analyzed using ADINA FE program. The predicted results were compared with the experimental results. Also, the predicted failure modes of the FE models were compared with the test beams. The following section presents the FE modeling procedure with regards to the beam analyses.

### 7.4.1 Description of FE Model

Since the purpose of the numerical study was to develop and to verify FE models with the beam test results, a full scale FE model of each beam to be analysed was carried out. The FE models included the following dimensions; shear span = 1080 mm, midspan = 750 mm, flange width = 166 mm and web height = 193.2 mm. The thicknesses of the flanges and webs were adjusted based on the measured dimensions of corresponding test beam. Web stiffeners of 6.3 mm thick were added at loading and support locations. The fillet area at the flange web corners was taken into account by the way the model was described. That is, since the mid surfaces of the beams were defined in the FE models, the area that entrapped within the web and the half of the flange may be considered to represent the fillet area.

Figure 7.3 shows a FE mesh for the solid beam. The flanges and web of the beam were modeled using four-node isoparmetric shell elements with mid-surface nodal points. As seen in Figure 7.3, a relatively fine mesh was used in the critical span region while a coarse mesh was used in the shear span region. The FE model for the solid beam specimen included a total of 3128 shell elements with 3231 nodes. Figure 7.4 presents a FE mesh used for the beam having holes in tension flange. As seen in the figure, the FE mesh was refined locally in the vicinity of the hole region for improved resolution of stresses and deformations. Away from the hole region, a relatively coarse mesh was used. The FE model for the beam specimen having holes in tension flange included a total of 9456 shell element with 9649 nodes. A FE mesh for the beam having holes in both flanges is shown Figure 7.5. This figure illustrates how the mesh size was increased from a fine mesh in the vicinity of the hole region to a coarse mesh away from the hole region. It was noted in this study that a mesh transition from a fine mesh to a coarse mesh required a smooth transition to avoid model convergence problems. Thus, a sudden transition from a fine mesh to relatively a larger coarse mesh was impossible. The FE model for the beam having holes in both flanges included a total of 21920 shell elements with 22215 nodes.

Boundary Conditions: Figure 7.6 illustrates the boundary conditions used in this FE study. As seen in the figure, one end of the flange edge was allowed to translate in-plane directions (in Y direction and in Z direction) as well as allowed to rotate about the major axis (Y-Y axis in this modeling). This end can be refereed to as roller end. The opposite edge of the bottom flange was permitted to translate in the lateral and to rotate about the major axis (Y-Y axis in this modeling) while restraining the remaining translations and rotations (see Figure 7.6). Additionally, the outer plane translations in the Y-direction were restrained at the bracing point locations (see Figure 7.6).

Material Model: As discussed in Chapter 4, the mechanical characteristics of the test beams were established using standard coupon tests. Three flange coupons and three web coupons were tested. Note that the stress-strain relationship of the flanges and webs of the test beams differed from the coupon results established in Chapter 6. Although the test beams and a set of coupon samples tested in Chapter 6 conformed to ASTM A992 steel (according to the steel suppliers mill certificate), a wide scatter in the mechanical characteristics was noted. As indicated earlier, the purpose of conducting tensile test in Chapter 6 was to develop a material model that is expected to capture the behavior up to fracture.

The element formulation used in the numerical analysis required knowledge of the true stress-strain characteristics of the material. The true stress-strain relationship, up to onset of necking, was directly obtained from the engineering stress-strain relationship established using tensile tests (see Chapter 6 for more details). In the post ultimate strength region, however, an experimental-numerical analysis was performed to establish the true stress-strain relationship (see Chapter 6). In the FE model of the test beams, the flanges and the web were assigned with their corresponding material models. Figure 7.7

shows the material model pertaining to the flange. As seen in the figure, a weighting constant of 0.7 was used to reproduce the tensile test results. Figure 7.8 relates the material model for the web, in which a weighting constant of 0.9 was used to reproduce the tensile test results. These figures also include the numerical values of the true stress-strain relationship up to an assumed maximum strain of 100%.

Geometric Imperfections: The following method was used to accommodate the geometric imperfections. The free edges of the flanges were defined to form a number of half sine waves in the member length direction. Also, the middle line of the web in the member length direction was defined to form a number of half sine waves as follows;

For the flange imperfection: $\delta = \delta_o \sin\left(\Pi \frac{y}{b}\right) \sin\left(\Pi \frac{z}{L}\right)$

For the web imperfection: $\delta = \delta_o \sin\left(\Pi \frac{x}{h}\right) \sin\left(\Pi \frac{z}{L}\right)$

where $\delta_o (= b/1000)$ is the maximum imperfection amplitude, $b$ and $h$ are the flange width and the web height, respectively and $L$ is the length of the beam. The wave length of the sinusoidal imperfection was considered to be half of the flange width ($b$ /2) along the flange edge and $h/2$ along the middle web.

Residual stresses: The applied residual stresses used in the FE model are as shown in Figure 7.9. The effects of residual stresses manifest itself in the moment-rotation and load-deflection diagrams as a “rounding off” of the curve as the beam yields (Yakel et al., 2002). The incorporation of residual stresses in the FE models of the solid beam in this study had no effect on the ultimate moment capacity. This trend was noted in various numerical studies, which have shown that the presence of residual stresses had a negligible effect on the behaviour of relatively compact beam sections. Therefore, precise modeling of the residual stresses is not a serious concern (Greschik et al., 1993, Huang 1994 and Yakel et al., 2002). This is true for relatively compact sections such as used in this study. In this modeling $F_y = 409$ MPa was used.

Finite Element Analysis Procedure: As discussed, the beam model was developed using four-node shell element. Web stiffeners were also modeled with the 4-node shell element. The loading was applied through a displacement control. As discussed, ADINA static analysis module was used. A total displacement of a required amount (depending on the problem) was applied varying linearly with a total time of 100. The total time was subdivided into 500 equal time steps. Thus, for each time increment, the displacement was increased by 0.8 mm.

### 7.4.2 Comparison of FE Results with Test Results

FE analyses were performed on twelve beam models. The beam models included solid beam, beam with holes in the tension flange and beams with holes in both flanges. In all cases, a full scale model was used to assess the FEA relative to the experimental results. The assessment was made based on the ability of the FE model to predict the behavior of test beams in terms of the global and local level.

Beam A100: Figure 7.10 compares the FE results with those of test results for solid beams. As seen in the figures, the FE results correlated well with the experimental results. The FE model reached a maximum load comparable to the test results. Moreover, the local deformations measured at the center midspan using the FE analysis and the test results were found to be in close agreement with each other (see Figure 7.10[B]). Figure 7.11 shows the deformed shape of the FE model of the solid beam. It can be seen from this figure that the beam exhibited a failure due to combined lateral torsional buckling and local buckling in the midspan region. A similar mode of failure was observed in the experiment (see Chapter 5).

Beam A90: Figure 7.12 compares the FE results with those of test results for beam A90-1. As seen in the figures, the FE results showed good agreement with the test results until a maximum load was attained. Beyond the maximum load level, the load-deflection response of the FE model was slightly higher than the experimental results, which may be due to the variations in geometrical imperfections, residual stresses, inhomogeneous material characteristics, etc. However, as seen in Figure 7.12[B], the local distortions measured at the center midspan of the beam were closely reproduced by the FE simulation. Figure 7.13 compares the deformed shape of the FE model with the test specimen. As seen in the figure, beam A90-1 exhibited a failure due to combined lateral torsional buckling and local buckling in the critical span region which was similar to the failure observed in the experiment.

Beam A85: In Figure 7.14, the FE responses were compared with the test results. The overall predictions from the FE analysis showed good agreement with the test results. Figure 7.15 shows the deformed shape of the FE model at failure. As seen in the figure, the failure was mainly due to combined lateral torsional buckling and local buckling in the critical span region which was similar to the test observations.

Beam A80: Figure 7.16 presents the FE responses along with the test results for beam A80-1. As seen in the figures, the initial stiffness of the FE model was slightly higher than the test response. However, the overall variation of the FE results were in close agreement with the test results until a maximum load was attained. Beyond the maximum load, the FE model unloaded relatively more gradually than the test results (see Figure 7.16[A]). Figure 7.17 shows the deformed shape of the FE model at failure. As seen in the figure, local buckling waves observed along the flange-edges in the midspan region. A similar nature of failure mode was observed in the test specimen A80-1 (see Chapter 5).

Beam A75: Figure 7.18 compares the FE results with the test responses for beams A75-1, A75-2 and A75-3. Overall, the responses obtained from the experiment and the FE models were well correlated. Figure 7.19 shows the deformed shape of the FE model. As can be seen from the figure, the FE model predicted a failure due to local buckling which was eventually followed by net section fracture at hole locations.

Figure 7.20 shows the variation of strain ($F_{zz}$) around hole region for the beam model A75. As seen in the figure, strains in the vicinity of hole region were several times larger than the strains in the tension flange away from the hole region. Once a maximum fracture strain of 100% was reached (in the vicinity of hole), the beam model began to shed load rapidly due to net section fracture at the hole location. As seen in Figure 7.20, although the strain in the vicinity of hole region was approximately 100% (at failure), the strain at the flange-web junction was less than 15%, which may be attributed to the fact that the flange-web interaction restrains the movement of the flange at the intersection. Therefore, this FE study supported the argument that a beam member may not fail suddenly once the tension flange having holes has reached a maximum fracture strain, as opposed to a direct tension member (Dexter et al., 2002).

Beam A70: Figure 7.21 presents the FE responses along with the test results for beam specimens A70-1, A70-2 and A70-3. As seen in the figures, the initial stiffness of the FE response was slightly higher than that of the test specimens, which may be due to the variations in shear-span of the test beam from the value used in the FE simulation. However, the predicted responses were closely correlated with the experimental results. Figure 7.22 illustrates the deformed shape of the FE model comparing with the test specimen. As can be observed from the figure, the FE model predicted failure due to fracture, which was preceded by necking at hole locations.

Beam A60: Figure 7.23 relates the FE response along with the test responses for beam specimens A60-1, A60-2 and A60-3. As seen in the figures, the FE results agreed closely with the test results. The deflected shape of the beam as obtained from the FE analysis presented in Figure 7.24. As seen in the figure, the failure pattern associated with the test beam and the FE model were comparable to each other. The FE model predicted eventual failure due to fracture at hole locations.

Beam A50: Figure 7.25 compares the FE results with the test results for beam specimen A50-1. One observes from the load-deflection curve that the FE model failed at slightly higher midspan deflection than the test specimen. This may be mainly due to the following factors:

(1) the variations in the assumed maximum fracture strain of 100% may be slightly higher than the actual fracture strain that the flange material possesses

(2) the method of hole making practice may influence the material property adjacent to the hole region, which was not taken into account in the FE simulation. In other words, the FE simulation assumed that the material was homogenous throughout a sample

Figure 7.26 presents the deflected shape of the FE model at failure. As seen in the figure, good correlation occurred between the test specimen and the corresponding FE model in terms of eventual failure pattern due to fracture.

Beam A85-B: Figure 7.27 relates the FE responses with the test responses for beam specimen A85-B-1. As seen in Figure 7.27[A], the initial stiffness of the FE model was slightly lower than the test results. Furthermore, the FE model reached a maximum load at slightly lower midspan deflection than the test beam. However, the overall load-deflection behaviour of the FE model was similar to the test results. The prediction of local deformation at the center midspan was compared closely with the test response (see Figure 7.27[B]). Figure 7.28 presents the deformed shape of the FE model at failure. The FE model indicated the failure of the specimen due to combined lateral torsional buckling followed by local buckling of the compression flange in the critical span region. A similar nature of failure mode was observed during the test on beam A85-B-1 (see Figure 7.28).

Beam A75-B: Figure 7.29 compares the FE predictions with the experimental responses for beam A75-B-1. As seen in the figure, the FE model closely predicted the experimental results. Moreover, the FE prediction of out-of-plane movement of the compression flange with respect to the tension flange at the center midspan was in close agreement with the test result (see Figure 7.29[B]). The strain readings (at strain gauges) for the test specimen and the FE model at a cross-section in the center midspan are compared in Figure 7.30. As presented in Figure 7.30, the effect of stress concentration in the vicinity of hole region was evident from the FE model and the test results. The overall strain variations at corresponding locations of the FE model and the test specimen were in close agreement until a gross cross-section plastic moment was attained. After reaching the plastic moment, slight variations occurred between the FE prediction and the test results. Figure 7.31 presents a deflected shape of the FE model and beam specimen A75-B-1 at failure. As seen in the figure, local buckling of the compression flange occurred within the midspan region. The deformed shape of the FE model was comparable to that of the test specimen at failure.

Beam A70-B: The load-deflection and the moment-rotation behavior of beam specimen A70-B-1 is compared with the FE model responses in Figure 7.32. As seen in the figure, the FE model described a load-deflection response similarly to the test results until a maximum load was attained. Beyond the maximum load, the unloading in FE model occurred relatively rapidly when compared to the test response. Figure 7.33 portrays the deformed shape of the FE model and the test beam at failure. The FE model predicted failure similar to the test beam, i.e., the beam specimen failed as a result of net section fracture preceded by local buckling of the compression flange.

Beam A60-B: Figure 7.34 compares the FE responses with the test results. As seen in the figure, the FE responses and the test results were similar until the gross cross-section plastic load (or moment) was reached. Beyond the plastic load, the FE predictions were slightly higher than the test responses. Nevertheless, the maximum load attained by the FE model and the experiment was in close agreement. After reaching the maximum load, the FE model unloaded gradually and failed eventually as a result of net-section fracture. Figure 7.35 presents the deformed shape of the FE model along with that of the test beam. As seen in the figure, the failure pattern associated with the FE model was comparable with the test beam.

A comparison of the predicted ultimate moment capacity and the test results is presented in Table 7.2. The ratios of the test capacity to the predicted capacity for the twelve specimens presented in Table 7.2 varied between 0.98 and 1.02. For most cases, the predicted moment capacity was slightly lower than the test capacity.

### 7.4.3 Sensitivity Study on Selection of True Strain Corresponding to Fracture

This portion of the study was to investigate the influence of the selection of true strain corresponding to fracture ($\varepsilon_{f,t}$) on the behaviour of flexural members having flange holes. Although various experimental studies on ductile fracture of structural steels under uniaxial loading have shown that the $\varepsilon_{f,t}$ varies between 80% and 120% (Khoo, 2000 and Hancock and Mackenzie, 1976), it is not clear as to when to define $\varepsilon_{f,t}$ for a particular steel grade. This was why $\varepsilon_{f,t}$ of 100% was assumed for the FE analyses performed on tension tests and beam tests in this study. Although the material modeling based on $\varepsilon_{f,t}$=100% showed reasonably good agreement with the test results, it was of interest to see how the selection of $\varepsilon_{f,t}$ influences the ultimate response of flexural member having flange holes. For this purpose, beam specimen A50-1 was considered. As shown in Figure 7.36, the beam was modeled with three different $\varepsilon_{f,t}$ values for the flange and web material; $\varepsilon_{f,t}$=80%, $\varepsilon_{f,t}$=100% and $\varepsilon_{f,t}$=120%. Figure 7.37 shows the predicted load-midspan deflection curves for the $\varepsilon_{f,t}$ of 80%, 100% and 120%. As seen in the figure, for $\varepsilon_{f,t}$=80%, the predicted results correlated well with the experimental results. However, for $\varepsilon_{f,t}$=80%, the maximum load predicted by the FE model was slightly lower than the test value. As seen in Figure 7.37, for $\varepsilon_{f,t}$=100% a sudden drop in load occurred approximately 36% higher midspan deflection when compared to the test results. For $\varepsilon_{f,t}$=120%, the load began to drop at 45% higher midspan deflection than the test results. Therefore, the selection of $\varepsilon_{f,t}$ had a certain impact on the fracture point, but had no significant impact until the beam specimen reached its ultimate load. By considering the analyses based on one beam model (A50-1) may provide an idea on how the effects of holes on flexural behaviour of steel beams or any member experiencing a stress concentration effects due to abrupt changes in cross-section (presence of holes, grooves, etc.) can be taken into account in FE modeling.

## 7.5 Summary

A total of twelve test beams were analyzed with the help of FE analyses. The numerical results of the load-midspan deflection curves, moment-rotation curves flange local deformation curves and deformed configurations were compared with experimental results. A comparison of those results indicated that the FE modeling could be used to analyze the inelastic response of beams with flange holes. The FE models described similar load-deformation curves and they reached a comparable maximum load. Also, the models were able to predict the failure mode and the location of the fracture. The strains obtained from the FE analyses showed good correlation with those in the test. Overall, the modeling technique used herein provided good predictions of the experimental results at both the local and global levels.

Table 7.1: Ultimate Strength of Plate with Different Sizes of Fastener Holes under Tension and Compression

| Fastener hole size including 2mm clearance (mm) | $\left[\frac{A_n}{A_g}\right]$ (%) | Tension | | Compression | |
|---|---|---|---|---|---|
| | | Ultimate strength (MPa) | % Strength reduction | Ultimate strength (MPa) | % Strength reduction |
| (1) | (2) | (3) | (4) | (5) | (6) |
| Solid-plate | 100 | 350 | 0.0 | 350 | 0 |
| 8.4 (1/4" bolt) | 96 | 335 | 4.3 | 347 | 0.9 |
| 18 (M16 bolt) | 91 | 320 | 8.6 | 344 | 1.7 |
| 26 (M24 bolt) | 87 | 306 | 12.6 | 340 | 2.9 |
| 32 (M30 bolt) | 84 | 295 | 15.7 | 338 | 3.4 |
| 40 (11/2" bolt) | 80 | 281 | 19.7 | 336 | 4.0 |

Table 7.2: Comparison of Maximum Moment between Test and FE Results

| Beam ID | $\left[\frac{A_{fn}}{A_{fg}}\right]$ | $\left[\frac{A_{fn}F_u}{A_{fg}F_y}\right]$ | Moment Capacity (kNm) | | Test/Predicted |
|---|---|---|---|---|---|
| | | | Test | FE Prediction | |
| (1) | (2) | (3) | (4) | (5) | (6) |
| A100-1,2,3,4 | 100 | 1.30 | 214 | 212.0 | 1.01 |
| A90-1 | 91 | 1.18 | 214 | 211.6 | 1.01 |
| A85-1 | 85 | 1.10 | 215 | 210.8 | 1.02 |
| A80-1 | 79 | 1.03 | 212 | 208.6 | 1.02 |
| A75-1,2,3 | 74 | 0.96 | 209 | 205.5 | 1.02 |
| A70-1,2,3 | 71 | 0.92 | 204 | 203.3 | 1.00 |
| A60-1,2,3 | 62 | 0.81 | 195 | 193.7 | 1.01 |
| A50-1 | 52 | 0.67 | 178 | 182.0 | 0.98 |
| A85-B-1 | 86 | 1.17 | 210 | 206.2 | 1.02 |
| A75-B-1 | 74 | 0.96 | 200 | 198.0 | 1.01 |
| A70-B-1 | 70 | 0.91 | 197 | 195.4 | 1.01 |
| A60-B-1 | 63 | 0.82 | 192 | 190.5 | 1.01 |

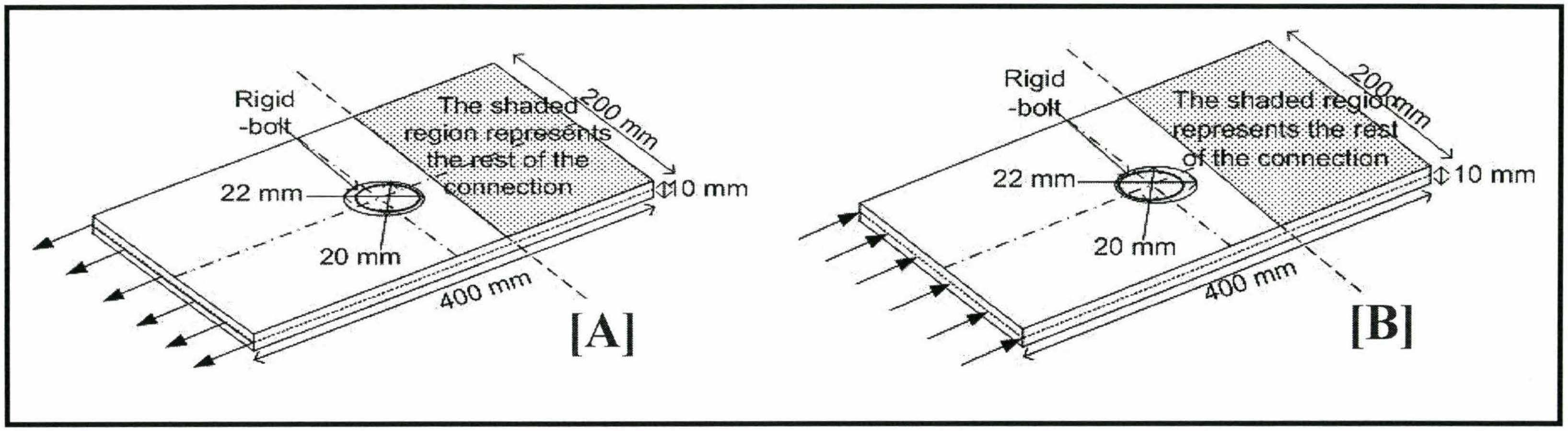


Figure 7.1: Plate with Fastener Hole

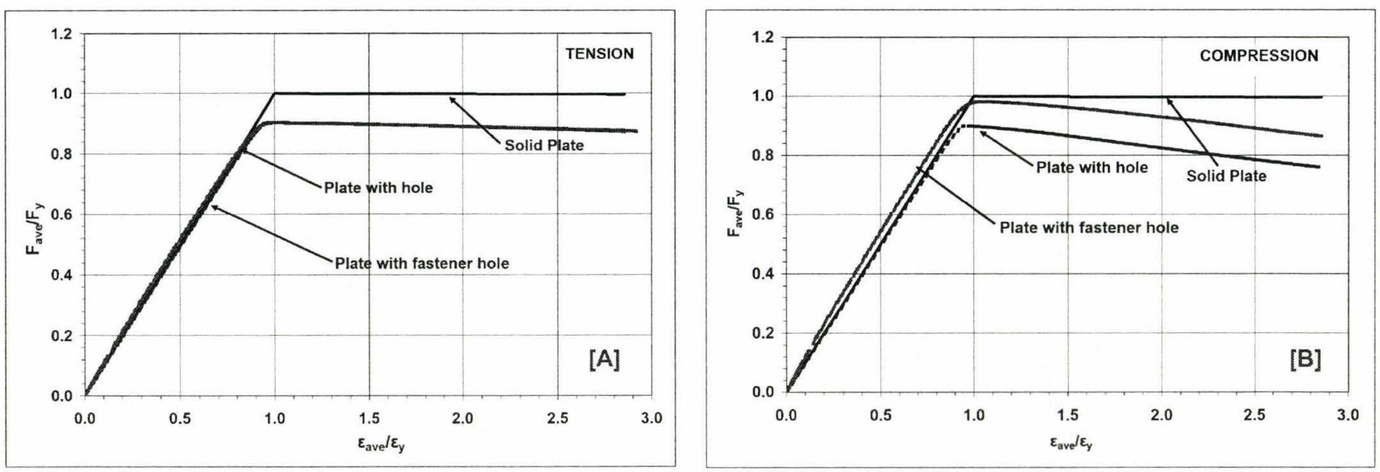


Figure 7.2: Normalized Axial Stress versus Axial Strain Relationship

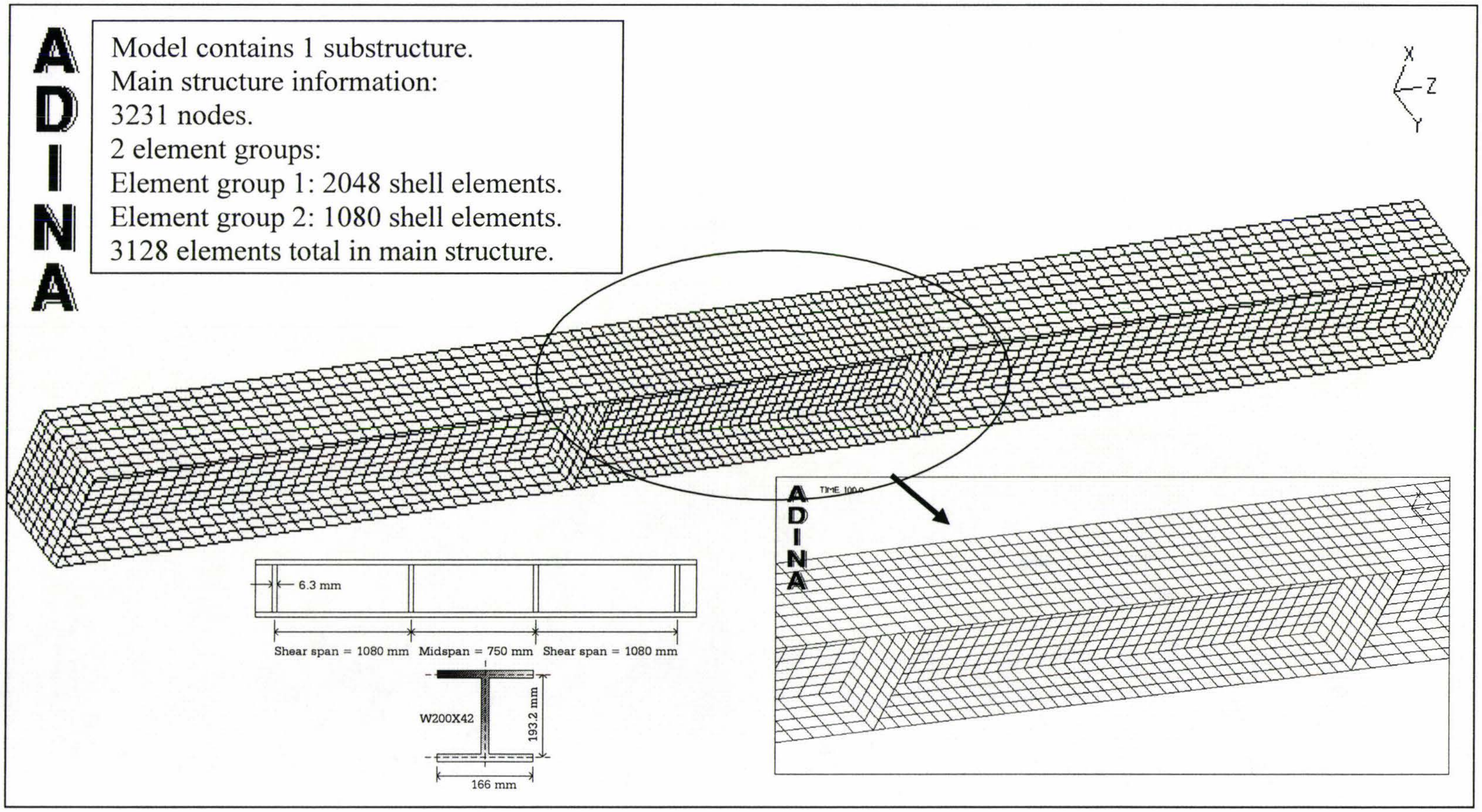


Figure 7.3: FE Model for Solid Beam

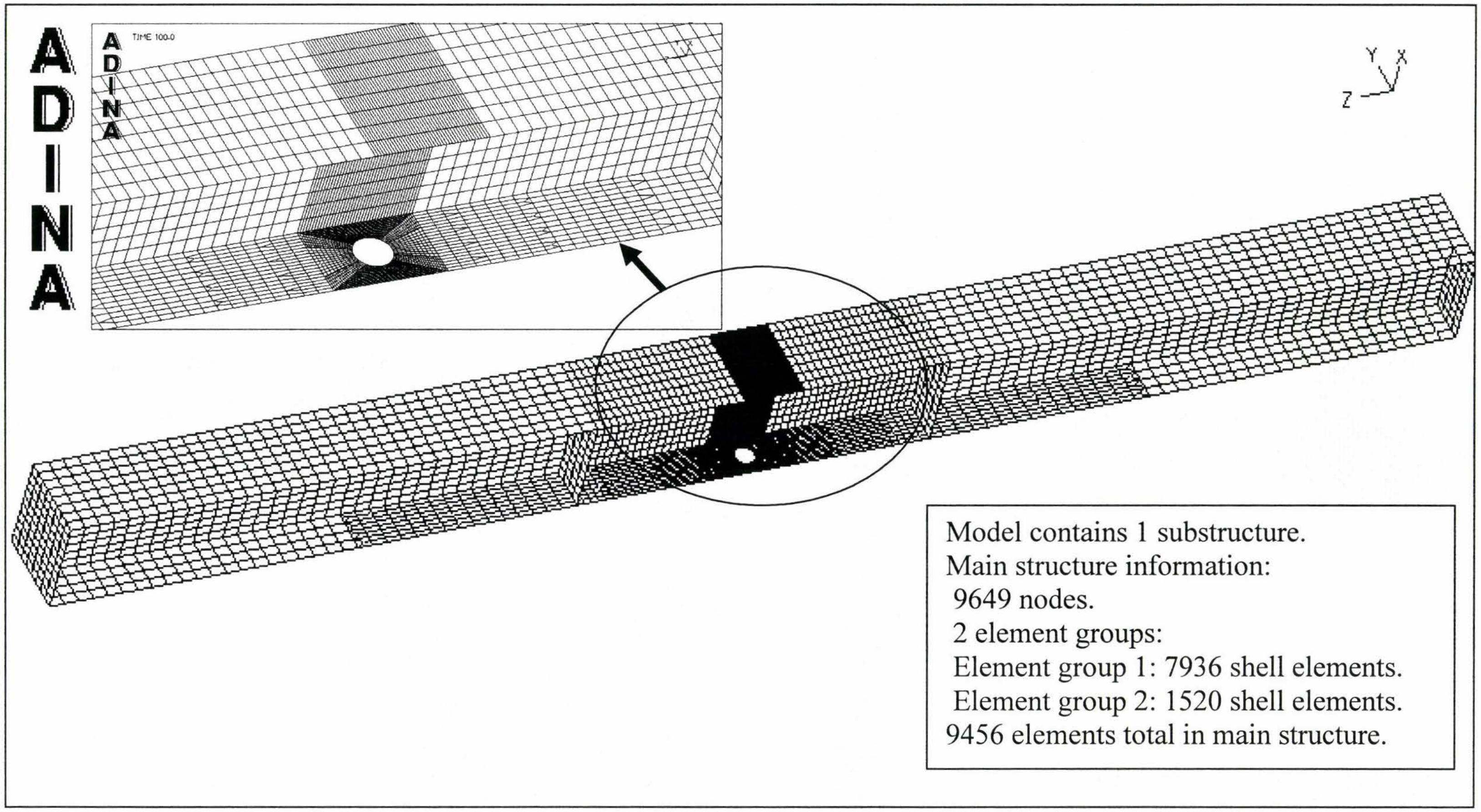


Figure 7.4: FE Model for Beam with Holes in Tension Flange

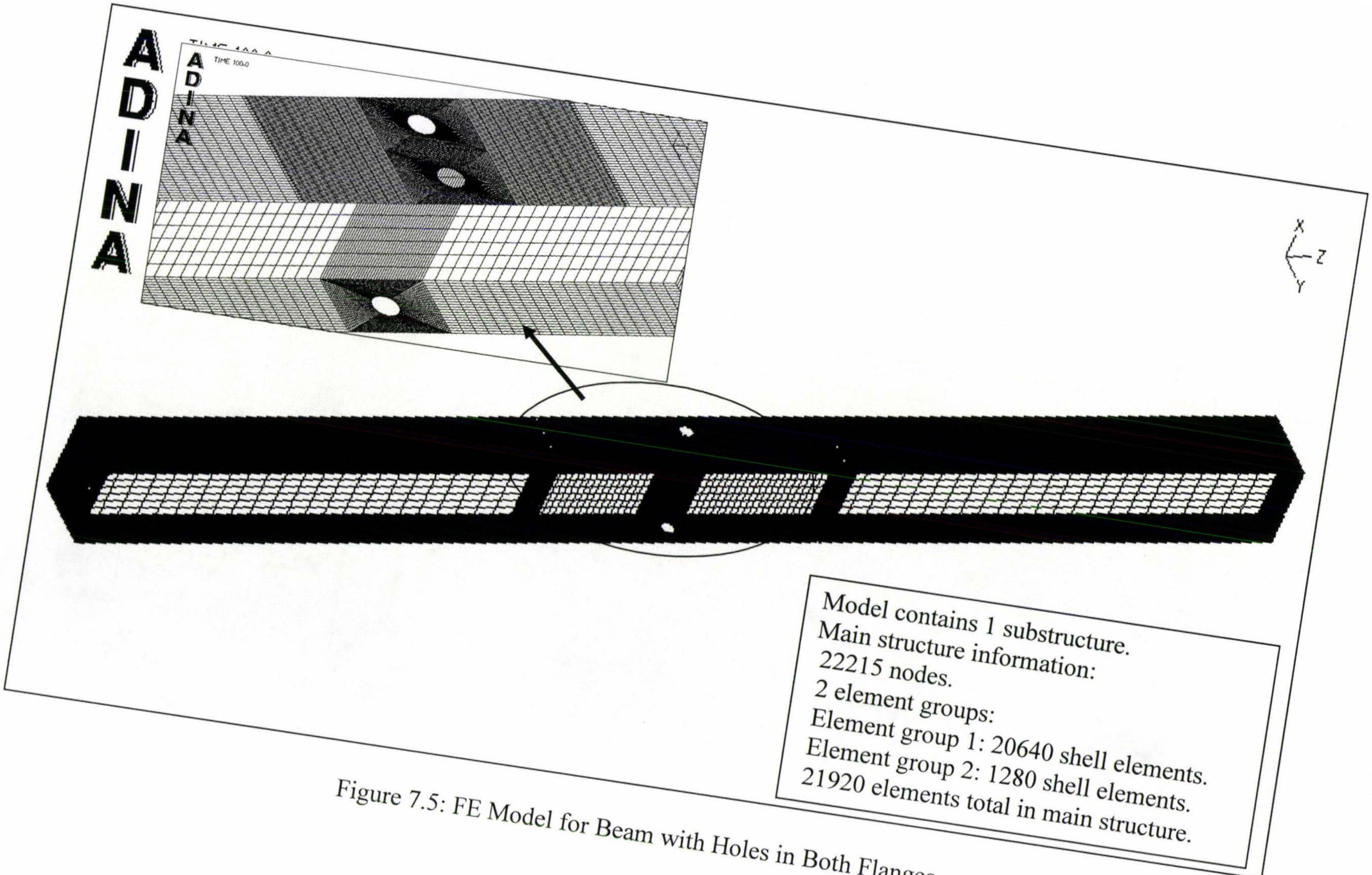


Figure 7.5: FE Model for Beam with Holes in Both Flanges

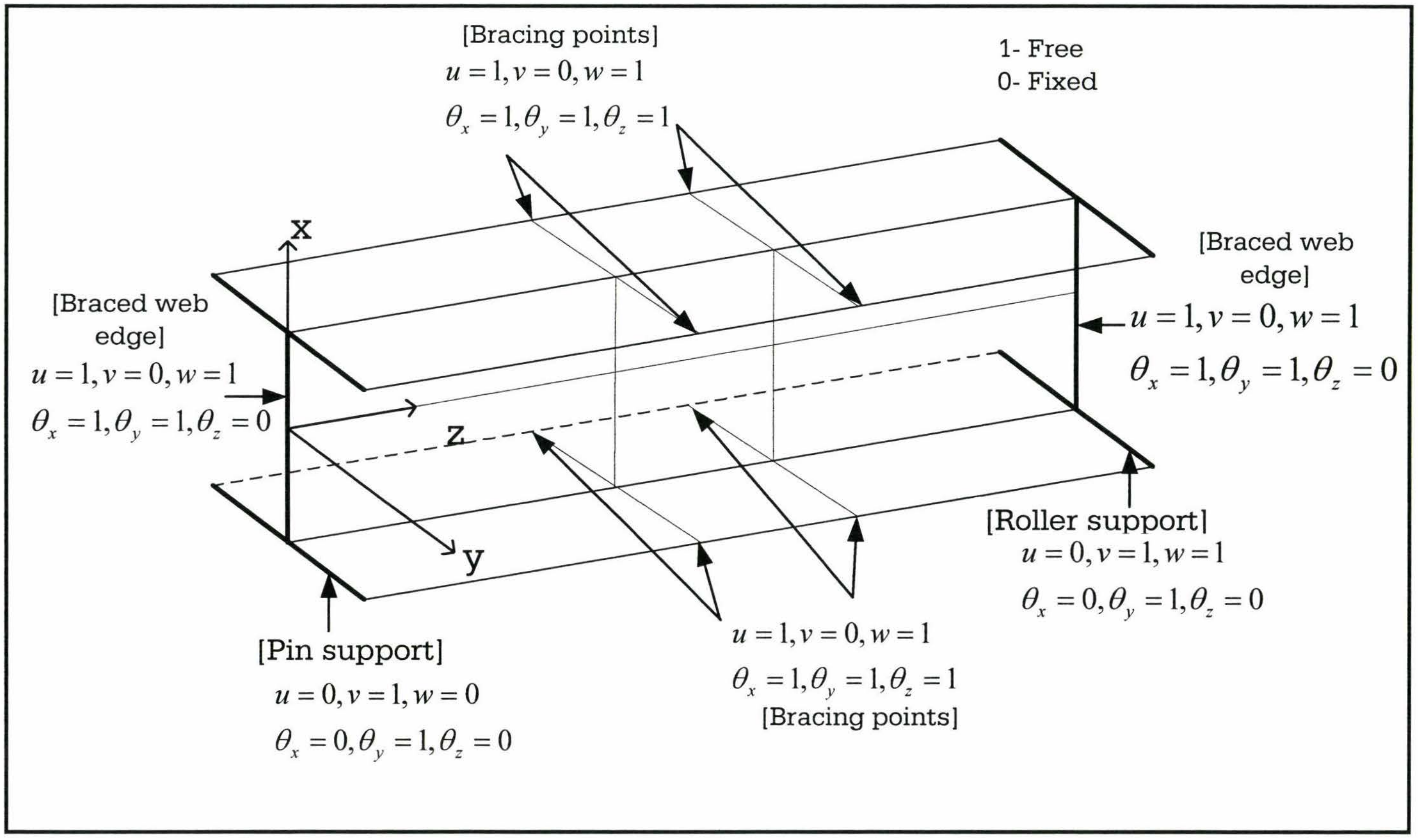


Figure 7.6: Boundary Condition for Full Scale Model

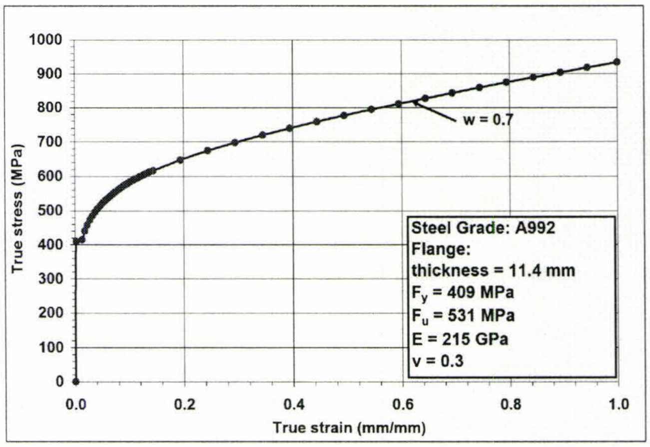


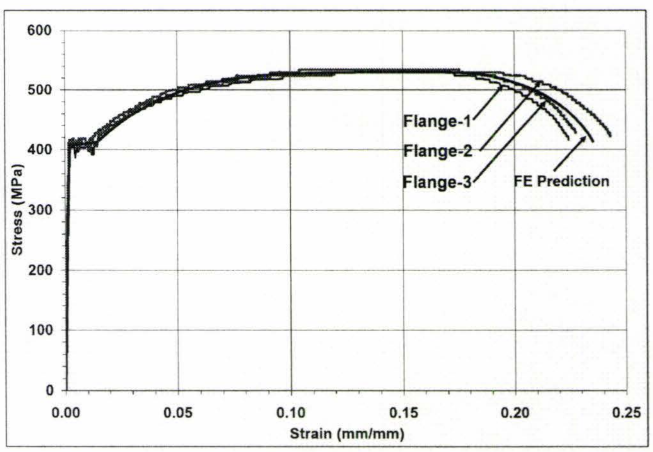


Figure 7.7: Flange Material Model

| True Stress-strain relationship | | | |
|---|---|---|---|
| Strain (mm/mm) | Stress (MPa) | | |
| 0.000 | 0 | | |
| 0.002 | 410 | | |
| 0.013 | 414 | | |
| 0.018 | 440 | | |
| 0.023 | 458 | | |
| 0.028 | 472 | | |
| 0.032 | 485 | | |
| 0.037 | 496 | | |
| 0.042 | 506 | | |
| 0.047 | 515 | | |
| 0.052 | 523 | | |
| 0.056 | 530 | | |
| 0.061 | 537 | | |
| 0.066 | 544 | | |
| 0.070 | 550 | | |
| 0.075 | 555 | | |
| 0.080 | 561 | | |
| 0.084 | 566 | | |
| 0.089 | 571 | | |
| 0.093 | 575 | | |
| 0.098 | 580 | | |
| 0.103 | 584 | | |
| 0.107 | 588 | | |
| 0.112 | 592 | | |
| 0.116 | 596 | | |
| 0.120 | 599 | | |
| 0.125 | 603 | | |
| 0.129 | 606 | | |
| 0.134 | 609 | | |
| 0.138 | 613 | | |
| 0.144 | 617 | | |
| 0.194 | 648 | | |
| 0.244 | 674 | 0.644 | 828 |
| 0.294 | 698 | 0.694 | 844 |
| 0.344 | 719 | 0.744 | 859 |
| 0.394 | 740 | 0.794 | 874 |
| 0.444 | 759 | 0.844 | 889 |
| 0.494 | 777 | 0.894 | 904 |
| 0.544 | 794 | 0.944 | 918 |
| 0.594 | 811 | 1.000 | 934 |

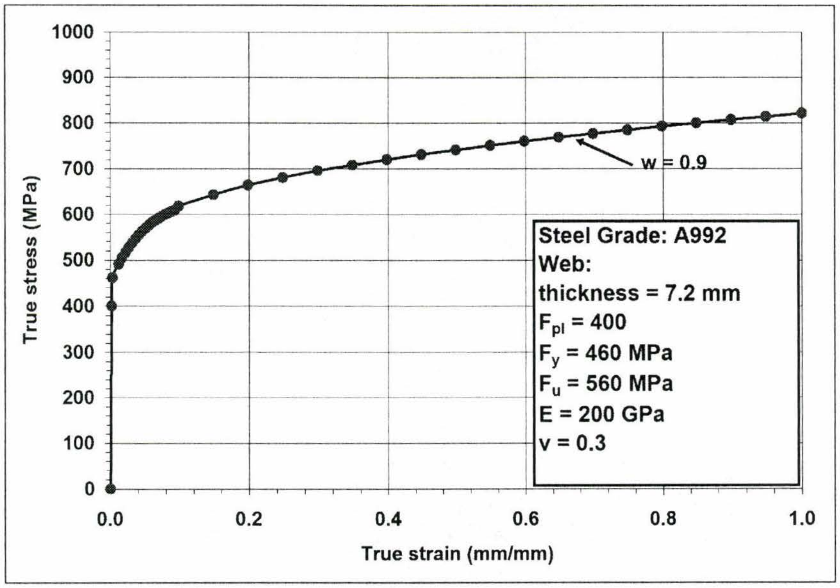


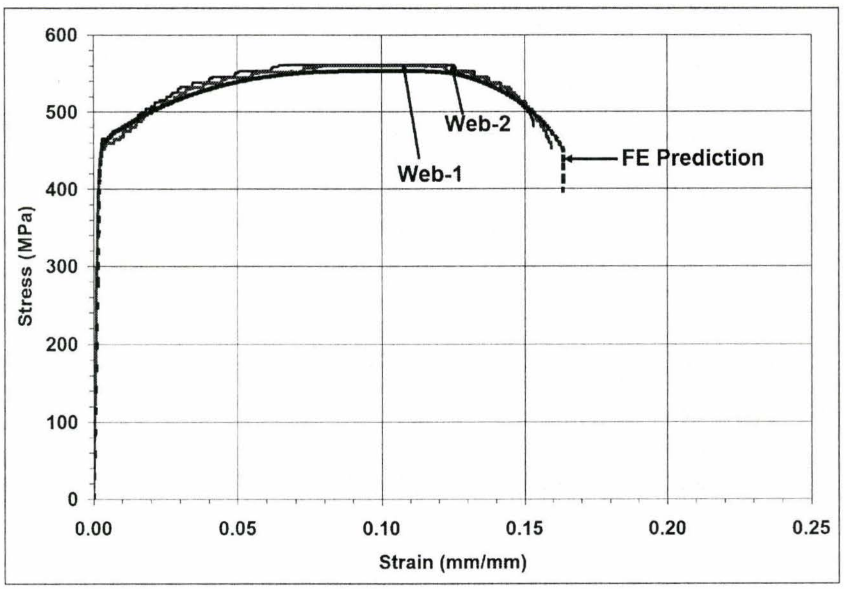


| True Stress-strain relationship | |
|---|---|
| Strain (mm/mm) | Stress (MPa) |
| 0.000 | 0 |
| 0.002 | 401 |
| 0.003 | 461 |
| 0.012 | 491 |
| 0.017 | 504 |
| 0.022 | 516 |
| 0.027 | 527 |
| 0.031 | 538 |
| 0.036 | 547 |
| 0.041 | 555 |
| 0.046 | 563 |
| 0.051 | 570 |
| 0.055 | 576 |
| 0.060 | 582 |
| 0.065 | 587 |
| 0.070 | 592 |
| 0.074 | 596 |
| 0.079 | 599 |
| 0.083 | 603 |
| 0.088 | 606 |
| 0.093 | 609 |
| 0.098 | 618 |
| 0.148 | 643 |
| 0.198 | 664 |
| 0.248 | 681 |
| 0.298 | 696 |
| 0.348 | 709 |
| 0.398 | 721 |
| 0.448 | 732 |
| 0.498 | 742 |
| 0.548 | 751 |
| 0.598 | 760 |
| 0.648 | 769 |
| 0.698 | 777 |
| 0.748 | 785 |
| 0.798 | 793 |
| 0.848 | 800 |
| 0.898 | 808 |
| 0.948 | 815 |
| 1.000 | 822 |

Figure 7.8: Web Material Model

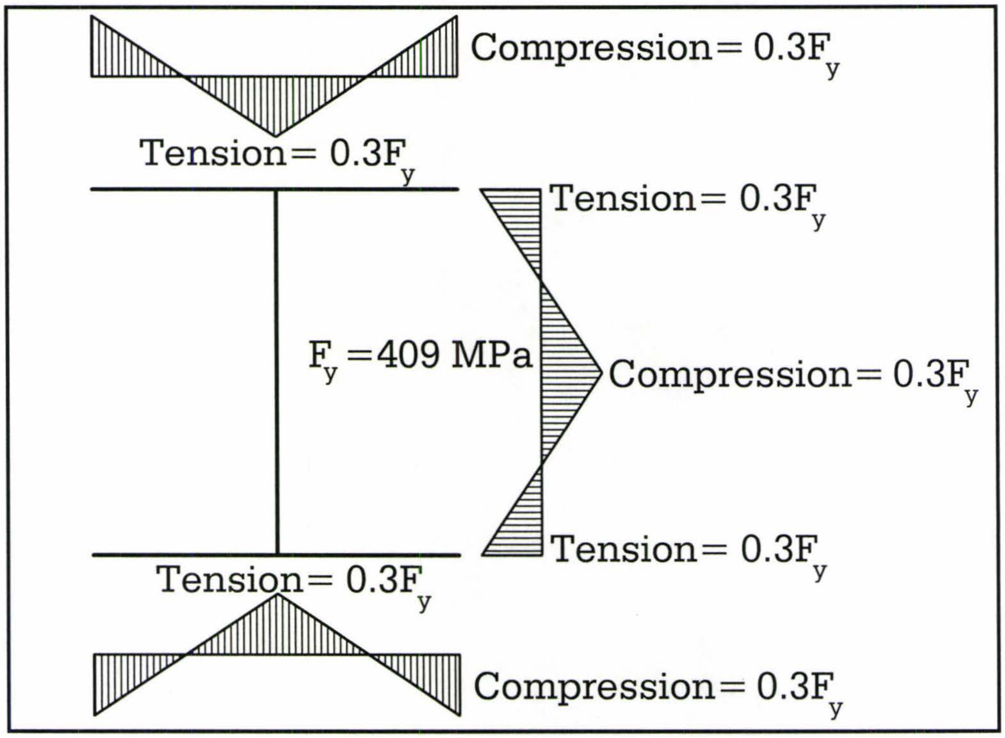


Figure 7.9: Idealized Residual Stresses

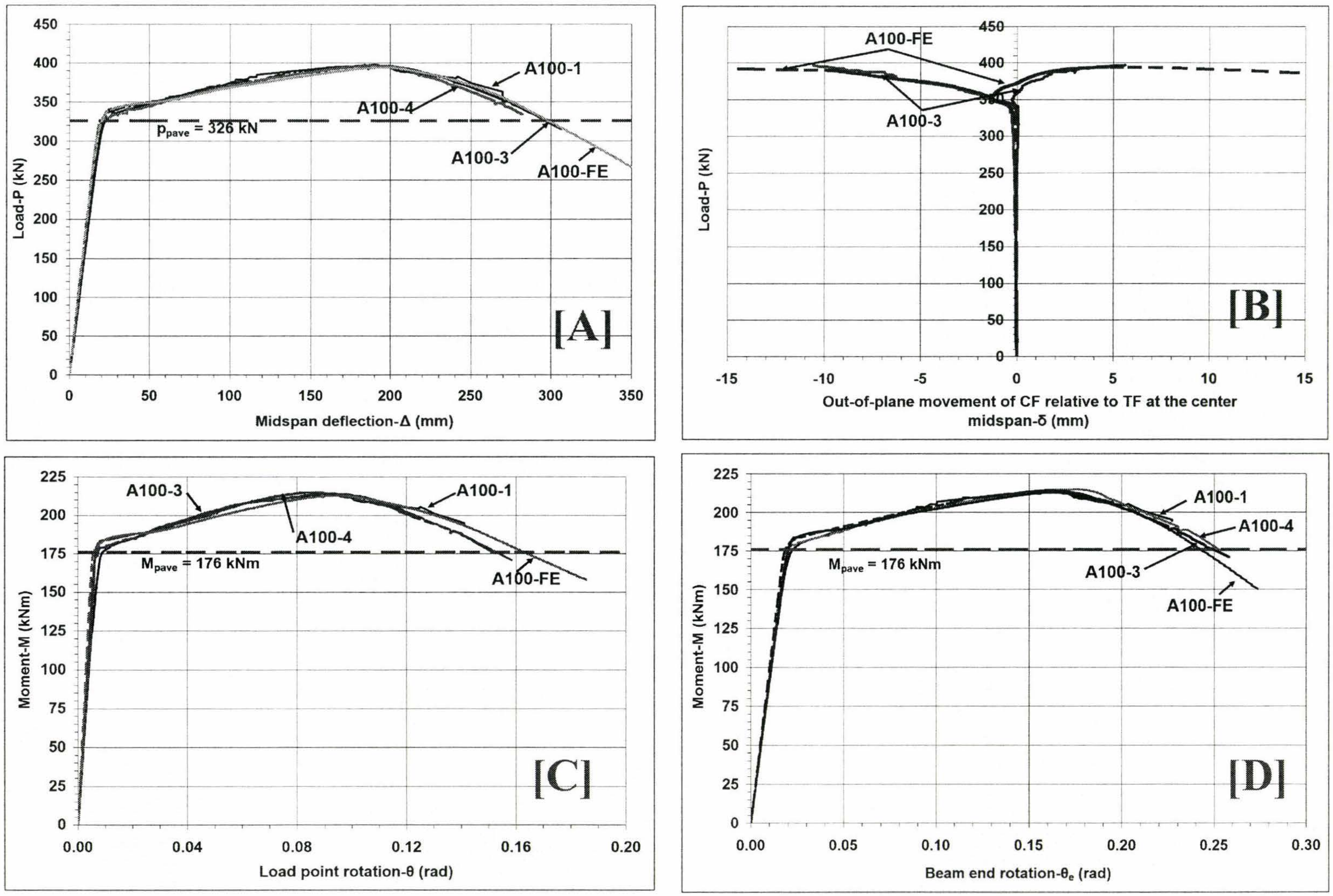


Figure 7.10: Comparison of Test Result with FE Prediction - Solid Beam

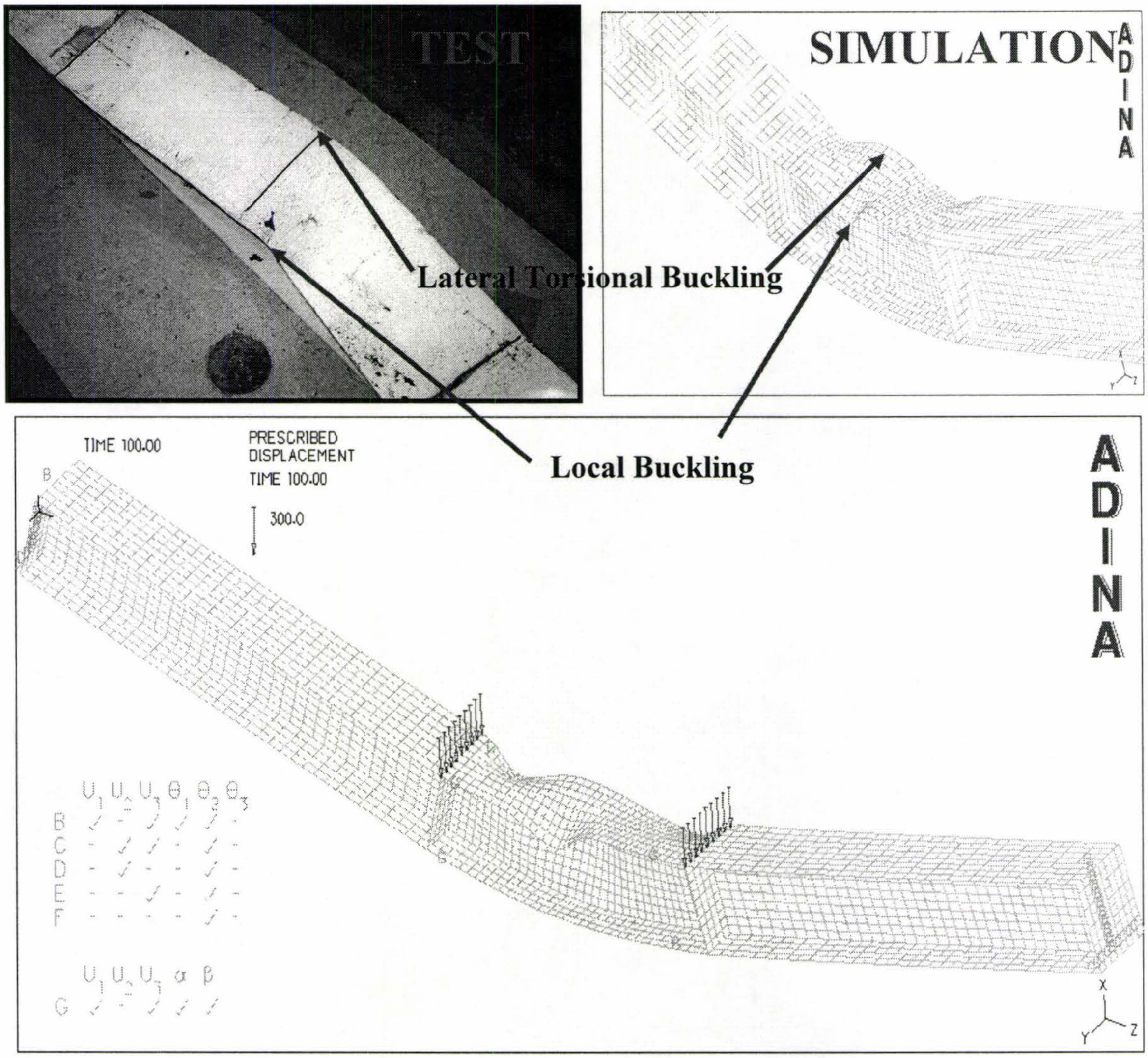


Figure 7.11: Deformed Shape of FE Model – Solid Beam

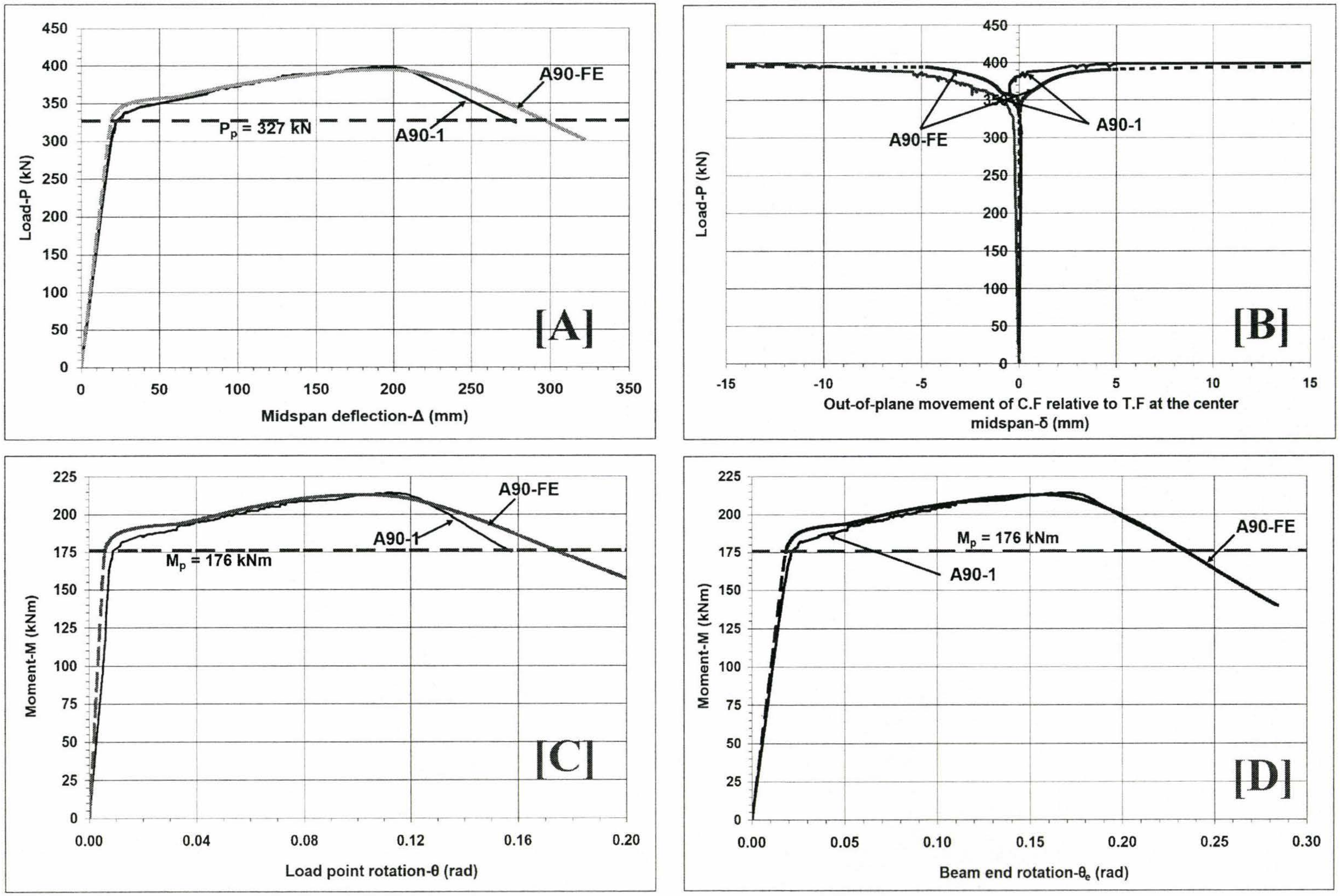


Figure 7.12: Comparison of Test Result with FE Prediction - Beam A90-1

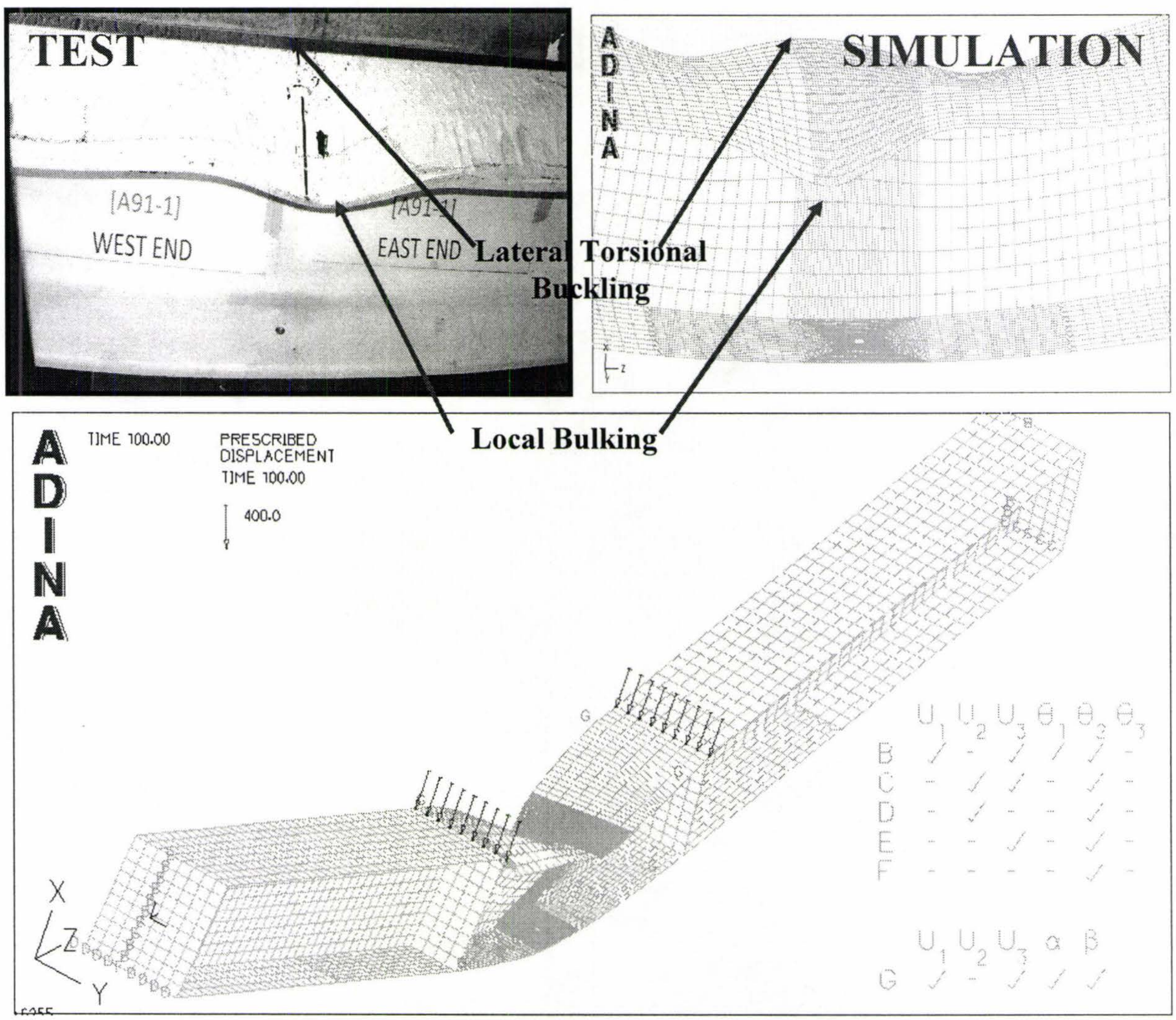


Figure 7.13: Deformed Shape of FE Model – Beam A90-1

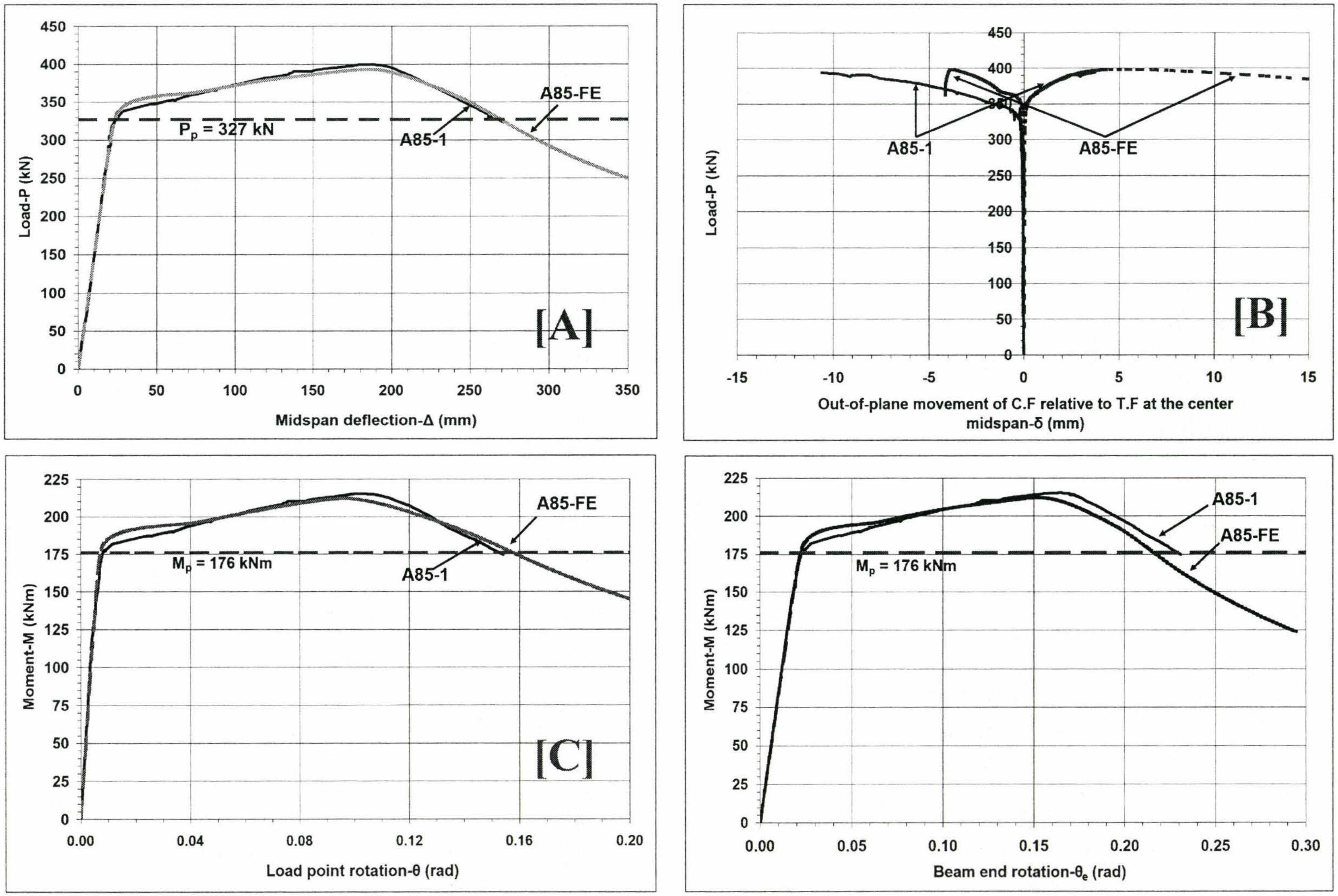


Figure 7.14: Comparison of Test Result with FE Prediction - Beam A85-1

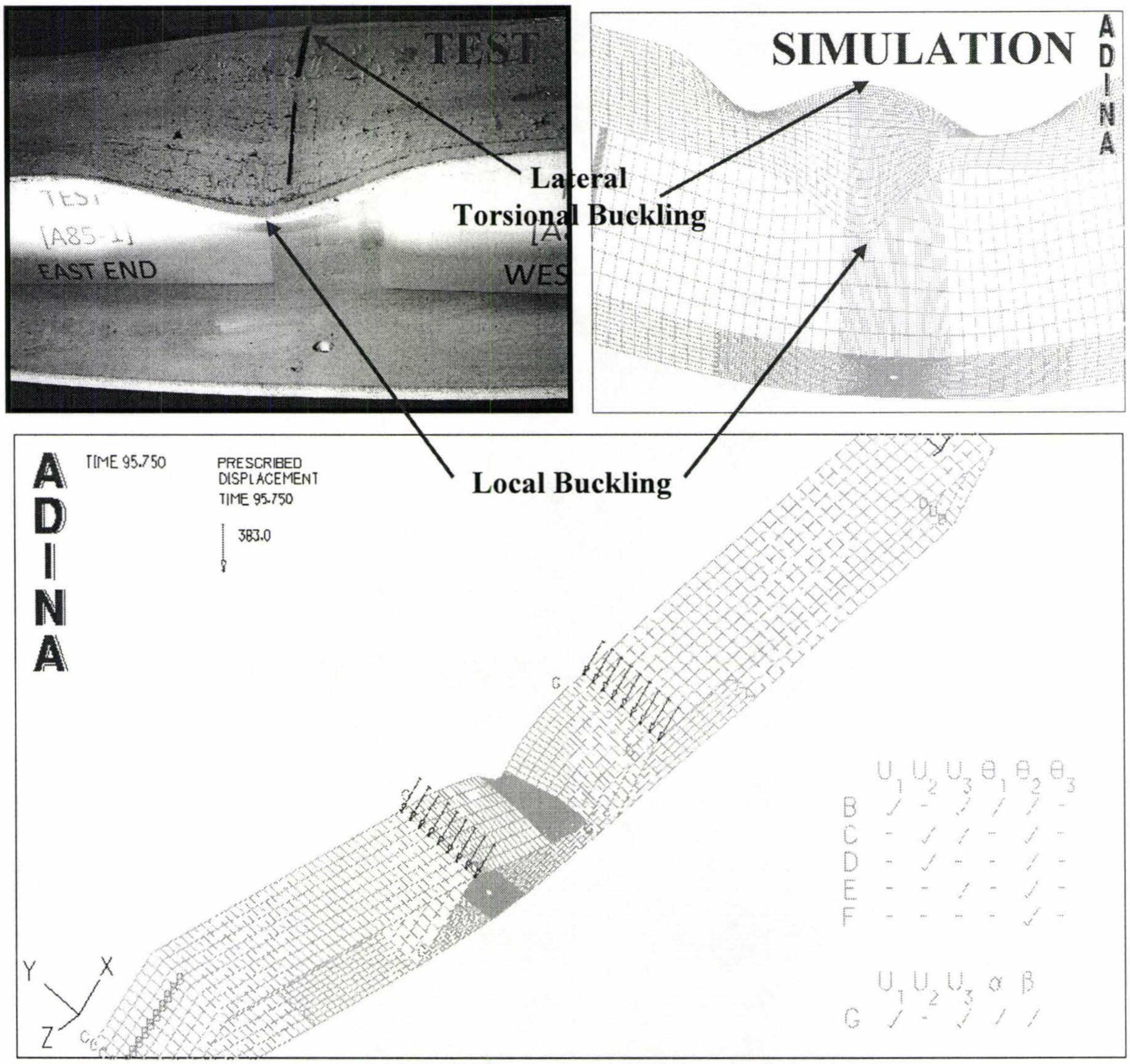


Figure 7.15: Deformed Shape of the FE Model – Beam A85-1

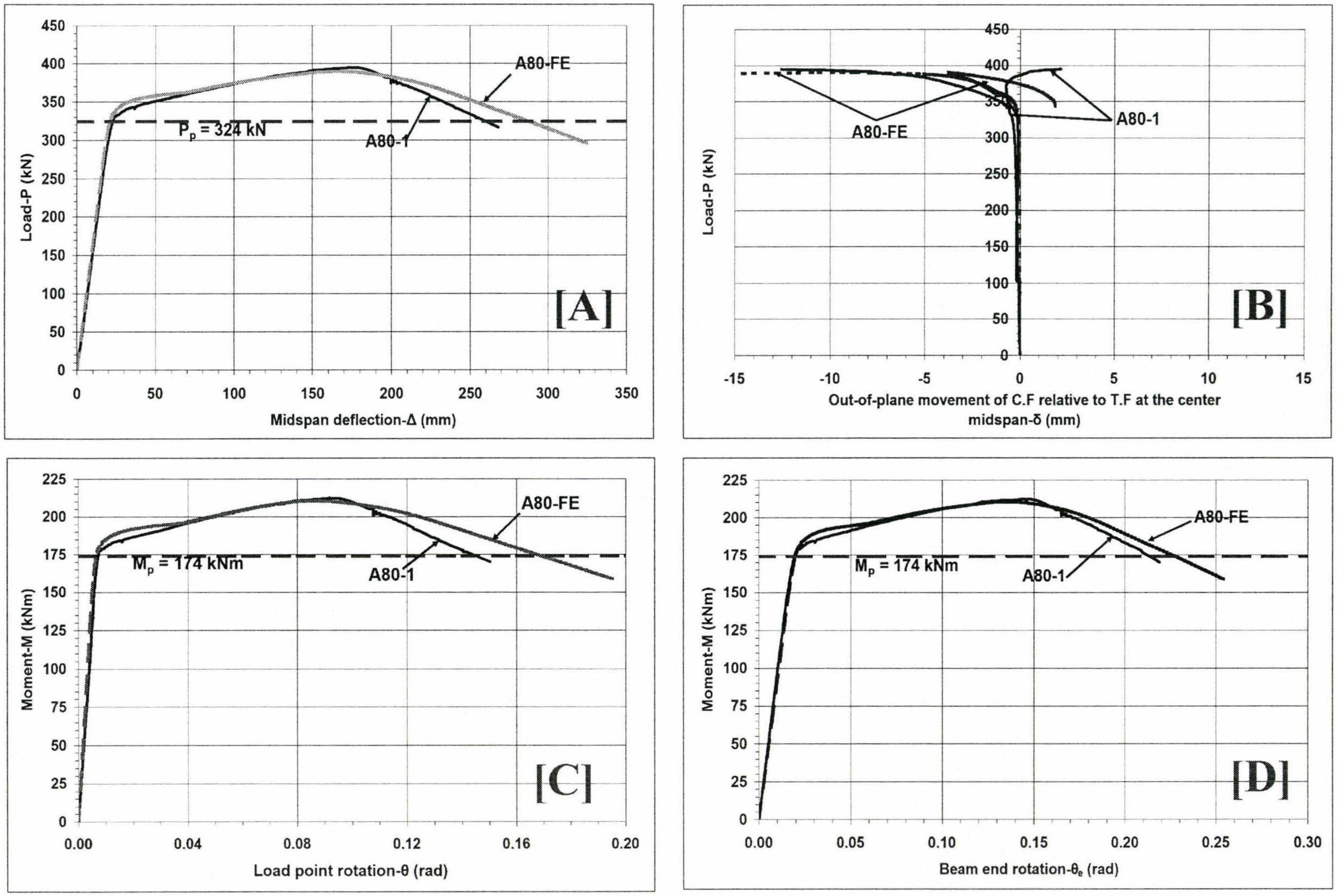


Figure 7.16: Comparison of Test Result with FE Prediction - Beam A80-1

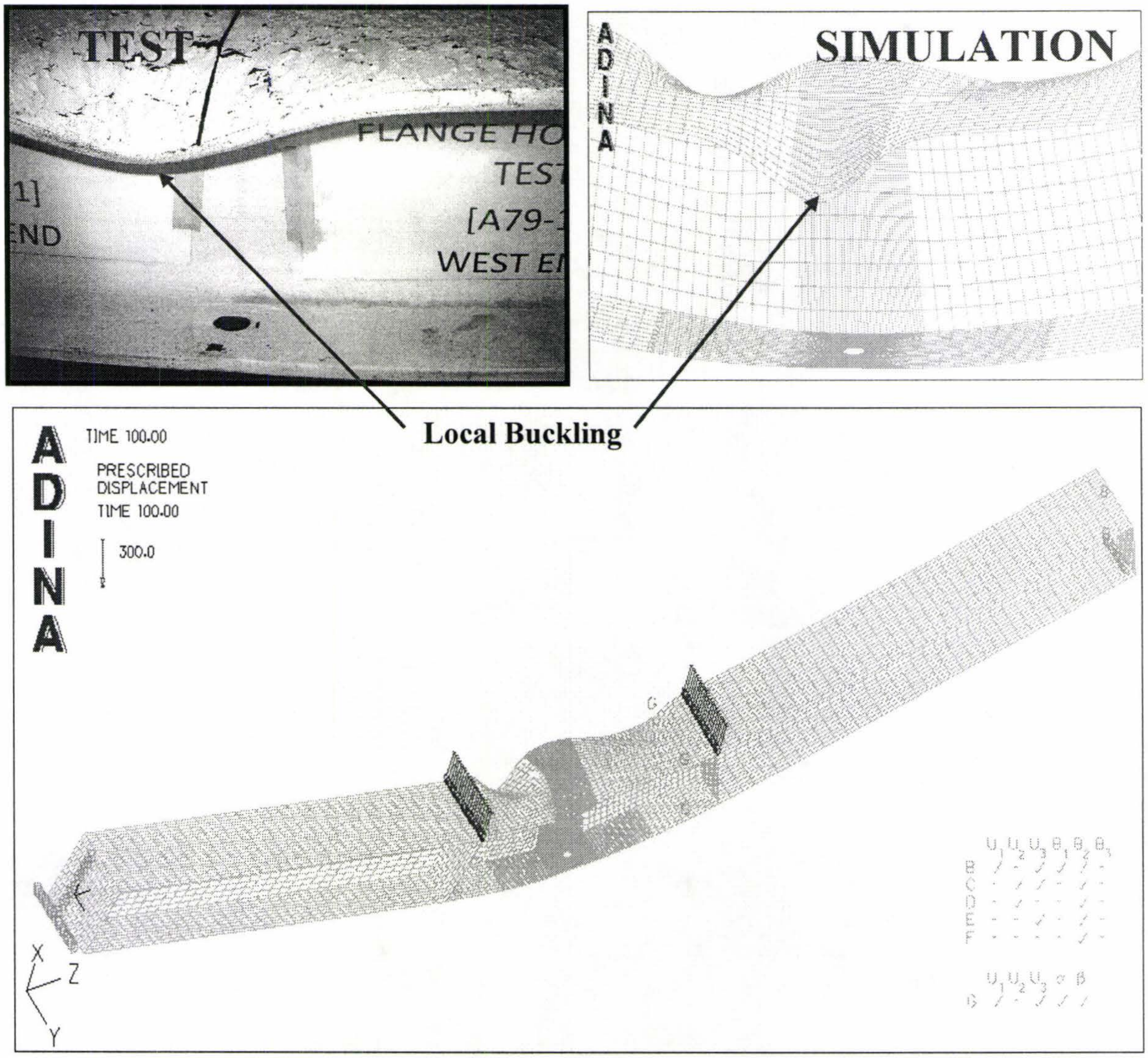


Figure 7.17: Deformed Shape of the FE Model – Beam A80-1

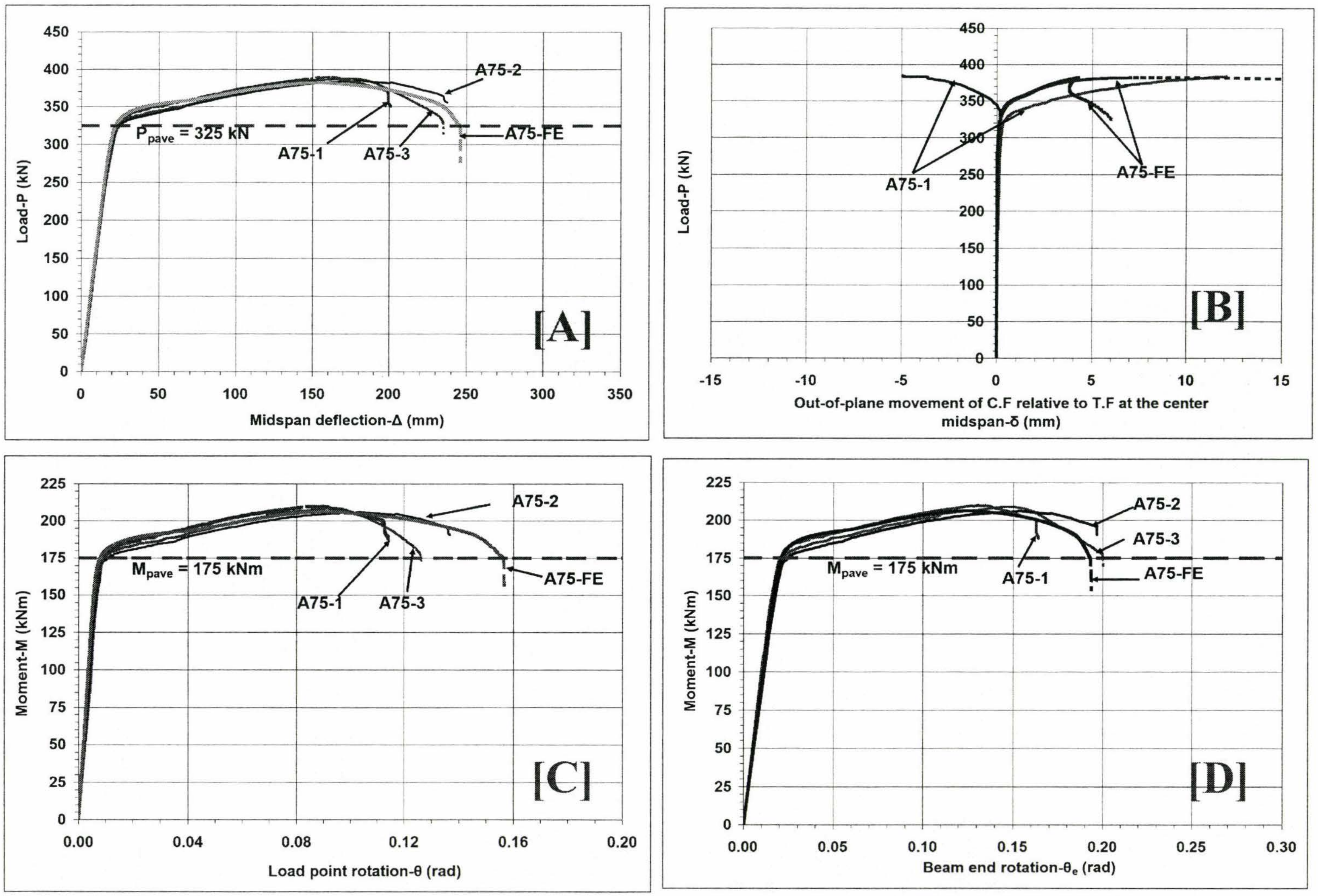


Figure 7.18: Comparison of FE Predictions with Test Responses - Beam A75 Series

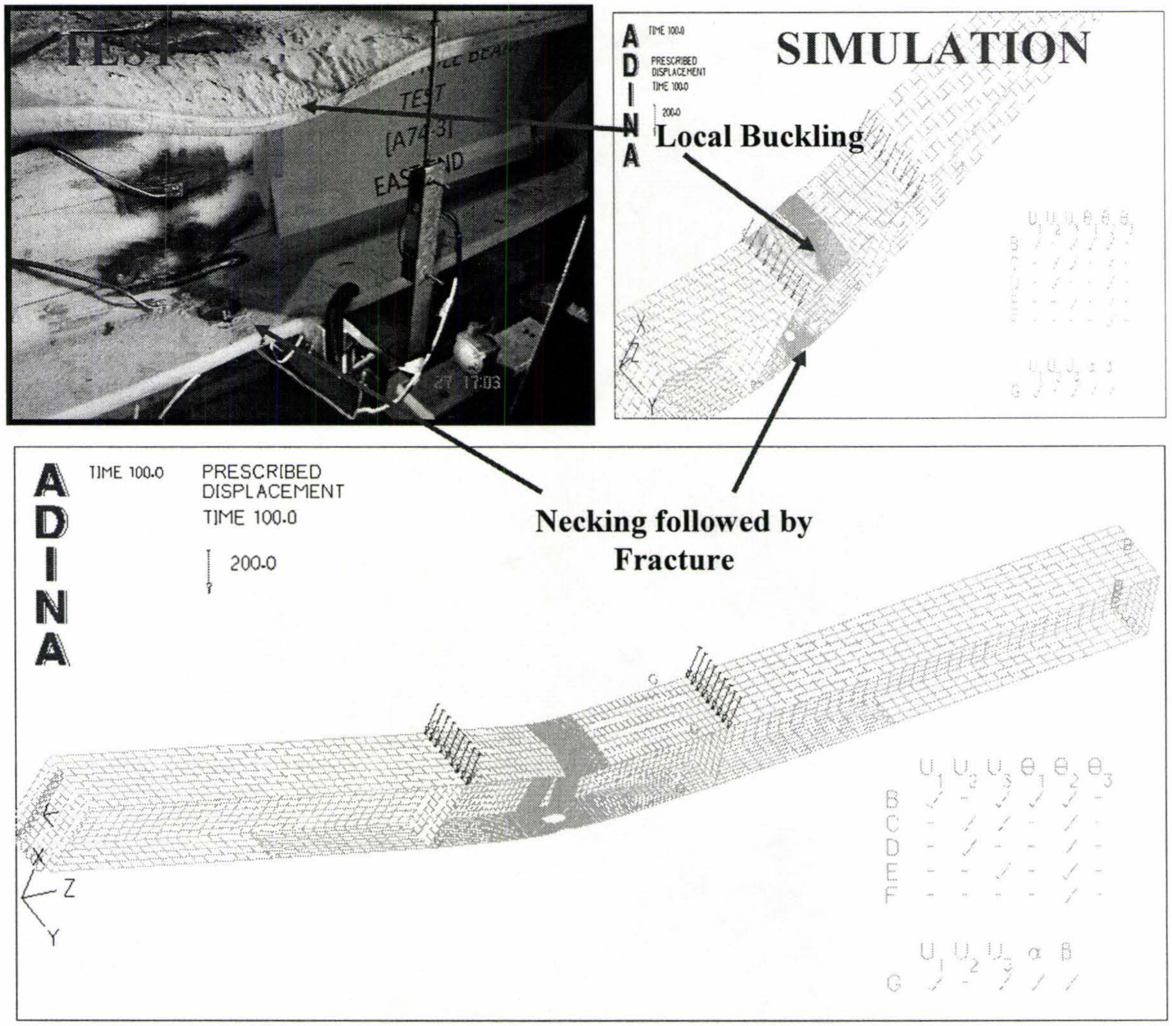


Figure 7.19: Deformed Shape of the FE Model - Beam A75 Series

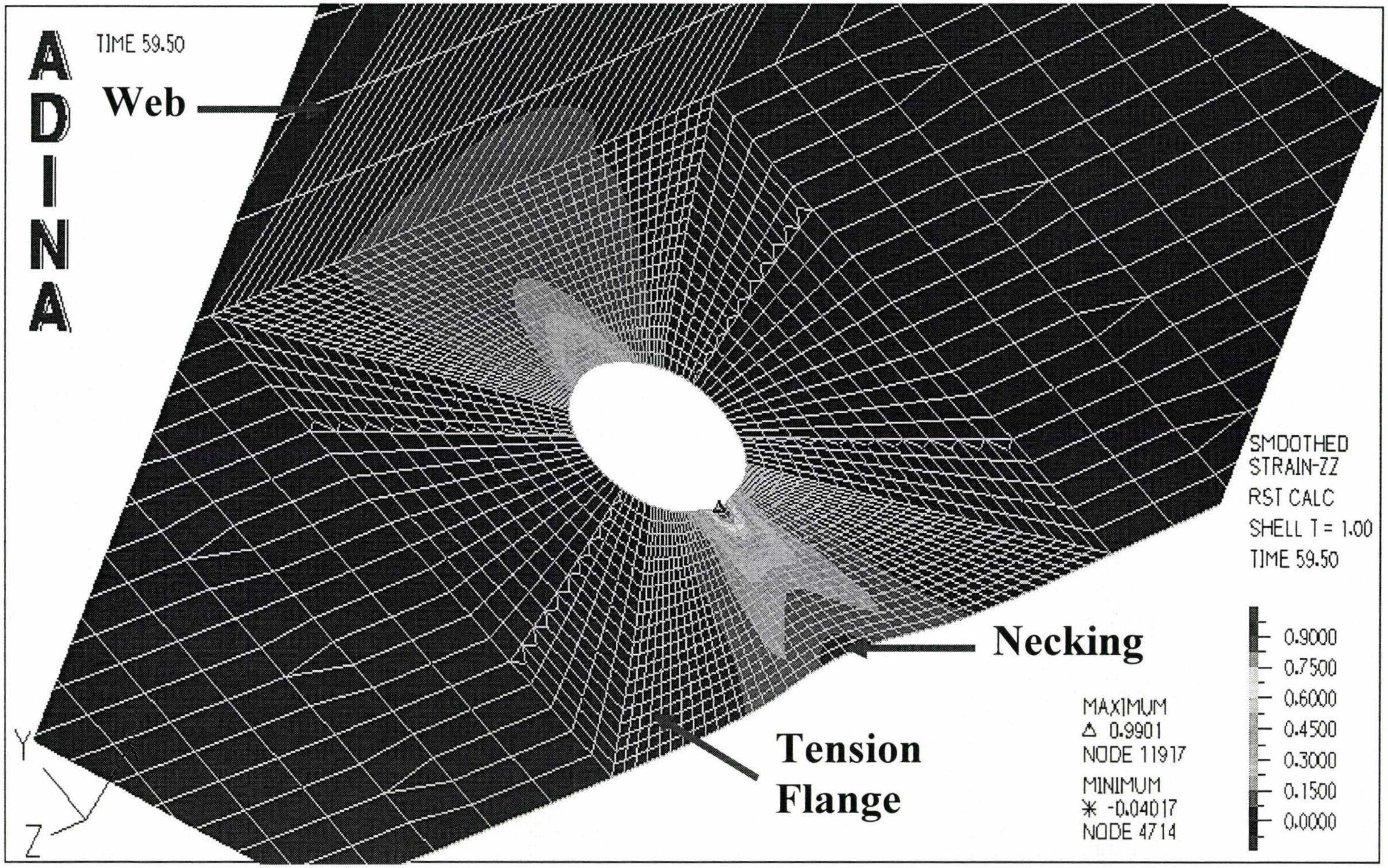


Figure 7.20: Contour Plot of Strains in the Longitudinal Direction of Beam A75

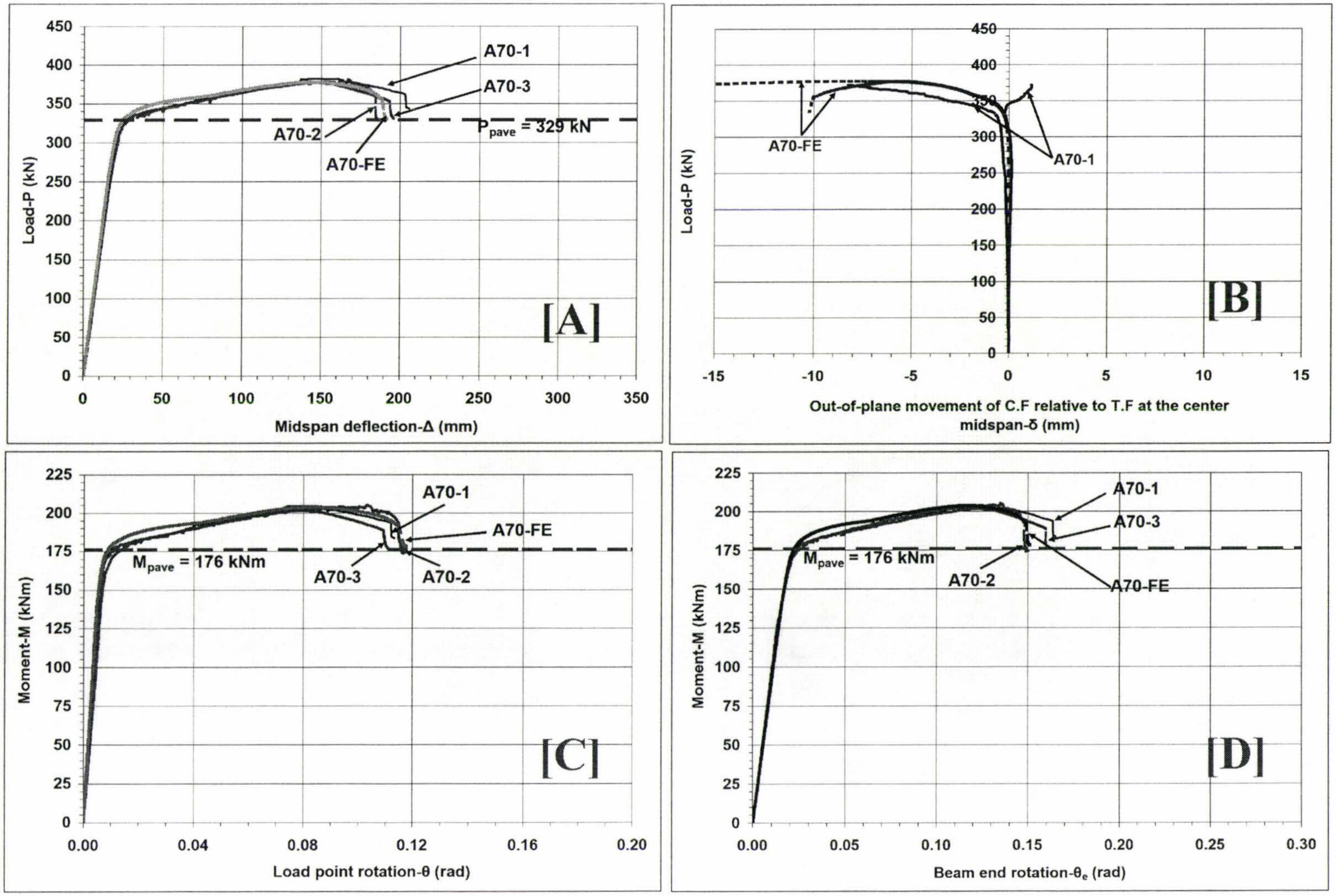


Figure 7.21: Comparison of FE Predictions with Test Responses - Beam A70 Series

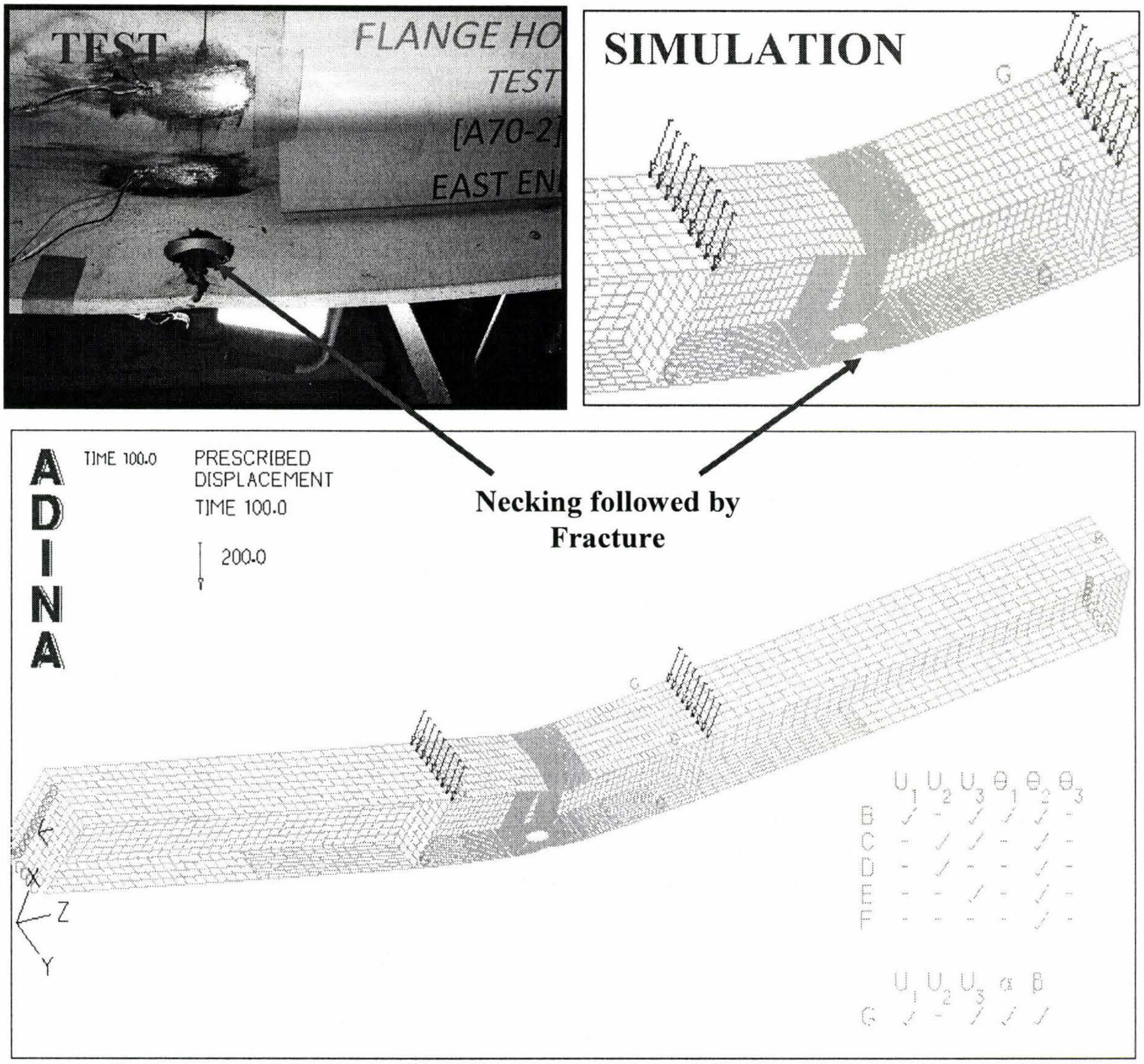


Figure 7.22: Deformed Shape of the FE Model - A70 Beam

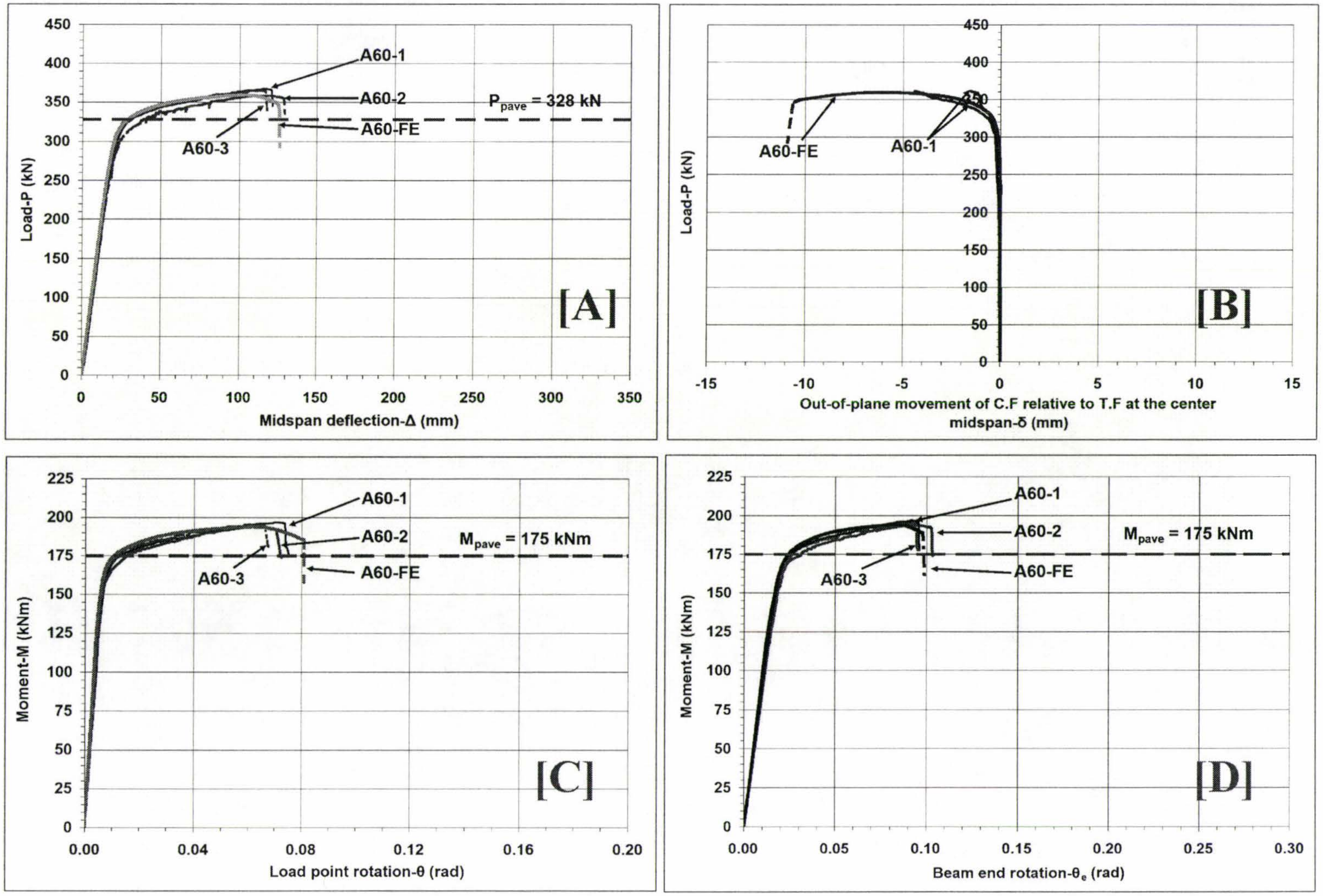


Figure 7.23: Comparison of FE Predictions with Test Responses - Beam A60 Series

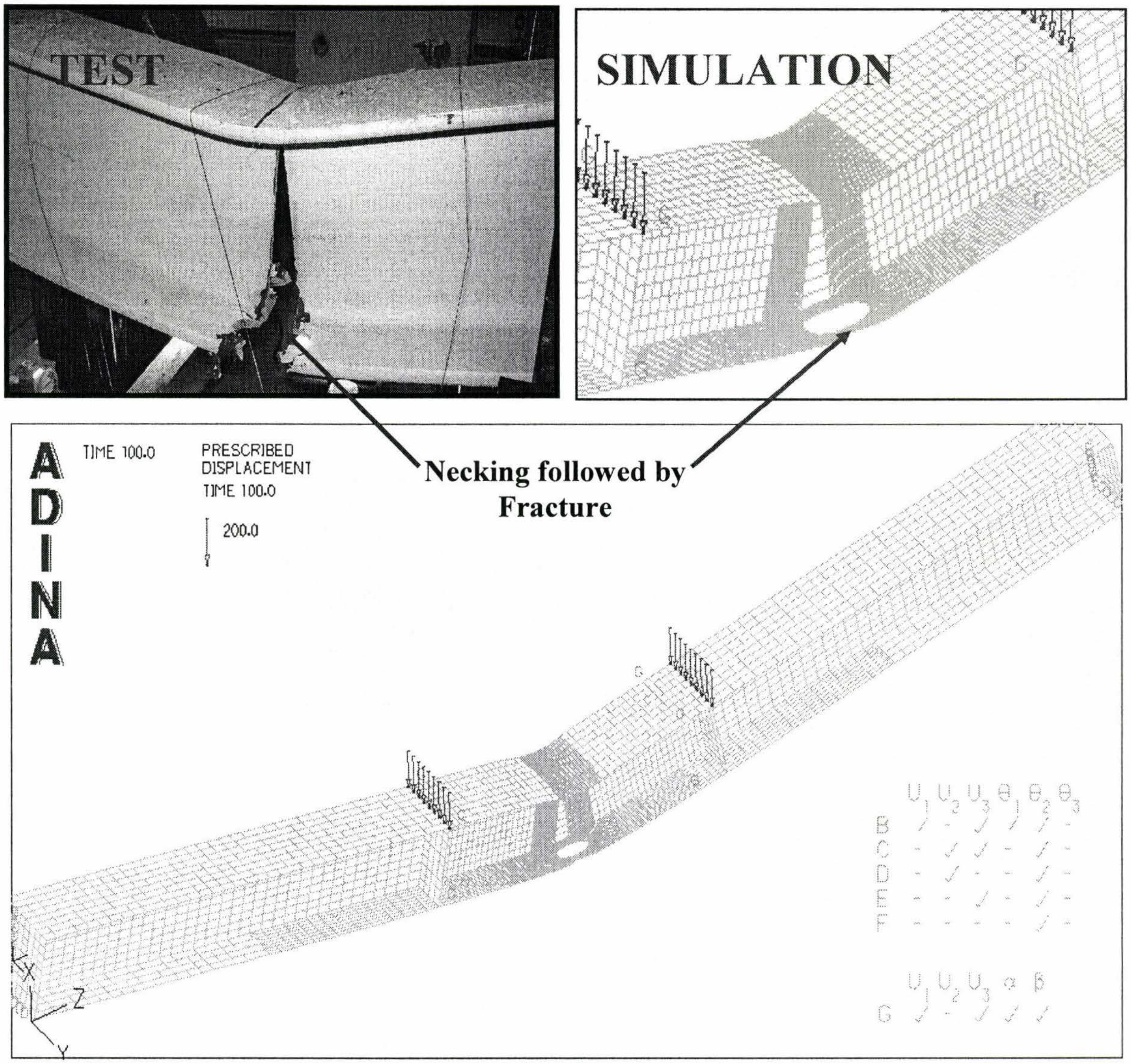


Figure 7.24: Deformed Shape of the FE Model - A 60 Series

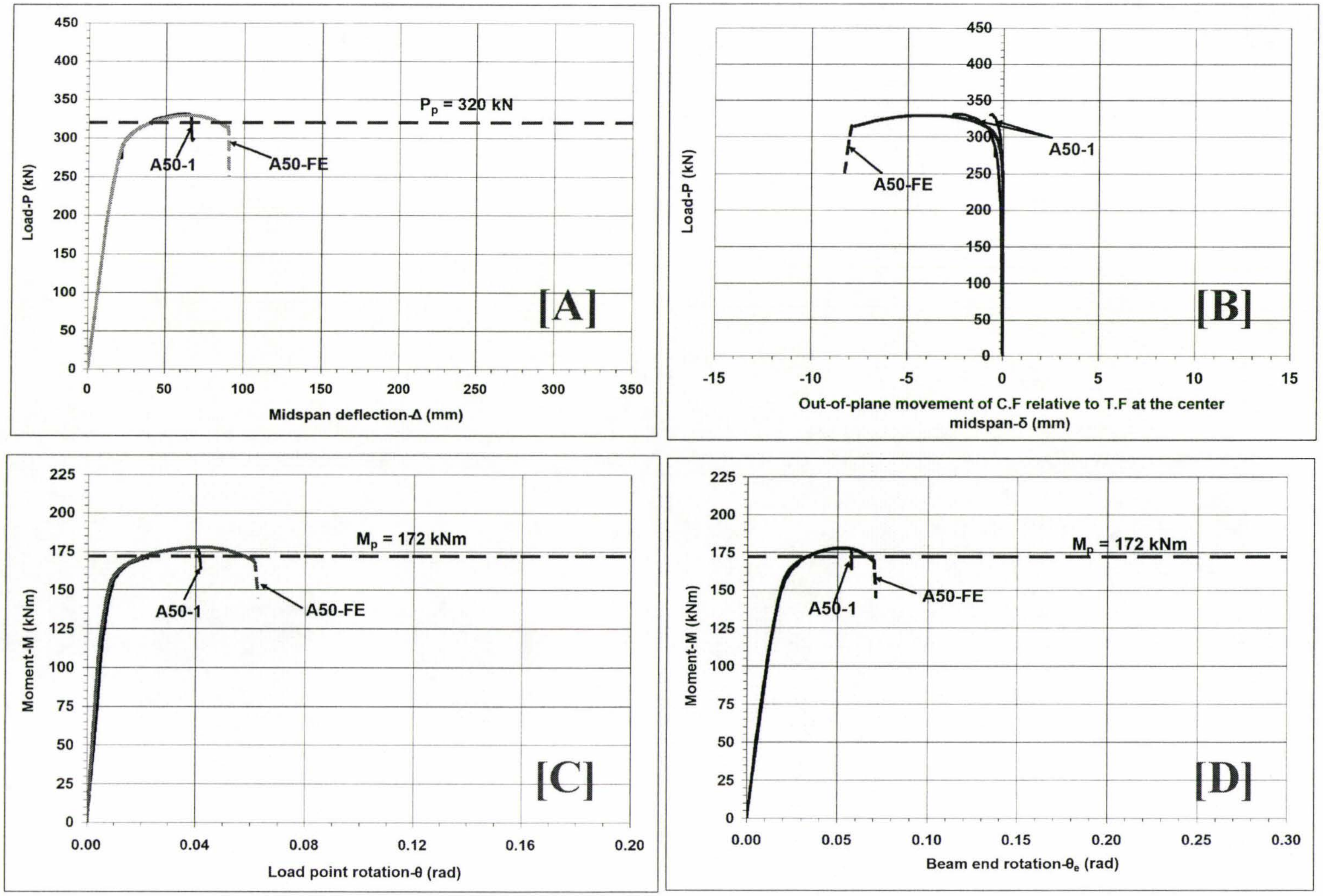


Figure 7.25: Comparison of FE Predictions with Test Responses - Beam A50 Series

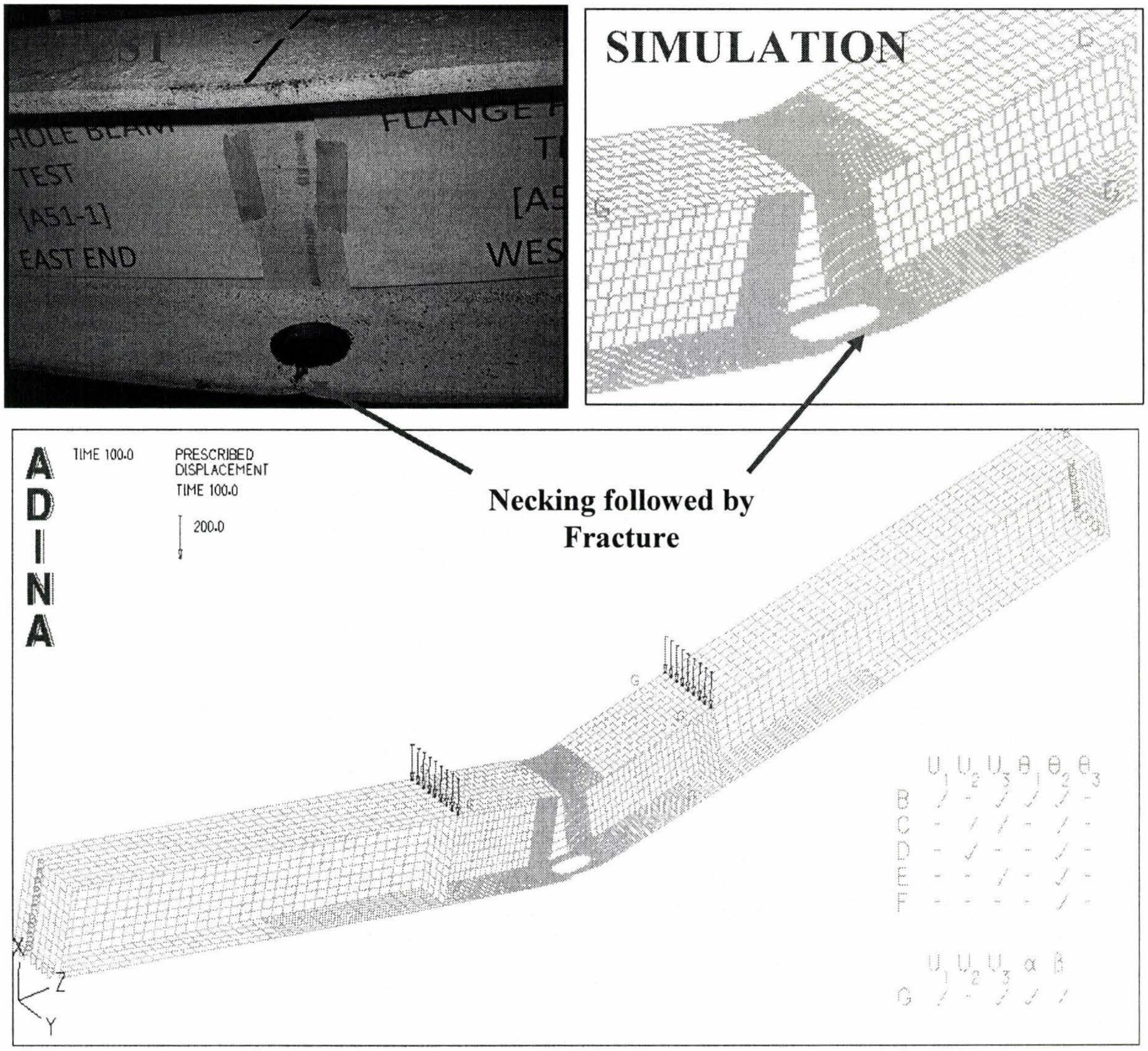


Figure 7.26: Deformed Shape of the FE Model - A 50-1

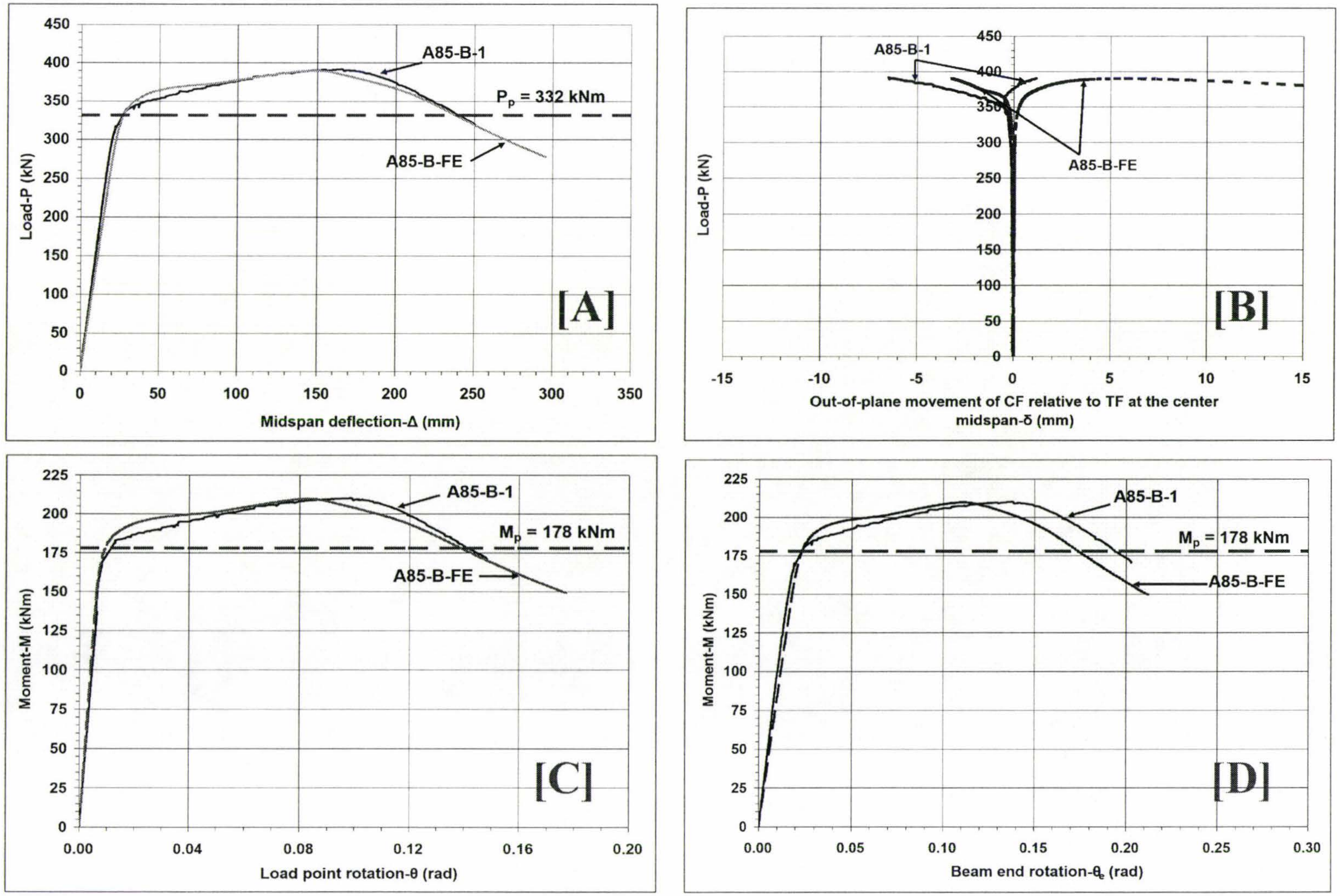


Figure 7.27: Comparison of FE Predictions with Test Responses - Beam A85-B-1

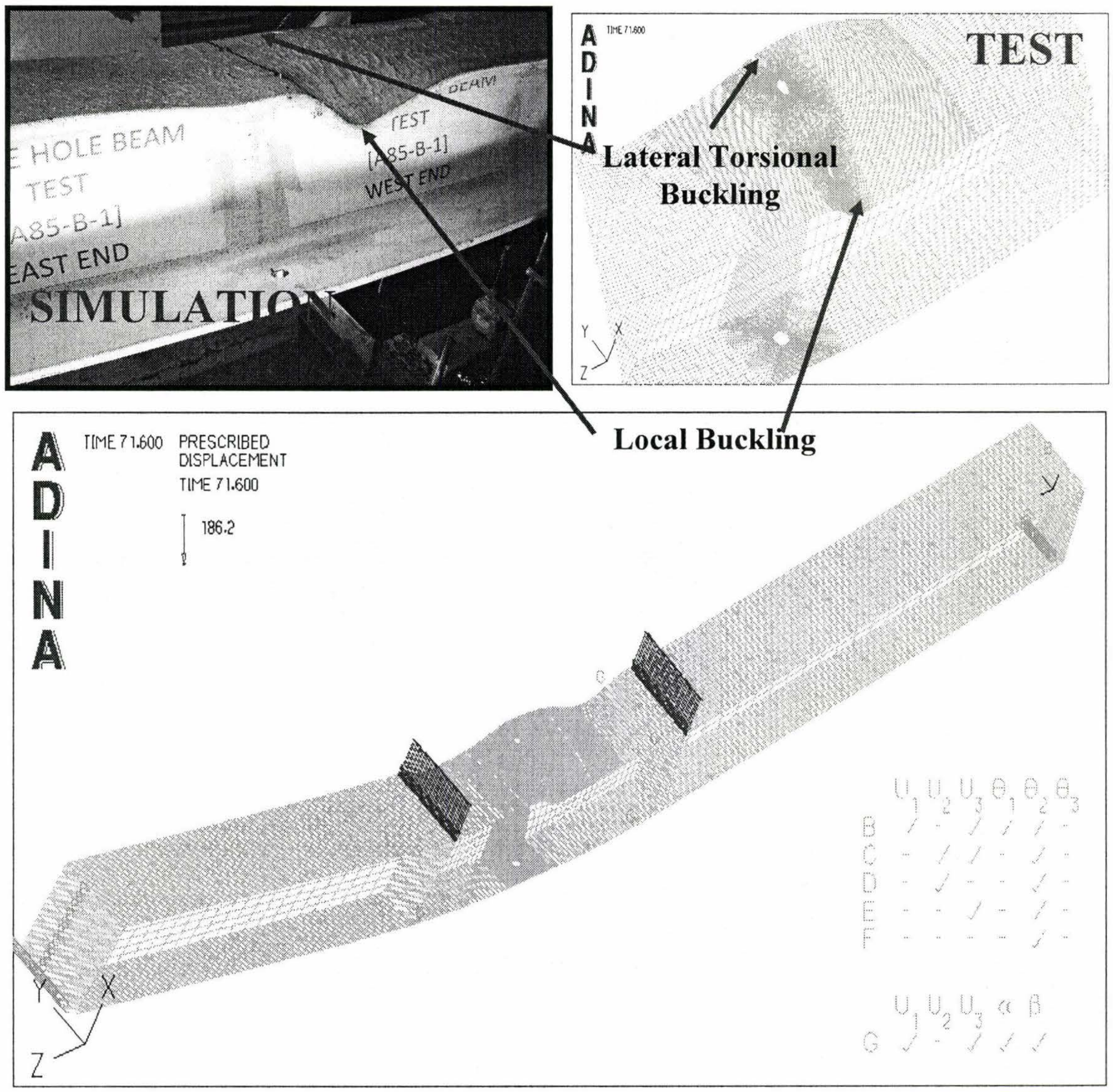


Figure 7.28: Deformed Shape of the FE Model – Beam A85-B-1

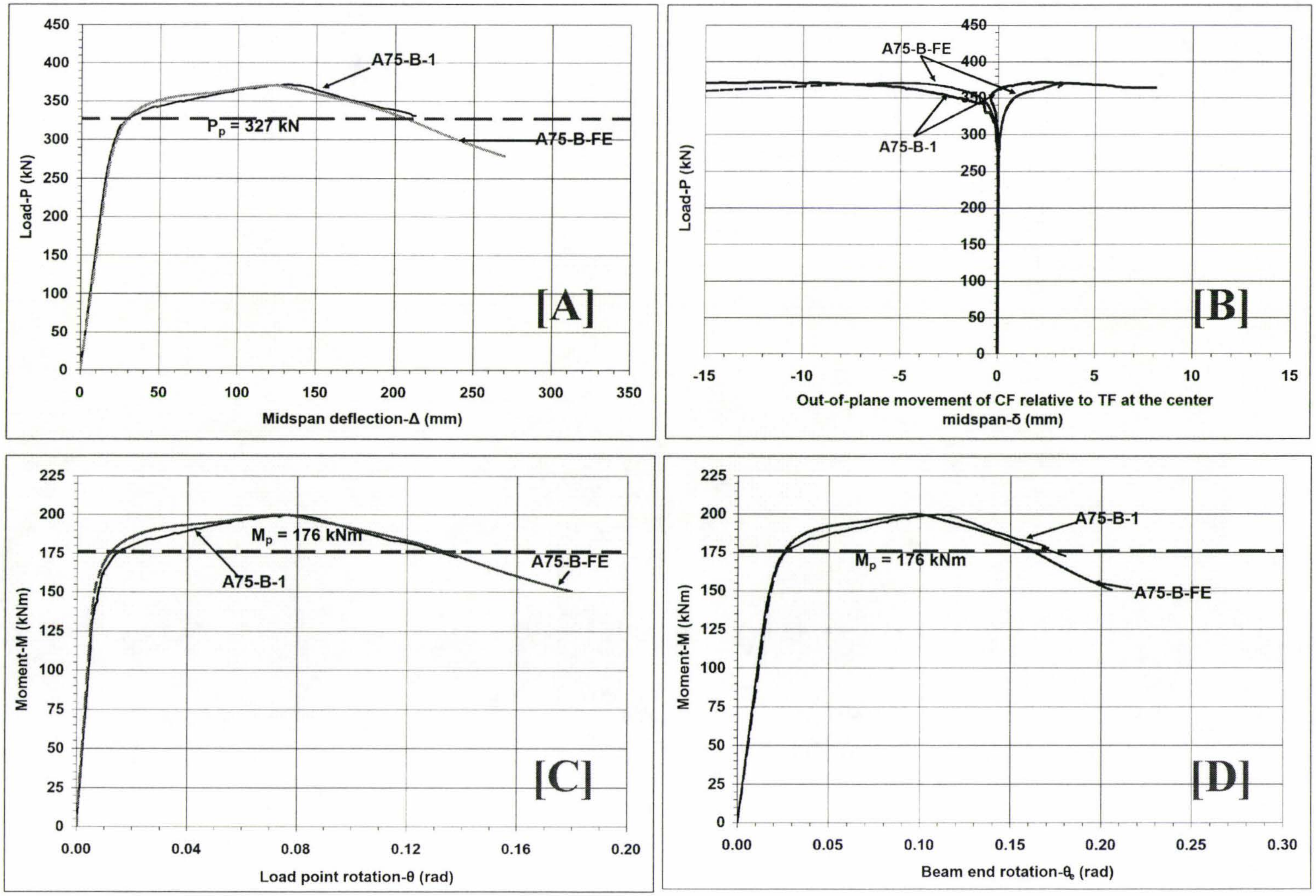


Figure 7.29: Comparison of FE Predictions with Test Responses - Beam A75-B-1

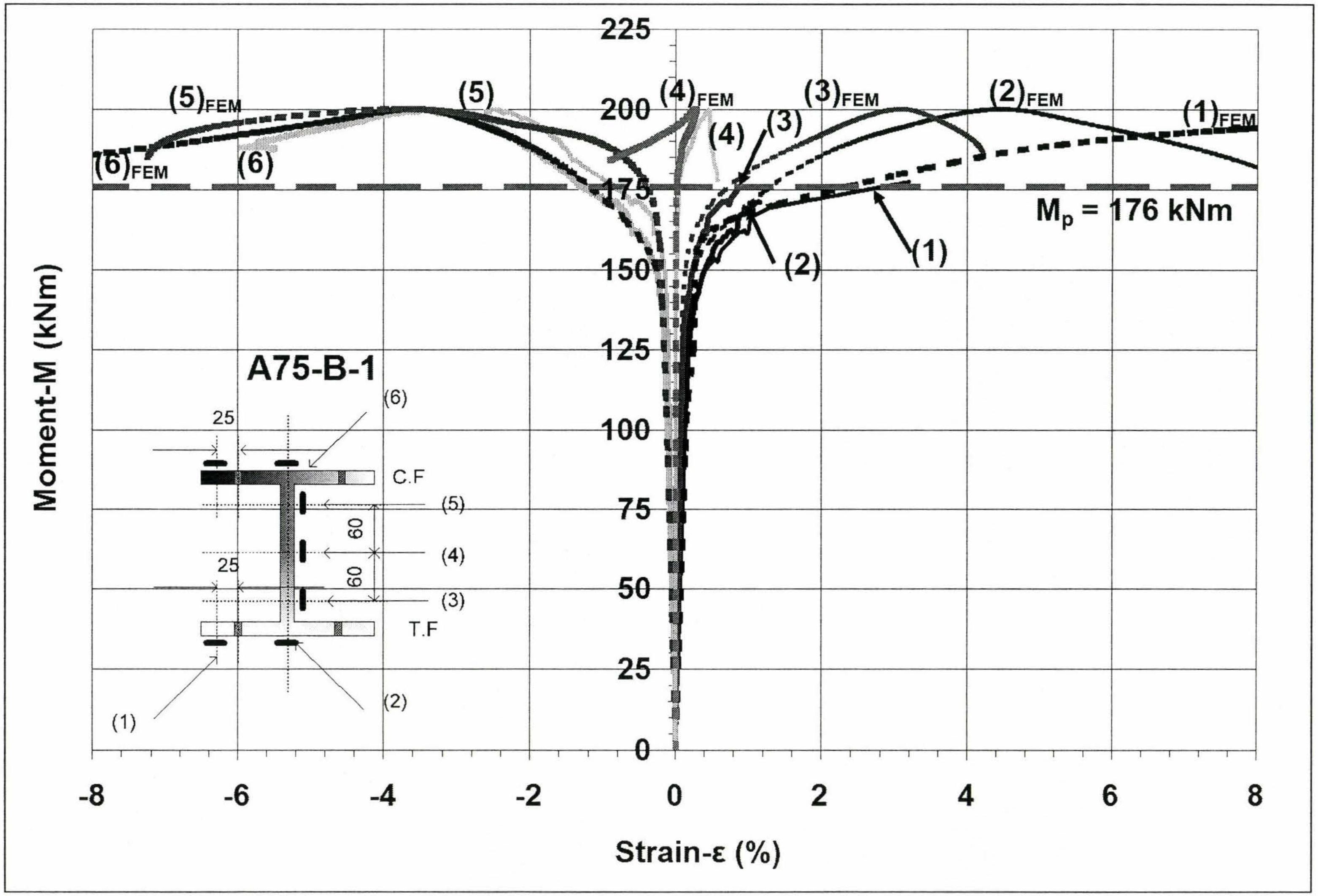


Figure 7.30: Strain Comparison of FE Predictions with Test Response - Beam A75-B-1

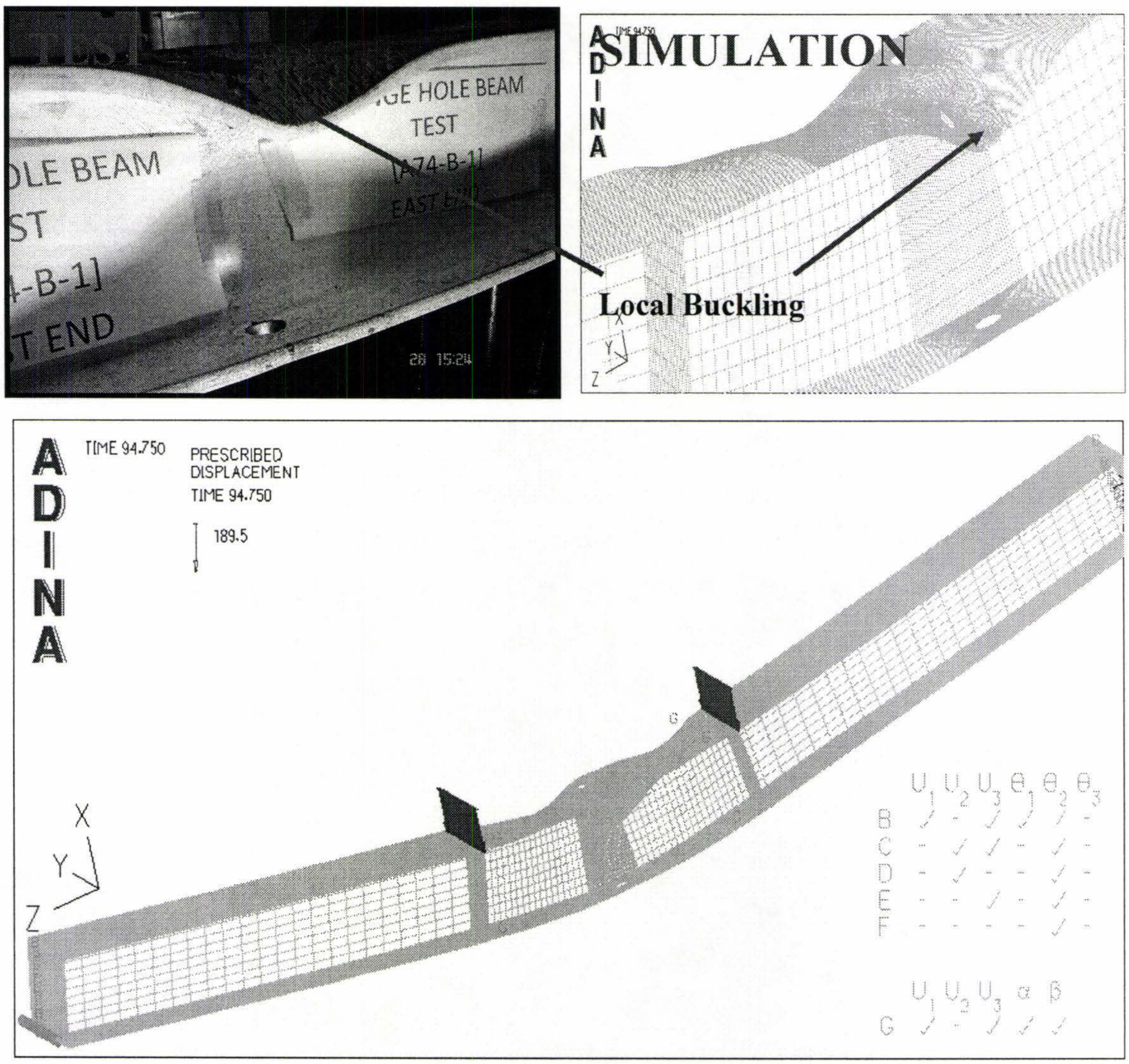


Figure 7.31: Deformed Shape of the FE Model - Beam A75-B-1

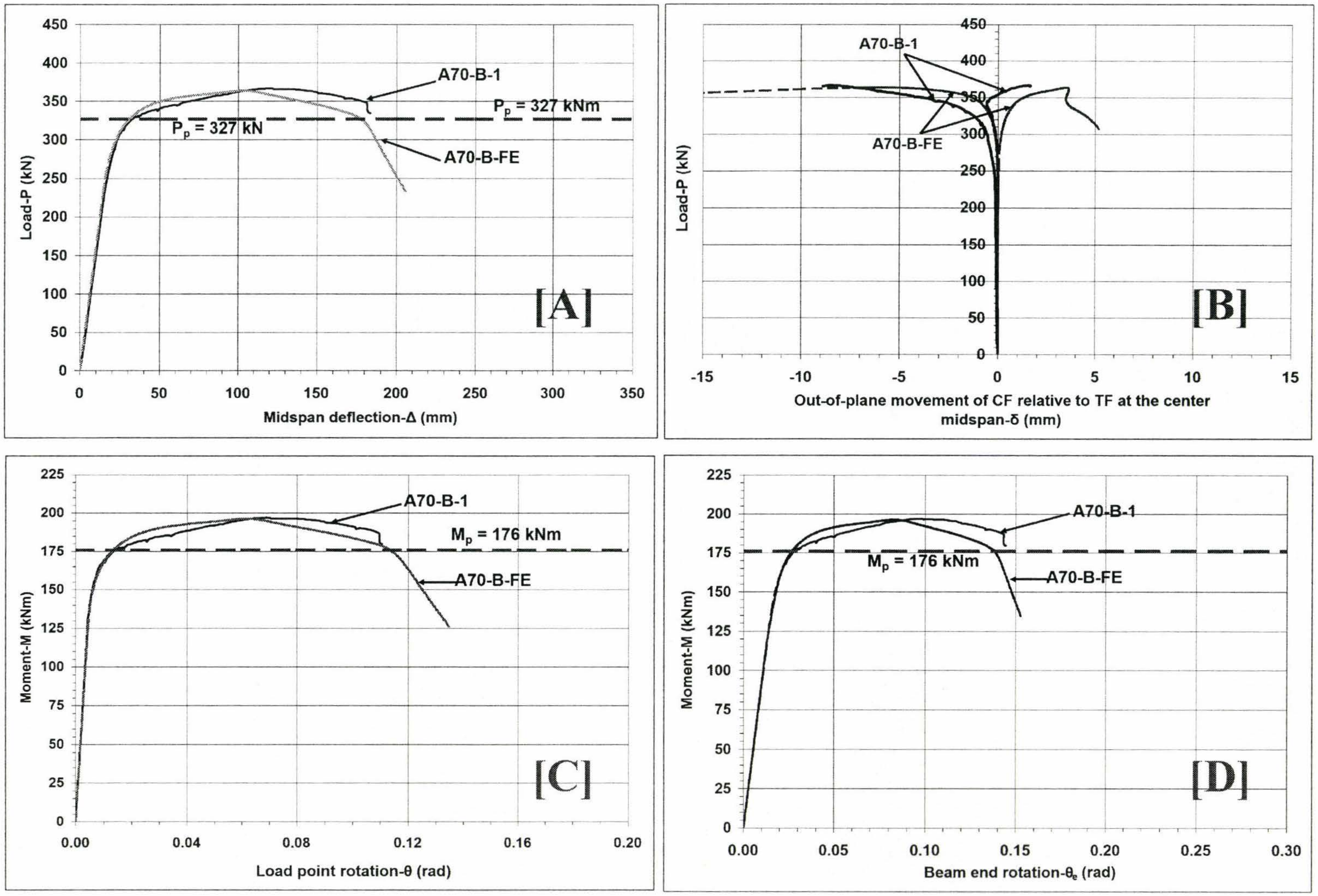


Figure 7.32: Comparison of FE Predictions with Test Responses - Beam A70-B-1

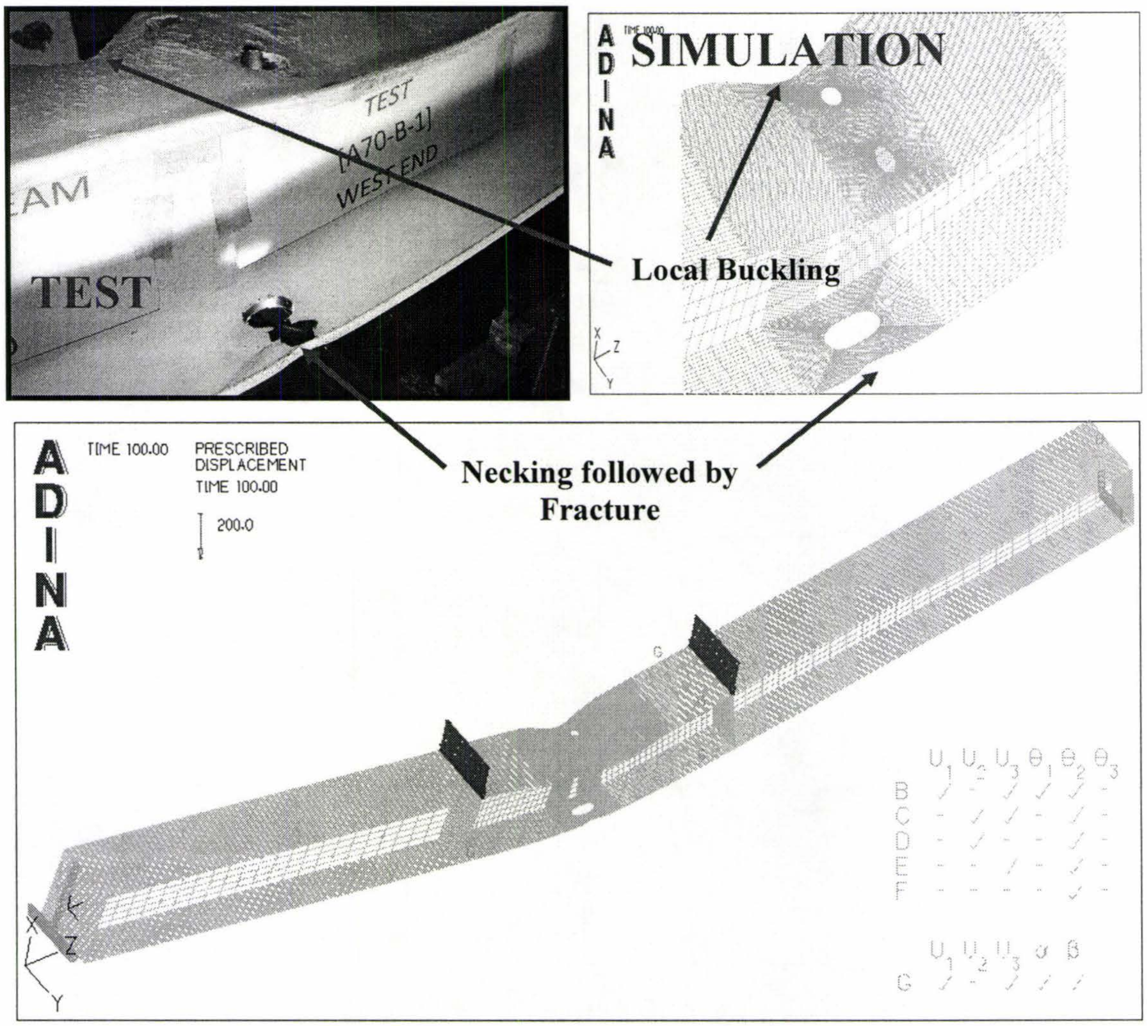


Figure 7.33: Deformed Shape of the FE Model- Beam A70-B-1

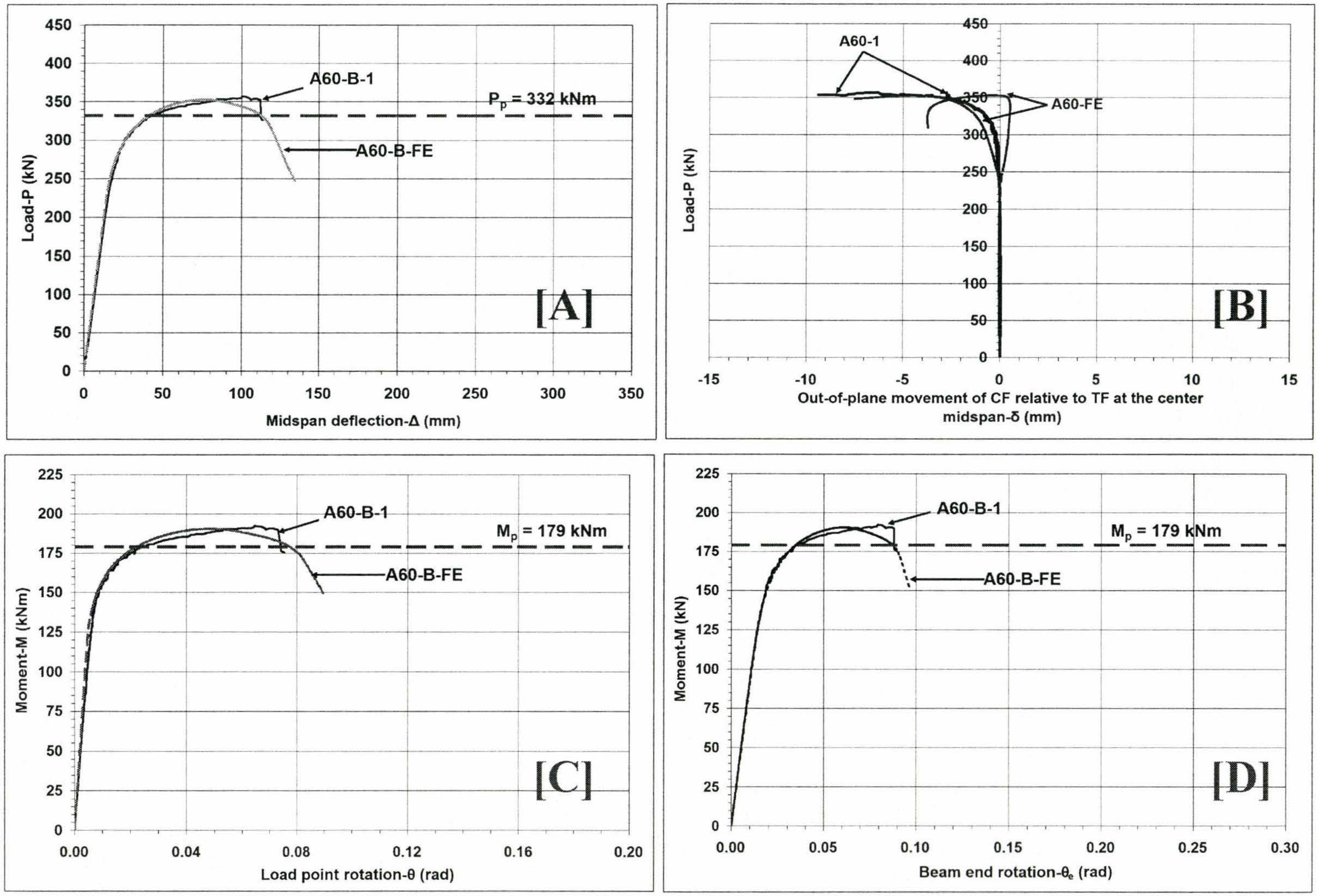


Figure 7.34: Comparison of FE Predictions with Test Responses - Beam A60-B-1

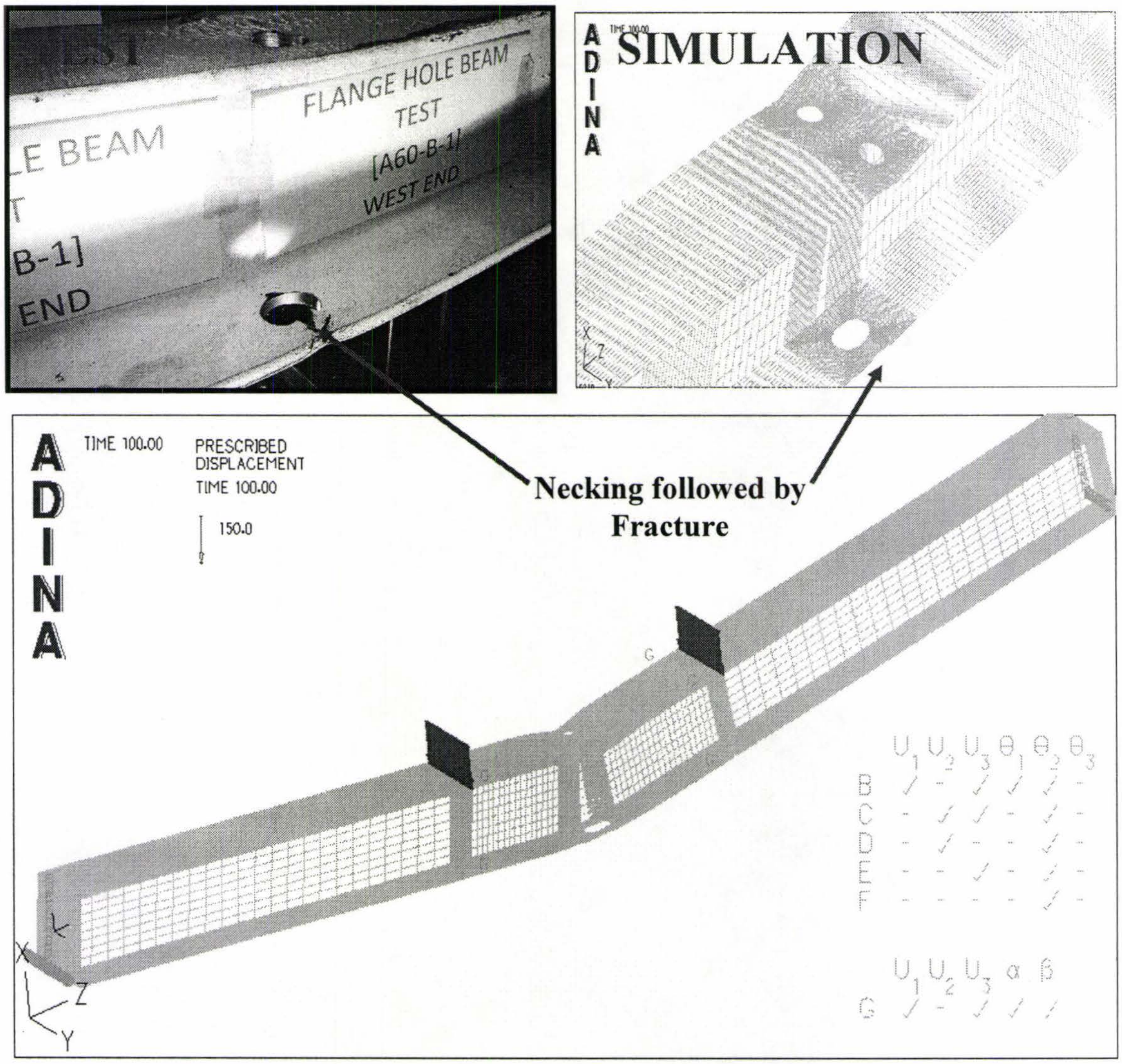


Figure 7.35: Deformed Shape of the FE Model- Beam A60-B-1

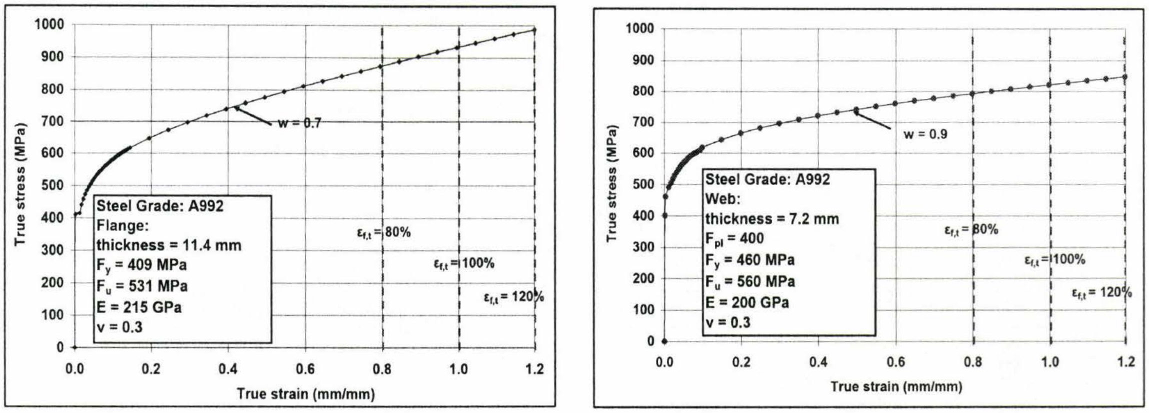


Figure 7.36: Material Model For Sensitivity Analysis of $\varepsilon_{f,t}$

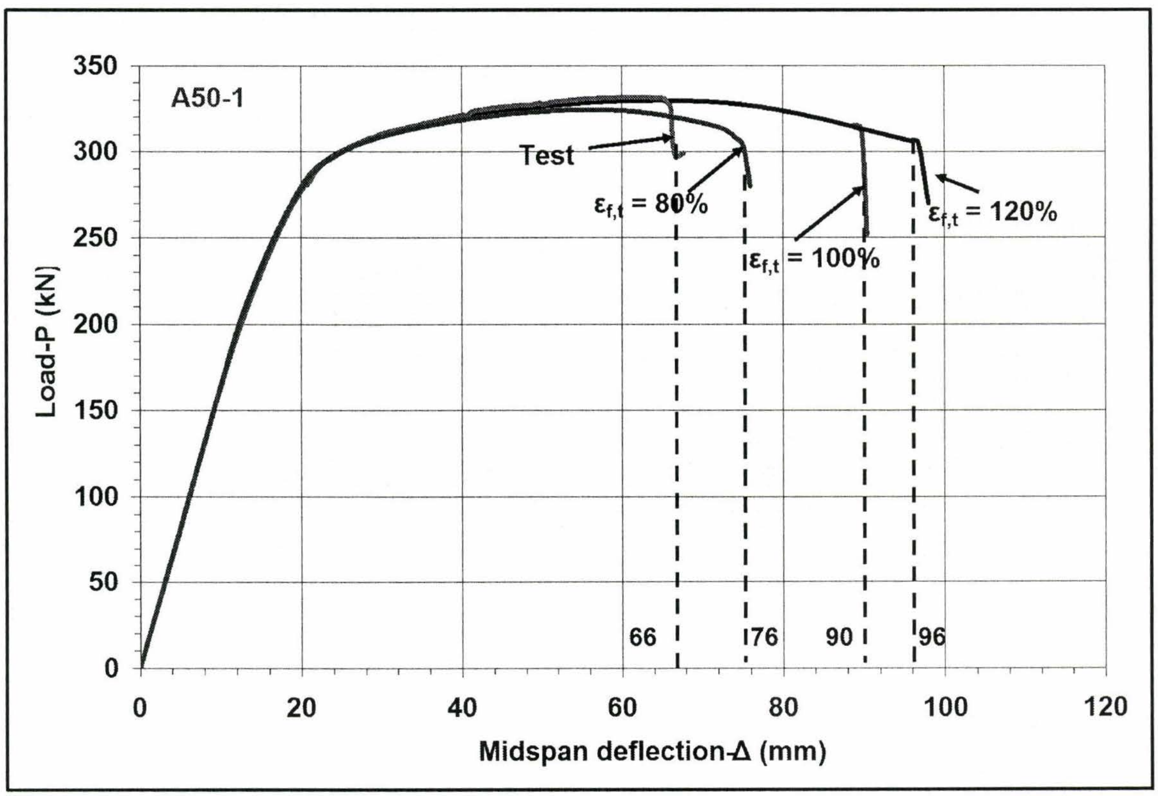


Figure 7.37: Comparison of Load-Midspan Deflection Response for Different Values of $\varepsilon_{f,t}$

# CHAPTER: 8

# CONCLUSIONS AND RECOMMENDATIONS FOR FUTURE CODE PROVISION

## 8.1 Summary

The main objective of this investigation was to evaluate the influence of flange holes on the flexural behavior of steel I-beams. To achieve the objective, a total of twenty five flexural tests were performed. The test beam specimens were obtained from the same production batch conforming to ASTM A992 steel, which is rapidly becoming the most common grade of steel produced. The tests were conducted under a four-point bending configuration by creating a constant moment in the midspan region. A pair of holes was laid in flanges on either side of the flange-web junction at the center midspan. In order to assess the influence of holes on the flexural behavior, the sizes of the holes were selected in a systematic manner considering standard fastener sizes, which are often used in practice. The mechanical properties of the test beams were established by performing standard coupon tests.

## 8.2 Conclusions

[1] Comparison of different standards revealed that the 15% exemption rule as per the current CSA (2003) standard was more restrictive for steel grades having $F_y / F_u \leq$ 0.8. However, this rule may be unconservative for steel grades having $F_y / F_u$>0.8 (see Table 3.2).

[2] Comparison of the current and the previous version of the AISC (AISC-LRFD 2005 and 1999) standards indicated that the current version allows 20% more holes to gross flange area than the previous version without any deduction in the gross section plastic moment capacity. This is true for steel grades having $F_y / F_u \leq$0.8. For steel grades having $F_y / F_u$>0.8, the current AISC code (AISC-LRFD 2005) permits 10% more holes to the gross flange area than the older version (AISC-LRFD 1999).

[3] Based on the flexural test results, all beam specimens, including A50-1, which had net flange area-to gross flange area ratio value of 52% (i.e., holes removed 48% of the gross flange area), attained a maximum moment more than $M_p$ (gross section plastic moment). In other words, net-section fracture of the tension flange did not limit the maximum moment to less than $M_p$. This may be true for beam sections satisfying Class 1 or Class 2 section classification.

[4] Test results indicated that, for beam specimens proportioned on the basis of flexural strength of the gross section, the dominant failure mode can be established based on

the $A_{fn}F_u / A_{fg}F_y$ ratio. The beam specimens having the $A_{fn}F_u / A_{fg}F_y \geq 1.0$ failed due to lateral torsional buckling followed by local buckling in the midspan region (ductile failure). On the other hand, the beams with the $A_{fn}F_u / A_{fg}F_y < 1.0$ exhibited an eventual failure due to net-section fracture through the tension flange holes (brittle failure).

[5] The strains measured at the middle webs of beams A75-3 and A70-2, which had holes exclusively in the tension flange, indicated that no significant movement associated with the position of neutral axis of the gross cross-section took place during the test. This FE analysis of the corresponding beam specimens performed in this study also supported this observation. This may be true due to the fact that the holes accommodated only a small portion of the midspan, thus a sudden jump in the neutral axis across the net section is impossible. However, if a series holes were laid closely, then it would be likely to have a significant movement in the neutral axis.

[6] The maximum moment ($M_m$)-to-net-section fracture moment ($M_{fn}$) ratio varied between 97% to 109% for the beams having a maximum holes of 48% to the gross flange area in the tension flange only. The $M_m / M_{fn}$ ratio ranged from 103% to 119% for the case where open holes of 14%-37% to the gross flange area occurred in both flanges. When holes contained fasteners ("snug tight") of corresponding standard sizes, $M_m / M_{fn}$ ratio spanned between 99% and 106%.

[7] From the test results, it was observed that strength and ductility of the beam specimens having holes in the tension flange only and similar beams having

fastener holes in both flanges were closely correlated. Hence, it can be construed that the use of fasteners (of standard sizes) in the compression flanges was effective in resisting the flexural stresses.

[8] When open holes occurred in the tension flange only or when fastener holes occurred in both flanges, the beam specimens having the $A_{fn}F_u / A_{fg}F_y \geq 1.0$ experienced failure primarily due to lateral torsional buckling followed by local buckling in the midspan region. In such cases, the $M_p / M_{fn}$ ratio values were less than 0.85 (see the eighth column of Table 5.10).

[9] When open holes existed in the tension flange only and when fastener holes occurred in both flanges, the beams having the $A_{fn}F_u / A_{fg}F_y$<1.0 exhibited failure mode as a result of net-section fracture through the tension flange holes. In such cases, the $M_p / M_{fn}$ ratio values were greater than 0.85 (see the eighth column of Table 5.10).

[10] When open holes were laid in both flanges, the beams having the $A_{fn}F_u / A_{fg}F_y$<0.95 failed due to either the combined lateral torsional buckling followed by local bulking or mainly local buckling. In such cases, the $M_p / M_{fn}$ ratio values were less than 0.98. On the other hand, the beams having $A_{fn}F_u / A_{fg}F_y$>0.95 failed as a result of net-section fracture and in such cases, $M_p / M_{fn}$ ratio values were greater than 1.0.

[11] Based on the assessment of the test results, it can be proposed that by limiting the ultimate strength ($F_u$) to 0.85 $F_u$, the probability of (unwanted) failure due to net-

section fracture may be significantly reduced. This may be true for steels having the $F_y / F_u$ ratio of less than 0.8.

[12] From the test results (a design approach, which is analogous to the tension member provision, can be proposed as follows;

- Calculate the gross-section plastic moment capacity, $M_p (= Z_g F_y)$
- Calculate the factored net-section fracture moment, $M_{fnm} = (0.85\, Z_n F_u)$

If $M_p \leq M_{fnm}$, ignore the effects of holes and design a flexural member for its gross-section plastic moment capacity. Otherwise, the flexural member shall be designed to carry the modified net-section fracture moment, $M_{fnm} = 0.85\, Z_n F_u$, where $Z_n$ is the plastic section modulus of the net-section and $F_u$ is the tensile strength of flange material.

Note that this method may be applicable for Class 1 or Class 2 sections as per the current CAN/CSA-S16.01 standard (CSA 2003).

[13] The design moment calculation in accordance with the proposed method was comparable to the current AISC-LRFD (2005) code provision in terms of the establishment of a threshold value (for a particular steel grade).

[14] However, beyond a threshold limit, the proposed method predicted slightly higher moment resistance than the current AISC-LRFD (2005) code and various other standards considered. Note that the design moment calculation based on the proposed method was found to be lower than the measured maximum moment

(more than 20%). Thus, the predicted moment (based on the proposed method) had a reasonable margin of safety as compared to the maximum moment.

[15] Based on the test results, the rotation capacity of flexural members having holes in the tension flange only and similar members having fastener holes in both flanges were in close agreement.

[16] All beam specimens tested attained a rotation capacity of more than 3, which is required by the current AISC-LRFD (2005) specification for non-seismic applications. However, the required rotation capacity for seismic application as per the current AISC-LRFD (2005) standard is approximately 9. The test results indicated that the beams having the $A_{fn}F_u / A_{fg}F_y \geq 0.9$ possessed an inelastic rotation capacity of more than 9.

[17] It should be noted that the available rotation capacities would vary depending on many parameters such as the geometry of the beam specimens tested, bracing locations (closer bracing will result in higher rotation ductility), material strain hardening, local instabilities associated with flange and/or web buckling, presence of initial geometric imperfections, etc. Thus, the generalization of available rotation ductility from a certain type of flexural test is highly subjective.

[18] It is essential to avoid the limit state of net-section fracture of the tension flange to have adequate rotational ductility for beams. Based on the test results, the limit state of tension fracture was found to be controlled by a ratio between the net-section fracture strength ($A_{fn}F_u$)-to-the gross-section yield strength ($A_{fg}F_y$) of the tension flange.

[19] The FE techniques employed in this study were able to capture the local as well as global behavior of flexural members with flange holes.

[20] The use of true strain at fracture, $\varepsilon_{f,t}$ = 100%, seemed to provide a reasonably good prediction for the behavior of flexural member with flange holes in this study.

## 8.3 Recommendation for Future Code Provision

Based on the test results, it is proposed that the Clause 14.1 of the current CAN/CSA-S16.01 (CSA 2003) standard be changed to; if a beam member is proportioned on the basis of flexural strength of the gross cross-section and if $M_p \leq M_{fnm}$, the effects of flange holes shall be ignored. Otherwise, the beam shall be designed to carry the modified net-section fracture moment, $M_{fnm} = 0.85\, Z_n F_u$, where $Z_n$ is the plastic section modulus of the net-section and $F_u$ is the tensile strength of flange material.

The proposed design method has following merits over the current CAN/CSA-S16.01 (CSA 2003) code provision:

- The proposed method considers the impact of holes or fastener holes in a similar manner (a unified approach) which is analogous to the current AISC-LRFD (2005) code provision. However, the current CSA (2003) code provision treats the effects of fastener holes differently than that of open holes, in which case net-section calculation shall be used to establish flexural strengths.

- The proposed design method is analogous to the design procedure associated with an axial tension member in accordance with the current CSA (2003) standard.
- Unlike the current CSA (2003) code, which does not consider the material characteristics in the design of flexural members with flange fastener holes, the proposed method takes into account $F_y / F_u$ ratios of steel grades.

## 8.4 Recommendation for Future Work

The following recommendations may be considered for future research involving tests and analysis of flexural members having flange holes (fastener holes):

- Conduct experiments on high strength and high-performance steels having the yield-to-ultimate strength ratio of more than 0.85 since the increasing yield-to-ultimate strength ratio has been shown to cause a significant decrease in rotation capacity and premature tension fracture of solid flanges before the instability occurred as a result of compression flange and/or web buckling.
- The type of loading to which the beam is subjected must be considered, although the current code specifications as per the AISC-LRFD (2205) and the CSA (2003) deal mainly with static loadings. Because, a repetitive cyclic type of loading generally, results in lower fatigue life causing early fracture.
- More detailed FE based numerical study should be performed to enhance interpretation of test results.

## REFERENCES


Adams, F.P, Lay, G.M, and Galambos, V.T, (1964), Plastic Design in High Strength Steel: Experiments on High Strength Steel Members, Fritz Engineering Laboratory (Report No. 297.8), Dept. of Civil Engineering, Lehigh University, Bethlehem, Pennsylvania, USA.

ADINA 8.4 Version User Manual, (2007), ADINA R&D, Inc., Watertown, MA 02472, USA.

Ahmad, S., Irons, B.M., and Zienkiewicz, O.C., (1970), Analysis of Thick and Thin Shell Structures by Curved Finite Elements, International Journal for Numerical Methods in Engineering, Vol.2, pp. 419-451.

AISC, (2005), Load and Resistance Factor Design Specification for Structural Steel Buildings, 4th Edition, American Institute of Steel Construction, Inc., Chicago, Illinois, USA.

AISC, (1999), Load and Resistance Factor Design Specification for Structural Steel Buildings, 3rd Edition, American Institute of Steel Construction, Inc., Chicago, Illinois, USA.

AISC, (1993), Load and Resistance Factor Design Specification for Structural Steel Buildings, 2nd Edition, American Institute of Steel Construction, Inc., Chicago, Illinois, USA.

AISC, (1989), Allowable Stress Design for Structural Steel Buildings,9th Edition, American Institute of Steel Construction, Inc., Chicago, Illinois, USA.

AISC, (1986), Load and Resistance Factor Design Specification for Structural Steel Buildings, American Institute of Steel Construction, Inc., Chicago, Illinois, USA.

AISC, (1963), Specification for Design, Fabrication and Erection of Structural Steel for Buildings, Section 1.10.1.

American Railway Engineering Association (AREA), Specification for Steel railway Bridges, (1956), Section 60, USA.

ASTM Standards A370-02, (2002), Standard Test Methods and Definitions for Mechanical Testing of Steel Products, American Society for Testing and Materials, pp. 106-141.

Astaneh-Asl, A., (1997), Seismic Design of Steel Column-Tree Moment-Resisting Frames, Steel Tips Report, Structural Steel Educational Council, Moraga, CA, USA.

Bao, Y., (2004), Dependence of Ductile Crack Formation in Tensile Tests on Stress Triaxiality, Stress and Strain Ratios, Engineering Fracture Mechanics, 72, pp. 505-522.

Barth, K.E., (1996), Moment-Rotation Characteristics for Inelastic Design of Steel Bridge Beams and Girders, Ph.D Dissertation, Purdue University, West Lafayette, Indiana.

Bathe, K.J.,(1996), Finite Element Procedures, Prentice Hall, Englewood Cliffs, NJ, USA.

Bjorhovde, R., Engstrom, F, M., Griffis, G, L., Kloiber, A.L., and Malley, O, J., (2001), Structural Steel Selection Consideration, A Guide for Students, Educators, Designers, and Builders, ASCE, Virginia 20191-4400, USA.

Bridgman, P.W, (1952), Studies in Large Flow and Fracture, McGraw-Hill, N.Y, USA.

Brockenbrough, R.L., and Merritt, F.S., (1999), Structural Steel Designers Handbook, 3rd Edition, by McGraw-Hill Companies, Inc, N.Y, USA.

Bruneau, M., Uang, C.M., and Whittaker, A., (1998), Ductile Design of Steel Structures, McGraw-Hill Companies, Inc, N.Y, USA.

BSI (2001), Structural Use of Steelwork in Building-Code of Practice for Design-Rolled and Welded Sections- BS5950-2000, British Standards, UK.

Cabezas, E.E., and Celentano, D.J., (2004), Experimental and Numerical Analysis of the Tensile Test Using Sheet Specimens, Finite Elements in Analysis and Design 40, pp. 555-575.

Chen, W.F., and Patel, K.V., (1981), Static Behaviour of Beam-to-Column Moment Connections, Journal of Structural Division, ASCE, ST9, pp.1815-1839.

Cheng, J.J.R., Kulak, G.L., and Khoo, H., (1998), Strength of Slotted Tubular Tension Members, Canadian Journal of Civil Engineering, Vol.25, pp.982-991.

CISC, (2005), Advantage Steel, Canadian Institute of Steel Construction, Toronto, Ontario, Vol. 23, p.6.

CISC, (2007), Handbook of Steel Construction, Canadian Institute of Steel Construction, Willowadale, Ontario, Canada.

Coelho, A.M.G., Luìs Simões da Silva, and Bijlaard, F.S.K, 2006, Finite-Element Modeling of the Nonlinear Behavior of Bolted T-Stub Connections, Journal of Structural Engineering, ASCE, pp. 918-928.

CSA, (2003), Limit States Design of Steel Structures, CAN/CSA-S16-01, Canadian Standard Association, ON, Canada.

Dalli, M.L, and Korol, R.M, (1995), Prediction of Local Buckling Capacity at Maximum Moment, Journal of Constructional Steel Research, Vol.32, pp. 1-13.

Davison, B., and Owens, G.W., (2003), Steel Designer's Manual, The steel Construction Institute, 6th Edition, Blackwell Science Ltd, Oxford, UK.

Dexter, R.J., and Alttstadt, A., (2003), Recent Development in Bridge Engineering, Proceedings of the Second New York City Bridge Conference, pp 67-81, NY, USA.

Dexter, R.J., Alttstadt, A., and Gardner, C.A., (2002), Strength and Ductility of HPS70W Tension Members and Tension Flanges With Holes, Research Report, University of Minnesota, Minneapolis, MN, 55455-0116, USA.

Douty, T.R., and McGuire, W, (1965), High Strength Bolted Moment Connections, Journal of the Structural Division, ASCE, Vol.91, ST2, pp.101-128.

Earls, C.J., and Shah, B.J., (2000), Compactness and Bracing Requirements for Use in the Analysis and Design of High Performance Steel Highway Bridges, Report No. CE/ST17, Department of Civil and Environmental Engineering, University of Pittsburgh.

Fisher, J.W., and Struik, J.H.A., (1974), Guide to Design Criteria for Bolted and Riveted Joints, John Wiley & Sons, N.Y, USA.

Fletcher, E.E., (1979), A Review of the Status, Selection, and Physical Metallurgy of High-Strength Low-Alloy Steels, Metals and Ceramic Information Center, MCIC-79-39, Columbus, Ohio, USA.

Futakawa, M, and Butler, N., (1996), A Homologous Ductile Failure Criterion for Generalized Stress States, Engineering Fracture Mechanics, Vol. 54, No.3, pp. 349-359.

Galambos, T.V., (1977), History of Steel Beam Design, Engineering Journal, AISC, 4th Quarter, pp.141-151.

Galambos, T.V., (1998), Guide to Stability Design Criteria for Metal Structures, 5th Edition, by John Wiley & Sons, Inc, N.Y, USA.

Green, P.S., (2000), The Inelastic Behavior of Flexural Members Fabricated from High Performance Steel, Ph.D Dissertation, Department of Civil Engineering, Lehigh University, Bethlehem, Pennsylvania.

Green, P.S., Sause, R., and Ricles, J.M., (2002), Strength and Ductility of HPS Flexural Members, Journal of Constructional Steel Research, Vol.58, pp. 907-941.

Greco, N., and Earls, C.J., (2003), Structural Ductility in Hybrid High Performance Steel Beams, Journal of Structural Engineering, Vol.129, No.12, pp. 1584-1595.

Greschik, G., White, D.W., McGuire, W., and Abel, J.F, (1993), On the Correlation of Analysis and Tests of the Flexural Behavior of Wide Flange Steel Beams, Computers and Structures, Vol.48, no.3, pp. 511-522.

Günther, H, (2005), Use and Application of High-Performance Steels for Steel Structures, International Association for Bridge and Structural Engineering, IABSE-AIPC-IVBH, ETH Honggerberg, CH-8093 Zurich, Switzerland.

Hancock, J.W., and Mackenzie, A.C., (1976), On the Mechanism of Ductile Failure in High–Strength Steels Subjected to Multi-Axial Stress-States, Journal of Mechanical Physics Solids, Vol. 24, pp. 147-169.

Hollomon, J.H, (1945), Tensile Deformation, Transaction of American Institute of Mechanical Engineering, Vol. 162, pp.268-277.

Huang, P., (1994), Finite Element Analysis of Inelastic Behavior of Structural Steel Beams and Bridge Girders, Ph.D Dissertation, School of Civil Engineering and Environmental Engineering, Cornell University, Ithaca, NY.

Huns, B.B.S., Grondin, G.Y., Driver, R.G., (2006), Tension and Shear Block Failure of Bolted Gusset Plates, Canadian Journal of Civil Engineering, Vol.33, pp. 395-408.

Jaquess, K.T, and Frank, K, (1999), Characterization of the Material Properties of Rolled Sections, Report No. SAC/BD-99/07, SAC Joint Venture, USA.

Kicinski, S.E., (1963), An Experiment Investigation of the Influence of Flange Holes Upon the Flexural Stresses in a Wide-Flange Steel Beam, M.Sc Thesis, Michigan College of Mining and Technology, USA.

Khoo, A, H., (2000), Ductile Fracture of Steel, Ph.D Thesis, University of Alberta, Alberta, Canada.

Kulak, G.L., Fisher, J.W., and Struik, J.H.A.,(1987), Guide to Design Criteria for Bolted and Riveted Joints,2nd Edition, John Wiley & Sons, N.Y, USA.

Kulak, G.L., and Green, D.L., (1990), Design of Connectors in Web-Flange Beam or Girder Splices, Engineering Journal, AISC, 2nd Quarter, pp.41-48.

Kulak, G.L., and Grondin, G.Y., (2002), Limit States Design in Structural Steel, Canadian Institute of Steel Construction, ON, Canada.

Lee, W, (2001), Behavior of Connection with Beam Bearing on Bottom Flange of Girder, M.Sc Thesis, Virginia Polytechnic Institute and State University, USA.

Lilly, S.B., and Carpenter, S.T., (1940), Effective Moment of Inertia of A Riveted Plate Girder, Transactions, ASCE, Vol.105, pp.1462-1518.

Ling, Y, (1996), Uniaxial True Stress-Strain after Necking, AMP Journal of Technology, Vol. 5, pp. 37-48.

Liu, A, (2005), Mechanics and Mechanisms of Fracture, An Introduction, ASM International, Materials Park, OH, 44073-0002.

Mackenzie, A.C, Hancock, J.W, and Brown, D.K, (1977), On the Influence of State of Stress on Ductile Failure Initiation in High Strength Steels, Engineering Fracture Mechanics, Vol.9, pp. 167-188.

Mahmoud, K.M (ed.), (2003), Recent Developments in Bridge Engineering, Swets and Zeitlinger, Lisse, The Netherlands, ISBN 90 5809 606 8.

Matic, P., Kirby, C.G., and Jolles, M.I., (1988), The Relation of Tensile Specimen Size and Geometry Effects to Unique Constututive Parameters for Ductile Materials, Proccedings of the Royal Society of London, Series A, Mathematical and Physical Sciences, Vol. 417, No. 1853, pp. 309-333.

Nazamy, A.S., and El-Sawy, K.M., (2003), Inelastic Buckling of Thin Plates Under Uni-axial Compression, the Fourth Annual U.A.E University Research Conference, U.A.E.

OSHA (2004), Safety and Health Regulations for Construction- 1926.757- Open web steel joists, Occupational Safety and Health Administration, US Department of Labor, Washington, D.C., U.S.A.

Ricker, D.T., (1982), Tips for Avoiding Crane Runway Problems, Engineering Journal, AISC, 4th Quarter, pp. 181-205.

SA (1998), Steel Structures-AS4100-1998, Standards Association of Australia, Homebush, NSW 2140, Australia.

Scheider, I., Brocks, W., and Cornec, A., (2004), Procedure for the Determination of True Stress-Strain Curves From Tensile Tests with Rectangular Cross-Section Specimens, Journal of Engineering Materials and Technology, ASME, Vol.126, pp. 70-76.

Schneider, S.P., and Teeraparbwong, I., (2002), Inelastic Behavior of Bolted Flange Plate Connections, Journal of Structural Engineering, Vol.128, No.4, pp.492-500.

Tamboli, A.R., (1997), Steel Design Handbook, LRFD Method, 1st Edition, by McGraw-Hill Inc, N.Y, USA.

Tseng, A.A., (1990), Material Characterization and Finite Element Simulation for Forming Miniature Metal Parts, Finite Elements in Analysis and Design, Vol.6, pp. 251-265.

Tvergaard, V., (1993), Necking in Tensile Bars with Rectangular Cross-Section, Computer Methods in Applied Mechanics and Engineering, Vol. 103, pp. 273-290.

Vinnakota, S., (2006), Steel Structures: Behavior and LRFD, 1st Edition, by McGraw-Hill Inc, N.Y, USA.

White, D.W., and Dutta, A., (1993), Numerical Studies of Moment-Rotation Behavior in Steel and Composite Steel-Concrete Bridge Girders, Transportation Research Record, No. 1380, Transportation Research Board, National Academy Press, Washington D.C.

Williams, C.D., and Harris, E.C., (1957), Structural Design in Metals, 2nd Edition, The Ronald Press Company, N.Y, USA.

Yakel, A.J., Mans, P., and Azizinamini, A., (2002), Flexural Capacity and Ductility of HPS-70W Bridge Girders, Engineering Journal, First Quarter, pp. 38-51.

Yang, L., (2004), Evaluation of Moment Redistribution for Hybrid HPS-70W Bridge Girders, Maters Thesis, Department of Civil and Environmental Engineering, West Virginia University, Morgantown, WV.

Yuan, Q., (2004), Investigation of Hole Making Practice in the Fabrication of Structural Steel, M.Sc. Thesis, University of Cincinnati, USA.

Yura, J.A., Galambos, T.V., and Ravindra, M.K., (1978), The Bending Resistance of Steel Beams, ASCE Journal of Structural Division, Vol. 104, No. ST9, pp. 1355-1370.

Zahorsky, M.J., (1994), Flexural Strength of Steel Beam with Holes in the Tension Flange, M.Sc Thesis, Mississippi State University, USA.

Zhang, K.S, and Li, Z.H, (1994), Numerical Analysis of the Stress-Strain Curve and Fracture Initiation for Ductile Material, Engineering Fracture Mechanics, Vol.49, pp. 235-241.

Zener, C., (1945), The Fracture of Steel, Reviews of Modern Physics, Vol.17, Number 1, pp. 20-26.